

WATER-MAGMA INTERACTION AND PLUME PROCESSES IN THE  
2008 OKMOK ERUPTION

By Joel Unema

A Thesis

Submitted in Partial Fulfillment  
of the Requirements for the Degree of  
Master of Science  
in Geology

Northern Arizona University

December 2011

Approved:

Michael Ort, Ph.D., Chair

Nancy Riggs, Ph.D.

Jessica Larsen, Ph.D.

**ABSTRACT**  
**WATER-MAGMA INTERACTION AND PLUME PROCESSES IN THE**  
**2008 OKMOK ERUPTION**  
JOEL UNEMA

Okmok volcano, Aleutian Arc, Alaska, produced five weeks of explosive eruption in July/August 2008 from vents in a 10-km-wide caldera. Water from lakes and aquifers in the caldera interacted with erupting magma (~56% SiO<sub>2</sub>) as evidenced by white steam clouds, fine grain size of deposits, and consumption of caldera lakes during eruption. The eruption produced abundant fine ash and columns of sufficient height to cause significant hazards to air traffic in the North Pacific air traffic corridor, which lies above the Aleutian Arc.

I logged sections within the caldera and on caldera flanks. Grain-size analysis on samples from 25 sites and tephra componentry on selected samples was carried out. MODIS, ASTER, and Landsat data show wind directions and plume distributions during eruption. Shapes and surface features of fine ash particles were examined on the SEM to study variations in water-magma interaction during eruption.

Field observations and results from lab analysis indicate that the eruption opening sequence was dominantly magmatic and that contributions from phreatomagmatic fragmentation increased throughout the eruption through deposition of the upper units, which show evidence for high water-magma ratios. The average grain size of deposits decreases from basal units through the upper units, which have median grain sizes around 4 phi (63-88 μm). Fine ash particles from the basal Unit 1A display complex shapes and high vesicularity, indicating a magmatic origin, while fine ash particles from all other units are predominantly blocky and poorly vesicular, suggesting phreatomagmatic fragmentation as the dominant mechanism in most of the eruption.

The opening sequence on July 12 produced a 16-km-high column, the eruption's highest, and emplaced 3 basal units of ash and lapilli on east caldera flanks. The deposits above these 3 basal units, designated 'upper units', are fine-medium ash with facies including layers of 2-6-mm ash pellets, medium ash laminae interpreted as 'mud rain', and very fine 'ash mist' deposits. Upper units compose the majority of deposit thicknesses within 5 km of vents but thin more rapidly than basal units and disappear at 15 km from vents. I interpret that excess water in the plume scrubbed fine-medium ash, emplacing ash pellets and 'mud rain' in proximal sites, leaving little fine-medium ash to deposit in distal sites. These plume processes reduced the distribution of fine ash downwind of the island and limited the area of aviation hazards.

## **Acknowledgements**

This project was funded primarily by a grant from the American Recovery and Reinvestment Act Volcano Hazards Program. Other funding came from the Bruce “Biff” Reed Scholarship Fund through the GSA Student Research Grants program, the Jack Kleinman Grant for Volcano Research, and the NAU Friday Lunch Clubbe.

I am grateful to the organizations and persons who have provided me with financial, academic, and personal support during my time at Northern Arizona University. All of the faculty and staff in the Geology Department were important in shaping me as a scientist and I would like to thank a few who were especially helpful and influential. Darrell Kaufman, Mary Reid, Larry Middleton, and Jim Sample were particularly important in helping me improve and making my time at NAU more enjoyable.

The Okmok 2010 field season was an incredible experience I will always remember and was made special by my colleagues. Tina Neal, Janet Schaefer, Jim Begét, Ed Clark, Jessica Larsen, and Michael Ort were a fun and encouraging crew to work with and I learned much from each of them. Jess Larsen was also a member of my committee and I am grateful for her input and comments that have truly improved my work. I would also like to thank Nancy Riggs not only for her invaluable contributions to my thesis and writing, but her instruction in volcanology, true friendship, and contagious enthusiasm for geology.

I am truly grateful for my advisor Michael Ort and the many ways he has taught me. I could not have asked for a better thesis topic or a better advisor to guide me

through the many stages of completing research. Michael has been an excellent teacher, a mentor, an introduction to the real world of geology, and a great friend.

My years at NAU were made really enjoyable by my friends and fellow geology students. I am thankful for many of the students, but Zach Anderson, Chuck Samra, Phil Lindner, Megan Arnold, Christina Davis, Jeff Hamlin, and Amanda Cains have been especially important to me. I owe much to my roommate and good friend Jeremy Winston. I am grateful for his friendship and wisdom.

The love and support of my family have always been essential in my life, and never more so than during my graduate studies. I am thankful for the unending love of my parents, the continuing support from my grandparents, and the friendship of my sisters Jodi and Rachel and brothers-in-law Dave and Kyle.

# Table of Contents

<b>Abstract</b> .....	<b>2</b>
<b>Acknowledgements</b> .....	<b>4</b>
<b>Table of Contents</b> .....	<b>6</b>
<b>List of Tables</b> .....	<b>10</b>
<b>List of Figures</b> .....	<b>11</b>
<b>Chapter 1: Introduction and Background</b> .....	<b>16</b>
1.1: Introduction .....	16
1.2: Setting .....	17
1.2a: Tectonic Setting and Aleutian Volcanism .....	17
1.2b: Okmok History and Previous Work .....	17
1.2c: Description of 2008 Eruption .....	19
1.3: Previous work on phreatomagmatism .....	21
1.3a: MFCI-type phreatomagmatism .....	22
1.3b: Continuous phreatomagmatism .....	23
1.3c: Thermal Granulation .....	24
1.3d: Grain-size signatures produced by phreatomagmatism .....	24
1.3e: Componentry and grain shape signatures produced by phreatomagmatism .....	27
1.3f: Surface feature produced by phreatomagmatism .....	29
1.4: Fractal dimension of volcanic particles.....	31
1.5: Previous work on plume processes .....	34
1.6: Hypotheses to test .....	36
<b>Chapter 2: Methods</b> .....	<b>37</b>
2.1: Field methods .....	37
2.2: Remote sensing methods .....	39
2.3: Grain-size analysis .....	40
2.4: Componentry procedure .....	44

2.5: Procedure for grain-shape and surface feature analysis .....	46
2.6: Eruption parameter calculation methods .....	48
2.6a: Eruption volume calculations .....	48
2.6b: Estimation of column height by isopleth area .....	53
<b>Chapter 3: Remote Sensing Results .....</b>	<b>55</b>
3.1: Plume series results .....	55
3.1a MODIS plume series .....	55
3.1b AVHRR plume series results .....	59
3.1c GOES plume series results .....	60
3.2: Plume Character from MODIS, ASTER, GOES, and Landsat.....	66
Interpretations from satellite images of plume characteristics .....	69
3.3: Vent Locations from ASTER and Landsat Data .....	70
<b>Chapter 4: Field Characteristics .....</b>	<b>73</b>
4.1: Overview of 2008 Deposits .....	73
4.1a: Intra-caldera deposits .....	73
4.1b: Extra-caldera deposits .....	73
4.2: Generalized stratigraphic section and unit descriptions .....	74
Unit 1 .....	79
Unit 2 .....	80
Unit 3 .....	80
Interpretations from field observations of basal units .....	82
Upper Units.....	83
Pyroclastic Surge Deposits .....	87
Interpretations from field observations of upper units .....	89
4.3: Distribution of 2008 Deposits .....	90
4.3a: Distribution of Basal Units .....	90
Interpretations from distribution of basal units.....	101
4.3b: Distribution of Upper Units .....	102
Interpretations from distribution of upper units .....	105
4.4: On-axis and across-axis changes in deposits .....	105
4.5: Syn-depositional and post-depositional reworking of 2008 deposits .....	110
4.6: Mass-per-unit-area (MPUA) measurements .....	112

<b>Chapter 5: Grain-size analysis results .....</b>	<b>113</b>
5.1: Grain-size data by unit .....	113
5.1a: Basal Units .....	114
5.1b: Upper Units .....	124
5.1c: Summary of grain-size distribution by unit and facies .....	133
5.2: Quantitative determination of fragmentation mechanism .....	137
Unit 1A .....	138
Unit 1B .....	141
Unit 2 .....	143
Unit 3A .....	145
Unit 3B .....	147
Coarse ash units .....	149
Ash pellets .....	151
Laminated ash .....	153
Upper vesicular ash units .....	156
Interpretations of quantitative grain-size data .....	157
5.3: Qualitative examination of grain-size distributions .....	158
<b>Chapter 6: Componentry Results .....</b>	<b>164</b>
6.1: Componentry categories .....	164
6.1a: Lithic grains .....	164
6.1b: Juvenile grains .....	168
6.1c: Free crystals .....	171
6.2: Error bound calculation .....	172
6.3: Componentry results by location: on-axis sites .....	173
6.4: Componentry results for upper fine units .....	186
<b>Chapter 7: Grain-shape, surface feature, and geochemistry results from SEM analysis....</b>	<b>191</b>
7.1: Examination of componentry categories by SEM .....	191
7.2: Qualitative description of surface features.....	194
Interpretation of qualitative examination of surface features .....	197
7.3: Glass geochemistry from Energy Dispersive Spectroscopy (EDS) .....	198
Interpretations from glass geochemistry .....	199
7.4: Fractal analysis of glass particles .....	200

Interpretations from fractal analysis .....	211
<b>Chapter 8: Discussion .....</b>	<b>212</b>
8.1: Eruption Parameters .....	212
8.1a: Estimation of total eruption volume .....	215
8.1b: Estimation of basal unit volume .....	216
8.1c: Estimation of mass flux during opening sequence .....	217
8.1d: Comparison of measured column height with calculated column height .....	219
8.2: Eruption Mechanisms .....	222
8.2a: Vent Mechanisms .....	222
Classifying Eruptive Style .....	222
Water-magma Interaction .....	229
Style of Phreatomagmatism .....	236
Eruption conduit and multiple vents.....	239
8.2b: Eruption column mechanisms .....	240
8.3: Eruption Model .....	244
<b>References .....</b>	<b>250</b>
<b>Appendices .....</b>	<b>257</b>
Appendix A: Stratigraphic Section .....	257
Appendix B: Selected SEM images .....	294
Appendix C: Guide to digital appendices .....	315

## List of Tables

### Chapter 2: Methods

Table 2.1: Categories used in componentry analysis

### Chapter 4: Field Characteristics

Table 4.1: MPUA calculations for site 10JAUOK002

### Chapter 5: Grain-size analysis results

Table 5.1: Subpopulation modes and fractions for each unit or facies composite

Table 5.2: Grain-size graphical statistics for analyzed averaged units.

Table 5.3: Unit 1A subpopulation information

Table 5.4: Unit 1B subpopulation information

Table 5.5: Unit 2 subpopulation information

Table 5.6: Unit 3A subpopulation information

Table 5.7: Unit 3B subpopulation information

Table 5.8: Coarse ash subpopulation information

Table 5.9: Ash Pellet subpopulation information

Table 5.10: Laminated ash subpopulation information

Table 5.11: Upper vesicular ash subpopulation information

Table 5.12: R (phreatomagmatic fraction) estimated for units and upper facies

Table 5.13: Subpopulation modes and dispersion sorted by mode

Table 5.14: Percentages of phreatomagmatic modes in units and facies

### Chapter 6: Componentry Results

Table 6.1: Error bound calculation from repeat analysis of sample 10JAUOK011A.

Table 6.2: 2-phi and -0.5-phi componentry results for Unit 1A at on-axis sites

Table 6.3: 2-phi and -0.5-phi componentry results for Unit 1B at on-axis sites.

Table 6.4: 2-phi and -0.5-phi componentry results for Unit 2 at on-axis sites.

Table 6.5: 2-phi and -0.5-phi componentry results for Unit 3 at on-axis sites.

Table 6.6: 2-phi and -0.5-phi componentry results for upper fine units at on-axis sites.

Table 6.7: 2-phi componentry results for upper ash-pellet and laminated ash units.

### Chapter 7: Grain-shape, surface feature, and glass geochemistry results from SEM analysis

Table 7.1: Qualitative description of pyroclast shapes, textures and surface features.

### Chapter 8: Discussion

Table 8.1: Eruption Parameter Calculations using ArcGIS method

Table 8.2: Eruption Parameter Calculations using method of Fierstein and Nathanson (1992)

# List of Figures

## Chapter 1: Introduction and Background

- Figure 1.1: Location of Okmok volcano on Umnak Island in central Aleutian Islands.
- Figure 1.2: Geologic map of Okmok caldera with approximate locations of features related to the 2008 eruption.
- Figure 1.3: Illustrations of (a) MFCI experiments and (b) continuous glassy rind growth and disintegration.
- Figure 1.4: Grain-size distributions for dry (a) and wet (b) phreatomagmatic eruptions.
- Figure 1.5: Grain-size distributions of products from thermal granulation experiments.
- Figure 1.6: Plot of conversion efficiency of thermal energy to explosive mechanical energy versus water to melt mass ratio.
- Figure 1.7: SEM images of particles produced by MFCI.
- Figure 1.8: SEM images and Mandelbrot-Richardson plots of a phreatomagmatic particle (top) and a magmatic particle (bottom).

## Chapter 2: Methods

- Figure 2.1: Locations of sample sites from 2008 and 2010 fieldwork.
- Figure 2.2: Averaged results from six analyses of 10JAUOK002E with upper and lower error bounds ( $\pm 2$  S.D.).
- Figure 2.3: Sample plots from Wohletz et al. (1995)
- Figure 2.4: Sites analyzed for componentry.
- Figure 2.5: Triangulated Irregular Network (TIN) surface of total deposits from the 2008 eruption for volume calculation.
- Figure 2.6: Best estimated tephra thickness surface for basal units.
- Figure 2.7: Estimated tephra thickness surface for Unit 1A
- Figure 2.8: Main features of a convecting eruption column, from Carey and Sparks (1986).

## Chapter 3: Remote Sensing Results

- Figure 3.1: MODIS Emissive Data
- Figure 3.2: MODIS Reflectance Data
- Figure 3.3: Plume outlines July 12-14
- Figure 3.4: AVHRR images from the opening sequence of the 2008 eruption
- Figure 3.5: GOES images from the opening sequence of the 2008 eruption
- Figure 3.6: GOES images from the opening sequence of the 2008 eruption
- Figure 3.7: GOES images from the opening sequence of the 2008 eruption
- Figure 3.8: a) Plume directions (MODIS), b) plume height, and c) seismic amplitude by date and time.
- Figure 3.9: MODIS TERRA July 13, 2008 22:25 UTC image showing separated steam and ash plumes
- Figure 3.10: Landsat image from July 13, 2008

Figure 3.11: MODIS images from July 18, July 30, August 2, and August 4 of dark ash-rich plumes.

Figure 3.12: Satellite images from July 13 (top) and July 20 (bottom) with estimated vent locations shown

Figure 3.13: Satellite images from July 22 (top) and after eruption (bottom) with estimated vent locations shown

#### **Chapter 4: Field Characteristics**

Figure 4.1: Isopachs of the total thickness of 2008 Okmok deposits.

Figure 4.2: Isopachs of the total thickness of 2008 deposits within the caldera.

Figure 4.3: Generalized stratigraphic section for extra-caldera deposits (from medial caldera flanks).

Figure 4.4: Annotated photograph of typical medial deposits from station 10JAUOK002

Figure 4.5: Basal units from site 10JAUOK007

Figure 4.6: Units 3A and 3B from site 10JAUOK064

Figure 4.7: Ash pellets from site 10-MOK-30 (photo by Michael Ort)

Figure 4.8: Upper laminated ash from site 10JAUOK012

Figure 4.9: Vesicular top ash from site 10JAUOK005

Figure 4.10: Coarse ash units (within the massive fine ash) from site 10JAUOK075 (top) and 10JAUOK074 (bottom)

Figure 4.11: Pinch-and-swell laminations and possible duneforms from site 10JAUOK079.

Figure 4.12: Surge deposit sample sites. Fort Glenn (red building) and Crater Creek (blue) shown for reference.

Figure 4.13: Isopachs for total coarse basal material (Units 1 and 2). Fort Glenn (red building) and Crater Creek (blue) shown for reference

Figure 4.14: Isopachs for Unit 1 total (Unit 1A + 1B). Crater Creek (blue) shown for reference

Figure 4.15: Isopachs for Unit 1A. Fort Glenn (red building) and Crater Creek (blue) shown for reference

Figure 4.16: Isopachs for Unit 1B. Fort Glenn (red building) and Crater Creek (blue) shown for reference

Figure 4.17: Isopachs for Unit 2. Fort Glenn (red building) and Crater Creek (blue) shown for reference

Figure 4.18: Isopachs for Unit 3. Fort Glenn (red building) and Crater Creek (blue) shown for reference

Figure 4.19: Isopachs for Unit 3A. Fort Glenn (red building) and Crater Creek (blue) shown for reference

Figure 4.20: Isopachs for Unit 3B. Fort Glenn (red building) and Crater Creek (blue) shown for reference

Figure 4.21: Unit 1 Isopleths. Average of the three major diameters of largest five clasts is plotted

Figure 4.22: Upper fine unit isopach map. Fort Glenn (red building) and Crater Creek (blue) shown for reference

Figure 4.23: Contour map of fine ash thickness as a percentage of total deposit thickness

Figure 4.24: On-axis fence diagram

- Figure 4.25: Mid-flanks traverse across-axis fence diagram  
Figure 4.26: Upper-flanks traverse across-axis fence diagram  
Figure 4.27: Examples of post-depositional reworking of 2008 eruption deposits.

## **Chapter 5: Grain-size analysis results**

- Figure 5.1: Unit 1A Sample Sites  
Figure 5.2: Unit 1A grain-size distributions with subpopulation modes in table  
Figure 5.3: Unit 1B grain-size distributions with subpopulation modes in table  
Figure 5.4: Unit 1B Sample Sites  
Figure 5.5: Unit 2 Sample Sites  
Figure 5.6: Unit 2 grain-size distributions with subpopulation modes in table  
Figure 5.7: Units 3A and 3B Sample Sites  
Figure 5.8: Unit 3A grain-size distributions with subpopulation modes in table  
Figure 5.9: Unit 3B grain-size distributions with subpopulation modes in table  
Figure 5.10: Coarse Ash Sample Site Locations  
Figure 5.11: Coarse Ash grain-size distributions with subpopulation modes in table  
Figure 5.12: Ash Pellet Sample Site Locations  
Figure 5.13: Ash Pellet grain-size distributions with subpopulation modes in table  
Figure 5.14: Laminated Ash Sample Site Locations  
Figure 5.15: Laminated ash grain-size distributions with subpopulation modes in table  
Figure 5.16: Upper Vesicular Ash Sample Site Locations  
Figure 5.17: Upper Vesicular Ash grain-size distributions with subpopulation modes in table  
Figure 5.18: Coarse material grain-size distribution normalized to 100% (5-phi through 2-phi material) for composite basal units.  
Figure 5.19: Coarse material grain-size distribution normalized to 100% (5-phi through 2-phi material) for 10JAUOK023.  
Figure 5.20: Coarse material grain-size distribution normalized to 100% (5-phi through 2-phi material) for 10JAUOK002 Units 1A-3.  
Figure 5.21: Coarse material grain-size distribution normalized to 100% (5-phi through 2-phi material) for Units 1-3B from 10JAUOK019.  
Figure 5.22: Grain-size Comparison of Basal Units  
Figure 5.23: Grain-size comparison of Upper Units  
Figure 5.24: Subpopulation fraction vs. mode for Unit 1A.  
Figure 5.25: Subpopulation fragmentation factor vs mode phi size for Unit 1A.  
Figure 5.26: Grain-size distribution of Unit 1A from caldera-rim (012), mid-flanks (007), and island coast (023) locations.  
Figure 5.27: Subpopulation fraction vs. mode for Unit 1B.  
Figure 5.28: Subpopulation fragmentation factor vs mode phi size for Unit 1B.  
Figure 5.29: Subpopulation fraction vs. mode for Unit 2.  
Figure 5.30: Subpopulation fragmentation factor vs. mode phi size for Unit 2.  
Figure 5.31: Subpopulation fraction vs. mode for Unit 3A.  
Figure 5.32: Subpopulation fragmentation factor vs. mode phi size for Unit 3A.  
Figure 5.33: Subpopulation fraction vs. mode for Unit 3B.  
Figure 5.34: Subpopulation fragmentation factor vs mode phi size for Unit 3B.  
Figure 5.35: Subpopulation fraction vs. mode for coarse ashes.

- Figure 5.36: Subpopulation fragmentation factor vs. mode phi size for coarse ashes.  
 Figure 5.37: Subpopulation fraction vs. mode for ash pellets.  
 Figure 5.38: Subpopulation fragmentation factor vs mode phi size for ash pellets.  
 Figure 5.39: Subpopulation fraction vs. mode for laminated ash.  
 Figure 5.40: Subpopulation fragmentation factor vs. mode phi size for laminated ash.  
 Figure 5.41: Subpopulation fraction vs. mode for upper vesicular ash.  
 Figure 5.42: Subpopulation fragmentation factor vs. mode phi size for upper vesicular ash.  
 Figure 5.43: R values and % of 2, 3, and 4-phi subpopulations plotted for each unit and facies type.

## **Chapter 6: Componentry Results**

- Figure 6.1: Lithic grain componentry category examples.  
 Figure 6.2: Juvenile grain and free crystal componentry category examples  
 Figure 6.3: Componentry sample site locations with basal isopachs.  
 Figure 6.4: Stratigraphic section for 10JAUOK011  
 Figure 6.5: Stratigraphic section for 10JAUOK002  
 Figure 6.6: Stratigraphic section for 10JAUOK006  
 Figure 6.7: Stratigraphic section for 10JAUOK023  
 Figure 6.8: Grain-size distribution of Unit 1A samples  
 Figure 6.9: Grain-size distribution of Unit 1B samples  
 Figure 6.10: Grain-size distribution of Unit 2 samples  
 Figure 6.11: Grain-size distribution of Unit 3 samples  
 Figure 6.12: Grain-size distribution of upper unit samples  
 Figure 6.13: Selected 2-phi componentry results.  
 Figure 6.14: -0.5-phi brown pumice abundance by location and unit  
 Figure 6.15: Stratigraphic section for 10JAUOK005  
 Figure 6.16: Stratigraphic section for 10JAUOK066  
 Figure 6.17: Grain-size distribution of ash-pellet and laminated ash units  
 Figure 6.18: 2-phi componentry for upper ash-pellet and laminated ash units.

## **Chapter 7: Grain-shape, surface feature, and glass geochemistry results from SEM analysis**

- Figure 7.1: SEM images of juvenile grains and free crystals from componentry categories described in Chapter 6  
 Figure 7.2: SEM images of lithic grains from componentry categories described in Chapter 6.  
 Figure 7.3: Glass geochemistry of 2-phi component types  
 Figure 7.4: SEM images showing characteristic textures, surfaces features and grain shapes  
 Figure 7.5: Percentage of grains with stepped surfaces and blocky shapes in analyzed samples.  
 Figure 7.6: Glass geochemistry for analyzed samples, from EDS analysis on the NAU SEM.  
 Figure 7.7: Glass grains 074A g5 and 074A g6 with 65 wt% SiO<sub>2</sub>.

Figure 7.8: SEM image and fractal analysis of high fractal dimension particle 011C g6  
Figure 7.9: SEM image and fractal analysis of high fractal dimension particle 011B g10.  
Figure 7.10: SEM image and fractal analysis of low fractal dimension particle 011D g12.  
Figure 7.11: SEM image and fractal analysis of low fractal dimension particle 074A g13  
Figure 7.12: SEM image and fractal analysis of intermediate fractal dimension particle 011F g10.  
Figure 7.13: SEM image and fractal analysis of intermediate fractal dimension particle 011E g6  
Figure 7.14: SEM image and fractal analysis of multifractal particle 011A 2.  
Figure 7.15: SEM image and fractal analysis of multifractal particle 011D g16.  
Figure 7.16: Percentage of fractal grain types by unit.

### **Chapter 8: Discussion**

Figure 8.1: Log of thickness versus the square root of area for Okmok 2008 total deposits  
Figure 8.2: Log of thickness versus the square root of area for Okmok 2008 Units 1-3A  
Figure 8.3: Isopleths for Unit 1 with calculated areas.  
Figure 8.4: Isopleth area vs. maximum pumice size for lithic clasts with density of 1500 kg/m<sup>3</sup>.  
Figure 8.5: Isopleth area vs. maximum pumice size for lithic clasts with density of 2500 kg/m<sup>3</sup>.  
Figure 8.6: Plot of tephra thickness vs. isopach area.  
Figure 8.7: Plot of standard deviation versus median diameter (phi size) for samples from 2008 Okmok Deposits  
Figure 8.8: Post-eruption geology and features of Okmok Caldera  
Figure 8.9: Contour map of fine ash thickness as a percentage of total deposit thickness

# Chapter 1: Introduction and Background

## 1.1 Introduction

Water-magma interaction produces a variety of eruption styles ranging from passive magma quenching to violent vapor explosions in Surtseyen, Vulcanian, and phreatoplinian eruptions. Phreatomagmatic eruptions, in which rising magma interacts with water in lakes or aquifers, are often made more explosive by this involvement of water, producing abundant fine ash and energetic eruption columns (Wohletz 1983). Okmok volcano, a historically active shield volcano on Umnak Island, Aleutian arc, Alaska, erupted explosively in 2008 from vents within a 2050 BP caldera. This eruption produced 16-km-high columns and deposited thick beds of fine-ash dominated tephra. The explosivity, fine-ash production, observations of white steam clouds, and the consumption of caldera lakes during eruption suggest that water-magma interaction was important in controlling the eruption mechanism (Larsen et al. 2009).

While water-magma interaction was likely important in the 2008 eruption, the characteristics of the eruption and deposits are not typical for explosive phreatomagmatism. Deposits from the 2008 eruption lack typical maar-type repetitive bedding, juvenile clasts are vesicular, and observations of the eruptions suggest more continuous eruption than maar-type pulsing. Understanding the production and deposition of fine ash in the 2008 Okmok eruption is crucial to anticipating hazards from similar eruptions in Alaska and expanding knowledge of phreatomagmatism.

## **1.2 Setting**

### **1.2a Tectonic Setting and Aleutian Volcanism:**

Subduction of the Pacific plate beneath the North American plate drives volcanism on the Aleutian chain and Alaska Peninsula, making the Aleutian arc one of the most active on Earth, with 54 historically active volcanoes (Alaska Volcano Observatory 'About Alaska's Volcanoes'). The Aleutian arc is divided, at around 165° W longitude, into an eastern continental margin section and western oceanic island arc (Miller et al. 1998). The angle at which the Pacific and North American plates interact is closest to normal in the eastern-central Aleutians and becomes oblique in the western Aleutians.

Eastern Aleutian continental-margin volcanoes typically erupt magmas with 56-65 wt% SiO<sub>2</sub>, whereas western Aleutian oceanic arc magmas are commonly 47-59 wt% SiO<sub>2</sub> (Miller et al. 1998). Aleutian volcanoes have erupted on average 1.1-1.3 times per year since consistent reporting began in AD 1760. Seven volcanoes, including Okmok, have produced 60% of recorded historical eruptions and most eruptions from these seven volcanoes are strombolian or vulcanian. Areas surrounding most Aleutian volcanoes are sparsely populated, but the heavily used North Pacific air traffic corridor connecting Asia and the west coast of the United States lies above the Aleutian arc, making eruptions from these remote volcanoes hazardous to many aircraft (Begét et al. 2005).

### **1.2b Okmok history and previous work**

Okmok is a shield volcano located on Umnak Island in the central eastern Aleutian Islands (Fig. 1.1) and has been frequently active throughout historic times. Historic

eruptions have issued from several vents within a 10 km-wide caldera that formed around 2050 BP (Begét et al. 2005). The 2050 BP caldera is nested within another caldera that formed around 12,000 BP. The three most recent eruptions prior to the 2008 event came from Cone A on the southwest margin (Fig. 1.2) of the caldera, and the most recent hazards maps were made based on the assumption that the most likely next eruption would also be produced by Cone A and be similar in style to prior Cone A eruptions (Begét et al. 2005).

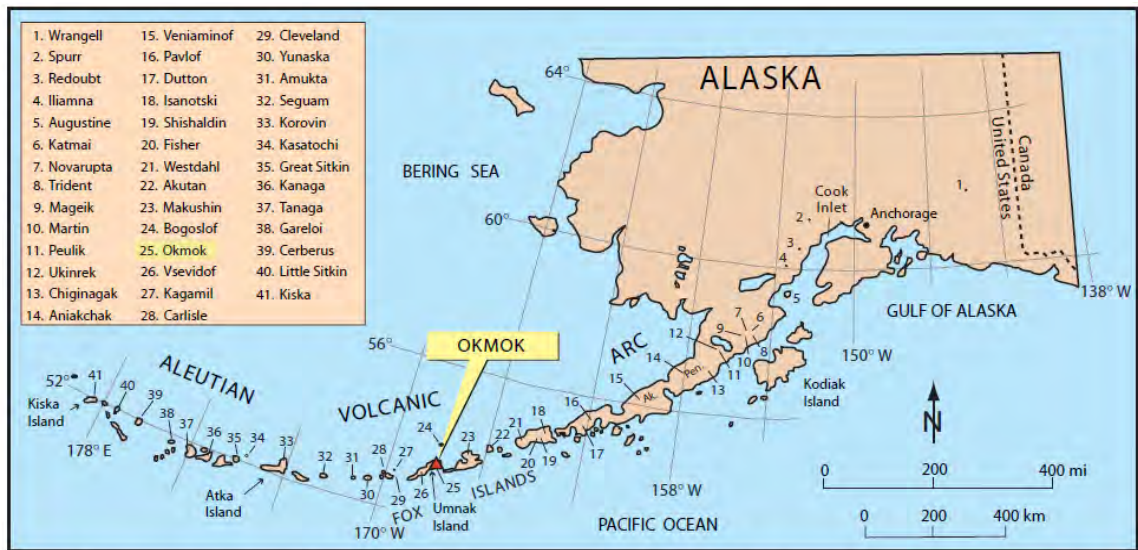


**Figure 1.1:** Location of Okmok volcano on Umnak Island in central Aleutian Islands. From Begét et al. (2005).

The eruption prior to the 2008 event occurred over eight months in 1997, sending ash clouds up to 9 km above sea level and producing lava flows extending 6 km from Cone A (Begét et al. 2005). Okmok volcano also had some activity in 1981, 1983, and 1987 that was not closely observed. Ash and steam clouds were reported to reach 5 km above sea level and a small pyroclastic flow was observed emitting from Cone A (Begét et al. 2005). An eruption from Cone A in 1958 had several explosive events that deposited tephra up to 10 cm thick at 9 km from the vent on the southern flanks of the caldera

(Begét et al. 2005). The 1958 eruption also produced lava flows that blocked Crater Creek, the stream draining the caldera, and formed a lake north of Cone D (Fig 1.2). This lake was involved in the 2008 eruption and currently drains through alluvium beneath the 1958 lava flow. Crater Creek exits through a breach in the caldera walls and enters the Bering Sea.

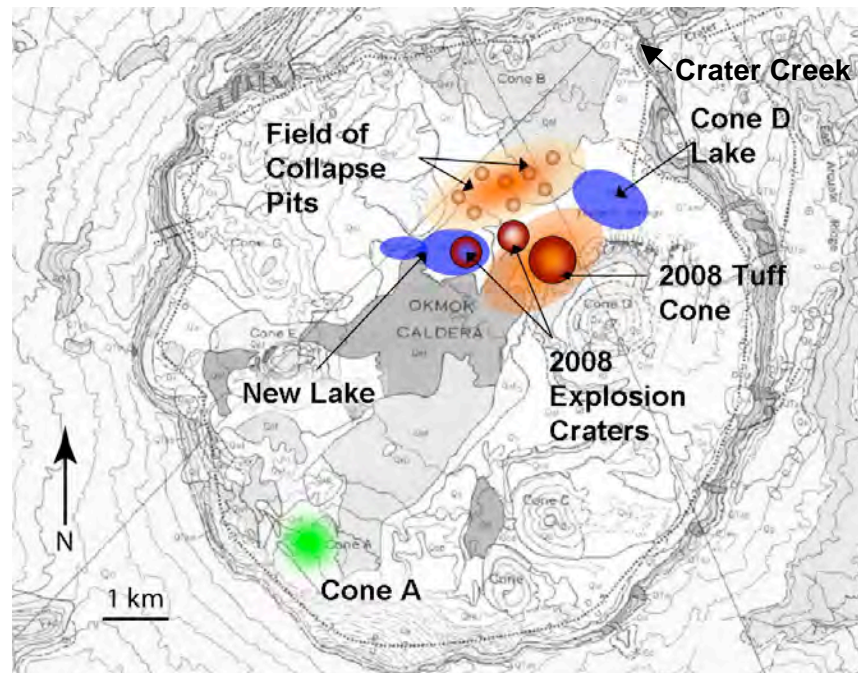


**Figure 1.2:** Geologic map of Okmok caldera with approximate locations of features related to the 2008 eruption. Base map is from Byers (1959).

### 1.2c Description of 2008 eruption

Larsen et al. (2009) described the opening of the 2008 eruption on the morning of July 12. The U.S. Coast Guard received an emergency call from residents of a cattle ranch on the flanks of the volcano and notified the Alaska Volcano Observatory (AVO). The opening sequence of the eruption produced a 16-km-high column that was driven east by west winds. After several hours of violent eruption, the intensity decreased and

remained at lower levels for the duration of the eruption, until August 19. Seismic activity preceding the eruption opening was limited to 5 hours of low-level activity that was not recognized as precursory until after the eruption had begun. Upon the eruption beginning at 1943 UTC, strong continuous seismic tremor began and lasted for 10 hours.

Satellite data from MODIS, AVHRR, and GOES showed water-rich plumes with a weak ash signal and allowed estimation of the column height for the opening sequence at 16 km. After the opening sequence, plume heights decreased and ranged from 2-12 km for the duration of the eruption, as observed by the AVO and measured by remote sensing. AVO personnel observed the eruption from aircraft and from the ground during the eruption and noted multiple active vents around Cone D (Fig. 1.2). Vents opened through the Cone D lake and on the caldera floor north of Cone D, but by August 13, activity was limited to a single tuff cone.

AVO personnel returned to Umnak Island for field mapping and sample collection after the eruption ended, in September 2008. AVO personnel described fine-grained fall deposits covering much of the island and sampled multiple stratigraphic units at several sites. The described deposits consisted of coarse-grained basal fall units and upper deposits made up of massive and laminated beds of fine ash. The repetitive bedding patterns often seen in maar-type phreatomagmatic deposits were not observed; rather, the bulk of deposits consisted of thick packages of fine ash. This correlated well with observations of the eruption after the opening sequence, when columns appeared predominantly continuous with some distinct pulses within the steady column.

AVO geologists found clasts from the 2008 eruption to be finely vesicular, an unexpected characteristic for products of an eruption that appeared to be predominantly

phreatomagmatic. I received samples in fall 2009 and sieved them to examine grain-size distributions. Samples from basal deposits were found to be coarse grained, consisting mainly of lapilli and coarse ash, while most samples from higher stratigraphic positions were dominated by fine ash. I also examined 2- and 3-phi ash fractions separated during sieving and found that the ash particles were typically blocky but had significant vesicularity.

The field observations made by AVO geologists during the eruption and September 2008 field work combined with the sample analysis data prompted a number of questions that guided this study. The apparent phreatomagmatic character of the 2008 eruption was suggested by the steam-rich plumes, enhanced explosivity, the consumption of caldera lakes during eruption, and fine grain size of deposits. However, common characteristics of maar-type MFCI phreatomagmatism were absent in the eruption dynamics and the deposits. The eruption columns did not appear dominantly pulsatory and the deposits lack repetitive bedding. The larger clasts and ash grains are vesicular, an unusual characteristic for products of phreatomagmatic fragmentation. In the 2010 fieldwork and lab analysis of tephra characteristics, I sought to examine water-magma interaction in the 2008 eruption, and how it may have differed from the well-understood mechanism of maar-type MFCI phreatomagmatism.

### **1.3 Previous work on phreatomagmatism**

Phreatomagmatic eruptions are important because they have great explosive potential and many types, like the 2008 Okmok event, are poorly understood. These eruptions result from the interaction of magma with non-magmatic water, resulting in

explosions, rapid cooling, and fragmentation, producing fine ash. Several mechanisms of phreatomagmatic have been described, including Molten Fuel Coolant interaction, thermal granulation, and continuous phreatomagmatism.

### **1.3a MFCI-type phreatomagmatism**

Fragmentation in some phreatomagmatic eruptions occurs by the well-understood mechanism of Molten Fuel Coolant Interaction (MFCI), a phenomenon well studied in industrial settings in which molten metal interacts with liquid water. MFCI experiments have been adapted to study volcanoes and simulate water-magma interaction by injection of water into a silicate melt (Fig. 1.3a) (Zimanowski et al. 1991). After the water encounters the surface of the magma, a film of water vapor forms on the surface of the melt, providing insulation until vapor-film collapse occurs spontaneously or is initiated by a shock wave, allowing rapid transfer of heat from magma to water. This converts thermal energy into mechanical energy in the form of extensive and explosive fragmentation (Zimanowski et al. 1991). MFCI is a coupled, self-propagating interaction that, through fragmentation, increases surface area and provides more sites for water-magma interaction. MFCI appears to accurately describe the interaction and deposits of maar-type phreatomagmatism with pulsing eruptions. MFCI experiments have been unable to produce explosive interaction of water with a vesicular magma, as gas bubbles within magma are compressible and absorb shock waves travelling through the magma. Fragmentation in MFCI interactions propagates with shock waves, so absorption of shock waves by gas bubbles prevents efficient fragmentation and fine ash production.

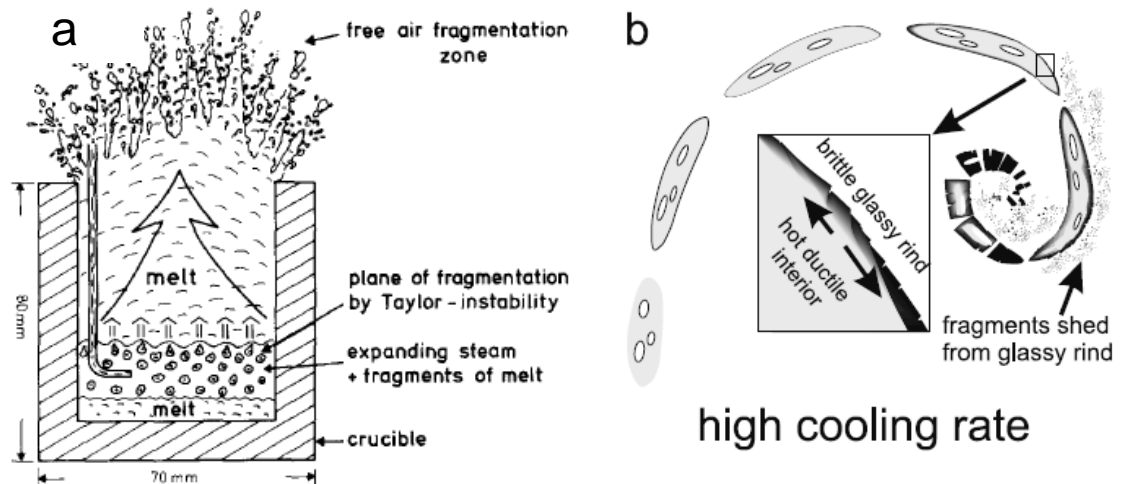


**Figure 1.3:** Illustrations of (a) MFCI experiments (Zimanowski et al. 1991) and (b) continuous glassy rind growth and disintegration (Mastin 2007).

### 1.3b Continuous phreatomagmatism

An alternative model developed by Mastin (2007) suggests that fine ash can be produced in phreatomagmatic eruptions by the growth and disintegration of glassy rinds (Fig. 1.3b). Magma fragments erupting into a setting with abundant water cool rapidly and may develop thin exterior glassy rinds while their interiors remain liquid and deform, shedding the glassy rinds as fine ash fragments (Mastin 2007). Mastin's glassy rind model (2007) also provides a mechanism for generation of fine ash for vesicular magmas interacting with water, which has posed a significant problem for MFCI.

The growth and generation of glassy rinds requires external momentum inputs to cause the turbulent deformation or shredding of magma particles in order to shed glassy rinds. The generation of fine ash by this process has been observed at littoral cones where momentum for turbulent deformation is supplied by ocean wave energy. In non-littoral settings, momentum may be supplied by a primary magmatic eruption driven by

gas expansion, and water-magma interaction may serve to reduce grain size rather than provide explosive energy.

### **1.3c Thermal Granulation**

When water and magma interact on a timescale longer than observed for MFCI vapor explosions but shorter than observed for pillow-lava formation, magma fragments by thermal granulation (Sonder et al. 2011). Magma in contact with water rapidly cools and contracts, breaking into blocky particles (Sonder et al. 2011). Thermal granulation consumes thermal energy from the magma but does not add energy to an eruption column in a way similar to MFCI vapor explosions. The conversion of thermal energy to fragmentation in thermal granulation is much less efficient than in a vapor explosion, producing coarser-grained pyroclasts than are produced in vapor explosions (Sonder et al. 2011). The vesicularity of a magma likely has little effect on thermal granulation.

### **1.3d Grain-size signatures produced by phreatomagmatism**

Phreatomagmatic eruptions in basaltic systems produce significant amounts of fine ash (smaller than 0 phi) and very fine ash (smaller than 5 phi) (Wohletz 1983). Fine ash can be generated by rapid vesiculation in explosive eruptions, grain-size reduction in pyroclastic currents, and rapid fragmentation in water-magma interactions (Rose and Durant 2009). Fine-ash generation in a phreatomagmatic eruption requires both turbulence and rapid cooling (Mastin 2007). In MFCI, both of these are supplied by the collapse of the vapor film, bringing magma and water in direct contact. Rapid cooling and high deformation rate fragment magma in a brittle fashion, forming cooled blocky

fine-ash particles. Generation of fine ash requires high energy to cause the mechanical breakage and the tremendous increase in surface area (Büttner et al. 2002). The rapid conversion of thermal energy into mechanical fragmentation in MFCI vapor explosions provides the energy required to generate fine ash. Büttner et al. (1999) give sample grain-size distributions for phreatomagmatic eruptions with low water-magma ratios (dry) and high water-magma ratios (wet) (Fig. 1.4). Thermal granulation produces coarser-grained tephra than MFCI vapor explosions, as the conversion of thermal to mechanical energy is less efficient (Fig. 1.5). Grain-size peaks for products of thermal granulation experiments are around -1 to 0 phi, while those of products of MFCI experiments range from 2 to 4 phi. The grain-size distributions of tephra produced by the continuous phreatomagmatism described by Mastin (2007) have not been studied. Fine ash would be abundant in the products of a continuous phreatomagmatic eruption, but median grain size would likely be larger than that in MFCI-type interaction, as the rate of conversion from thermal energy to mechanical fragmentation is lower.

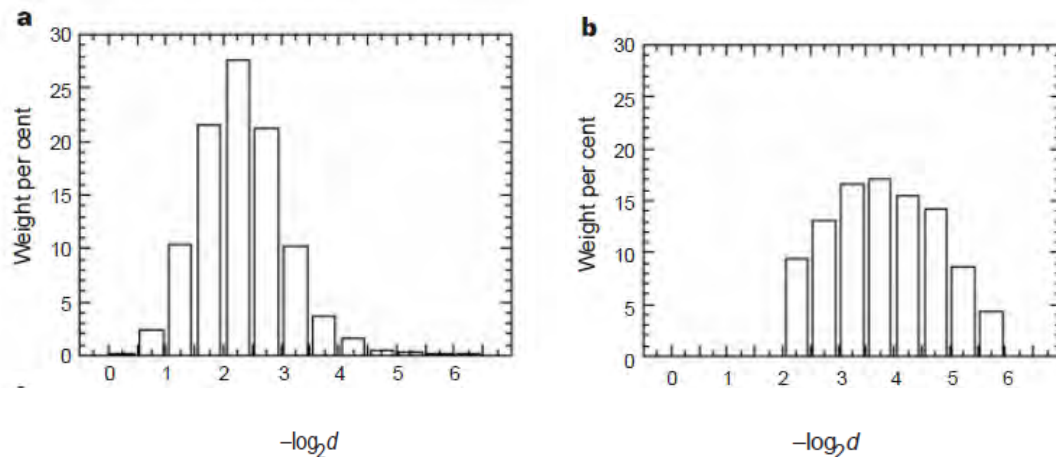


**Figure 1.4:** Grain-size distributions for dry (a) and wet (b) phreatomagmatic eruptions (Büttner et al. 1999). ‘d’ is particle diameter, ‘ $-\log_2 d$ ’ is equal to phi size.

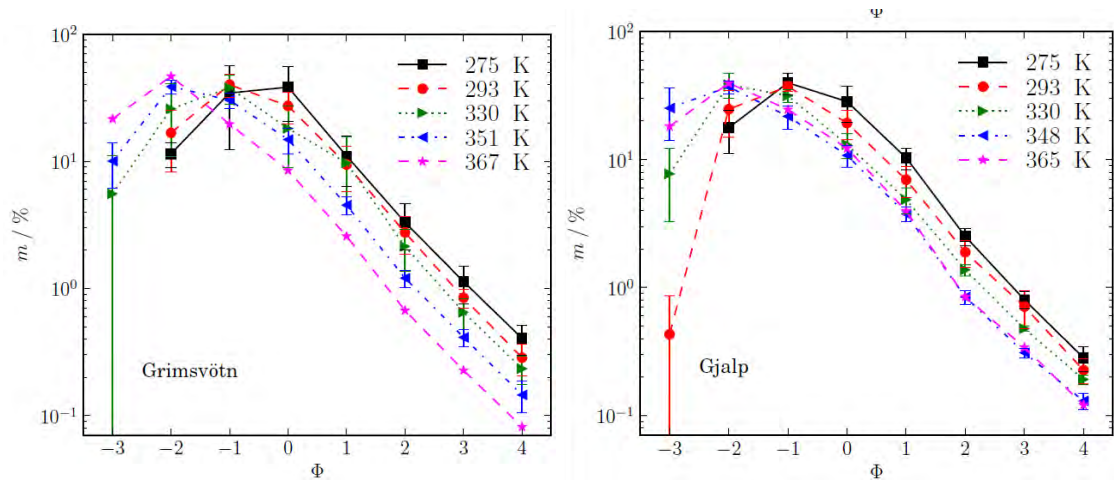


**Figure 1.5:** Grain-size distributions of products from thermal granulation experiments at varying coolant temperatures (shown in varying colors and symbols). (Sonder et al. 2011). The x-axis shows phi size ( $\log_2$  of particle diameter in mm), and the y-axis shows mass percent (m/%).

The ratio of magma to water in a phreatomagmatic eruption is a major control on the fragmentation efficiency and the resulting deposit grain-size distribution ( Wohletz 1983). Fragmentation efficiency reaches a maximum and median grain size reaches a minimum when water:magma ratios are close to 0.3:1 by weight or around 1:1 by volume (Fig 1.6).

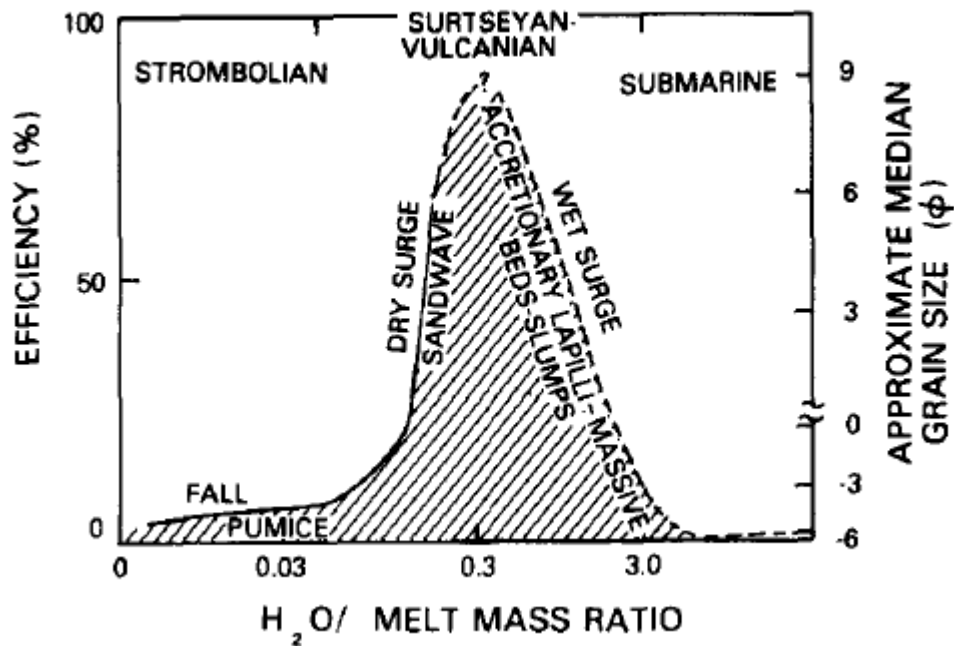


**Figure 1.6:** Plot of conversion efficiency of thermal energy to explosive mechanical energy versus water to melt mass ratio (Wohletz 1983).

When water-magma ratios are low, insufficient water exists to cause rapid cooling and brittle fragmentation. In eruptions with excess water (water-magma mass ratios above 0.3), fragmentation efficiency decreases and a ‘wet’ or condensed steam eruption occurs (Wohletz 1983).

### 1.3e Componentry and grain shape signatures produced by phreatomagmatism

Phreatomagmatic fragmentation produces ash particles with shapes distinct from those fragmented magmatically. Phreatomagmatic eruptions commonly produce equant, blocky grains with poor vesicularity. Water-magma interaction induces rapid cooling of magma and fragmentation resulting in broken edges. MFCI experiments demonstrate

that the rapid transformation of thermal energy into mechanical energy produces fine ash fragments with blocky, equant shapes and edges reflecting brittle failure, features discussed in detail below (Büttner et al. 2002).

An important difference between tephra from phreatomagmatic and magmatic eruptions is that the grains in the former show broken edges, while the grains in the latter show edges controlled by surface tension or more rounded edges (Mastin 2007). When magma fragments cool more slowly in the absence of groundwater interaction, their edges become rounded as surface tension reduces fragment surface area during cooling. These magmatic fragments are commonly angular and display curvilinear surfaces. Ash produced in a continuous phreatomagmatic eruption displays grain shapes distinct from either MFCI phreatomagmatism or magmatic eruption. The spalling of glassy rinds produces fine ash with curved flake-like shapes (Mastin 2007). Spalled glassy rinds described by Mastin (2007) range from 20  $\mu\text{m}$  to 500  $\mu\text{m}$ .

Pyroclasts produced by phreatomagmatic fragmentation generally have lower vesicularity than those fragmented magmatically. Gas expansion is the primary mechanism in magmatic fragmentation, and it produces bubble-shard shapes and vesicular frothy particles. The vesicularity of magmatically fragmented pyroclasts varies based on the amount of dissolved volatiles in the magma at depth. Water-magma interaction does not directly control the vesicularity of erupted clasts. Rather, the vesicularity of products is a result of the gas content and degree of gas exsolution in the magma. Magma with exsolved gas bubbles is a poor material for the rapid transformation of thermal energy to mechanical energy that takes place in phreatomagmatism and causes fragmentation and fine ash generation. Magma is a nearly

incompressible liquid and exsolved gas bubbles are compressible. Gas bubbles may act as a cushion, preventing the propagation of energy waves through magma, and inhibiting fragmentation. In phreatomagmatic interactions, a shock wave is required to break the vapor film that insulates the magma from water. High vesicularity magmas are unable to propagate this shock wave, and phreatomagmatic fragmentation cannot occur (Zimanowski 1991). In eruptions alternating between magmatic and phreatomagmatic, tephra produced show a decrease in vesicularity during phreatomagmatic events.

The ratio of juvenile and lithic clasts in deposits can also be affected by the degree of water-magma interaction in an eruption. Phreatomagmatic eruptions commonly deposit more lithic-rich tephra than magmatic eruptions. Phreatomagmatic steam explosions at depth fragment country rock surrounding the conduit and expel tephra with up to 90% lithic clasts (Raue 2004; Zimanowski 1998.) Magmatic fragmentation in basaltic to intermediate eruptions occurs more gradually as gas expands and drives magma ascent, so lithic clast content is typically lower than in a phreatomagmatic tephra.

### **1.3f Surface features produced by phreatomagmatism**

Water-magma interaction is well evidenced in the grain shapes and surface features of ash particles, producing blocky equant grains with quenching cracks (Fig. 1.7 c, d) or stepped surfaces (Fig. 1.7 a, b) (Büttner et al. 1999). Stepped surfaces on fine ash particles are produced in phreatomagmatic eruptions with both low and high water-magma ratios. Stepped surfaces are formed when cooling and deformation rates are so high that magma fragments in a brittle manner. Quenching cracks result from sudden

cooling and contraction after fragmentation has occurred. Eruptions with high water-magma ratios produce more particles with quenching cracks than eruptions with low water-magma ratios. These features show the contact of magma with external water, and the abundance of such features in each layer can be linked to water-magma mass ratios in each layer (Büttner et al. 1999). The abundance of blocky, poorly vesicular grains and grains with quenching cracks or step fractures can be used to qualitatively compare the level of water-magma interaction between units.

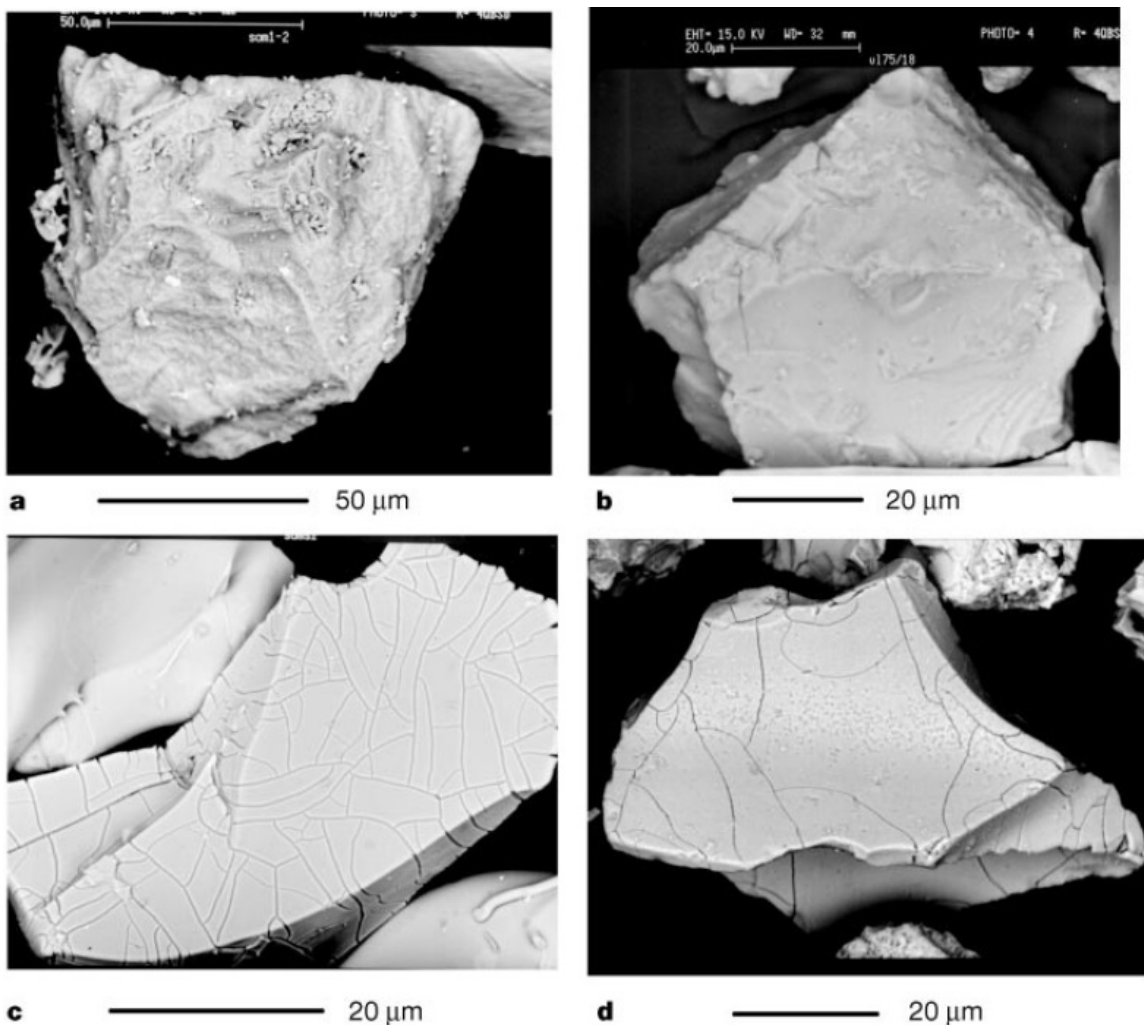


**Figure 1.7:** SEM images of particles produced by MFCI (a, c) and natural deposits of La Fossa di Vulcano (b, d) showing stepped surfaces (a, b) and quenching cracks (c, d) (from Büttner et al. 1999).

#### **1.4 Fractal dimension of volcanic particles**

Dellino and Liotino (2002) used fractal analysis of volcanic glass grains to distinguish particles fragmented magmatically from those fragmented phreatomagmatically. Fractal analysis is carried out by calculating the perimeter of a grain by approximating it with a polygon with a defined step size. This process is repeated for many (50) step sizes and the resulting perimeters are plotted against step size on a logarithmic scale in a Mandelbrot-Richardson (M-R) plot (Fig. 1.8). Fractal analysis examines the irregularity of an outline from a small textural scale to a large structural scale. The shape of an entire particle is described by the structural scale, while the smaller scale irregularity of the individual surfaces of a particle is described by the textural scale. A true fractal (monofractal) particle has a constant degree of irregularity from textural to structural scale and plots as a single straight line on an M-R plot, while a multi-fractal particle has varying degrees of irregularity from the textural to structural scale, and will plot as multiple line segments on an M-R plot (Dellino and Liotino 2002).

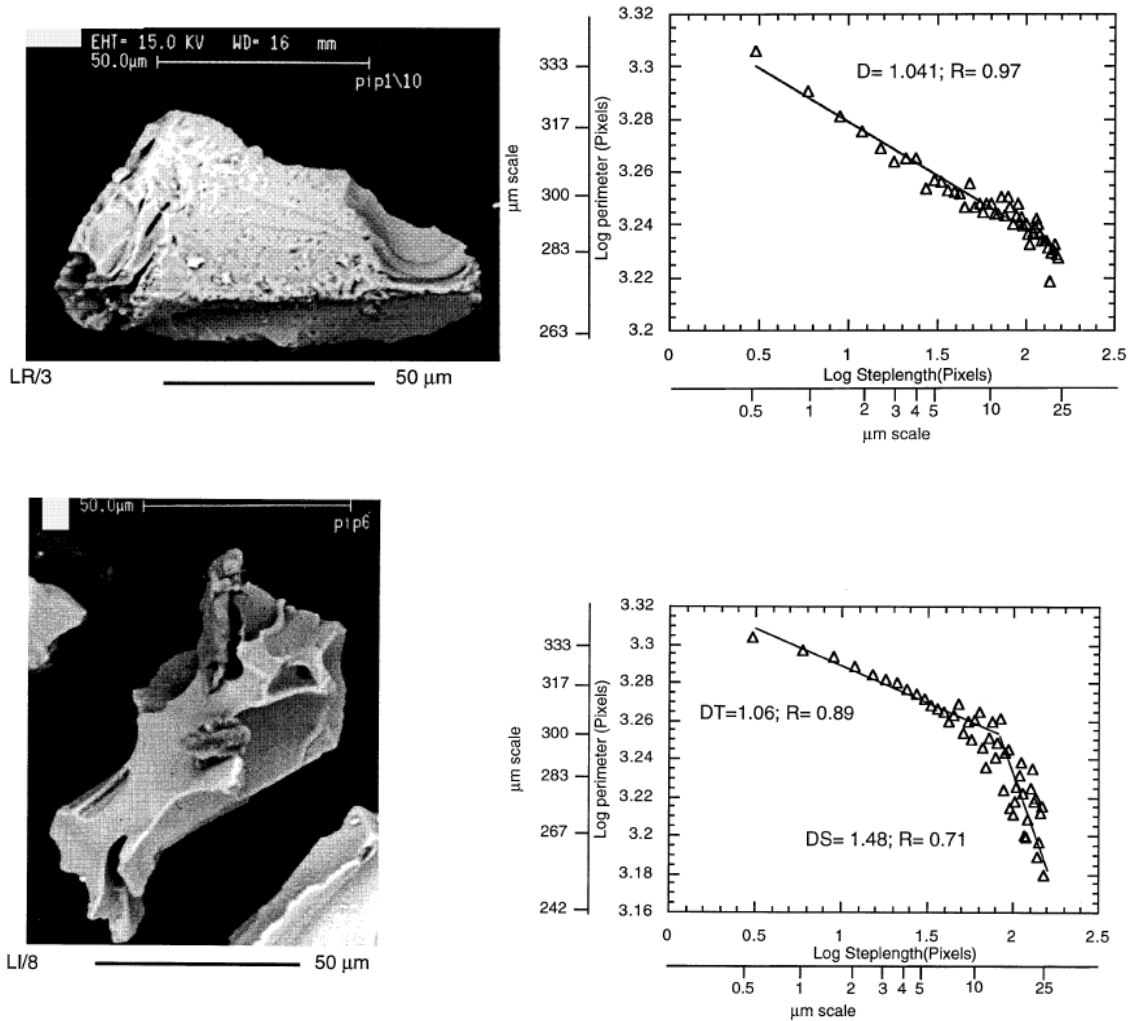


**Figure 1.8:** SEM images and Mandelbrot-Richardson plots of a phreatomagmatic particle (top) and a magmatic particle (bottom) (Dellino and Liotino 2002).

Phreatomagmatic fragmentation produces true fractal particles with simple shapes on a small (textural) scale as well as on a whole-particle (structural) scale because all regimes of phreatomagmatic fragmentation are dominated by brittle fragmentation (Dellino and Liotino 2002). A phreatomagmatic particle plots as a single straight line on an M-R plot (Fig. 1.8 top). Magmatic fragmentation produces multi-fractal particles with more complex shapes on a structural scale created by the vesicle walls left by gas

expansion and simple shapes on a textural scale, as breakage at a textural scale is dominantly brittle (Dellino and Liotino 2002).

The D value, or fractal dimension, of a particle is calculated by  $D=1-S$ , where S is the slope of the line of best fit to the points on the M-R plot (Fig 1.8). The D value represents the degree of irregularity of a particle. A simple shape such as a perfect square or triangle has a D value of 1, a shape with infinite complexity has a D value of 2, and shapes of geologic interest have D values typically in the range 1-1.36 (Dellino and Liotino 2002). Monofractal particles have a single D value, signifying that there is a constant degree of irregularity from the smallest textural scale to the largest structural scale. This constant degree of irregularity is produced by a single fragmentation regime being dominant at all measured scales. In a phreatomagmatic particle, a brittle form of fragmentation produces the grain shape (typically blocky) and the texture of grains (typically non-complex). Multifractal particles have multiple D values, indicating that the degree of irregularity is different on a small textural scale than on a large structural scale. The magmatic particles examined by Dellino and Liotino (2002) were multifractal particles, having lower D values (less irregular) on textural scales and higher D values (more irregular) on structural scales. Magmatic fragmentation by gas expansion produces complex shapes formed by vesicle walls, leading to highly irregular particle shapes and a high D value on structural scales. On a smaller textural scale, these magmatically fragmented particles break in a brittle fashion, producing textures that are less complex (low D) and similar to those observed in phreatomagmatic particles (Dellino and Liotino 2002).

Different fragmentation regimes occurring at a textural scale and structural scale will create multifractal particles. The fractal dimensions of particles alone cannot characterize them as magmatically or phreatomagmatically fragmented, but these indications can be confirmed by qualitative examination of grain vesicularity, shape, and surface features. Phreatomagmatic fragmentation in a MFCI vapor explosion or thermal granulation occurs in a brittle fashion, producing monofractal particles. The growth and shedding of glassy rinds also breaks particles in a brittle fashion, as rinds are solid when they are spalled off of pyroclasts. It is unlikely that different regimes of phreatomagmatic fragmentation would produce particles with multifractal shapes.

### **1.5 Previous work on plume processes**

Ash aggregation and other plume processes can control fine-ash deposition and emplace deposits with distinct features. Ash aggregation can occur through the capillary forces of liquid films from condensed moisture or by electrostatic attraction between charged particles (Schumacher and Schmincke 1995). Liquid-film binding plays a greater role in aggregation in wet plumes, like those produced in the 2008 Okmok eruption. Experiments on liquid film binding of volcanic ash show that agglomeration (aggregation) is possible with 10-25 wt.% water and is most successful between 15 and 25 wt.% water (Schumacher and Schmincke 1995). Natural ash-aggregate deposits that formed through liquid-film binding are typically made up primarily of ash <350  $\mu\text{m}$  in diameter. Experiments by Schumacher and Schmincke (1995) show that more water is needed for aggregation when particles >350  $\mu\text{m}$  are included. The grain sizes of tephra produced at the vent and carried into eruption columns can affect the formation of ash

aggregates. Examining grain-size distribution of deposits with ash aggregates and those without may reveal if grain size produced at vents affects ash aggregation.

Electrostatic attraction can be a primary force for ash aggregation in plumes without liquid water to bind particles. Experimental ash aggregates produced by electrostatic attraction are finer grained than those formed by liquid film binding and exclude particles  $>180\ \mu\text{m}$  (Schumacher and Schmincke 1995). Larger ash particles can be included in aggregates through other processes. Particles  $>500\ \mu\text{m}$  in diameter can act as agglomeration nuclei around which liquid film binding can form an aggregate of fine ( $<350\ \mu\text{m}$ ) ash (cored or accretionary lapilli). Plume water contents above 30 wt.% do not effectively support ash aggregation by liquid film binding (Schumacher and Schmincke 1995), but may wash ash from the column, depositing ‘ash rain’ without discrete aggregate forms.

Walker (1981) observed microbedding and alternating laminations of fines-depleted ash and fine ash with millimeter-scale downbowings (flat-lying, slightly concave-up thin laminae) in the Taupo Hatepe ash, which he attributed to deposition in a ‘ash rain’. Vesicular ash units were also observed in beds inferred to be deposited by ‘ash rain’ (Walker 1981). Alternating laminations of medium-coarse ash and fine ash, millimeter-scale downbowings, and vesicular ash may indicate deposition by ‘ash rain’.

Ash aggregates are abundant in 2008 Okmok deposits and ‘ash rain’ was observed during the eruption. Both of these processes remove fine ash from eruption columns and deposit it more proximally than would be predicted if these processes are neglected. Understanding the factors controlling ash aggregation and washing of ash from eruption columns is important to interpreting the significance of the fine ash facies present.

## **1.6 Hypotheses to test**

The following hypotheses are proposed to examine water-magma interaction and plume processes in the 2008 Okmok eruption.

- 1) Water-magma interaction increased the explosivity of the 2008 Okmok eruption and the level of water-magma interaction varied throughout the eruption, producing variations in grain size, shape, and componentry.
- 2) Ash pellets and mud rain were deposited under different eruption column conditions and may have some measurable grain-size differences.
- 3) Plume scrubbing deposits, such as ash pellets and mud rain, reduce the areal extent of fine ash, reducing aviation hazards.

These hypotheses were tested by remote sensing, field observations, and lab analysis of collected samples. Chapter 2 describes each of the methods used in detail. Chapter 3 presents results from remote sensing of plumes from satellite images taken during the eruption. Chapter 4 describes field observations made during 2010 field work. Chapter 5 presents the grain-size data of analyzed tephra and analytical methods to estimate the contribution of phreatomagmatism. The componentry of selected grain sizes is described in Chapter 6. Chapter 7 shows results from SEM analysis of fine ash particles. Eruption parameters, eruption mechanisms, and a model of the 2008 eruption are discussed in Chapter 8.

## **Chapter 2: Methods**

### **2.1 Field Methods**

Field work was carried out July 23 - August 14, 2010. Data used in this study come from 47 sites described in September 2008 by AVO personnel and 106 sites I described in July-August 2010, with help from Michael Ort and AVO personnel. The 2008 sites served as supplemental data to those I described in 2010. Locations for section description were chosen by examination from ground or air. Sites were selected on elevated knobs or ridges, when possible, to limit secondary ash deposition by wind or water, so thicknesses at most sites are a minimum, as erosion may have thinned some deposits. We examined sites in the caldera and on the flanks, moving outward until either deposits thinned to 1 cm (at which point the ash is difficult to measure in the tussocks) or the coast was reached. Site density was increased on the axes of basal units to improve resolution of their marginal and on-axis downwind changes.

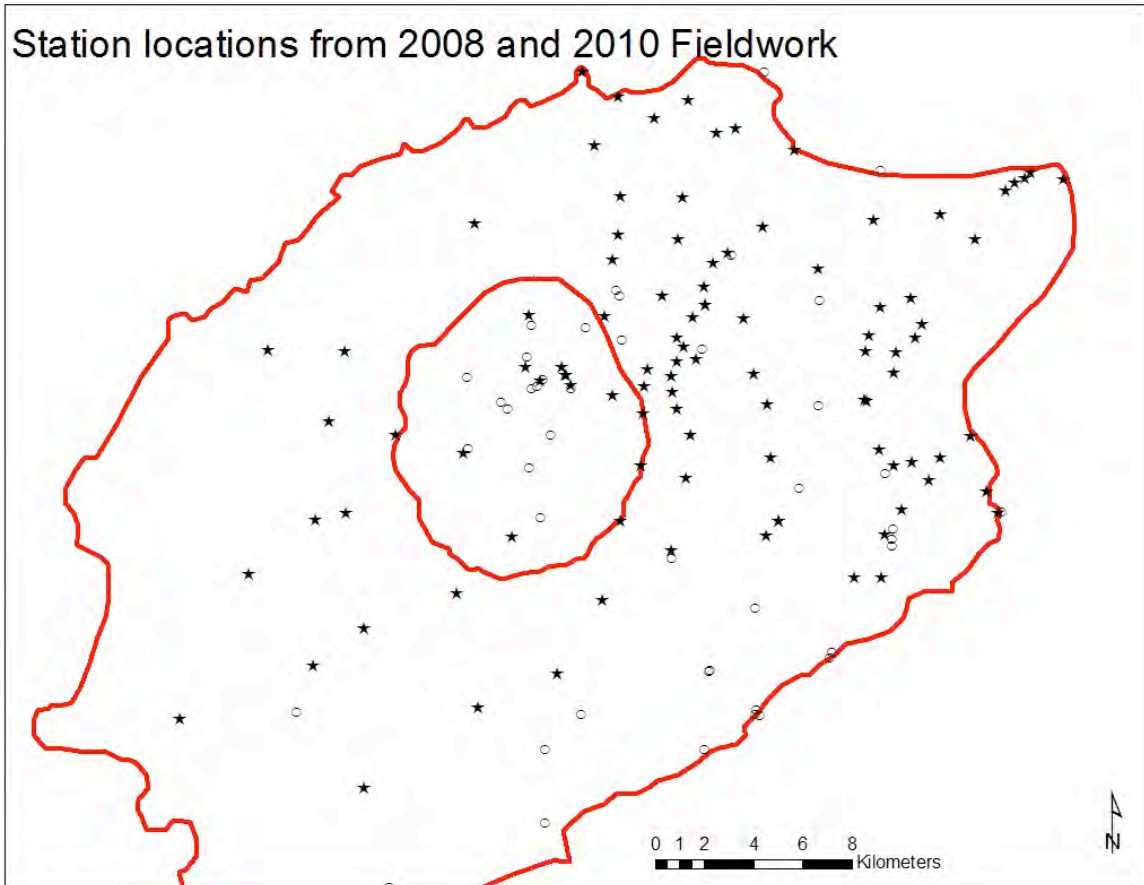


**Figure 2.1:** Locations of sample sites from 2008 and 2010 fieldwork. Red outlines show Umnak island coast and approximate caldera rim. 2010 sites are represented by stars, 2008 sites are represented by open circles.

At each site, UTM coordinates and elevation were recorded with handheld GPS units and a pit was excavated down to pre-2008-eruption material. Grass tussocks, sphagnum moss, brown soil horizons, or windswept clast-paved surfaces were accepted as pre-2008-eruption surfaces and sections were measured above these surfaces. Each section was photographed and sketched and total deposit thickness measured, which ranged from 0.3 mm to 25 m of 2008 tephra. Field descriptions of the stratigraphic sections revealed in each pit included grain size, shape, sorting, grading, color, grain rock types, sedimentary structures, degree of consolidation, nature of upper and lower

contacts, and thickness of each layer. Samples of layers of interest were collected in quart-sized bags at 25 sites. Maximum clast sizes from basal layers at selected sites were determined by measuring and averaging the three principal axes of the five largest clasts within a layer. Orientation of the outcrop to the vent was noted at sections with cross-stratified layers or other directional structures.

## **2.2 Remote sensing methods**

Satellite images were used extensively to determine wind direction, vent location, plume height, and plume characteristics. While pervasive cloud cover limited the quality of satellite imagery, images from Landsat, ASTER, and MODIS taken during the eruption were obtained from the USGS Glovis site or the NASA Land Processes Distributed Active Archive Center (LP DAAC). Landsat images were delivered georeferenced and were imported directly into ArcGIS. ASTER images were processed and georeferenced using ENVI image processing software and imported into ArcGIS. MODIS images were processed, georeferenced, and bands were selected in ENVI for import into ArcGIS. Once in ArcGIS, line files were created of plume outlines visible in each satellite image and each line file was assigned a name, date, and time. These line files were combined to create a time series of plume outlines and directions for the duration of the eruption. The visibility of the eruption column varied during the five weeks of eruption, so the resolution varies from around four outlines per day to one outline per four days. Line files of plume outlines were made for a total of 95 unique times during the eruption. GOES and AVHRR data were obtained from Peter Webley at the Alaska Volcano Observatory and were processed in ENVI. These data were used to

improve temporal resolution of plume and wind directions for the first 24 hours of the eruption.

Two Landsat images and four ASTER images taken during the eruption had resolution high enough to discern a plume source and estimate its location on the ground. This was performed in ArcGIS and circles of a diameter of the estimated error bounds were drawn to represent active vents on July 13, July 20, and July 22.

### **2.3 Grain-size analysis**

Grain-size analysis of 108 samples from 25 sites was performed by sieving and laser diffraction. Tephra samples taken in the field were shipped in sealed bags to facilities at Northern Arizona University, where each sample was dried for 7-20 days. Upon drying, samples were weighed and split using a sample splitter if the sample size was larger than around 80 grams for fine-grained samples. Samples ranged from 25 to 300 g depending on average grain size estimated before sieving. Each sample was sieved at half-phi intervals from the largest clast present down to 4.5 phi and each fraction weighed using a digital scale to 0.1 g precision.

All samples with >10 wt. % ash smaller than 4.5 phi, 80 in total, were further analyzed by laser diffraction using a Coulter LS 320 Particle Size Analyzer. Sieving of the 4.5-phi size was inconsistent in effectively separating 4.5-phi particles from finer ash, so these fractions were re-combined into one (pan fraction) for Coulter analysis. For each sample, 0.4 g of the pan fraction was 'spiked' with 0.1 g of 4-phi ash. This produced a mixture that was 20% known 4-phi ash and 80% unknown fine ash. This 'spiking' allowed comparison between sieving data and laser diffraction data. Each 0.5 g

sample was placed in a centrifuge tube and 10 ml of 5% sodium hexametaphosphate was added to each sample as a dispersant. Samples were placed on a horizontal shaker for two hours prior to analyzing on the Coulter LS 230. Each session on the Coulter LS 320 began with analysis of sample 10JAUOK002E as an internal standard. Every recorded analysis of 10JAUOK002E was averaged and the standard deviation was calculated. The error of analysis was taken as twice the standard deviation of these six analyses.

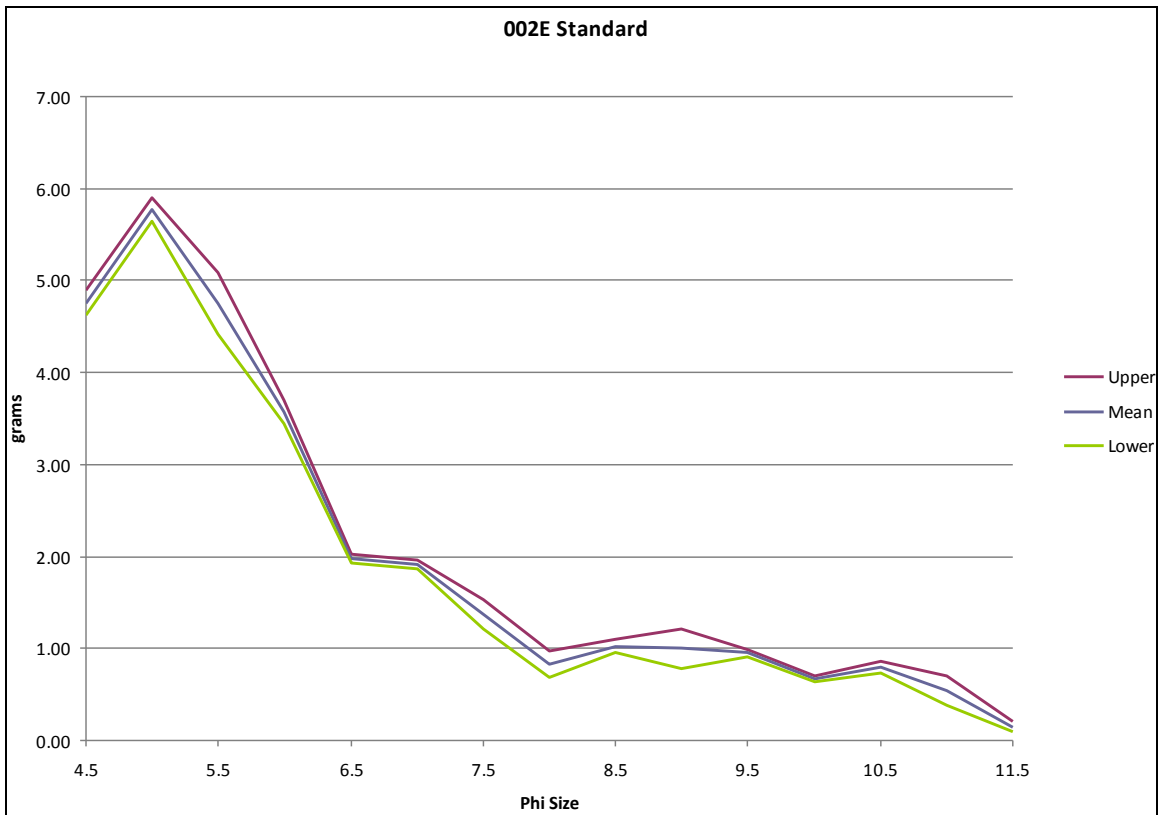


**Figure 2.2:** Averaged results from six analyses of 10JAUOK002E with upper and lower error bounds (+/- 2 S.D.).

Each sample analysis consisted of six runs, of which five were averaged and recorded. The data output from the LS 320 controller program was exported as volume percent of mm-size bands and was converted into phi-size weight percent by assuming constant density and grouping each mm-size band into the closest smaller half-phi size

(e.g. 10.6 phi, 10.8 phi, 10.95 phi are counted as 11 phi, and 11.1 phi is counted as 11.5 phi) to facilitate combination with sieving results.

Data from sieving and Coulter particle size analysis were combined and entered into Ken Wohletz' Sequential Fragmentation and Transportation (SFT) program (<http://geodynamics.lanl.gov/Wohletz/SFT.htm>). Data were entered as half-phi masses in grams and normalized to 100.0 grams. Subpopulations were found for each sample using the SFT modified normal distribution and were optimized using the automated optimize function and further refined by manual manipulation to minimize residuals while modeling the main visible modes. The number of subpopulations used was kept to a minimum to reduce artificial populations.

Determination of the contributions of magmatic and phreatomagmatic fragmentation in each unit was carried out following the procedures of Wohletz et al. (1995). SFT was used to find subpopulations that accurately describe each sample. The number of subpopulations needed to adequately describe sample grain-size distributions ranged from 3 to 10. Populations for each unit were assigned based on the subpopulations of all samples of that unit. Plots were constructed comparing subpopulation mode (phi size), dispersion (sorting), fraction of sample total, and fragmentation factor (mode / dispersion) (Fig. 2.3) (Wohletz et al. 1995).

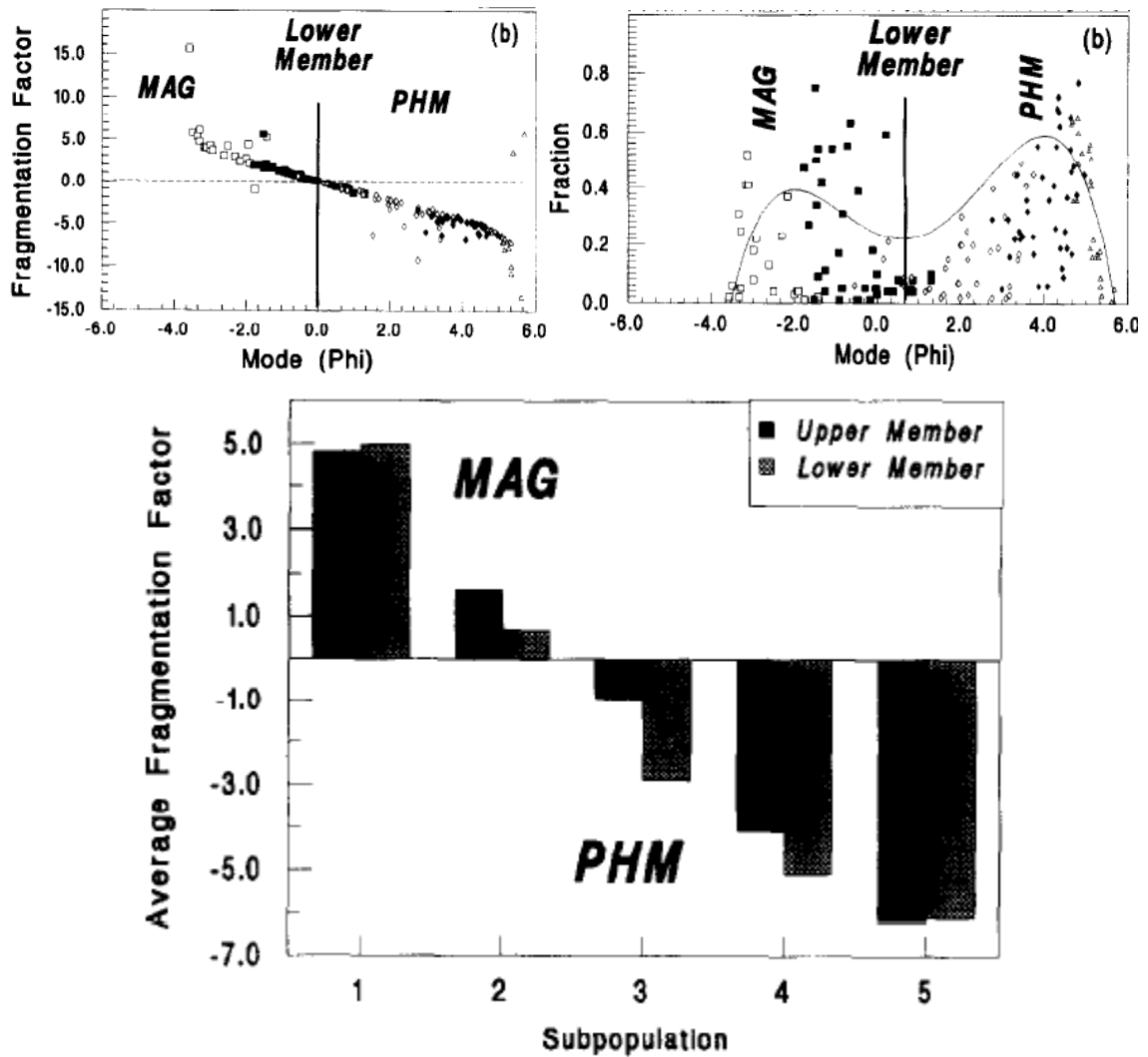


**Figure 2.3:** Sample plots of phreatomagmatic discriminators from Wohletz et al. (1995)

Wohletz et al. (1995) found that fine-grained units within deposits in the Neapolitan Yellow Tuff that showed field evidence of phreatomagmatism also had fine grain sizes and sorting similar to phreatomagmatic deposits described by Sheridan and Wohletz (1983). They found that fragmentation factor and mode of subpopulations can be plotted to show magmatic and phreatomagmatic fragmentation components, and that these regimes are divided at a fragmentation factor of 0 and a mode of 0 phi (Fig. 2.3). Graphing grain-size distribution of samples by plotting subpopulation fraction against

mode revealed two distinct regimes that the authors described as magmatic fragmentation below 0.5 phi and phreatomagmatic fragmentation above 0.5 phi. Examining average fragmentation factor by population (decreasing grain size from subpopulation 1 to 6) shows that finer subpopulations inferred to be phreatomagmatic have lower or more negative fragmentation factors than coarse subpopulations inferred to be magmatic and that fragmentation factor decreases as subpopulation size increases. Wohletz et al. (1995) used these plots to estimate the ratio of phreatomagmatic components to magmatic components in individual units, and further used the ratio of phreatomagmatic to total components as an estimate for R, the phreatomagmatic fraction and an estimate of the water-magma mass ratio. To reduce the dependence of calculated R on the sample's distance from the vent, samples were normalized to match a distance where fine enrichment matched fines depletion (20 km). These variables and graphic methods were used to examine magmatic and phreatomagmatic fragmentation contributions in individual units (Chapter 5).

## **2.4 Componentry procedure**

After samples were sieved and analyzed for subpopulations in SFT, selected grain sizes were chosen for componentry. Grain sizes for componentry were chosen based on common subpopulations found in SFT analysis. Most units from the majority of locations had peaks at about -0.5 phi, 2 phi, 3 phi, and 4 phi. The populations at 3 phi and 4 phi were eliminated as the grain size is too small for accurate identification of components with a binocular microscope. The resulting grain sizes examined were -0.5 phi and 2 phi. Samples 10JAUOK011, 10JAUOK002, 10JAUOK006, and 10JAUOK023

were chosen to examine changes with distance from the vent in on-axis locations for the basal fall units. The 2-phi and -0.5-phi fractions of five or six units at each of these locations were examined.

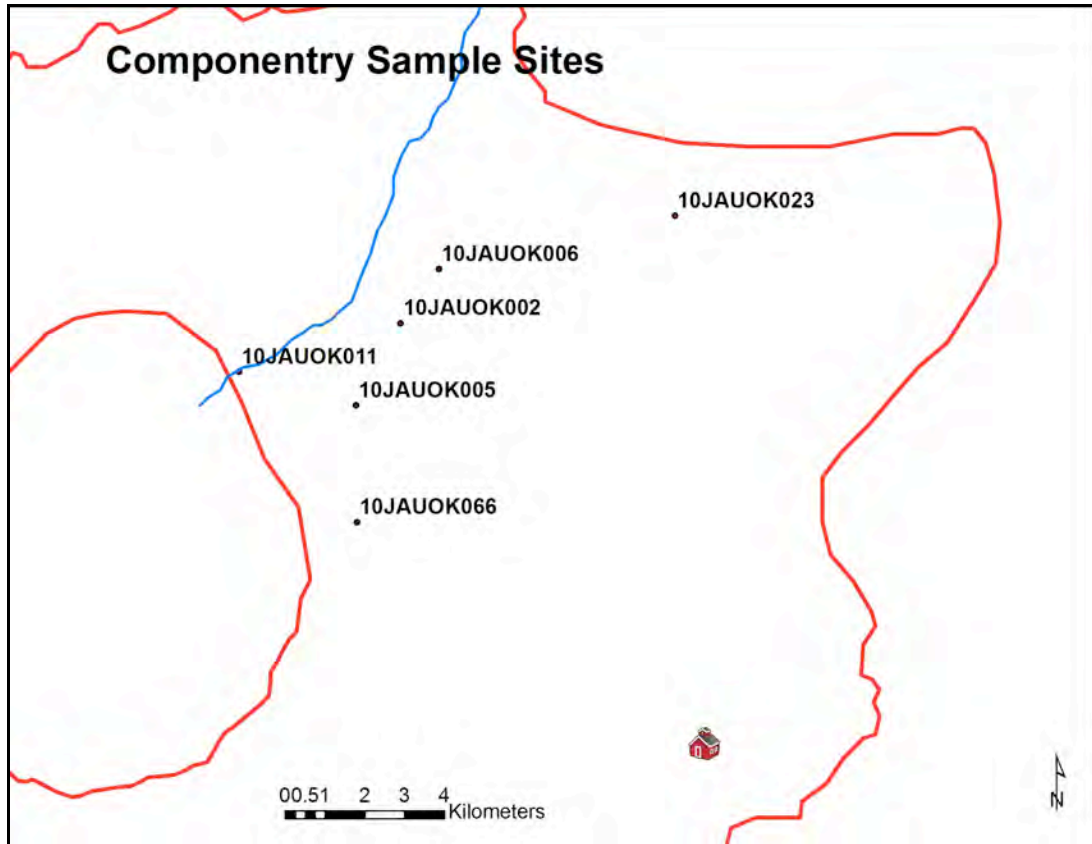


**Figure 2.4:** Sites analyzed for componentry. Fort Glenn (red building) and Crater Creek (blue line) are shown. Okmok caldera outline and Umnak Island outline shown in red.

Additional units from 10JAUOK005 and 10JAUOK066 were chosen to study the difference between ash-pellet deposits and laminated ash deposits. At least 200 grains from each selected size fraction for each sample unit were placed in a glass dish under a binocular microscope. Grains were sorted into the categories shown in Table 2.1.

<b>Lithic Grains:</b>	
Lava	Angular Plag-rich Aphyric Lava Plag + px/ol lava Other lava Dark Plag lava Lt grey lava
Scoria	Black Scoria Cauliflower dense Black Pumice Black Fluidal
Other non-juvenile	Orange oxidized Clear with dark grains
<b>Juvenile Grains</b>	
Brown Pumice	ash coated uncoated
Brown Vesicular Glass	coated uncoated
Blocky Dense Glass	Total
Crystals	Plagioclase Olivine

**Table 2.1:** Categories used in componentry analysis

The grains in each category were counted, recorded, and stored in small plastic zip-top bags.

## **2.5 Procedure for grain-shape and surface feature analysis**

Selected size fractions of samples were examined on the Scanning Electron Microscope (SEM) at Northern Arizona University. Separated components in the 2-phi size of Unit 1B from site 10JAUOK011 were examined under the SEM to examine chemical differences between clast types and thereby correlate visual identification under

the binocular scope with component identification using the SEM and its Energy-dispersive spectroscopy (EDS) chemical analysis.

To examine grain shapes and surface features, the 4-phi size fraction was used, as this size (64-125  $\mu\text{m}$ ) is the most useful for differentiating between fragmentation regimes (Dellino and Liotino 2002). Grains were taken from the 4-phi fraction and placed on double-sided adhesive tape on a standard glass microscope slide to hold them in place. Ten to seventeen glass grains were imaged for each sample, and each grain was chemically analyzed using the energy-dispersive spectroscope on the SEM to ensure that it was glass rather than a free crystal. Chemical data from some of these analyses were recorded and are included in Chapter 7. Images of glass grains were stored at 640x480 pixels and were examined qualitatively for vesicularity, grain shape, and surface features evidencing phreatomagmatic fragmentation.

Quantitative analysis of the fractal dimensions of glass grains was performed following the procedure of Dellino and Liotino (2002). Images were thresholded and converted to binary using NIH ImageJ or NIH Image (developed at the U.S. National Institutes of Health and available at <http://rsb.info.nih.gov/nih-image/about.html>) and fractal analysis was performed using the FRACCALC macro (written by M. Warfel) (Dellino and Liotino 2002) hybrid-fast method using 50 step-size intervals from 3 to 150 pixels. The scale unit was set to pixels for each analysis. The perimeter (in pixels) is calculated by the FRACCALC macro for each step-size and the perimeter was plotted against the step-size on a logarithmic scale (Mandelbrot-Richardson (M-R) plot) for each particle (Figure 1.8). Multi-fractal particles with multiple line segments describing the points were inferred to be magmatically fragmented and confirmed by examination of

textures in original SEM images. True fractal particles with a single line fitting points were inferred to be phreatomagmatically fragmented. These classifications of phreatomagmatic or magmatic origin were confirmed by qualitative examination of grain shapes, particle vesicularity, and surface features.

## **2.6 Eruption parameter calculation methods**

### **2.6a Eruption volume calculations**

I estimated the total volume of 2008 tephra and basal units (1-3A) using measured section thicknesses and field estimates of proximal thicknesses and tuff-cone dimensions combined with Quickbird imagery of intra-caldera features. Volume estimates were made using the two-straight-line exponential method of Fierstein and Nathanson (1992) and by direct volume calculation of a tephra thickness surface in ArcGIS.

The volume of the tuff cone was estimated using ArcGIS and added to the medial and distal deposit volumes in both methods. Points were placed along the rim and the base of the tuff cone and assigned tephra thicknesses based on field estimates of cone dimensions. Tuff-cone rim sites were given thicknesses of 250 meters on the high points of the rim and 180 meters on the lowest saddle. The center of the crater in the tuff cone was estimated to have a tephra thickness of 150 meters. Points along the base of the cone were assigned thicknesses of 30 meters.

Both methods used the ArcGIS calculation for proximal deposit volume, but differed in estimation of medial and distal deposits. The deposit thickness surfaces for total 2008 tephra and basal material (Fig 2.5-6) in the ArcGIS method was created by triangulation between point thicknesses. The volume beneath the surface approximates the bulk volume. This method accurately estimates deposits on Umnak island, where

thicknesses were measured, but neglects distal deposits lying offshore. Volume estimates following the Fierstein and Nathanson two-straight-line exponential fit were made for total deposits and basal units 1-3A and the exponential fit extends the volume estimate beyond the island margins, accounting for distal deposits. The volume of Unit 1A was also calculated using the ArcGIS method. Points of estimated 50 centimeter thickness were added around vents and points along the estimated extent of measureable deposits were added as 0 centimeters (Fig 2.6). Subtracting the volume of basal units from the total volume of deposits provides the total volume of material erupted during the eruption after the first four-hour opening sequence.

The bulk density of 2008 products was measured for a complete section at a medial site. The average density of 2008 tephra is  $1600 \text{ kg/m}^3$ . The bulk density of basal units was similar to the total bulk density for 2008 deposits so the average bulk density of  $1600 \text{ kg/m}^3$  is used here. The density of the glass produced in the 2008 eruption was calculated using the program MAGMA by Ken Wohletz (<http://geodynamics.lanl.gov/Wohletz/Magma.htm>). The average major-element-oxide composition was determined from all grains analyzed using energy-dispersive spectroscopy on the scanning electron microscope and the resulting density for 2008 basaltic andesite is  $2962 \text{ kg/m}^3$ . This value concurs with a density calculated from an XRF analysis of glass from 2008 products by Larsen (personal communication, November 2010).

Calculating densities of 2008 tephra and dense basaltic andesite allowed estimation of dense-rock-equivalent (DRE) values and total mass of deposits. The percentage of total deposits made up of juvenile material was estimated and used to

calculate total magmatic equivalent mass. Dividing magmatic equivalent mass by eruption times obtained from satellite imagery allowed estimation of magma mass fluxes for the entire eruption, Unit 1A, and basal units 1-3A.

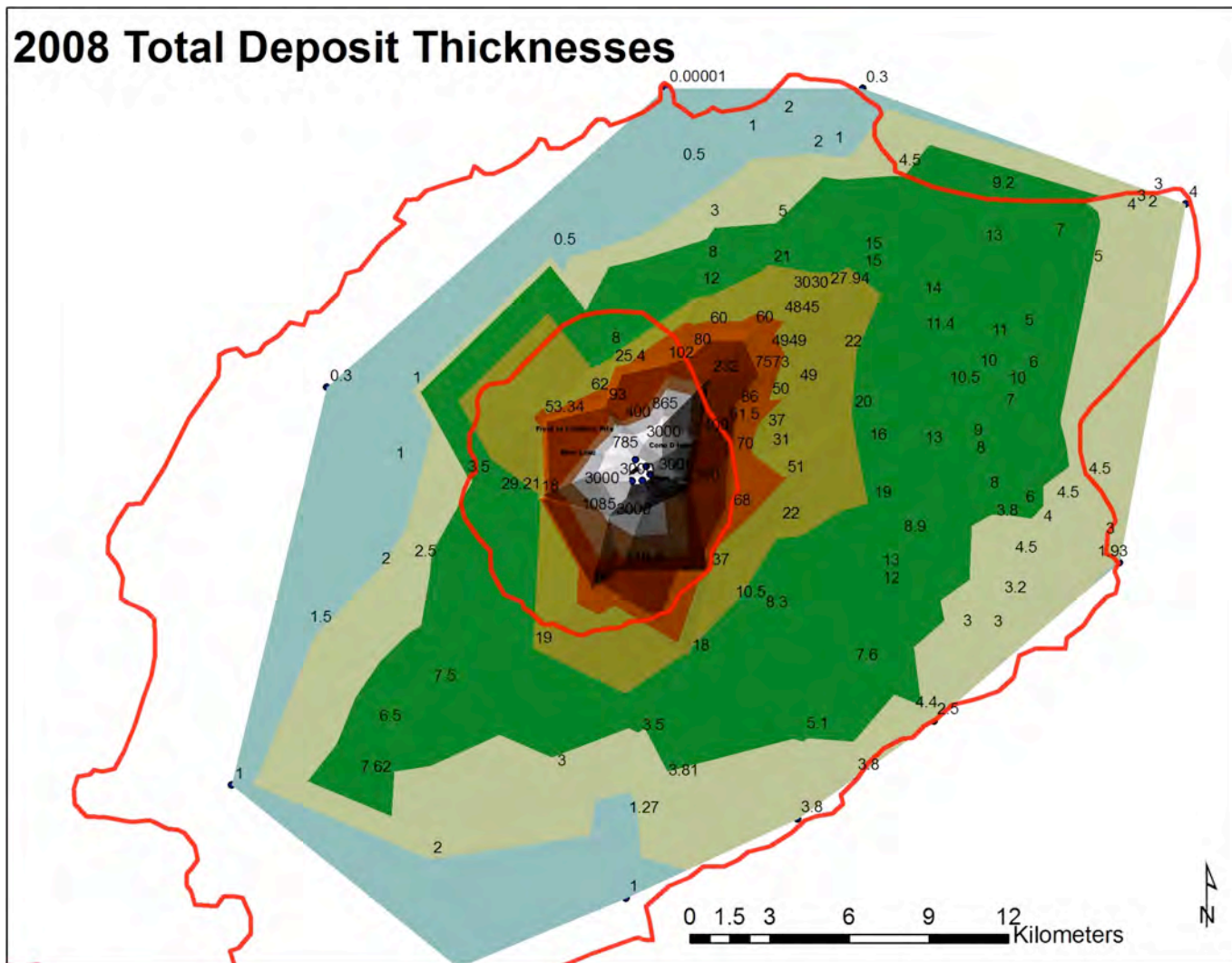


**Figure 2.5:** Triangulated Irregular Network (TIN) surface of total deposits from the 2008 eruption for volume calculation.

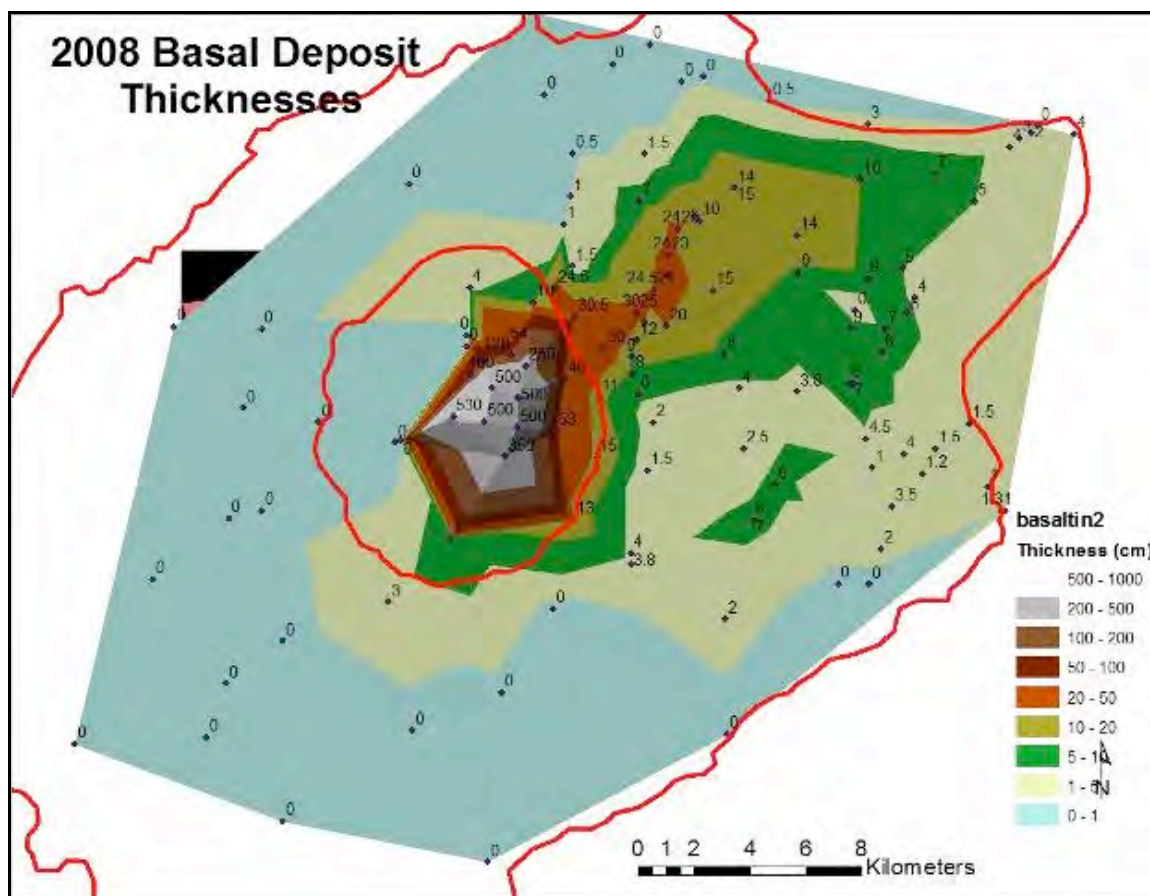


**Figure 2.6:** Best estimated tephra thickness surface for basal units.



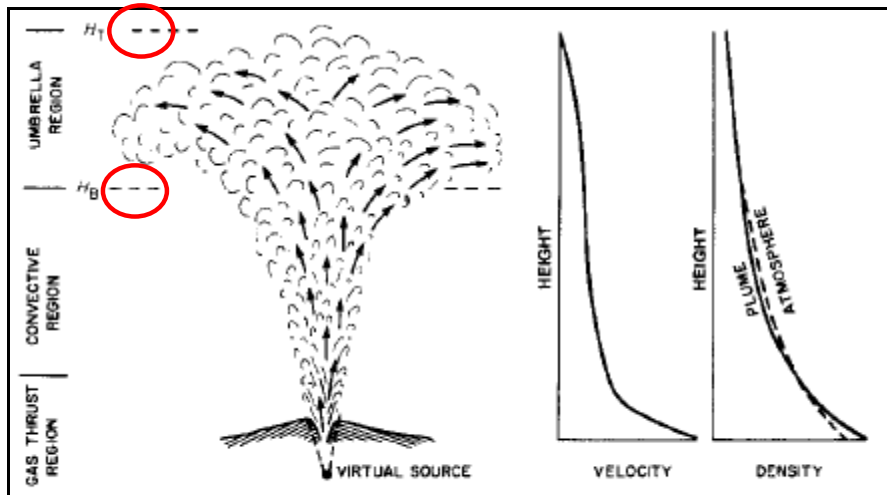


**Figure 2.8:** Main features of a convecting eruption column, from Carey and Sparks (1986). Height of buoyancy is abbreviated  $H_B$  and column-top height is abbreviated  $H_T$ .

## **Chapter 3: Remote Sensing Results**

Satellite images from MODIS, GOES, AVHRR, ASTER, and Landsat data sets are used here to study plume directions throughout the eruption, plume characteristics, and the location of vents throughout the eruption.

### **3.1 Plume series results**

#### **3.1a MODIS plume series**

Plume outlines were traced from MODIS Surface Reflectance Products with 250-m resolution for data acquired during hours of daylight and MODIS Emissivity bands (typically a combination of bands from 24-36) during night hours. Data were imported to ArcGIS as true color images from reflectance bands and false color images from emissivity bands. Plume outlines were traced in ArcGIS from both reflectance and emissivity images and stored as line files (e.g. Figs. 3.1 and 3.2). Outlines created from images for the duration of the eruption were compiled into a time series of panels (Fig. 3.3, remainder in digital appendix). The time, in UTC, is noted on each image, and local Alaska time is 8 hours earlier.

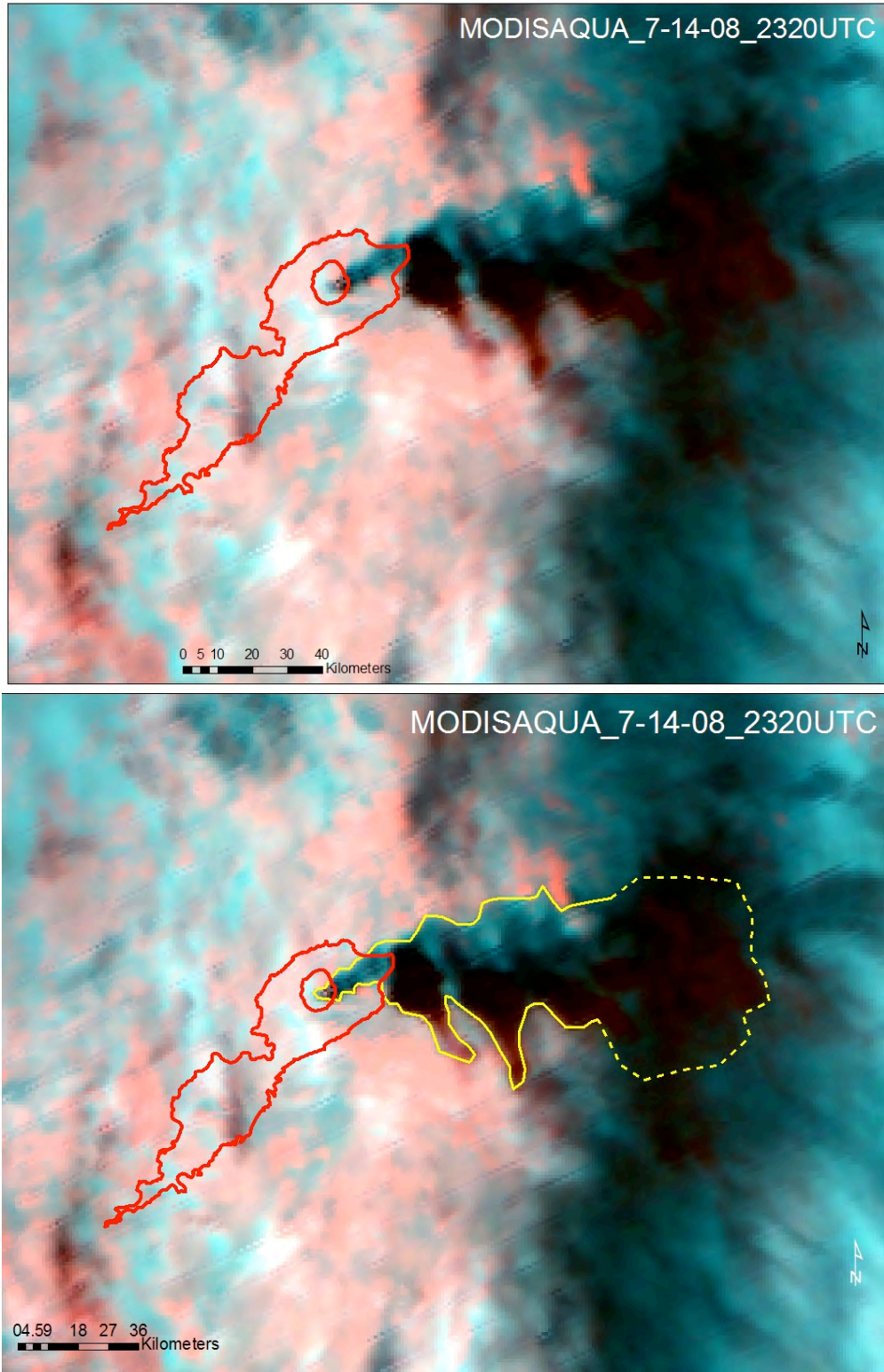


**Figure 3.1:** MODIS Emissive Data in both panels, with interpreted plume margins in yellow on lower panel. Data source, date, and time are given in the upper right.

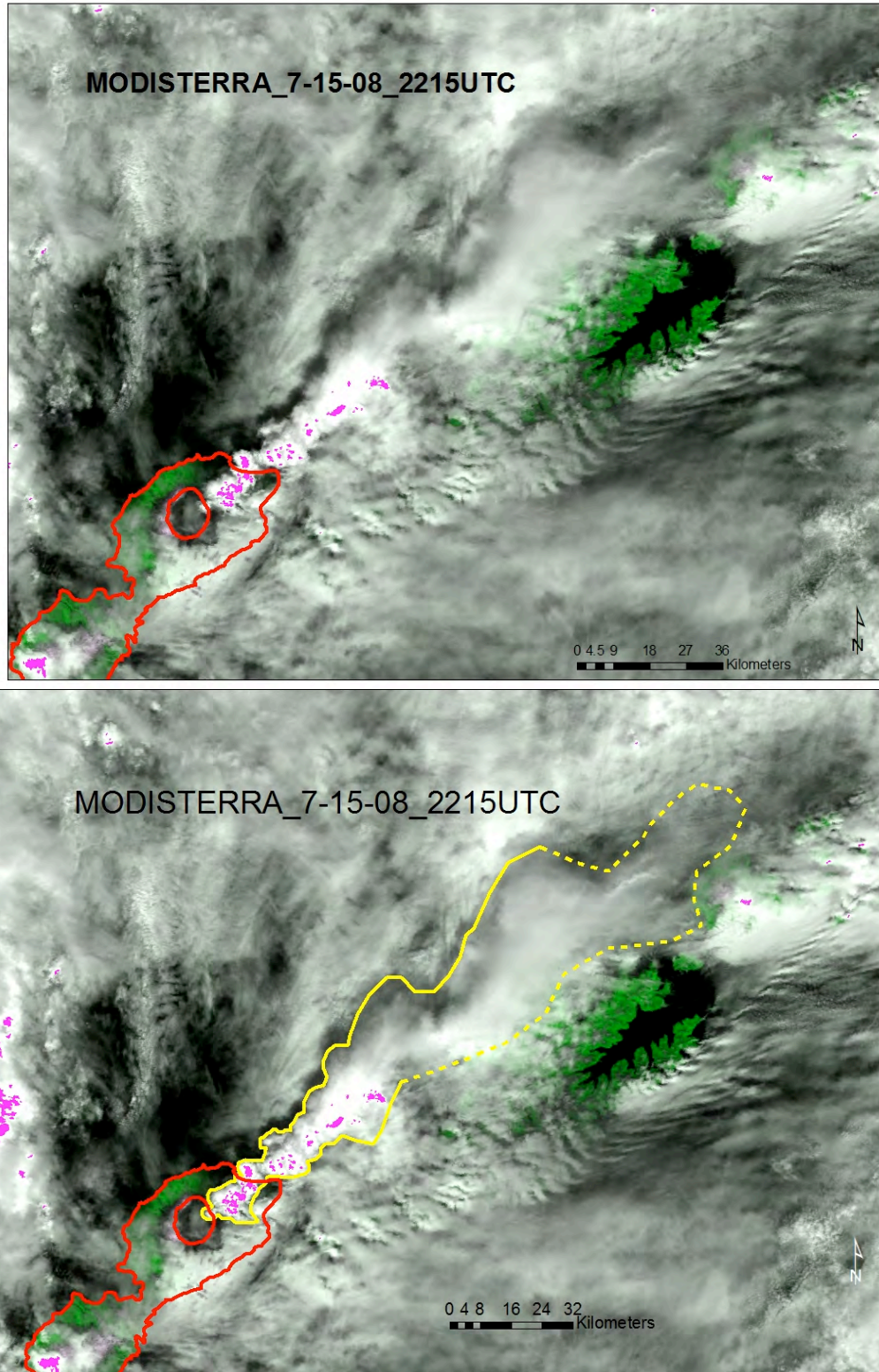


**Figure 3.2:** MODIS Reflectance Data in both panels, with interpreted plume margins in yellow on lower panel. Image approximates visible colors. Data source, date, and time are given in the upper right.

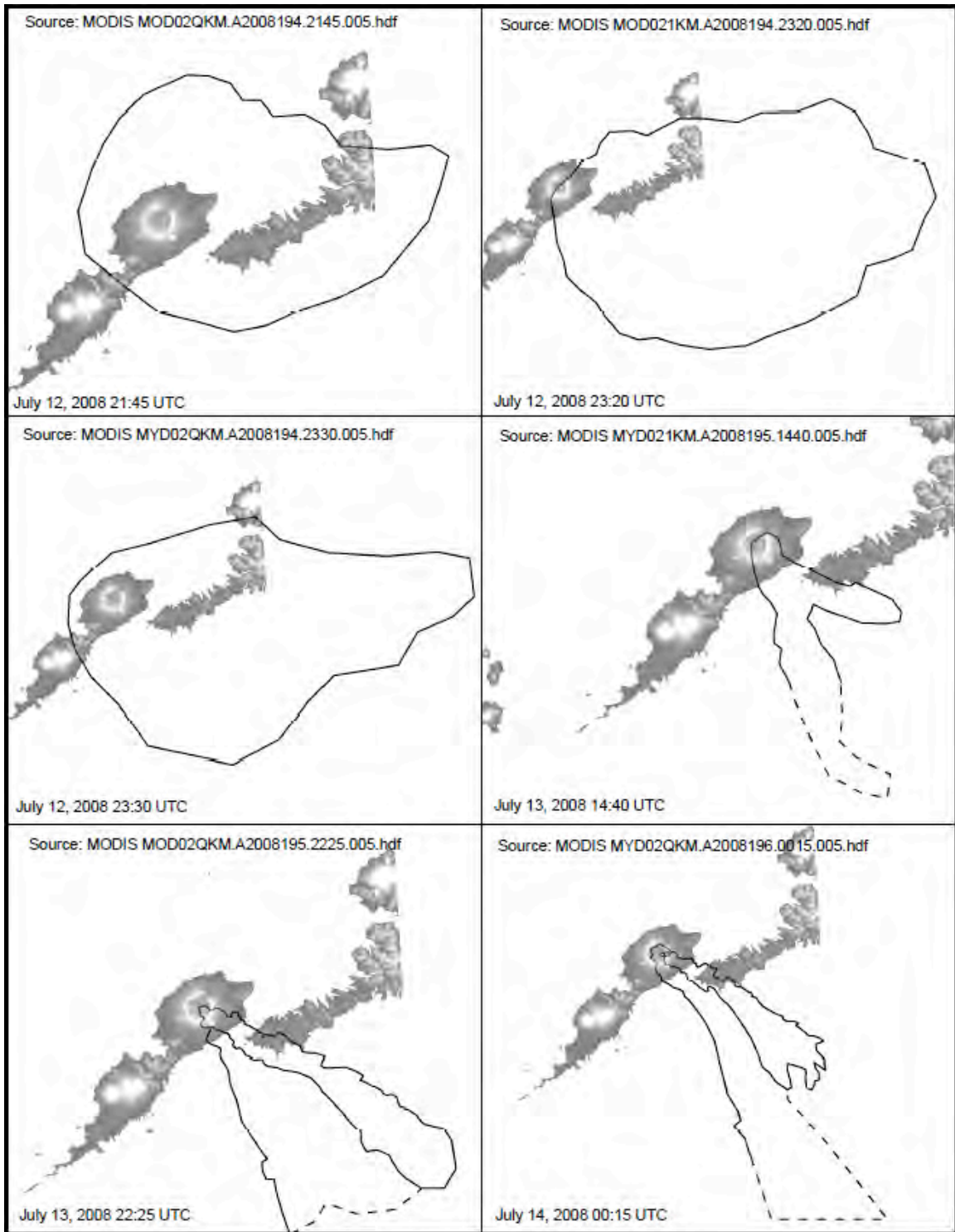


**Figure 3.3:** Plume outlines July 12-14, with Umnak and part of Unalaska islands shown. Solid lines are clear plume boundaries, dashed lines are uncertain boundaries or data margins. Data source, date, and time are given in the upper right.

### 3.1b AVHRR plume series results

Images from AVHRR data channels 1, 2, and 3 show the plume in the opening sequence of the eruption (Fig. 3.19). A switch in wind direction from west to northwest is visible between frames from 20:32 UTC July 12 (Black cloud in center-northeast portion of image) and 00:15 UTC July 13. AVHRR images shown below are not georeferenced, but orientation is consistent, so apparent wind-direction shifts correspond to actual wind-direction shifts.

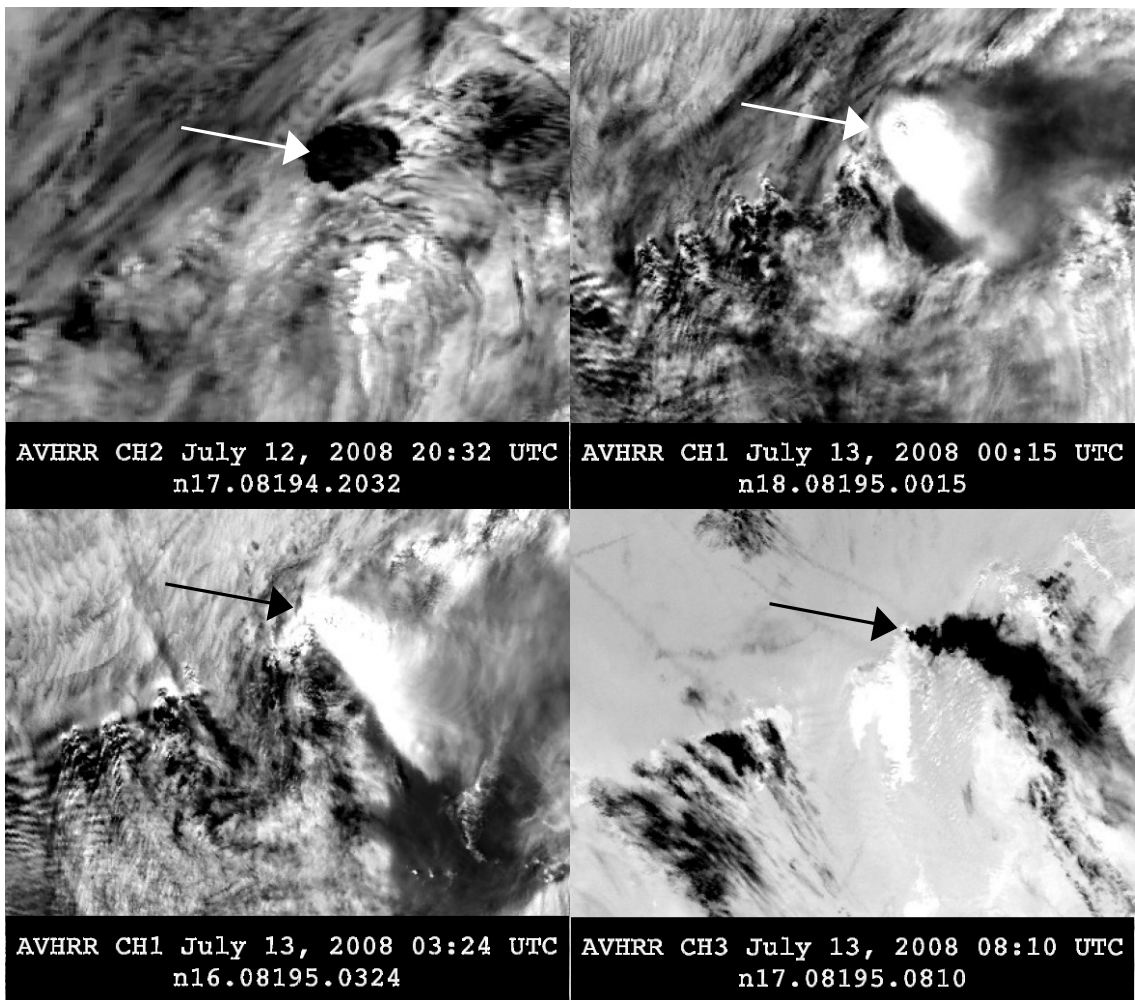


**Figure 3.4:** AVHRR images from the opening sequence of the 2008 eruption with arrows pointing to plumes. Images are not georeferenced, but images are oriented consistently and approximately correct. The lower right panel is AVHRR Ch3, an emissive spectrum image.

### **3.1c GOES plume series results**

Images from GOES visible spectra and channel 2 show the plume in the opening sequence of the eruption (Fig. 3.4). The development of the plume is visible from the start of the eruption and the first wind shift is captured around 23:20 UTC July 12 or 00:00 UTC July 13. Visible spectra images are darkened after 07:00 UTC, so emissive band images are used after that time.

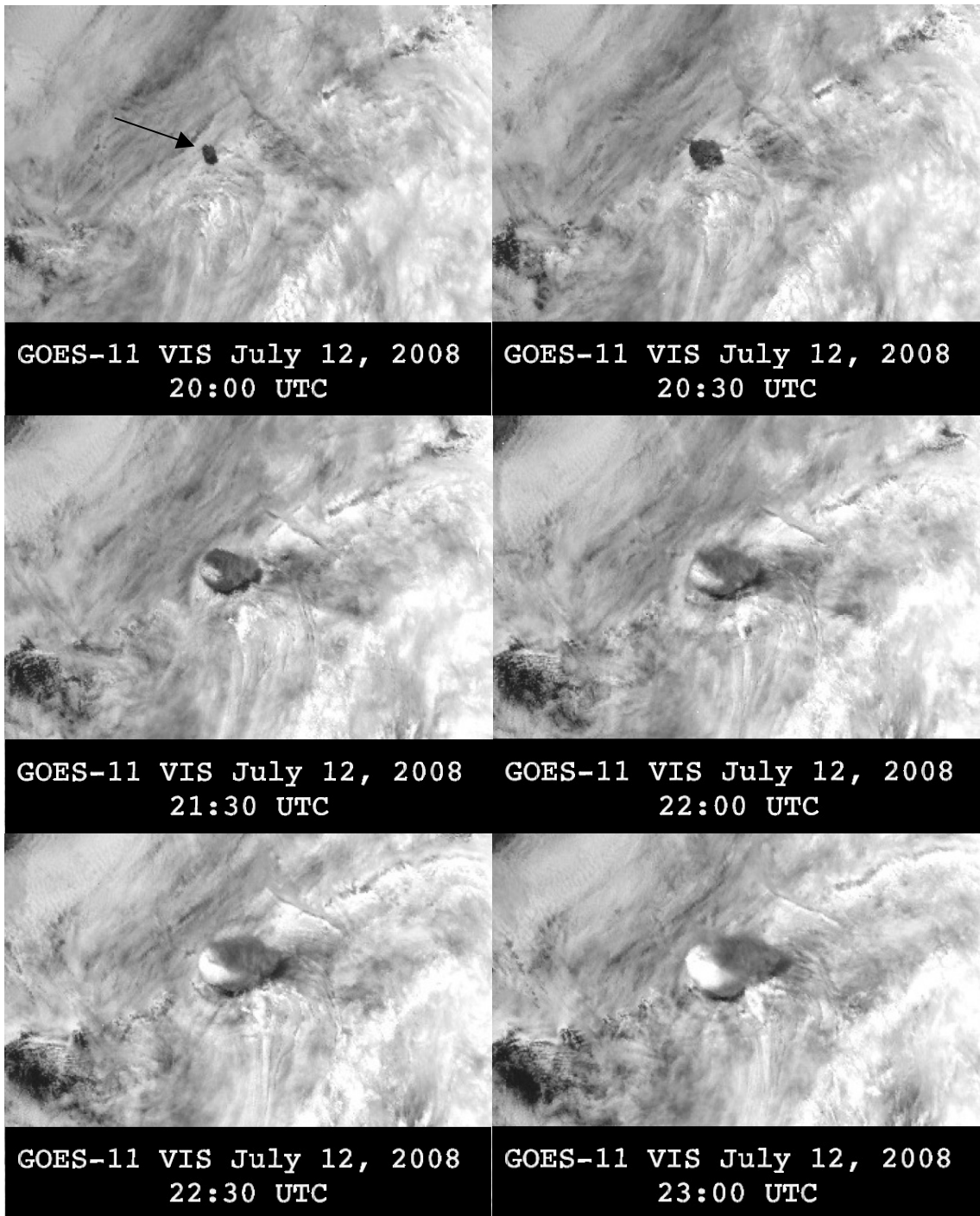


**Figure 3.5:** GOES images from the opening sequence of the 2008 eruption with arrow showing the plume. Images are not georeferenced, but images are oriented consistently and approximately correct.

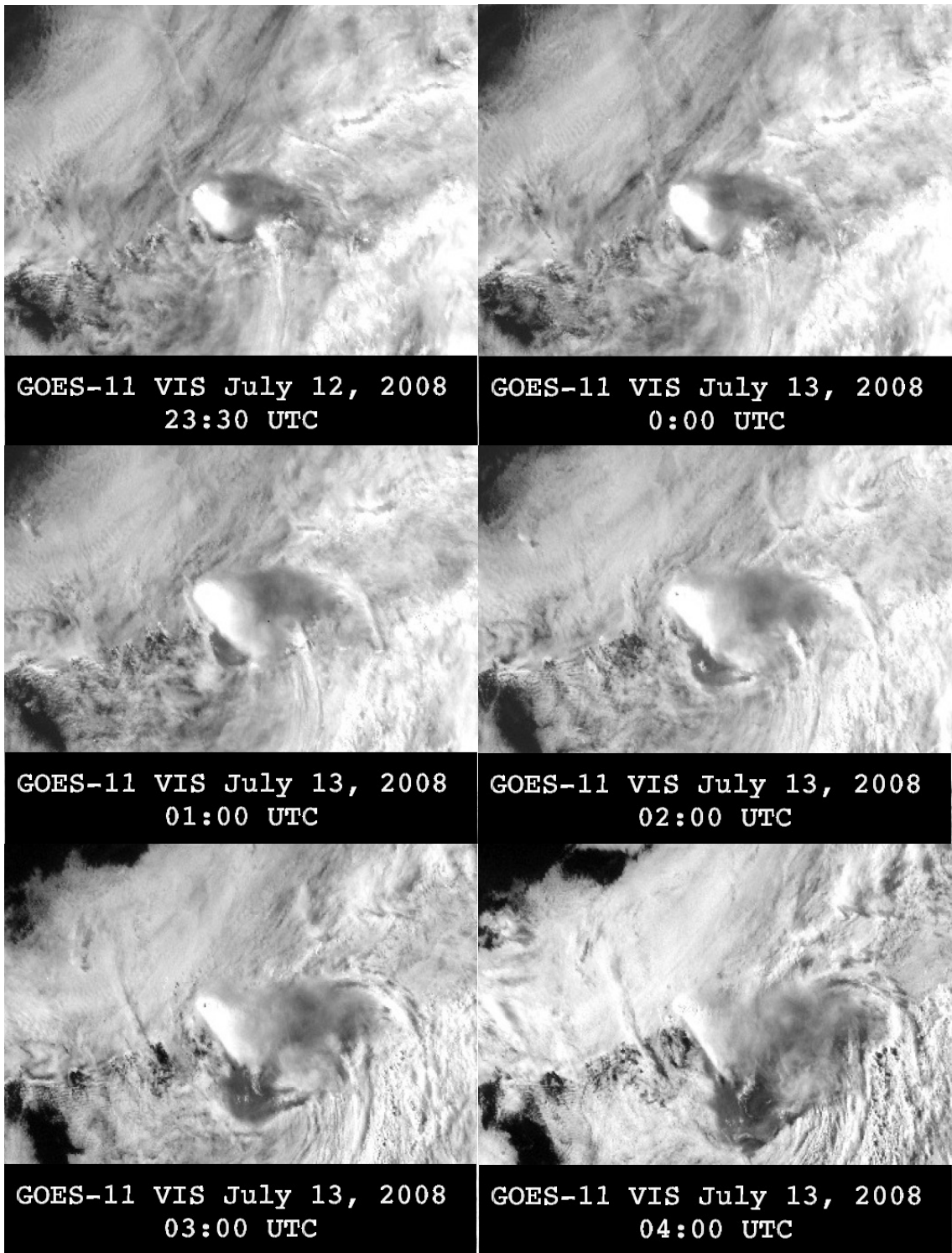


**Figure 3.6:** GOES images from the opening sequence of the 2008 eruption. Images are not georeferenced, but images are oriented consistently and approximately correct.

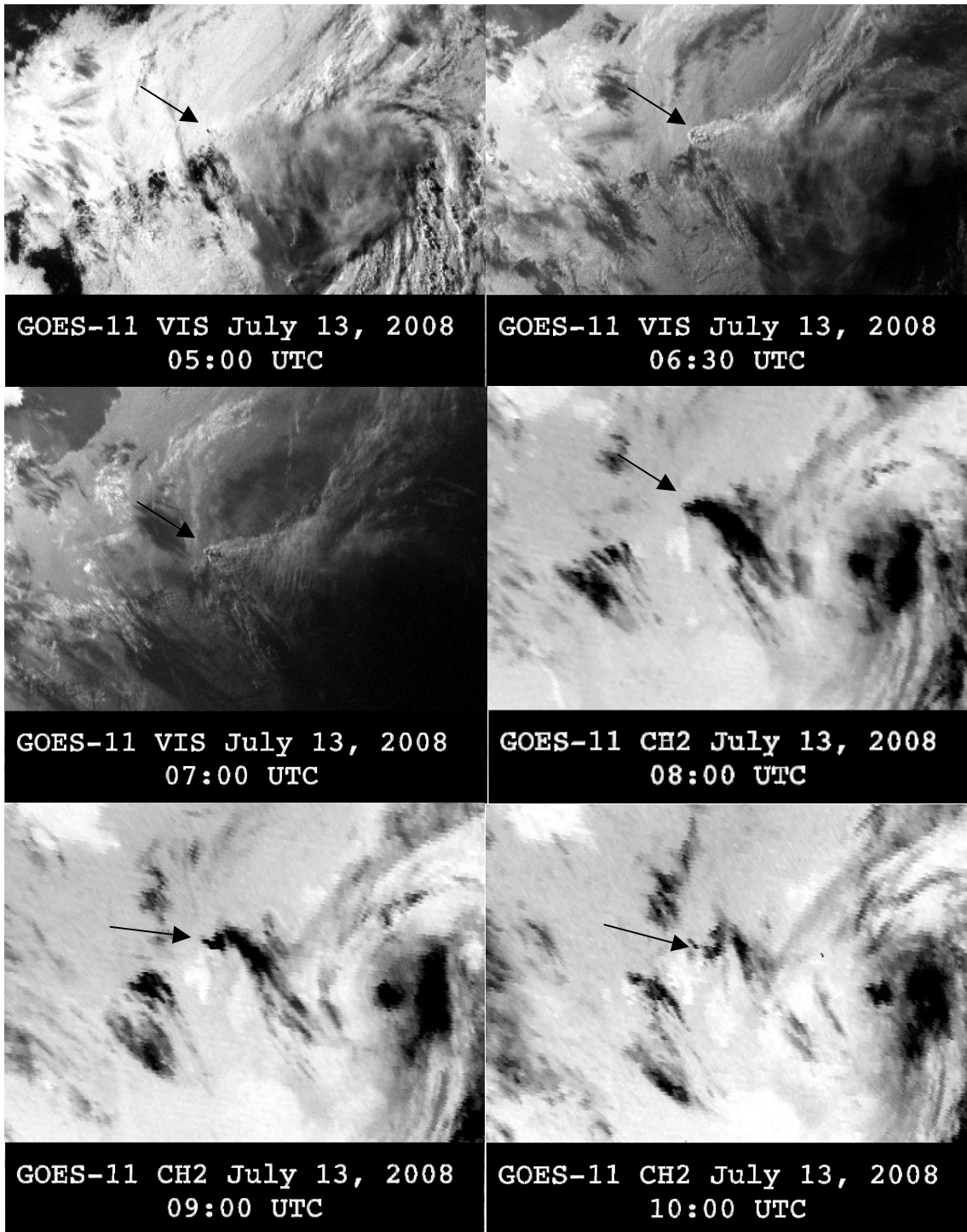


**Figure 3.7:** GOES images from the opening sequence of the 2008 eruption. Images are not georeferenced, but images are oriented consistently and approximately correct. Images switch from visible bands to emissive bands as night falls (08:00 UTC).

The compiled directions of plumes driven by winds during the eruption from MODIS data show the variation in wind direction (Fig 3.4). Plumes were driven east, northeast, or southeast for the first 19 days of the eruption, from July 12 through July 30, but important wind shifts exist during this time period. MODIS data collected at 21:45 UTC on July 12 show the large plume produced during the opening sequence of the eruption carried east from the caldera by west winds. West winds continued through 23:30 UTC on July 12, and shifted to northwest winds by 00:00 UTC on July 13, as shown by GOES data. During field work, I looked for evidence of this wind shift in the deposits to correlate the stratigraphy with times obtained from remote sensing. Estimating pre-wind-shift volume and eruption time allows an estimation of a minimum discharge rate for basal units.

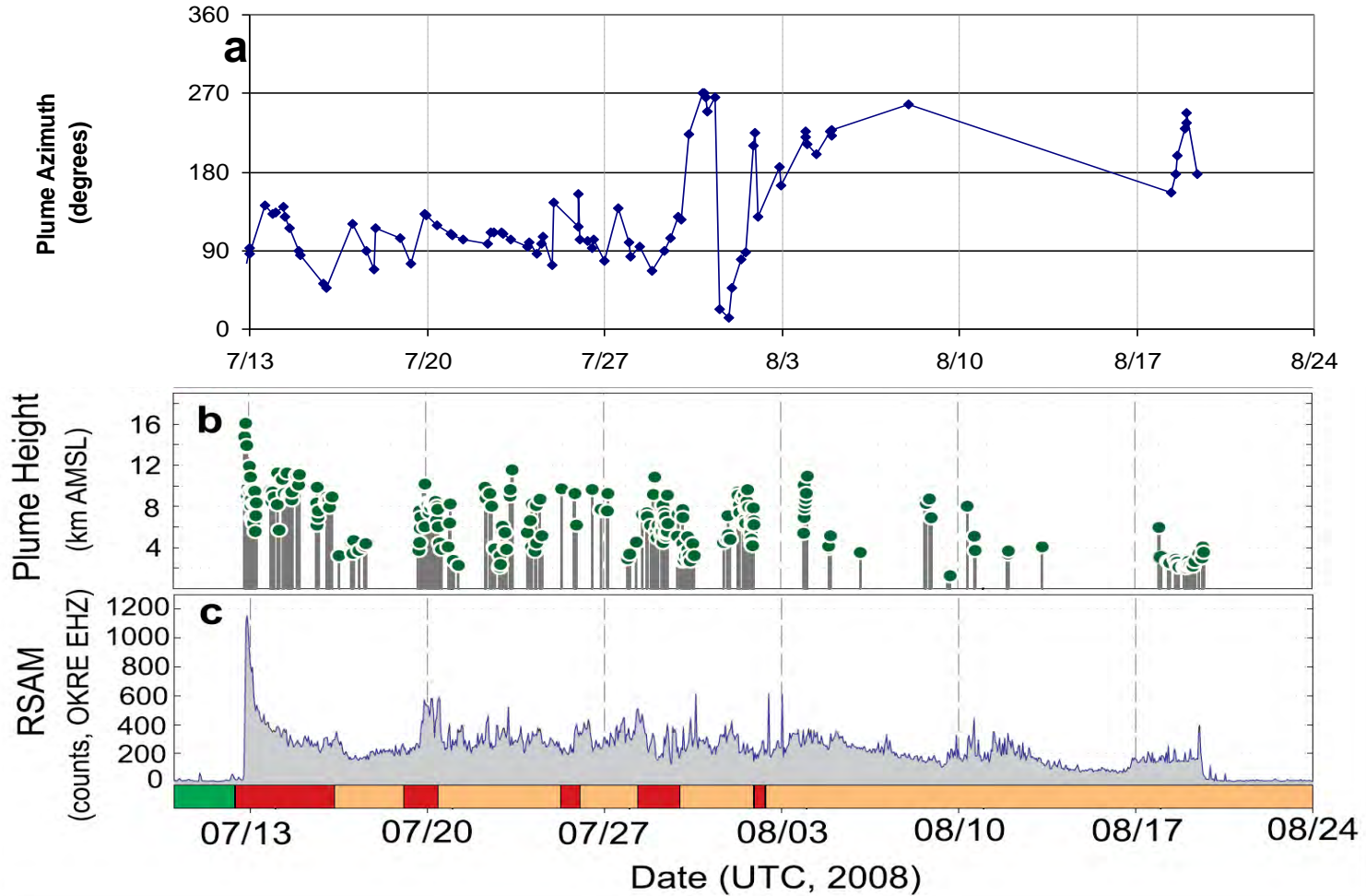


**Figure 3.8:** a) Plume directions (MODIS), b) plume height, and c) seismic amplitude by date and time. Plume direction shown as azimuth (north is 0° or 360°, east is 90°, south is 180°, and west is 270°). Plume height and seismic amplitude from Larsen et al. (2009).

Wind directions between July 30 and August 19 were primarily north, east, and northeast, driving plumes south, west, and southwest. Winds shifted to west and south at 12:50 UTC on July 31 but returned to northeast by 21:20 UTC on August 1. From the deposition of Unit 3B on July 13 to the end of the eruption on August 19, upper fine-grained units were deposited along with some coarse ash-fall units. The northeast winds driving plumes southwest between August 1 and August 4 deposited ash on the town of Nikolski on the southwest end of Umnak island, where ash thickness was measured at 3 mm on August 4 (AVO Okmok report 30 July-5 August 2008). This ash is part of the upper coarse ash-fall units. Extensive cloud cover and low plume heights from August 8-18 prevented the collection of satellite imagery showing plumes.

### **3.2 Plume Character from MODIS, ASTER, GOES, and Landsat**

The earliest images of the plume from the GOES sensor at 20:00 UTC and 20:30 UTC July 12 show a dark plume, indicating a column dominated by ash rather than water vapor (Fig. 3.5). As the plume grew, after 21:00 UTC, the color changed from dark gray to lighter gray with a section of very light gray to white (Fig. 3.5-6). The very light portion continued to expand and the overall color of the plume lightened through the next few hours. The lighter part of the plume extended from the plume source (vents) downwind and was probably the highest part of the plume (Fig. 3.5, 3.6). The appearance of the lighter part of the plume suggests that water began condensing to form visible droplets or freezing to ice crystals starting around 21:30 UTC. The lighter, water-rich character of the plume continued at least through 07:00 UTC July 13, when visible spectrum images were darkened and only emissivity bands could be used.

Several MODIS images captured during times of minimal cloud cover show interesting plume characteristics. Distinct and separated steam and ash plumes are visible in several images from July 13 and 14 (Figure 3.9). A Landsat image from the same time period with greater detail of the caldera shows two apparent plume sources: a source issuing a darker cloud northeast of a source producing a white plume that rises above the darker cloud (Fig. 3.10).

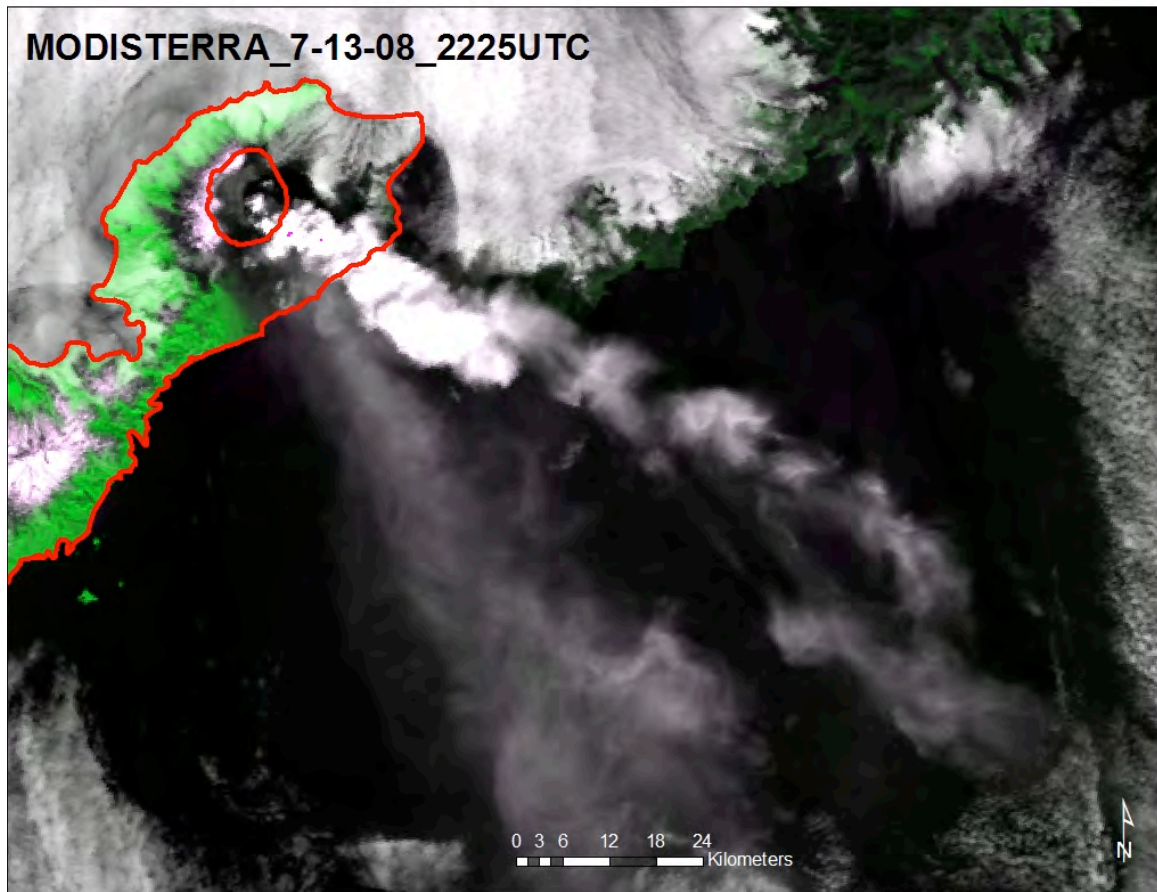


**Figure 3.9:** MODIS TERRA July 13, 2008 22:25 UTC image showing separated steam and ash plumes. Red lines show Umnak Island outline and the caldera margin.

Plumes for the remainder of the eruption, when visible in satellite data, are primarily light colored. However, three periods of dark, ash-rich plumes are visible in satellite imagery. Images from July 18 show an ash-rich plume carried east from vents

(Fig. 3.11). From July 30 to July 31, dark plumes were carried southwest (Fig 3.11). Again from August 2 through August 4, northeast winds carried dark, apparently ash-rich plumes southwest along the axis of the island (Fig. 3.11), likely depositing the ‘Nikolski ash’.



**Figure 3.10:** Landsat image from July 13, 2008. Red line marks the Okmok caldera margin.

### **Interpretations from satellite images of plume characteristics**

The early dark ash-rich plume present in the first hours of eruption seen in GOES images may have deposited the coarse ash and lapilli of Unit 1A. The appearance of a lighter colored plume at around 21:30 UTC July 12 may indicate an increase in plume water content or an increase in plume height to allow water droplet condensation or

freezing. Unit 1B was deposited at this time, and the addition of fine ash in Unit 1B may have been caused by the condensation of water allowing ash aggregation and ash rain, washing fine ash from the plume. An increase in the water-magma ratio at the vents may have provided the mechanism for an increase in plume water content. Unit 2 is open-framework ash and lapilli, but light-colored water-rich plumes persisted through the wind switch around 00:00 UTC July 13, between deposition of Units 3A and 3B. A return to a dark ash-rich plume was expected during Unit 2 deposition, but is not present in the satellite data. Only the top of the plume is visible in satellite images, which may obscure changes occurring lower in the column.

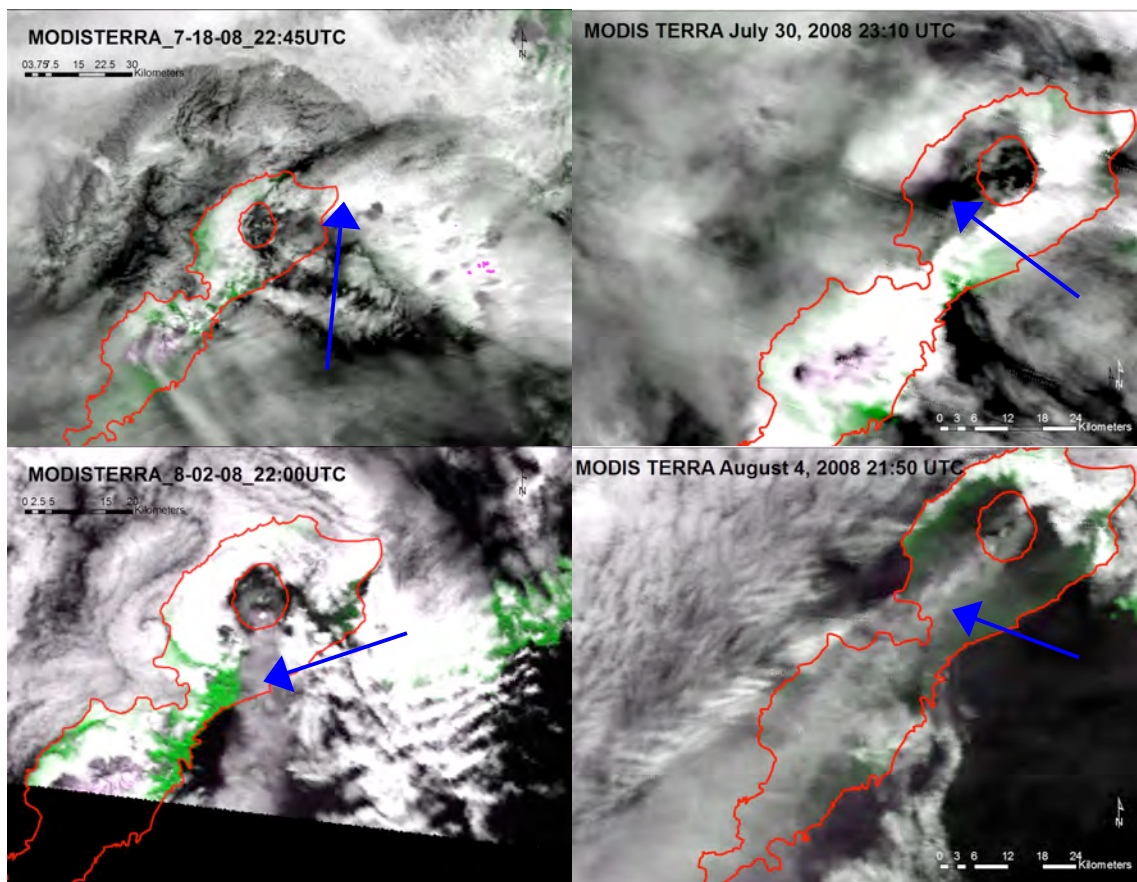


**Figure 3.11:** MODIS images from July 18, July 30, August 2, and August 4 of dark ash-rich plumes. Red lines show Umnak Island outline and the caldera margin and blue arrows point to plumes.

The light appearance of plumes for most of the eruption suggests a high level of water-magma interaction for those times and fits well with the fine-grained nature of upper deposits. The return to dark ash-rich plumes from July 30 through August 4 may indicate a decreased water-magma ratio. These ash-rich plumes may have produced the coarse ash layers present within upper units, including coarse ash that was deposited in Nikolski on August 4. Cloud cover was variable but heavy for the majority of the eruption, obscuring plumes during many time periods. Other described coarse ashes may have been deposited by similar dark plumes that are not visible in the satellite image record.

### **3.3 Vent Locations from ASTER and Landsat Data**

Frames from ASTER and Landsat data were captured during times of little cloud cover and vent locations can be estimated from plume source locations. A Landsat image from July 13 shows two distinct plume sources (Fig. 3.12). Aster images from July 20 and 22 each show one clear plume source (Figs. 3.12, 3.13). Images from these three times show three distinct vent locations, two on July 13, and one present on both July 20 and July 22. The plume source locations from these three images are plotted on a Quickbird image showing post-eruption topography and features produced during the 2008 eruption.

The plume source locations from the July 13 Landsat images plot directly on the new lake created during the 2008 eruption and the new enlarged portion of the old Cone D lake (Fig. 3.13). The plume source locations from July 20 and 22 both plot on the 2008 tuff cone (Fig. 3.13).



**Figure 3.12:** Satellite images from July 13 (top) and July 20 (bottom) with estimated vent locations shown: July 13 vents (red), July 20 vent (orange), July 22 vents (yellow).



**Figure 3.13:** Satellite images from July 22 (top) and after eruption (bottom) with estimated vent locations shown: July 13 vents (red), July 20 vent (orange), July 22 vents (yellow). Post eruption Quickbird image shows the 2008 tuff cone (within orange and yellow circles), the new lake west of the tuff cone, and the enlarged Cone D lake north of the tuff cone (both circled in red).

## **Chapter 4: Field Characteristics**

### **4.1 Overview of 2008 Deposits**

Deposits from the 2008 eruption extend from the 250-m-tall tuff cone at the last active vent to cover the entire caldera floor. Deposits are present at all caldera-rim sample sites and vary in thickness from 3 to over 200 cm. West winds during much of the eruption carried plumes eastward, depositing the thickest fallout east of the vent, inside and outside the caldera. The 2008 tephra thins rapidly to the west and north of the caldera (Fig 4.1-2). Northeast winds during the first week of August carried ash southwest, producing a lobe visible in isopach maps. The 2008 eruption primarily produced ash, with some lapilli and scarce blocks and bombs, especially near the vents. All described sections have been digitized and are included in Appendix A.

#### **4.1a Intra-caldera deposits**

Deposits within the caldera were emplaced by ash fall, pyroclastic density current, and ballistic ejection (Ort, personal communication, 2011). The 2008 products are thickest at the tuff cone on the side of Cone D. This tuff cone, which rises 250 m above the caldera floor, was the last observed active vent and is the final constructional feature of the 2008 eruption.

#### **4.1b Extra-caldera deposits**

Observations by AVO personnel during the eruption suggest that tephra deposited outside the caldera was emplaced almost exclusively by ash fall (Larsen et al. 2009). No pyroclastic density currents were observed to escape the caldera walls. Extra-caldera

deposits made up most of the sections examined and will be discussed exclusively in the following sections.

#### **4.2 Generalized stratigraphic section and unit descriptions.**

Extra-caldera deposits typically have a basal sequence of three distinct units with overlying fine-grained upper units. The lowermost depositional unit, Unit 1, is broken into two subunits at most locations. These subunits are distinguished by differences in their fine and medium ash content.

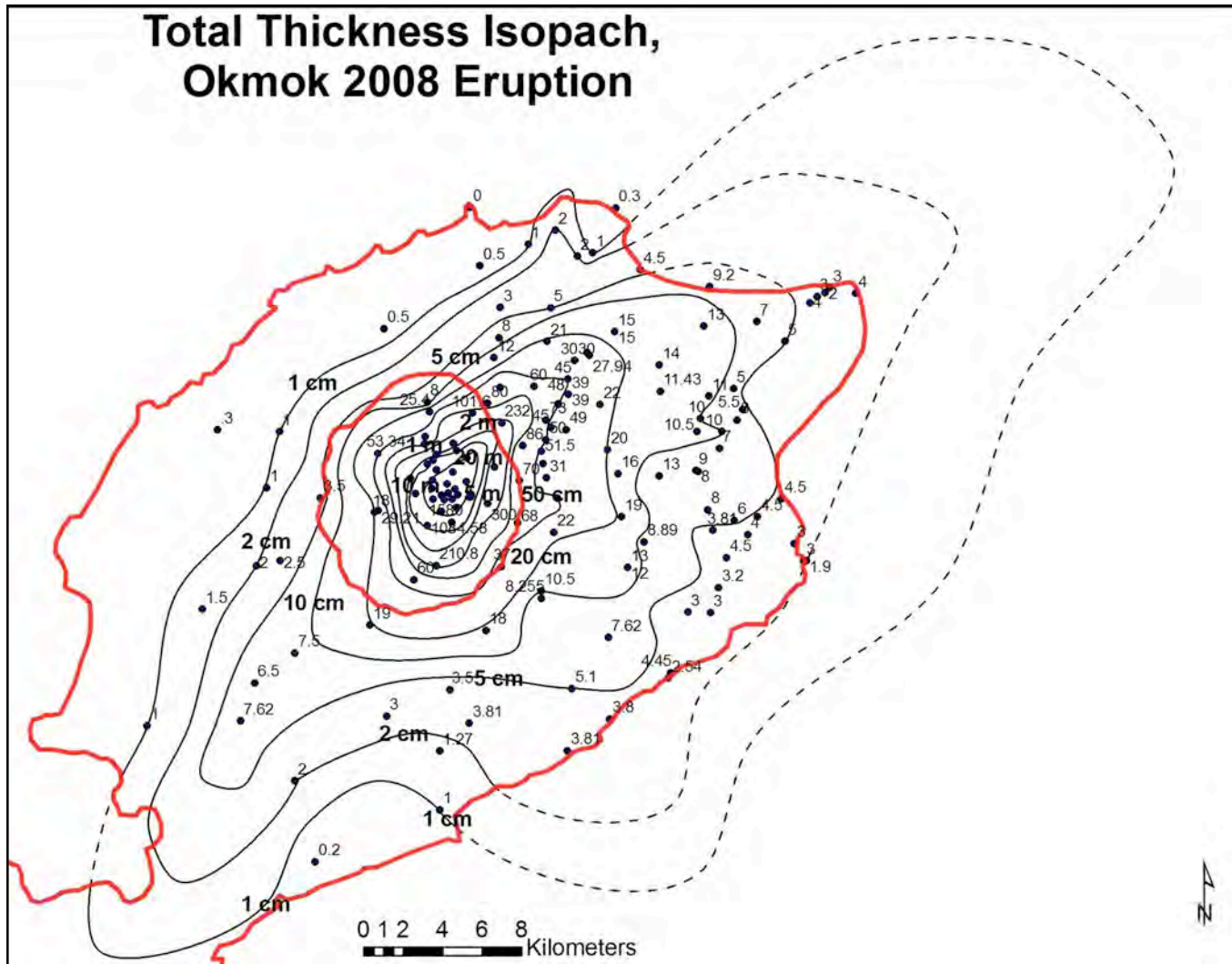


**Figure 4.1:** Isopachs of the total thickness of 2008 Okmok deposits. Sample sites are shown in dots and are labeled with total deposit thickness in cm.

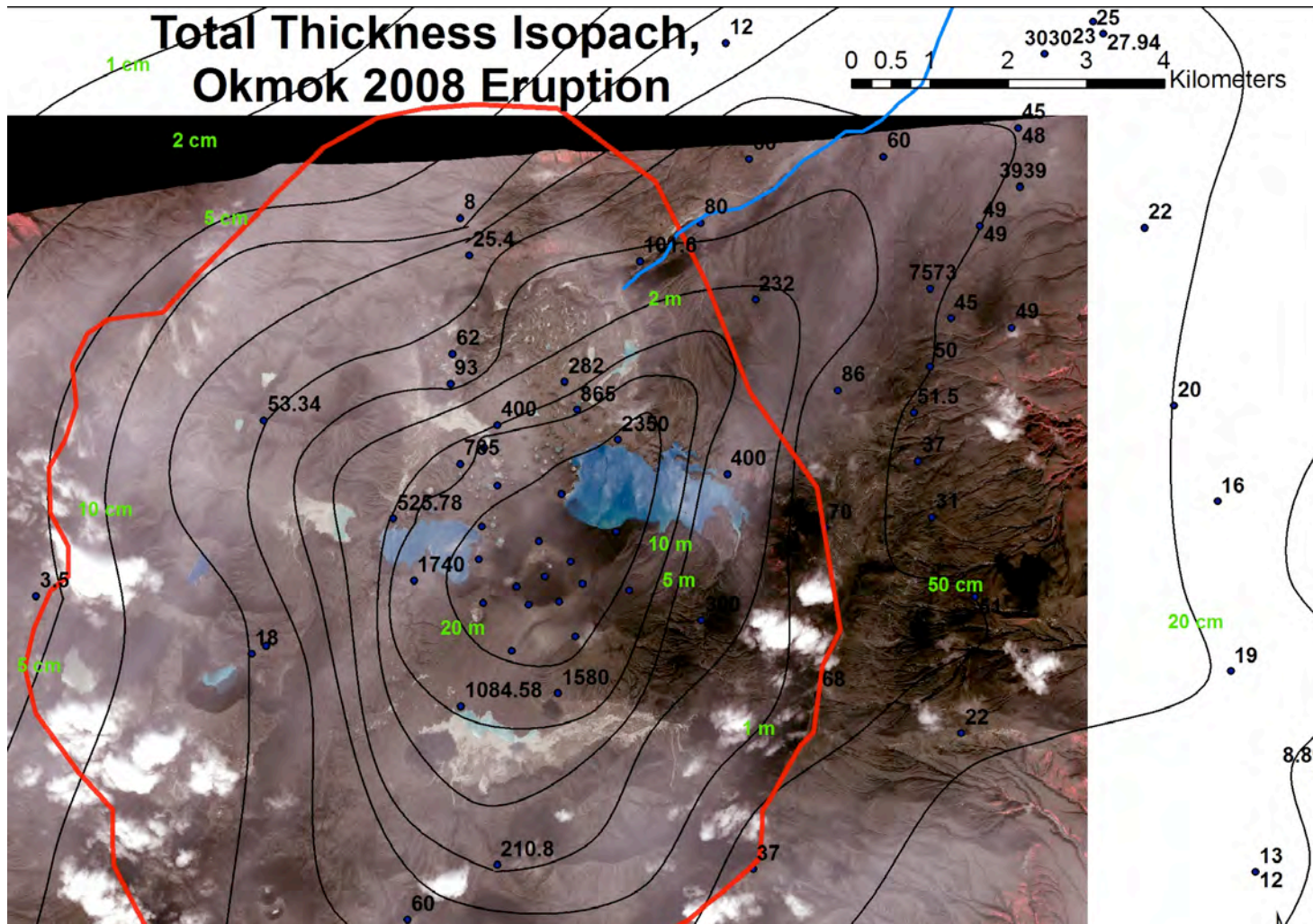


**Figure 4.2:** Isopachs of the total thickness of 2008 deposits within the caldera. Tuff cone is visible within the 20 m isopach. Sample sites are shown with blue dots and labeled with total deposit thicknesses (in cm). Isopach contour values are in green and red line is the caldera outline.

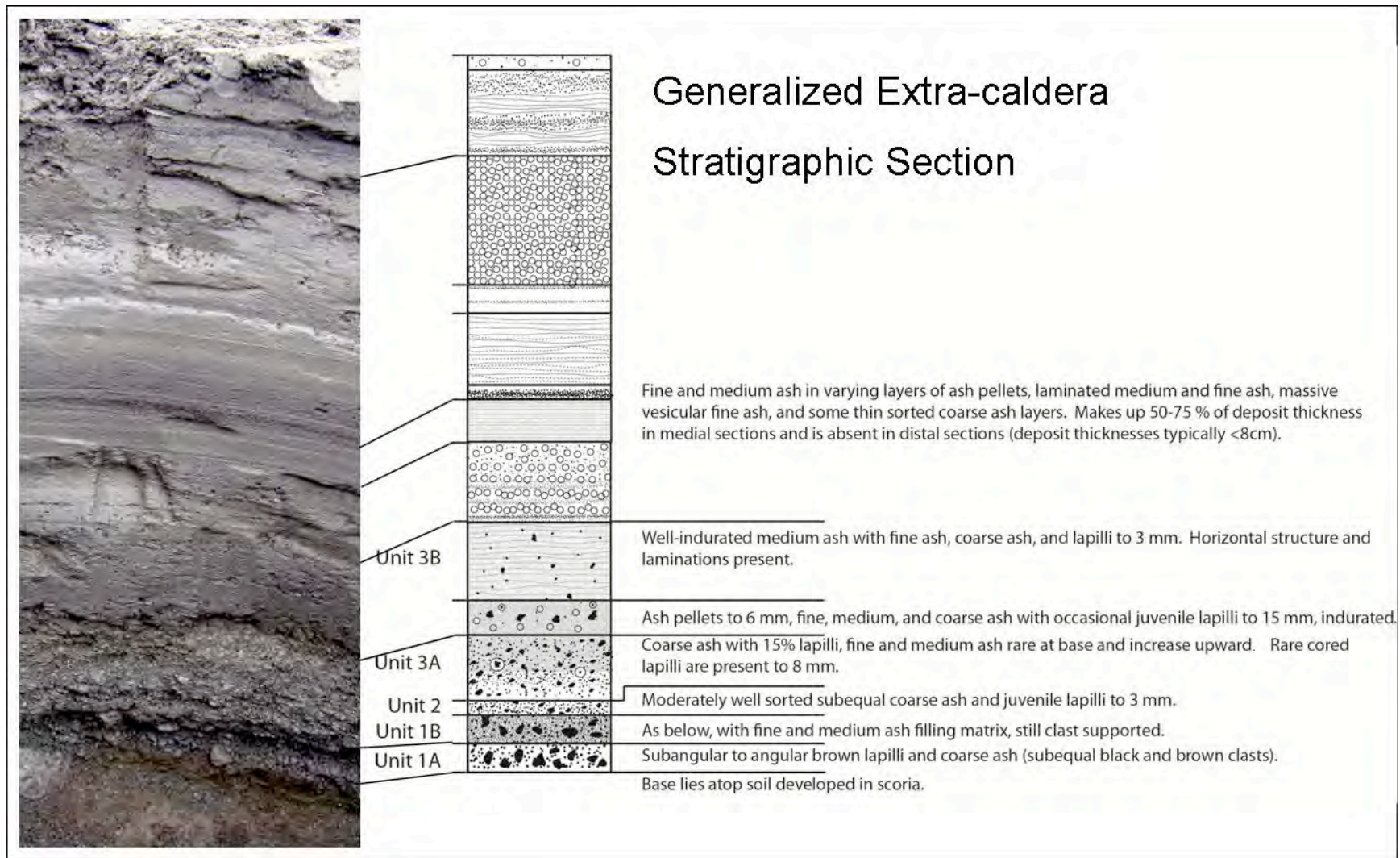


**Figure 4.3:** Generalized stratigraphic section for extra-caldera deposits (from medial caldera flanks).

# 10JAUOK002

Location: E. Side Crater Creek

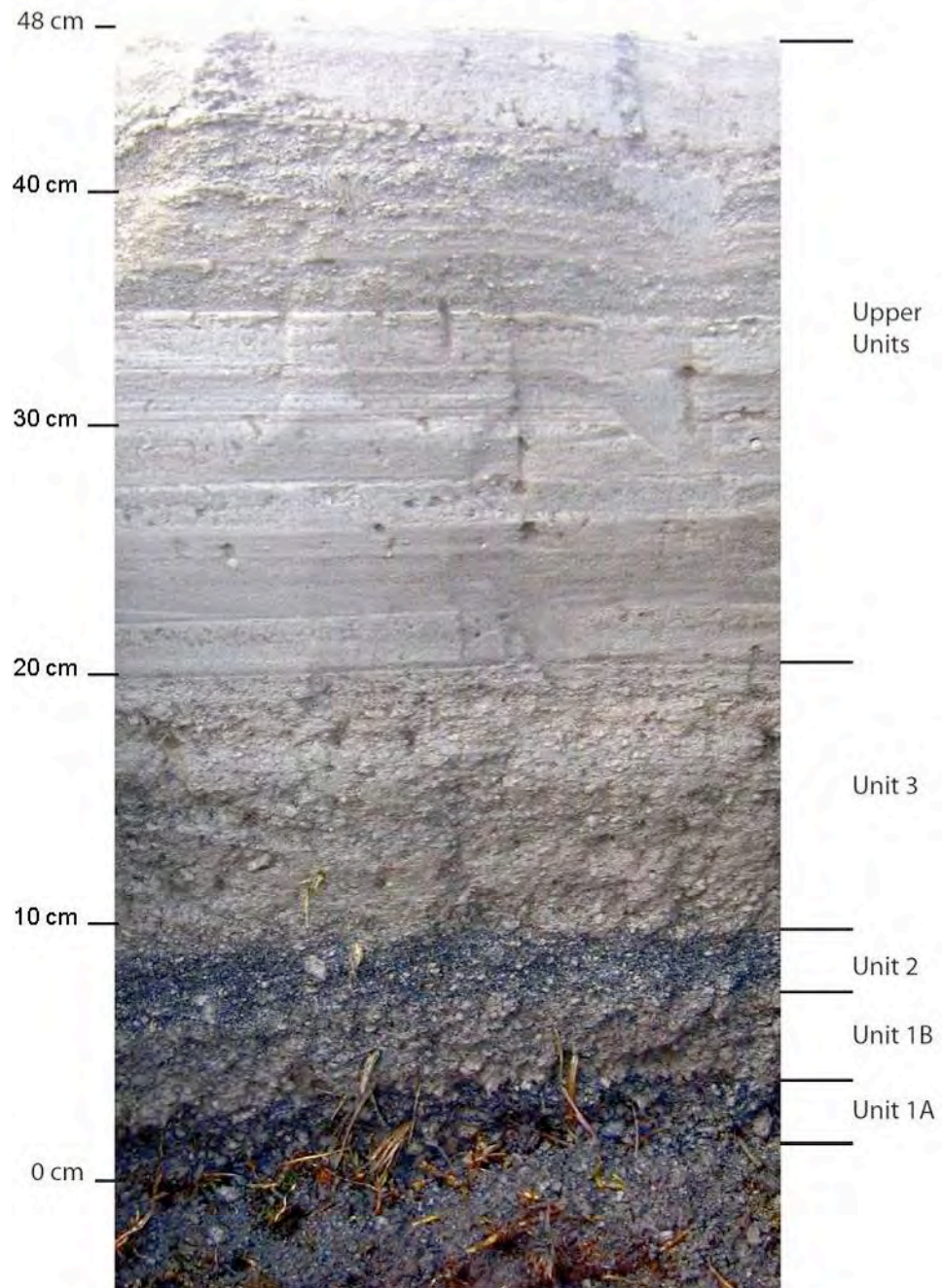


**Figure 4.4:** Annotated photograph of typical medial deposits from station 10JAUOK002.

## **Unit 1:**

Unit 1 is the basal unit and has two prominent sub-units in most locations (Fig. 4.5). Unit 1A is open-framework lapilli with coarse ash. Unit 1A is typically devoid of fine and medium ash and shows no grading. Unit 1B overlies Unit 1A and is similar but with the addition of a matrix of fine and medium ash, giving it a slightly more resistant erosional profile. Unit 1B also contains ash pellets and cored lapilli in many described sections. Unit 2, which lies atop Unit 1B, is nearly devoid of fine ash and could not be a source of fine ash to wash down. Upper units are rich in fine ash, but the absence of fine ash in Unit 2 indicates that the fine ash in Unit 1B was not washed from above but deposited with the coarse material in Unit 1B. The fine ash present in Unit 1B was deposited with the coarse material in Unit 1B rather than being washed down from units stratigraphically above.

The coarse ash and lapilli grade continuously through Units 1A and 1B and fine and medium ash first appear at the base of Unit 1B. The coarse ash is mixed black lithic and brown juvenile clasts. The lapilli are primarily brown juvenile pumice, with secondary black lava fragments. Ash pellets and cored lapilli are present in Unit 1B at some locations. The contact between Units 1A and 1B is typically sharply gradational.



**Figure 4.5:** Basal units from site 10JAUOK002

### **Unit 2:**

Unit 2 overlies Unit 1 and is moderately sorted open-framework coarse ash and lapilli (Fig. 4.5). The contact between Unit 1B and Unit 2 is typically sharp, notable mostly for the change in fine ash content. Unit 2 is made of subequal amounts of coarse ash and fine lapilli and is finer grained than Unit 1A, but is similarly devoid of fine and medium ash. The coarse ash in Unit 2 is mixed black lithic and brown juvenile material with abundant plagioclase crystals, giving the unit a ‘salt-and-pepper’ appearance. In some medial to distal sites, only one basal open-framework unit is recognizable and is most likely a combination of Units 1 and 2 without the fine-ash addition of Unit 1B.

### **Unit 3:**

Unit 3 is very poorly sorted ash with variable amounts of lapilli ranging from matrix-supported ash aggregates and scattered lapilli to clast-supported coarse ash and

lapilli, but is typically dominated by fine and medium ash. Unit 3 segregates into Units 3A and 3B at some locations (Fig. 4.6). Unit 3A is poorly indurated, contains abundant ash aggregates and cored lapilli, and displays weak or no horizontal structures. The overlying Unit 3B is commonly well indurated, devoid of ash aggregates, and strongly laminated. Unit 3B is also generally coarser grained than 3A, with dominant medium ash replacing much of the fine ash. Unit 3 appears transitional between basal coarse ash and lapilli units and the fine-ash-dominated units that lie above it.

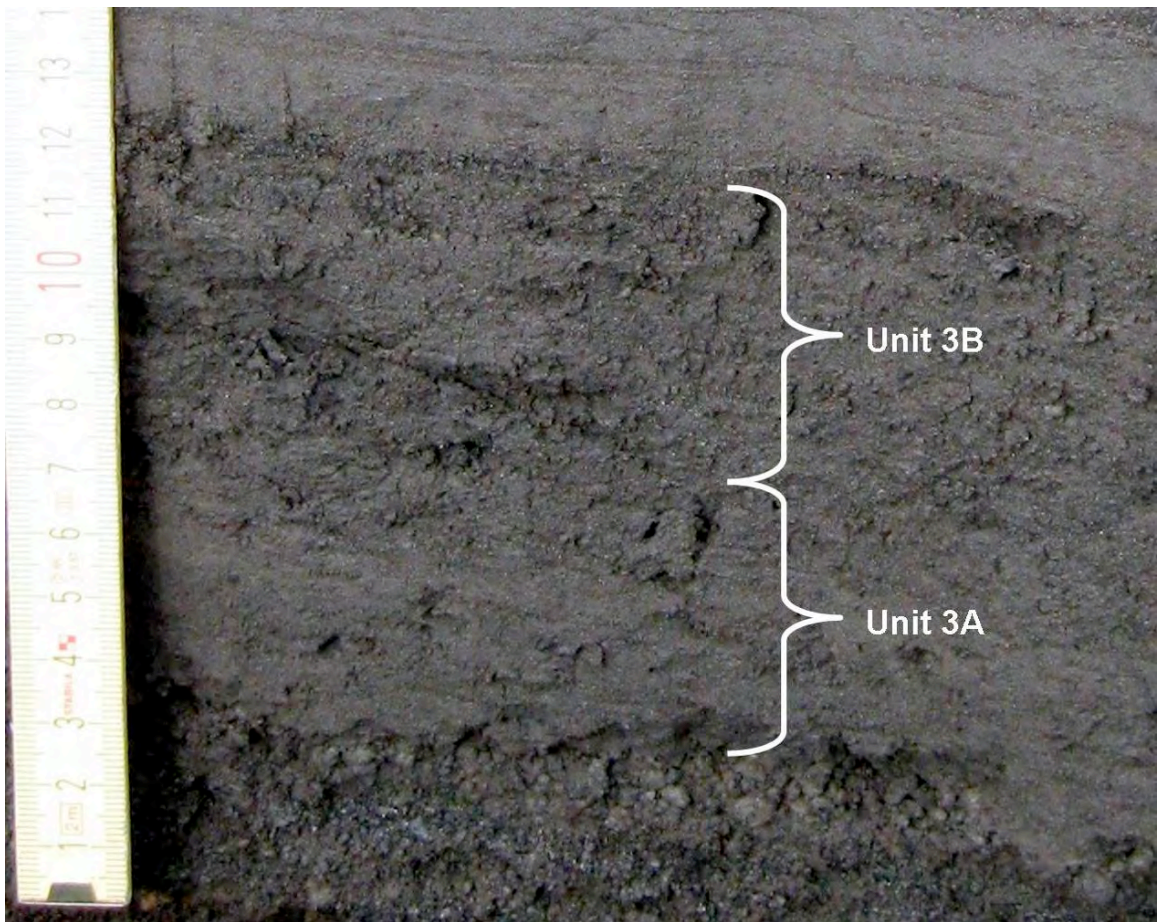


**Figure 4.6:** Units 3A and 3B from site 10JAUOK064.

### **Interpretations from field observations of basal units:**

Unit 1A is a moderately well-sorted open-framework deposit. Unit 1B contains coarse material similar to that in Unit 1A, but also includes significant fine and medium ash. Unit 2 is marked by a return to open-framework and better-sorted ash and lapilli. The coarse material in Units 1 and 2 is relatively well sorted and displays continuous normal grading, suggesting a continuous production of coarse material from the start of the eruption through Unit 2 deposition by a continuous high column. The modal sizes of ash and lapilli in Unit 2 are markedly finer than those in Unit 1A, which may have been caused by a change in fragmentation processes at the vent or a decrease in column height. Unit 1B shows the transition between Unit 1A and Unit 2, as Unit 1B coarse material is intermediate between Unit 1A and 2.

Unit 1B contains coarse material intermediate between that in Unit 1A and 2, but the fine ash content of Unit 1B suggests that plume conditions changed. The plume water content may have increased, initiating plume scrubbing and fine ash deposition. Unit 1B is absent in some locations, where there is a single coarse basal layer. This uneven distribution may be caused by the localization of fine ash deposition by ash-pellet 'storms' or rain storms. The continuous grading of basal material in those sections where Unit 1B is absent provides support to the interpretation that the coarse material in Units 1A, 1B, and 2 was deposited by a continuous column.

The base of Unit 3 is marked by another addition of fine and medium ash. The coarse ash and lapilli content of Unit 3 is much lower than Units 1 and 2, which may be caused by lower column heights for the column depositing Unit 3.

## **Upper Units:**

The upper units consist of all deposits stratigraphically above Unit 3. Locations outside and to the north, west, and south of the caldera typically lack the basal sequence of Units 1-3 and have no coarse ash or lapilli layer at the base. These upper units are dominated by several facies, including ash pellets, laminated medium and fine ash, massive fine ash, and thin beds of sorted coarse ash. Ash-pellet layers typically consist of fine ash with variable medium ash content (Fig. 4.7). Layers range from massive ash with scattered pellets to clast-supported ash-pellet 'conglomerates'. Most ash pellets found outside the caldera are massive and show no concentric rings or fine-grained rims. Ash-pellet diameters range from 1 to 8 mm, and most are 2-5 mm. Units 1B and 3 rarely contain ash pellets with cores of coarse or very coarse ash, referred to as 'cored lapilli'. The diameters of cored lapilli are larger than those of other ash pellets, ranging from 5 to 10 mm. Ash pellets rarely occur in laminated units.

Another primary facies in the upper units is laminated medium and fine ash (Fig. 4.8). A variety of structures is seen in these layers, but most have millimeter-scale laminations of alternating fine and medium ash. Some units of laminated ash contain coarse ash, but most are primarily medium and fine ash.

Massive vesicular fine ash is present in many sections, forming a cap in most medial sections and rarely appearing lower in the section (Fig. 4.9). This ash is moderately sorted, contains no medium ash, and includes poorly preserved ash pellets in about half of the described sections. Beds of massive ash are vesicular in almost all described sections. Sorted coarse ash layers are also common within the upper units in

medial deposits. These layers are typically 1-5 mm thick, and are commonly open framework and well sorted (Fig. 4.10).



**Figure 4.7:** Ash pellets from site 10-MOK-30 (photo by Michael Ort)



**Figure 4.8:** Upper laminated ash from site 10JAUOK012



**Figure 4.9:** Vesicular top ash from site 10JAUOK005.

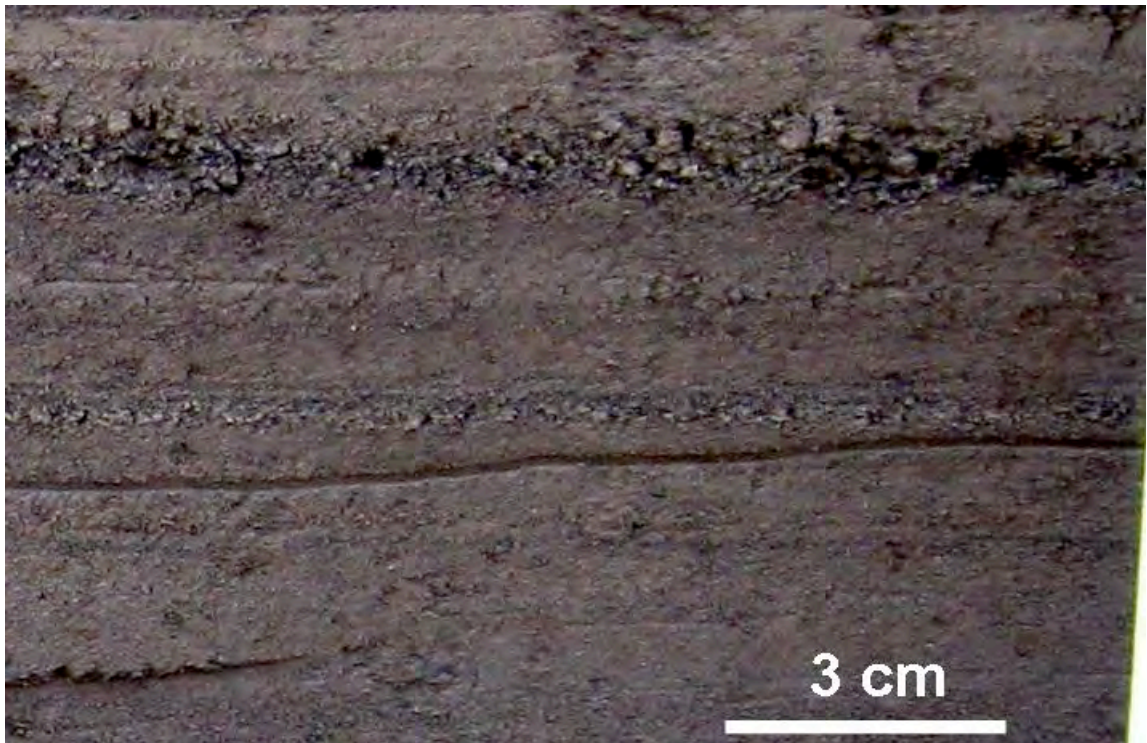


**Figure 4.10:** Coarse ash units (within the massive fine ash) from site 10JAUOK075 (top) and 10JAUOK074 (bottom)

## Pyroclastic-Surge Deposits

Beds of medium to coarse ash with pinch-and-swell laminations or duneforms (Fig. 4.11) are present in two sites along the east caldera rim (Fig. 4.12). These layers are 7-12 mm thick and dune features are approximately 10 mm in height and 2-4 cm in length. These features have alternating beds of fine-medium and medium-coarse ash and are asymmetrical.



**Figure 4.11:** Pinch-and-swell laminations and possible duneforms from site 10JAUOK079.

Deposits with these features could be emplaced by low-energy pyroclastic surges or eolian processes. Pyroclastic surges can emplace deposits with multiple grain sizes and relatively poor sorting. Surge deposits commonly have pinch-and-swell laminations

or small duneforms. Dunes produced by surges have axes perpendicular to the direction of travel. Eolian dunes or ripples are oriented perpendicular to the direction of the depositing wind. The observed dunes are oriented northeast-southwest, suggesting deposition by northwest or southeast winds or emplacement by a pyroclastic surge travelling from the northwest. Either of these mechanisms is possible, as prevailing winds are from the west-northwest and the active vents are located northwest of the deposits with these features.

The dune features were only observed at these two sites on the caldera rim nearest to vents. Wind-emplaced dunes would likely be present in many locations, as wind velocities and direction are fairly consistent over much of the island. Pyroclastic-surge dune deposits would be more localized, and the most likely location for surges to exit the caldera is the rim nearest to the vents. Because of the location and orientation of these dune deposits, I propose that they may have been emplaced by pyroclastic surges cresting the caldera rim.

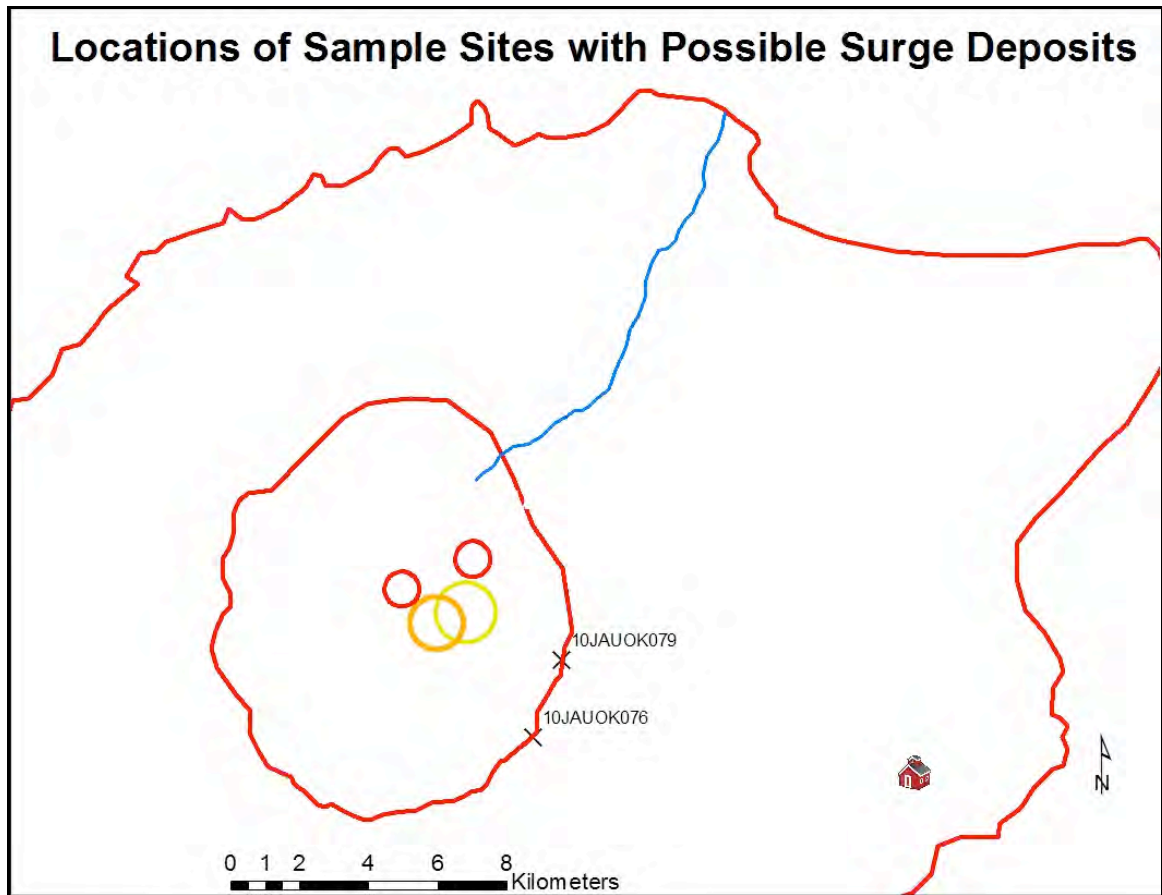


**Figure 4.12:** Surge deposit sample sites. Fort Glenn (red building) and Crater Creek (blue) shown for reference.

### **Interpretations from field observations of upper fine units**

Upper units are overall much finer-grained than basal units and consist of ash aggregates, laminated ash deposits, massive fine ash, and coarse ash units. Ash aggregate units provide evidence that plume water contents were 10-25%. The changes in upper unit facies from ash pellets to laminated ash and vesicular massive ash may be driven by plume characteristics such as water content. Laminated ash units show alternating layers of fine ash and fines-depleted ash and millimeter-scale downbowed laminae, features that are common to ‘ash rain’ units (Walker 1981). Down-bowed laminae are slightly wavy

and concave-up, but flat-lying thin layers of fine ash. Very thin light gray lenses of fine and very fine ash are present within many laminated ash layers and may show the end of an ash rainstorm. Laminated ash deposits were likely emplaced when rainstorms washed columns of ash and water contents were too high for ash aggregation. The laminated ash layers may have been affected by high wind velocities, which are common at Okmok, and laminations may be the result of syn-depositional eolian reworking.

I interpret that massive vesicular ash may have been deposited in an ‘ash mist’ or ‘mud rain’ in which ash pellets did not effectively form, resulting in a structureless deposit. Vesicular ash has been observed in other ‘ash-rain’ deposits, suggesting that these vesicular upper ashes are ‘ash rain’ deposits (Walker 1981). Weather conditions during the eruption may also have controlled the deposit type, as meteorological rain could wash ash from the column to produce ‘ash rain’ and wind may have syn-depositionally reworked upper units.

The coarse ash units present in upper units at many sites may represent discrete pulses from the vent that produced coarser material. Short-lived increases in magma flux at the vent could have produced coarser material and higher columns, transporting coarse ash farther from the vents.

### **4.3 Distribution of 2008 Deposits**

#### **4.3a Distribution of Basal Units**

Basal units 1-3 are distributed over the east caldera flanks. Isopachs for Unit 1+2 have a primary axis extending northeast from vents and a secondary lobe, visible in the 2-cm isopach line, extending southeast (Fig. 4.13). Isopachs for Unit 1 total, Units 1A and

1B, show a northeast plume similar to that shown by Units 1+2 but lack the secondary lobe (Fig. 4.14). Units 1A and 1B were deposited by plumes driven by similar winds, showing identical axis orientations and similar shapes (Figs. 4.15, 4.16). Isopachs for Unit 2 show a northeast distribution similar to Unit 1 but a smaller areal distribution (Fig. 4.17). Isopachs for Unit 2 display the southeast secondary lobe visible in Unit 1+2 isopachs.

Two distinct lobes are visible on the Unit 3 isopach map, the northeast lobe is Unit 3A and the east-southeast lobe is Unit 3B (Fig 4.18). Individual isopach maps of Units 3A and 3B support the idea of a change in wind direction, as the primary axis of Unit 3A is oriented northeast and the axis of Unit 3B is oriented east-southeast (Fig 4.19, 4.20). Unit 1 is typically the most prominent coarse ash and lapilli layer and contains the largest clasts at most sites. Average maximum clast diameter was calculated for Unit 1, with large clasts collected from both Unit 1A and 1B, and plotted as Unit 1 isopleths (Fig. 4.21).

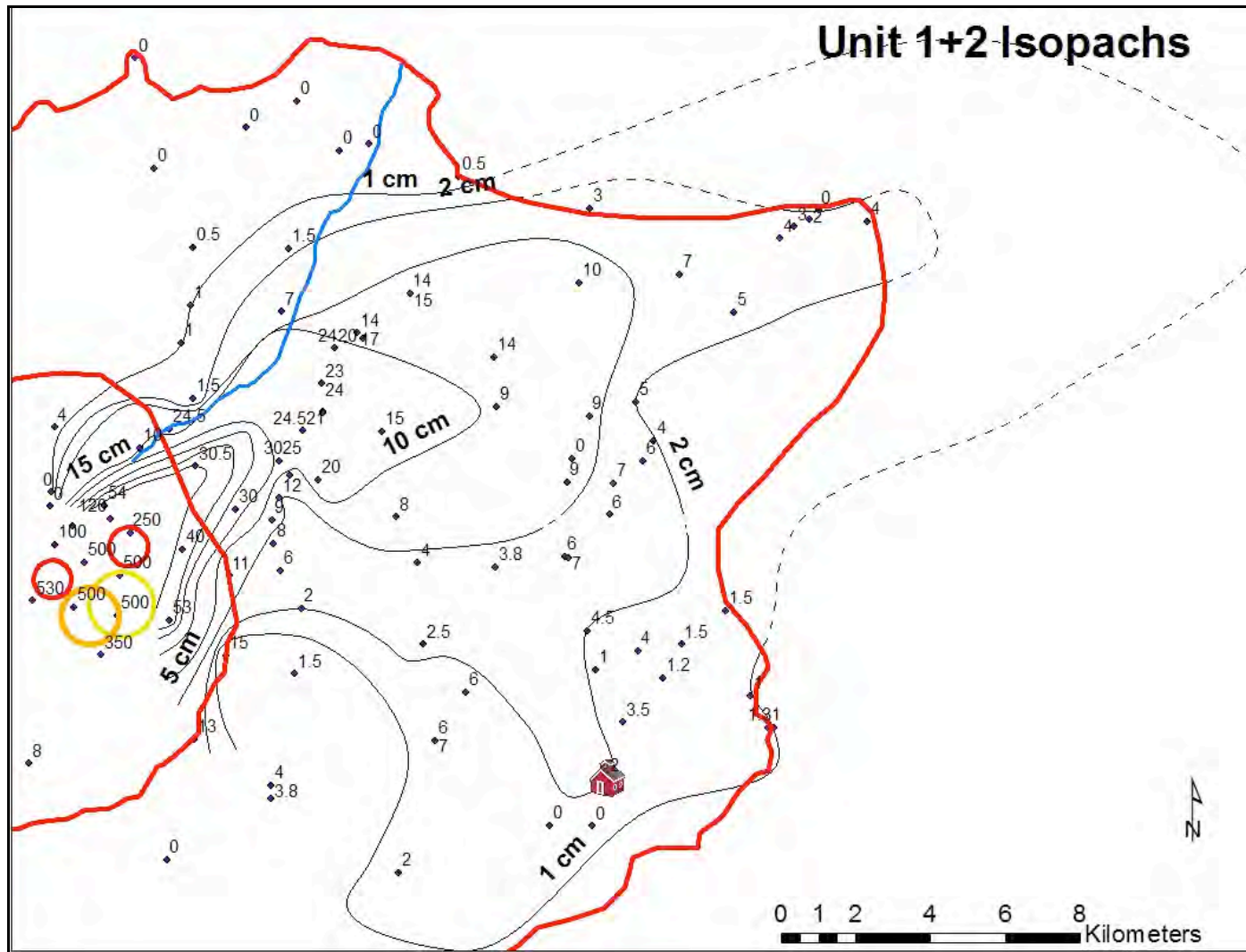


**Figure 4.13:** Isopachs for total coarse basal material (Units 1 and 2). Fort Glenn (red building) and Crater Creek (blue) shown for reference.





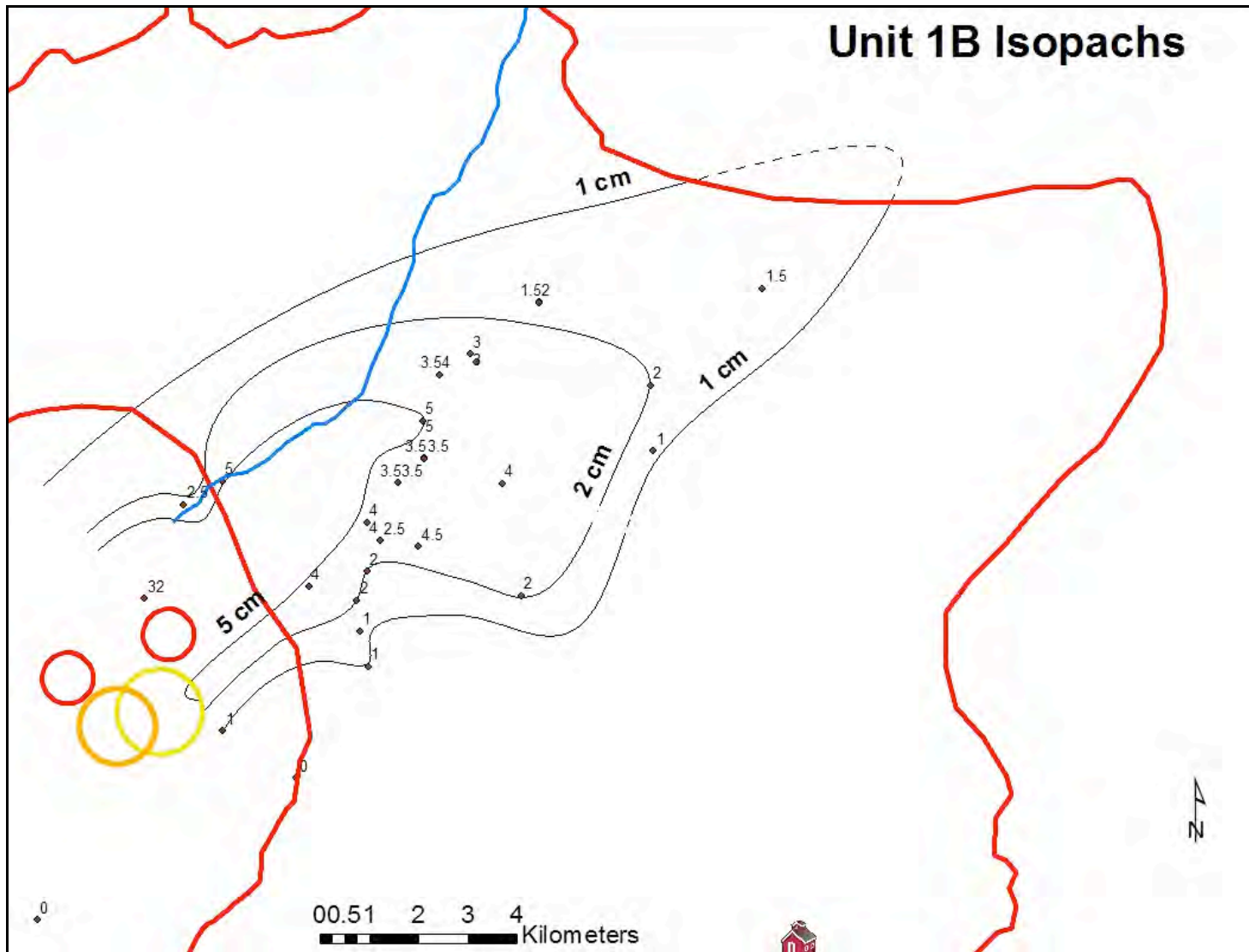


**Figure 4.16:** Isopachs for Unit 1B. Fort Glenn (red building) and Crater Creek (blue) shown for reference.

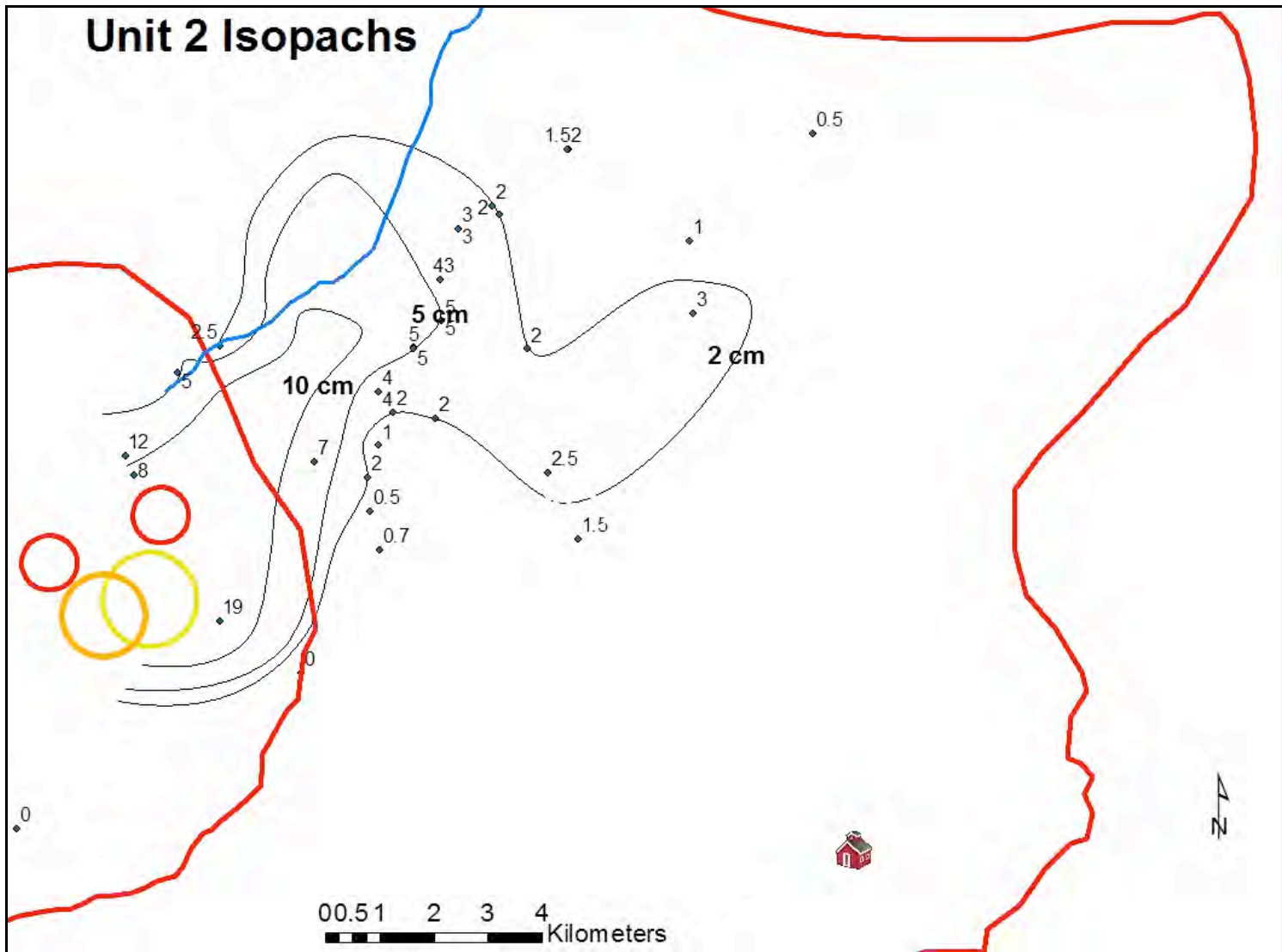


**Figure 4.17:** Isopachs for Unit 2. Fort Glenn (red building) and Crater Creek (blue) shown for reference

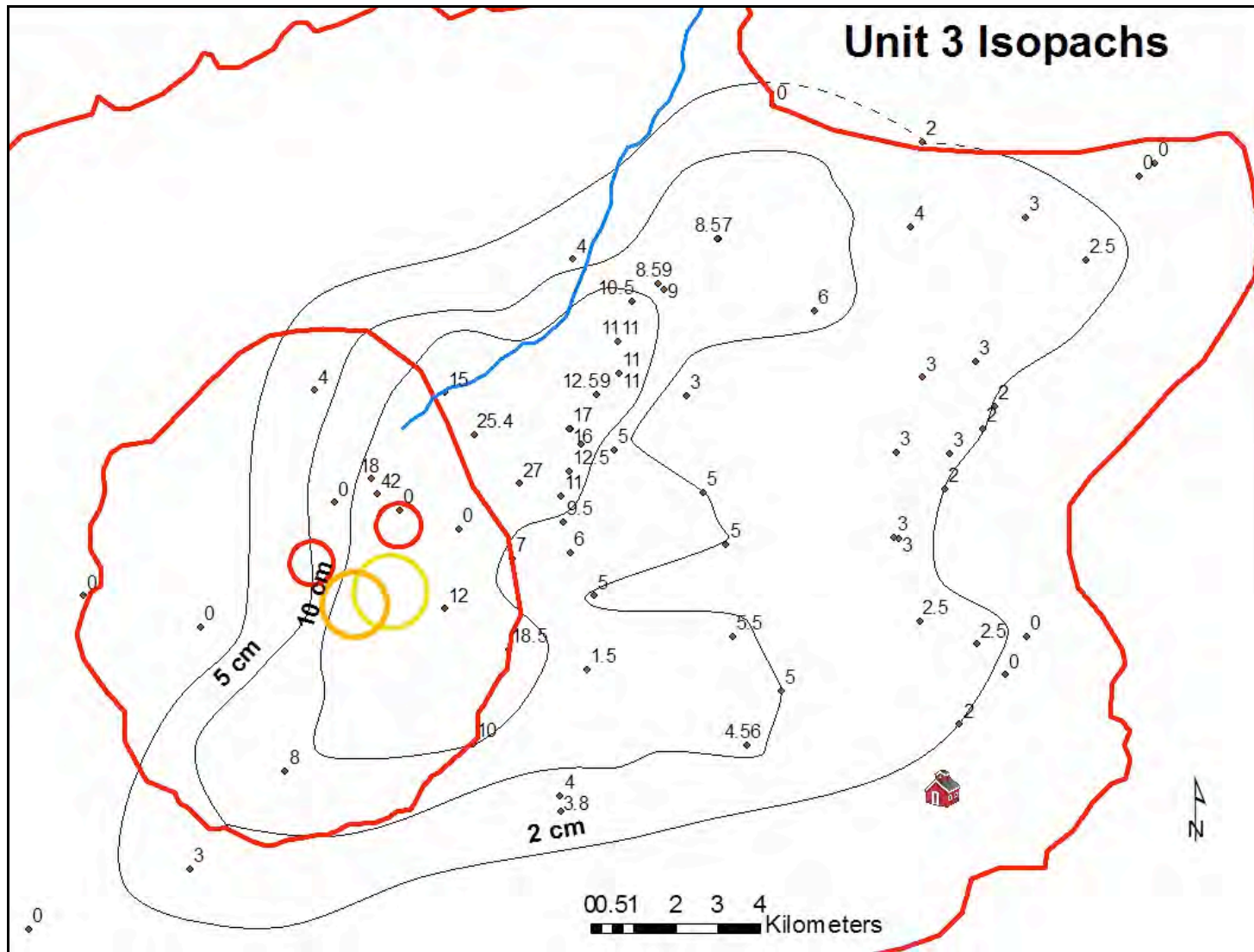


**Figure 4.18:** Isopachs for Unit 3. Fort Glenn (red building) and Crater Creek (blue) shown for reference.

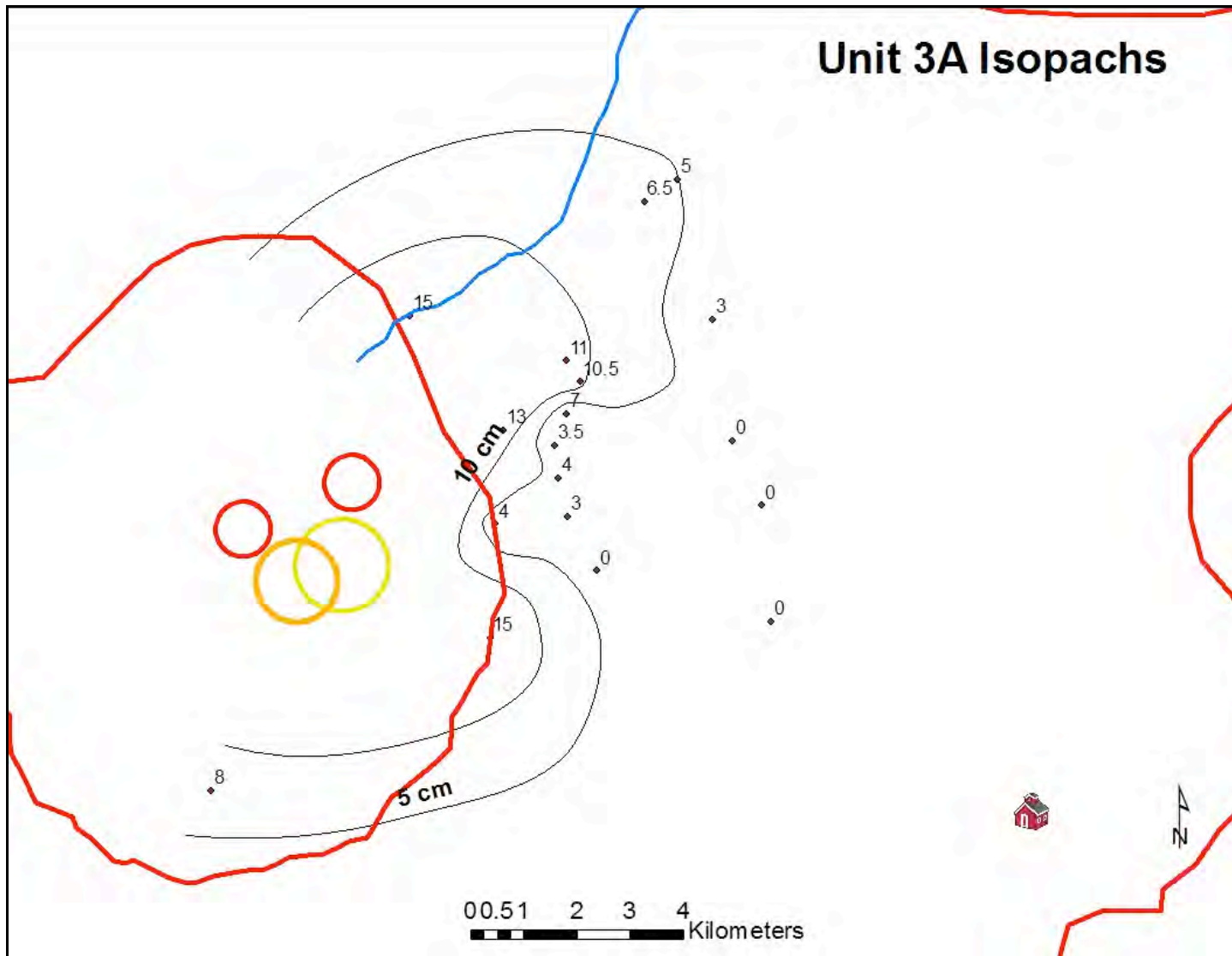


**Figure 4.19:** Isopachs for Unit 3A. Fort Glenn (red building) and Crater Creek (blue) shown for reference.

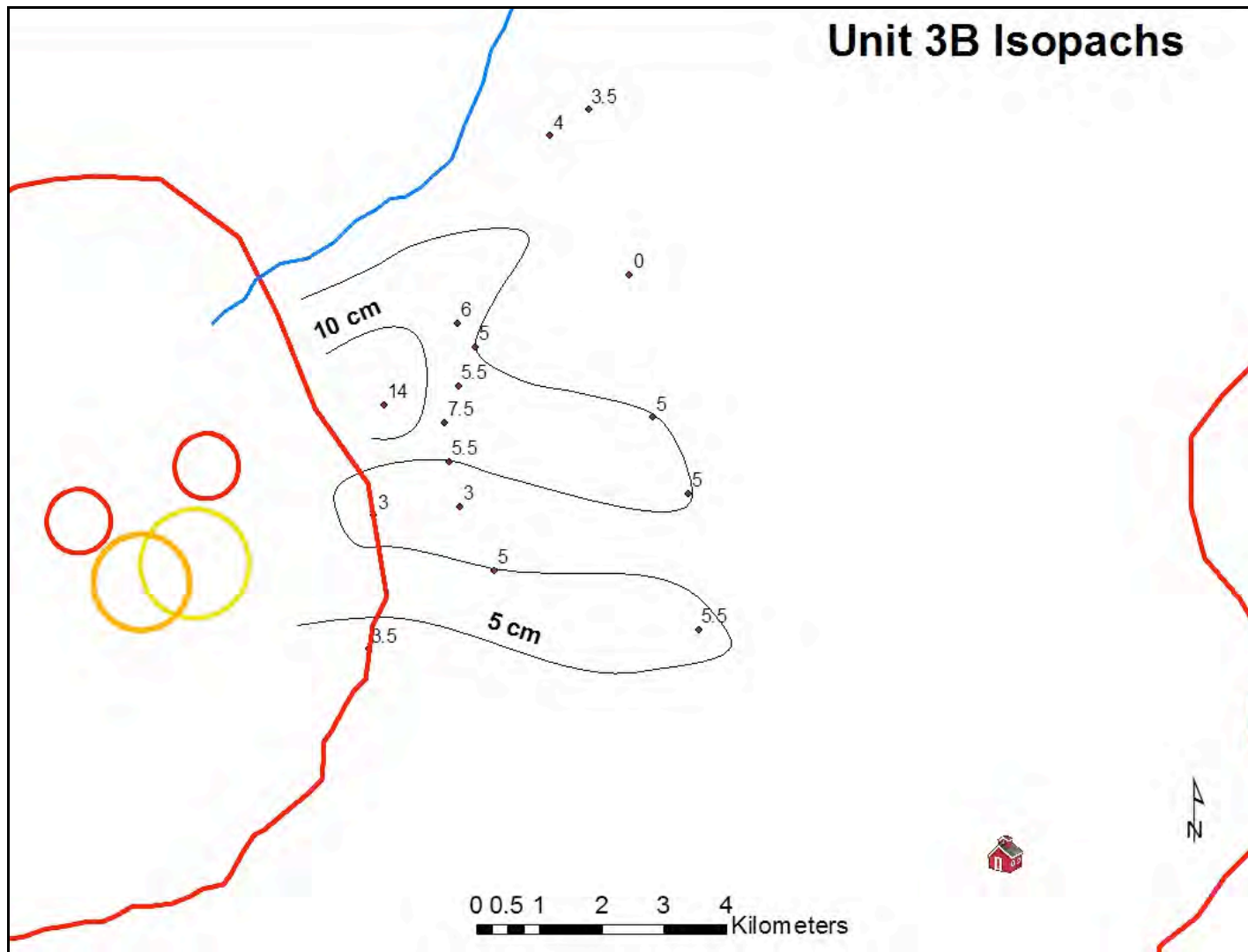


**Figure 4.20:** Isopachs for Unit 3B. Fort Glenn (red building) and Crater Creek (blue) shown for reference.

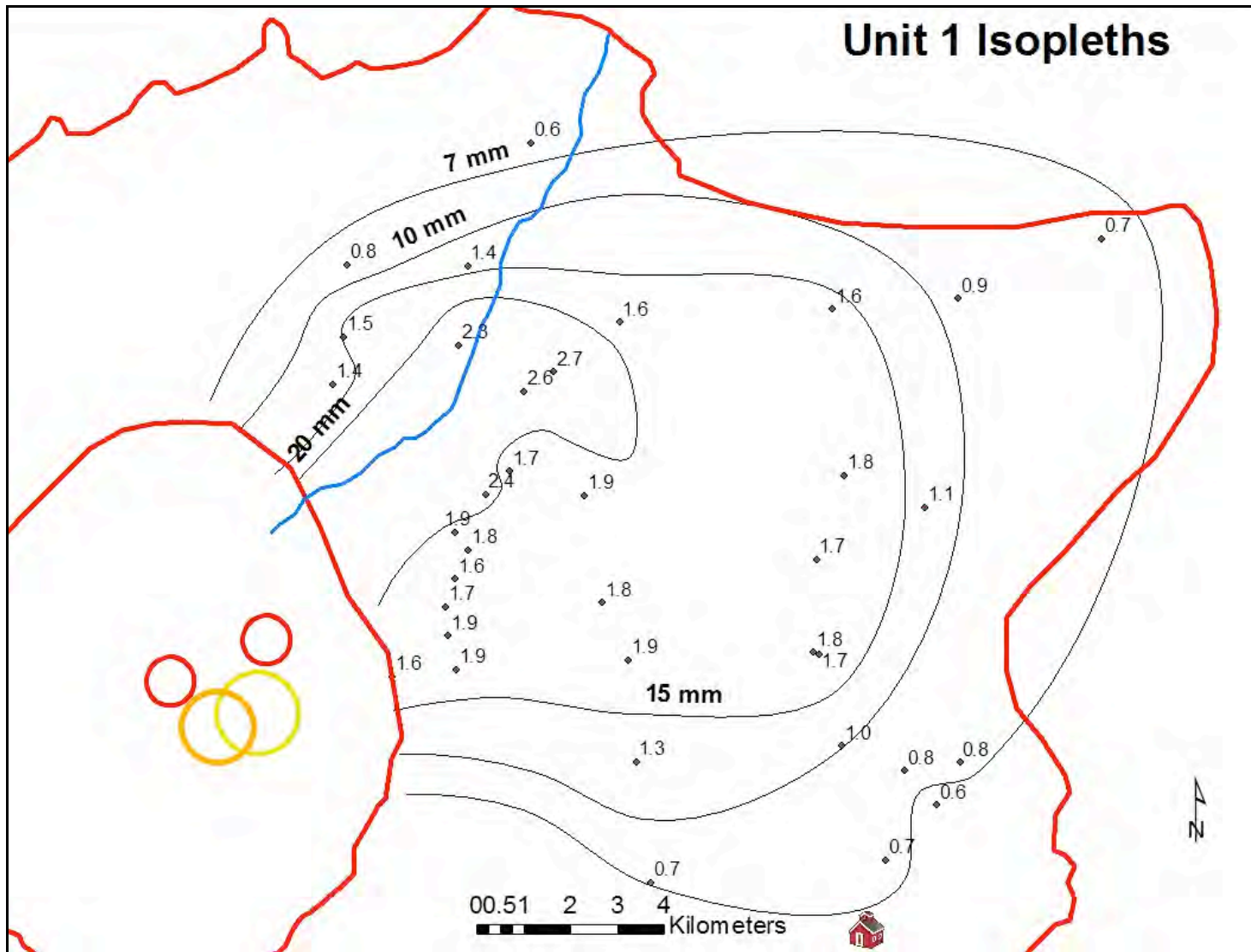


**Figure 4.21:** Unit 1 Isopleths. Average of the lengths of the three main axes of the largest five clasts is plotted

### **Interpretations from distribution of basal units**

Southwest winds were present at the onset of the eruption and persisted through the deposition of Unit 3A. The switch from southwest to west-northwest winds is recorded in the deposits between Unit 3A and Unit 3B. Satellite images of plume directions constrain the deposition of Units 1-3A to the first 4-5 hours of the eruption. Eyewitness accounts from ranch hands present at Fort Glenn (Fig. 4.13) during the opening sequence of the eruption confirm that, at around 1:00 pm local time (21:00 UTC), the plume axis was north of Fort Glenn, but ash and lapilli were falling at Fort Glenn. By the time the wind switch occurred around 00:00 UTC or 4:00 pm local time, all personnel had been evacuated from Fort Glenn and no oral description of the wind shift exists. Rain storms during the deposition of Units 3A and 3B may have increased deposition rates and localized deposition, as these units are finer grained than those below and contain ash aggregates, evidence of plume scrubbing.

The plume direction indicated by Unit 1 isopleths is similar to that indicated by Unit 1 isopachs, but the isopleth distribution is wider than the isopach distribution. Isopleth contours are commonly broader than isopach contours for the same unit, as large clasts are ejected and spread wider than the majority of deposits. This pattern is seen in deposits from other eruptions, such as the 2008 eruption of Chaitén volcano, Chile (Alfano et al. 2010). The sequence of deposit distribution seen from Unit 1A to Unit 2 shows a decrease in the deposit areal extent and may indicate a decreasing column height.

#### **4.3b Distribution of Upper Units**

Upper units are deposited in every direction from vents but are thickest to the northeast and southwest. Deposits are thinnest to the northwest, with total thicknesses of less than a few centimeters on the caldera rim.

Fine-grained upper units compose the majority of the deposit thickness within the caldera and on the upper flanks (0-5 km from vents) but thin more rapidly than the basal coarse units to the east of the caldera and disappear altogether at 15 km east of vents (Fig. 4.22, 4.23).





### **Interpretations from distribution of upper fine units**

Ash pellets made of predominantly fine ash are common at medial sites in Unit 1B, Unit 3A, and throughout the upper units. The percentage of upper units made up of ash pellets ranges from zero to nearly eighty percent, with most sites between twenty and sixty percent. Ash pellets indicate that fine ash was aggregating in the eruption column. Aggregation can occur by liquid film binding or electrostatic attraction (Schumacher and Schmincke 1995), and in this wet eruption with low plume heights late in the eruption, liquid film binding is the more likely process. Ash aggregation increases the effective diameter of ash particles and emplaces aggregates closer to the vent than similar non-aggregated ash would be deposited. The higher column emplacing the basal units distributed coarse material farther from the vents. The combination of these effects explains the apparent coarsening of the deposits to the east.

When plume water content rises above 30 wt %, ash aggregation is inhibited (Schumacher and Schmincke 1995), and ‘ash rain’ or ‘mud rain’ of water droplets carrying fine and medium ash may fall. Fine and medium ash deposits without evidence of ash pellets are typically laminated, and may have been emplaced by this ‘ash rain’. Both of these processes controlled the deposition of upper units by increasing fine and medium ash deposition in proximal and medial sites and limiting fine and medium ash deposition in distal sites.

#### **4.4: On-axis and across-axis changes in deposits**

Sites for section description were chosen systematically to examine on-axis changes in deposits and across-axis changes at several distances from vents (Figs. 4.24-

26). The dramatic thinning of upper fine units with distance from vents is visible in the on-axis fence diagram (Fig. 4.24). This diagram also shows the thinning of total deposits with distance from vents and the persistence of basal coarse material to sites on the island coast. The across-axis traverses show the appearance and differentiation of Unit 3 with increasing distance south. Sites on the north end of the traverse have thin layers of Unit 3. With increasing distance south along the traverse, Unit 3 thickens and differentiates into 3A and 3B. Unit 3B thickens and Unit 3A thins at the south end of the traverses (Figs 4.25-26).

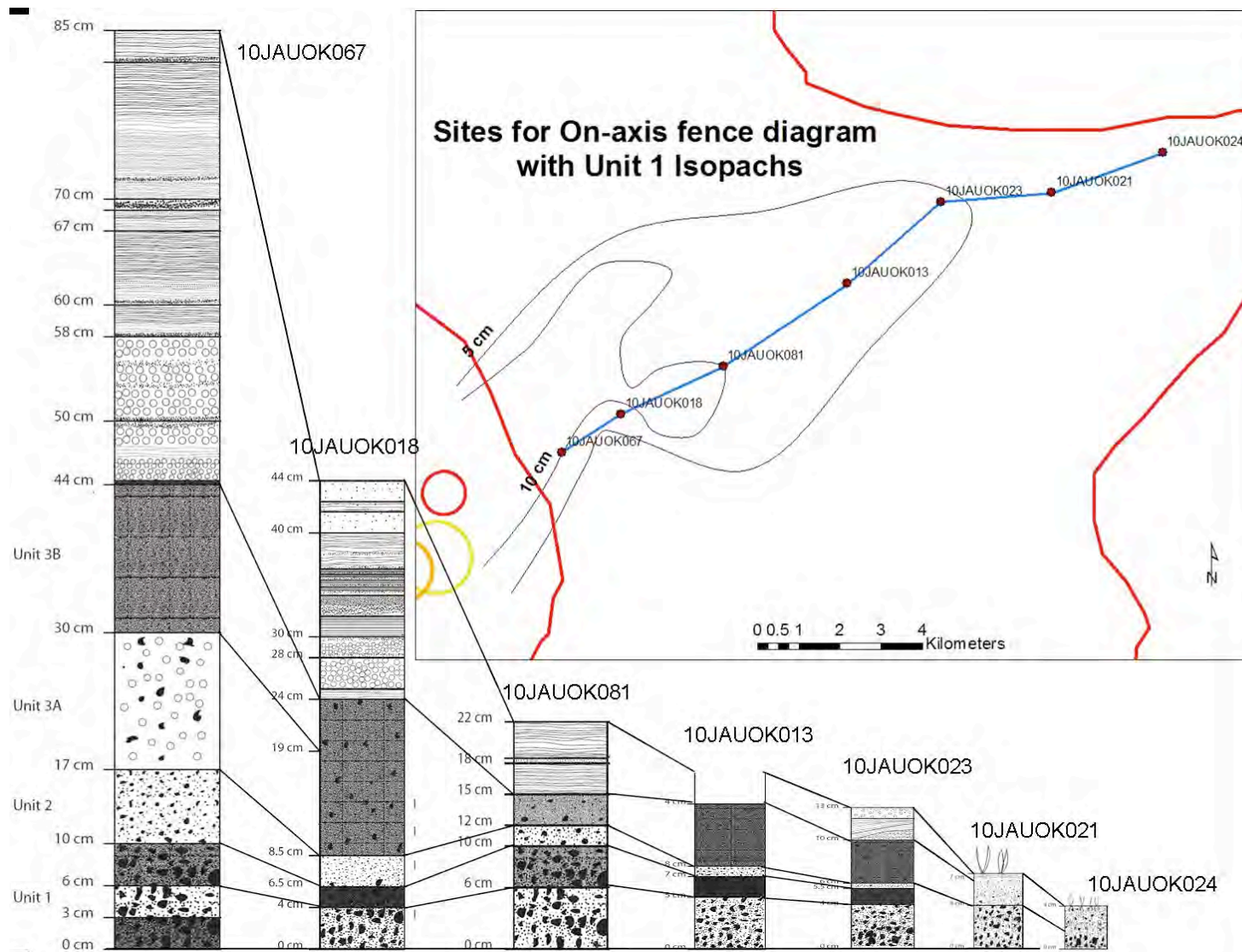
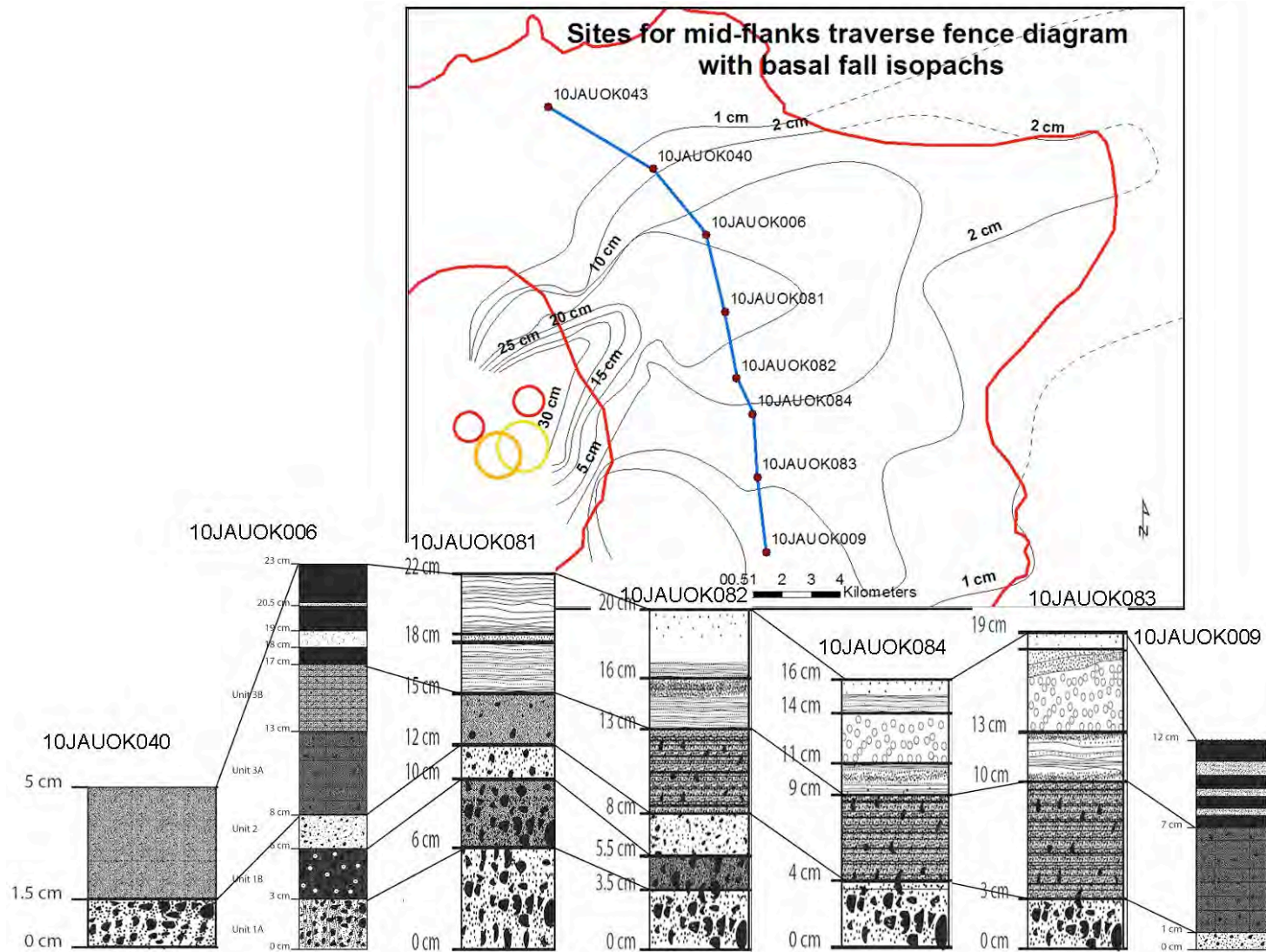
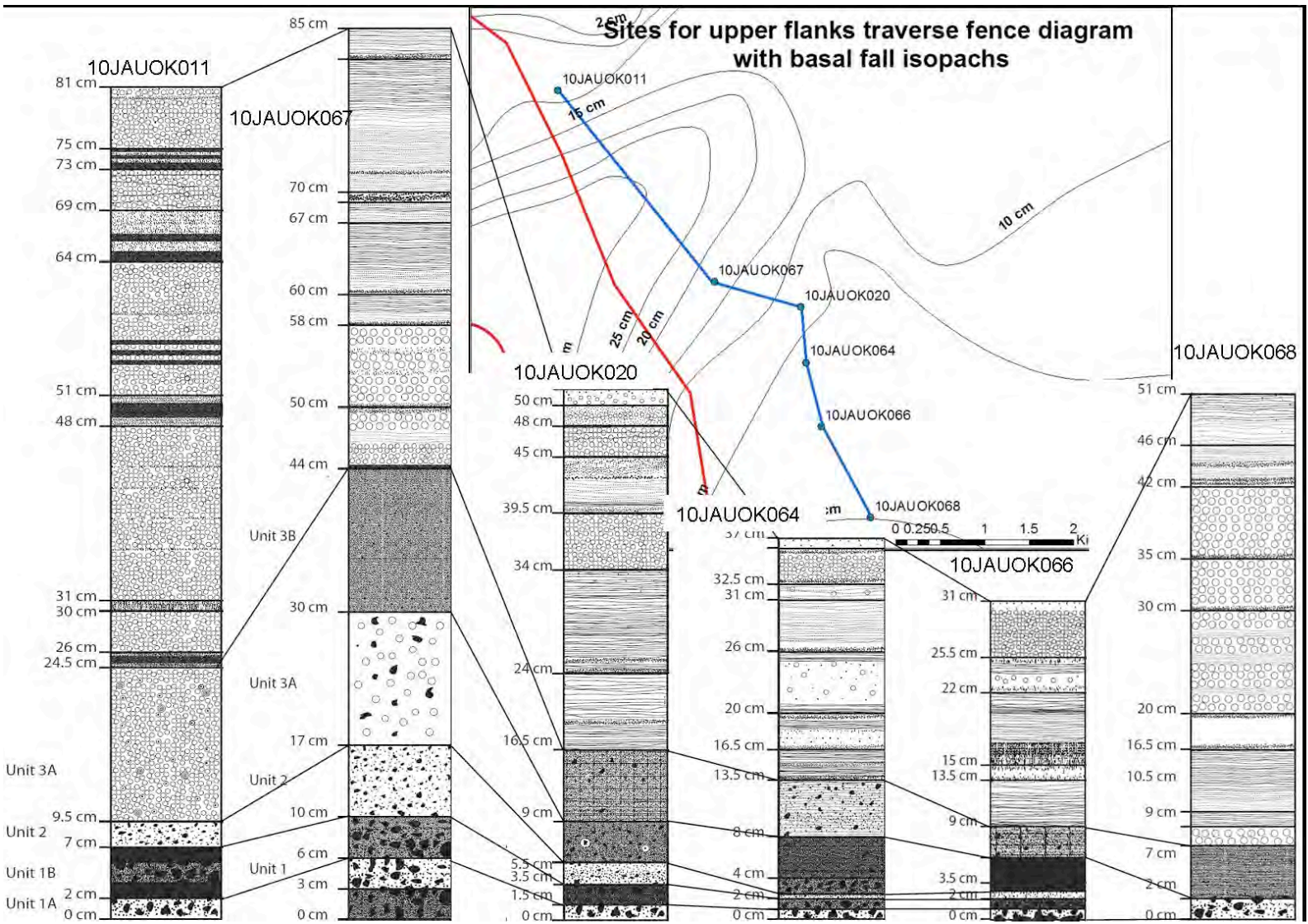


Figure 4.24: On-axis fence diagram



**Figure 4.25:** Mid-flanks traverse across-axis fence diagram



**Figure 4.26: Upper-flanks traverse across-axis fence diagram**

#### **4.5: Syn-depositional and post-depositional reworking of 2008 deposits**

In selecting sites for description of tephra stratigraphy, we were careful to avoid sites at which post-depositional reworking had added remobilized tephra to the section. Sites on ridgelines or high points were chosen over valleys or low areas to minimize secondary deposits and thus our measurements are minimum thicknesses. Evidence of post-depositional reworking is abundant on both small and large scales. During the five weeks of eruption, many lahars originated on upper flanks and transported large volumes of 2008 tephra and underlying sediments in nearly all major drainages on the island. Large lahar deltas were emplaced at the mouths of most streams, and were most prominent on the east and south coasts of the northeast lobe of Umnak Island, where deposits were thickest.

On a smaller scale, deep rilling and gullying has occurred, cutting through 2008 tephra and into underlying sediments in the two years between eruption and field work. The deposition of 2008 material triggered the erosion of underlying material and upset the stable vegetated platforms that were present before July 2008. Some sections were examined in lower areas, and secondary deposits were common in these locations. Slope-wash and hyperconcentrated flow deposits overlie 2008 ash-fall deposits in these localities (Fig. 4.27).

A few criteria were used to determine which sections were unaffected by post-depositional reworking. Obvious hyperconcentrated flow or other fluvial deposits overlying a typical 2008 tephra section eliminated sites from description as primary 2008 deposits. The presence of ash aggregates in upper units was taken to indicate a primary ash-fall deposit. A light gray vesicular fine ash cap was present at the surface in most complete

sections, and was also taken as the top of primary 2008 deposits. This particular feature was very helpful for choosing sites, as it was visible before commencing excavation.

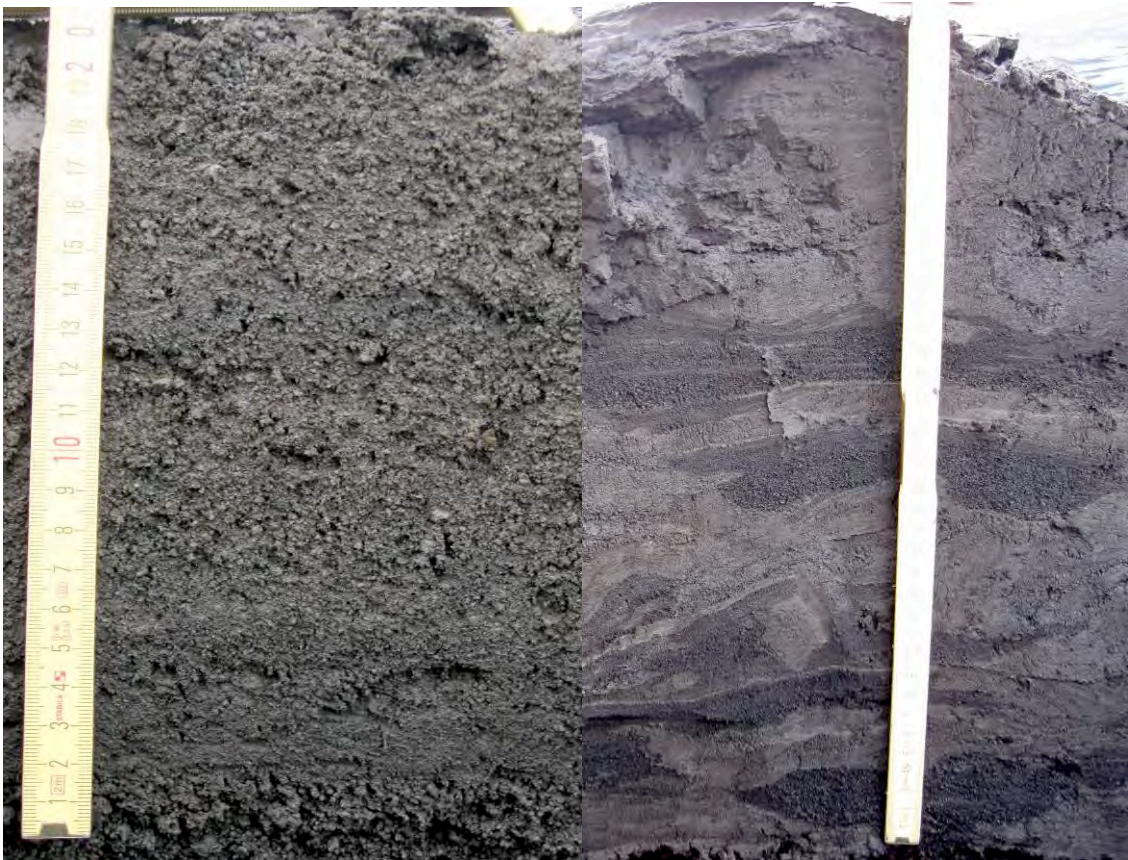


**Figure 4.27:** Examples of post-depositional reworking of 2008 eruption deposits.  
**Left Panel:** Hyperconcentrated flow deposit from site 10JAUOK035  
**Right Panel:** Channel forms from site 10JAUOK074A

Many complete primary 2008 ash-fall sections contained units with channel forms or other features that indicated fluvial, or alluvial reworking. Syn-depositional reworking was important in the emplacement of tephra in the 2008 Okmok eruption. Types of syn-depositional reworking included wind-driven ash lamination, rainfall saturation and fine-ash elutriation, and fluvial tephra remobilization to form small channel-forms.

#### 4.6: Mass-per-unit-area (MPUA) measurements

I measured MPUA for a complete section at site 10JAUOK002. Samples of each unit were measured for volume in the field and weighed in the laboratory after drying. The tephra bulk density was calculated by dividing the mass of each sample by its volume (Table 4.1). The average tephra bulk density for 2008 deposits is around 1600 kg/m<sup>3</sup>.

MPUA calculations								
	Sample Site 10JAUOK002	Dimensions (cm)						
Layer	Unit	a	b	c	Volume (cm <sup>3</sup> )	mass (g)	Density (kg/m <sup>3</sup> )	Density of Basaltic Andesite (kg/m <sup>3</sup> )
B	1B	5	4	5	100	145	1450	2962
C	2	5	4	3	60	94.2	1570	
D	3	5	2	10	100	162.7	1627	
E	ash pellets, lam. ash	5	2	14	140	264.2	1887	
F	crs ash with fn laminae	6	5	6	165	229.3	1390	
G	vesicular massive ash	8	6	5.2	214.5	349.2	1628	
				<b>Total</b>	<b>779.5</b>	<b>1244.6</b>	<b>1597</b>	

**Table 4.1:** MPUA calculations for site 10JAUOK002

AVO personnel took several mass-per-unit-area measurements in 2008, mostly in distal or off-axis sites with thin deposits. Apparent bulk densities calculated from these MPUA measurements range from 960-1760 kg/m<sup>3</sup> with an average of 1350 kg/m<sup>3</sup>. The disparity between measurements made in 2008 and 2010 is likely due to the compaction and settling the tephra underwent in the two years between measurements. With time, compaction and settling should increase the tephra bulk density, as is observed.

## **Chapter 5: Grain-size analysis results**

The grain-size distribution of individual units and facies from 25 sites are discussed below. In section 5.1, I describe grain-size distributions by unit and facies type qualitatively. Section 5.2 follows the methods of Wohletz et al. (1995) to quantitatively examine the contributions from magmatic and phreatomagmatic fragmentation based on grain-size subpopulations. Section 5.3 qualitatively examines contributions from magmatic and phreatomagmatic based on grain-size population dispersions.

### **5.1: Grain-size data by unit**

The grain-size data and modes were modeled using SFT. The grain-size distribution graphs were constructed in Microsoft Excel, which simply plots the data and connects points with a smoothed line, so all grain-size peaks appear on values of 1- or 0.5-phi intervals. SFT shifts grain-size peaks based on the values of the size fractions above and below a certain peak, leading to modes that fall slightly coarser or finer than the size fraction with the highest weight fraction. Modes calculated in SFT include multiple sieve sizes, so grain-size fractions in Excel plots and SFT tables differ. Modes from individual samples for each unit were grouped into unit modes. Sample modes that fell within around 0.5 phi of averaged unit mode size were included in that mode. Some small peaks visible in grain-size distribution figures are not included in modes, as the fraction of the sample made up by these sizes was insignificant.

### 5.1a: Basal Units

The basal unit, Unit 1A, was sampled at 12 sites (Figure 5.1) and is a fines-poor ash and lapilli deposit in all sampled locations. Unit 1A is one of the better-sorted deposits making up the 2008 deposits, has a median grain diameter of -1.1 phi (2.14 mm), but is classified as poorly sorted with a graphic standard deviation of 1.58 phi. Samples from Unit 1A commonly have grain-size peaks at -2.72, -1.74, -0.71, 0.27, and 1.74 phi. A few samples have small peaks at -4 phi, but the bulk of material in Unit 1A is between -3 and 0.5 phi. Most Unit 1A samples contain less than 10% grains smaller than 4.5 phi and were not analyzed below 4.5 phi, producing an artificial peak at 5 phi, which is the pan fraction, in these samples (Fig. 5.2).

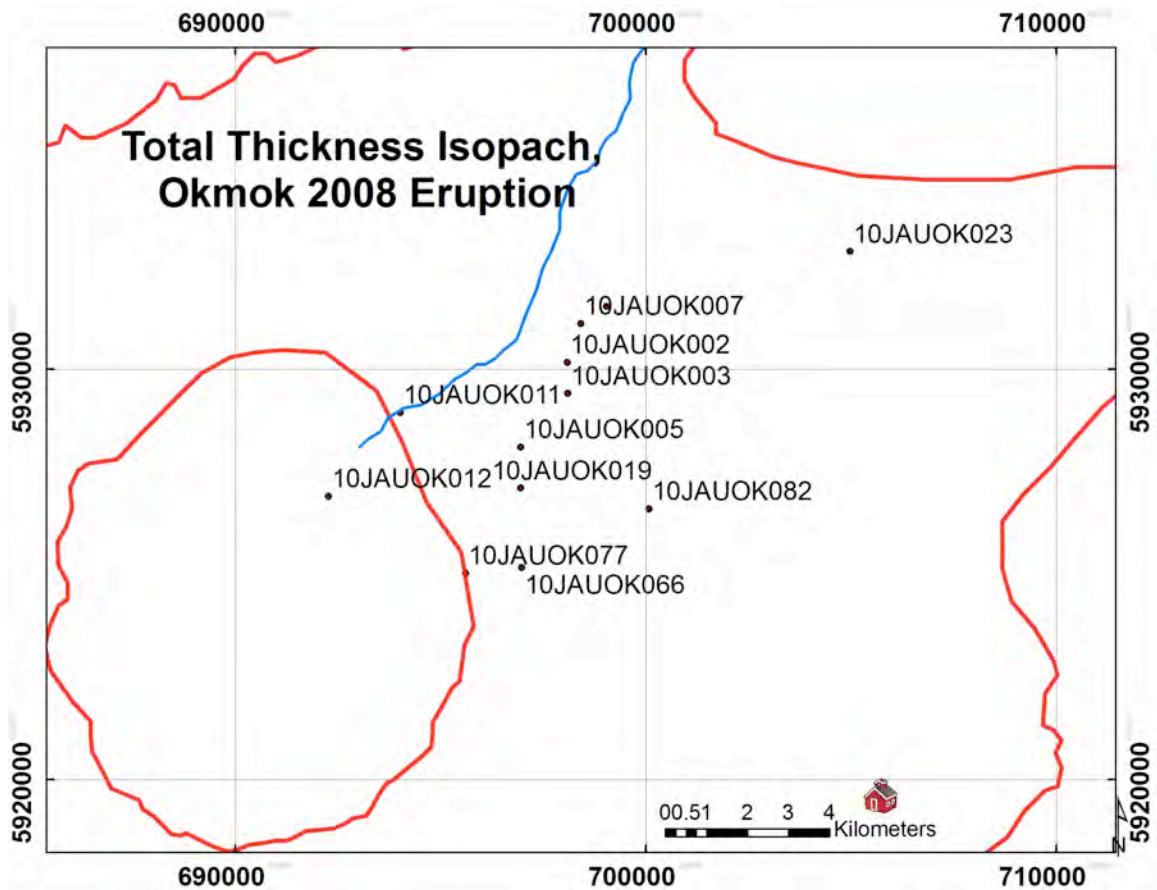
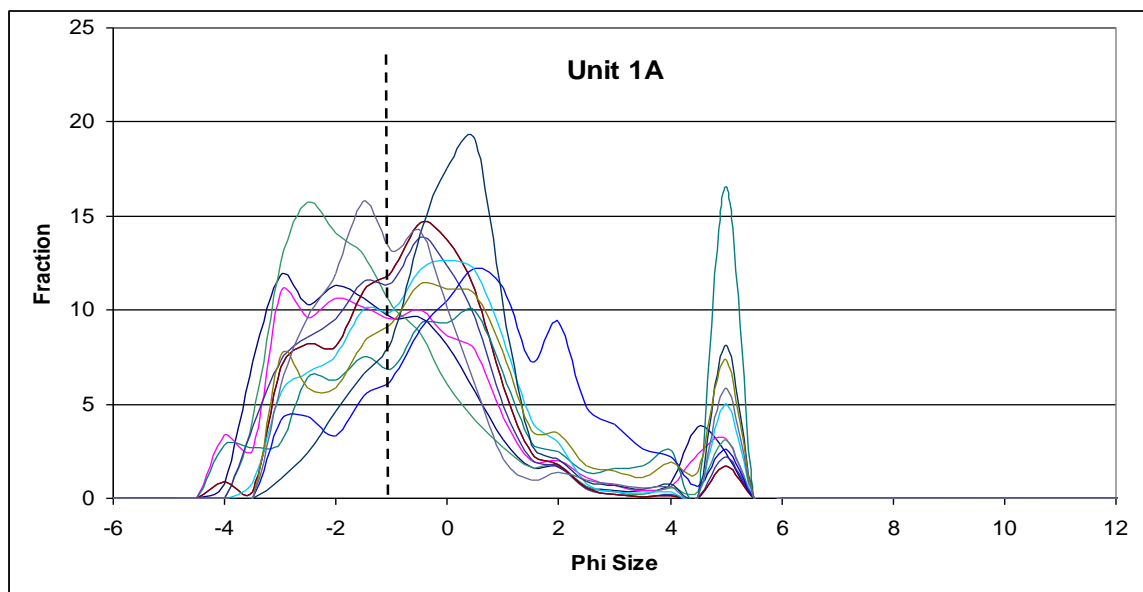


**Figure 5.1:** Unit 1A Sample Sites. Okmok caldera rim and Umnak Island outline shown in red. Grid on exterior is UTM coordinates WGS84 Zone 2N.

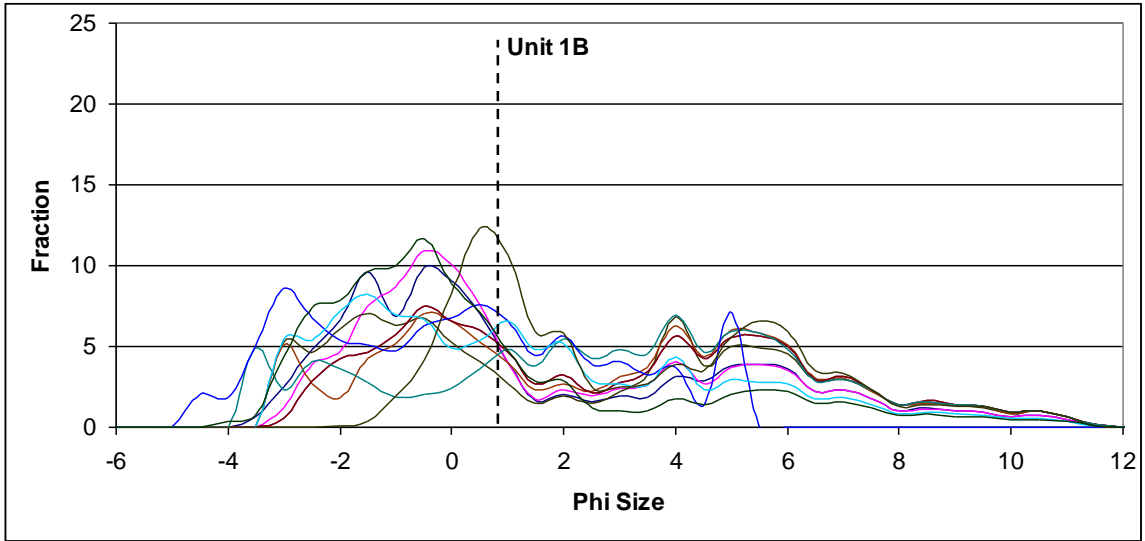


Sample	002A	003A	005A	006A	007A	011A	012A	019A	023A	066A	077A	082A	COMP
<b>Mode 1</b>		-4.25				-4.22							
<b>Fraction 1</b>		0.05				0.03							
<b>Mode 2</b>	-3.28	-3.14	-3.06	-3.21	-3.11		-2.82	-3.04	-2.72	-3.13	-3.67	-2.69	<b>-2.72</b>
<b>Fraction 2</b>	0.3	0.22	0.33	0.18	0.1		0.13	0.14	0.05	0.14	0.06	0.28	<b>0.33</b>
<b>Mode 3</b>	-1.89	-2.07	-1.88	-1.86	-1.35	-1.88		-1.84	-1.87	-1.88	-1.62	-1.67	<b>-1.74</b>
<b>Fraction 3</b>	0.31	0.2	0.4	0.33	0.59	0.43		0.22	0.11	0.16	0.28	0.28	<b>0.1</b>
<b>Mode 4</b>	-0.42	-0.48	-0.46	-0.36	-0.11		-0.02	-0.34	-0.28	-0.49	-0.3	-0.54	<b>-0.71</b>
<b>Fraction 4</b>	0.26	0.45	0.17	0.44	0.27		0.61	0.45	0.63	0.41	0.45	0.32	<b>0.29</b>
<b>Mode 5</b>						0.15		0.77	0.29	0.59	0.64		<b>0.27</b>
<b>Fraction 5</b>						0.31		0.13	0.09	0.12	0.12		<b>0.15</b>
<b>Mode 6</b>	1.78	1.75	1.34	1.53	1.8		1.75		2	1.89	1.88	1.92	<b>1.74</b>
<b>Fraction 6</b>	0.07	0.01	0.06	0.03	0.01		0.04		0.02	0.05	0.06	0.06	<b>0.07</b>
<b>Mode 7</b>		2.77				3.11	2.29						
<b>Fraction 7</b>		0.03				0.08	0.22						

**Figure 5.2:** Unit 1A grain-size distributions for individual samples and composite sample (COMP) with subpopulation modes in table. Median grain size is marked by dashed line. Some small peaks are not represented by a mode, as the fraction made up by that size is too small, like the lowest peak at -4 phi.

Unit 1B was sampled in 11 locations (Fig. 5.4), and the measured grain-size distribution confirms field observations that Unit 1B is a continuation of Unit 1A with the addition of fine and medium ash (Fig. 5.3). Grain-size peaks common to Units 1A and 1B, at -2.65, -1.83, -0.64, 0.64, and 1.83 phi, are joined in Unit 1B by peaks at 2.75, 3.75, and 5.25 phi. Minor peaks at 6.82 phi and 8.95 phi are also present in samples of Unit 1B. Unit 1B has a median grain size of 0.6 phi (0.66 mm) and is very poorly sorted, with a graphic standard deviation of 3.75 phi. Most samples of Unit 1B contained greater than 10% ash finer than 4.5 phi, and were analyzed to 11.5 phi, eliminating the false peak at 5 phi.

Unit 2 lies atop Unit 1B and is marked by a return to open-framework coarse ash and lapilli devoid of fine and medium ash. Samples of Unit 2 from 10 sites were analyzed for grain-size distribution (Fig 5.5). Unit 2 is similar to Unit 1A, but has a finer median grain size, around -0.4 phi compared to -1.1 phi for Unit 1A. Unit 2 is poorly sorted, with a graphic standard deviation of 1.5 phi. Samples of Unit 2 have grain-size peaks around -2.73, -1.48, -0.63, 0.29, and 1.92 phi (Fig 5.6), similar to the peaks present in Unit 1A; around -2.72, -1.74, -0.71, 0.27, and 1.74 phi, and Unit 1B; -2.65, -1.83, -0.64, 0.64, and 1.83 phi. The same peaks are present in Units 1A, 1B, and 2, but the fractions of these peaks change as material fines from Unit 1A to 2. The peaks at -0.63 and 0.29 phi dominate the grain-size distribution of Unit 2 in analyzed samples. Most Unit 2 samples contain less than 10% grains smaller than 4.5 phi and therefore were not analyzed below 4.5 phi, producing an artificial peak (pan fraction) at 5 phi in these samples.



Sample	002B	003B	005B	006B	007B	011B	012B	019B	023B	082B	COMP
						-3.78	-4.75				
						0.06	0.02				
<b>Mode 1</b>	-2.58	-2.49	-3.19	-3.2	-1.91	-2.38	-3.1	-2.81		-2.72	<b>-2.65</b>
<b>Fraction 1</b>	0.16	0.12	0.08	0.08	0.18	0.14	0.28	0.18		0.19	<b>0.16</b>
<b>Mode 2</b>	-1.74	-1.7	-1.96	-1.46				-1.84		-1.4	<b>-1.83</b>
<b>Fraction 2</b>	0.13	0.05	0.19	0.12				0.12		0.2	<b>0.05</b>
<b>Mode 3</b>	-0.32	-0.48	-0.44	-0.13	-0.84			-0.82		-0.41	<b>-0.64</b>
<b>Fraction 3</b>	0.34	0.44	0.22	0.24	0.03			0.16		0.35	<b>0.27</b>
<b>Mode 4</b>					0.06	0.73	0.03	0.64	0.33		<b>0.64</b>
<b>Fraction 4</b>					0.26	0.21	0.45	0.17	0.48		<b>0.08</b>
<b>Mode 5</b>	1.95	2	1.89	1.89	1.87	1.93	1.85	1.85	1.77	1.62	<b>1.83</b>
<b>Fraction 5</b>	0.04	0.05	0.05	0.05	0.04	0.06	0.05	0.08	0.03	0.06	<b>0.05</b>
<b>Mode 6</b>	2.72	2.88	2.91	2.92	2.9	2.85	2.84	2.85	3.04		<b>2.75</b>
<b>Fraction 6</b>	0.01	0.03	0.03	0.06	0.05	0.07	0.07	0.02	0.06		<b>0.04</b>
<b>Mode 7</b>	3.9	3.76	3.77	3.77	3.8	3.78	3.72	3.77	3.76	3.83	<b>3.75</b>
<b>Fraction 7</b>	0.11	0.08	0.13	0.11	0.1	0.13	0.05	0.06	0.04	0.06	<b>0.1</b>
<b>Mode 8</b>	5.37	5.31	5.16	5.29	5.22	5.14		5.14	5.3	5.41	<b>5.25</b>
<b>Fraction 8</b>	0.12	0.15	0.15	0.14	0.16	0.18		0.09	0.26	0.07	<b>0.14</b>
<b>Mode 9</b>	6.87	6.95	6.67	6.86	6.8	6.71		6.72	7.1	6.87	<b>6.82</b>
<b>Fraction 9</b>	0.04	0.04	0.08	0.1	0.09	0.08		0.05	0.05	0.03	<b>0.05</b>
<b>Mode 10</b>	8.94	9.16	9.02	9.34	9.21	9.02		9.02	9.26	8.84	<b>8.95</b>
<b>Fraction 10</b>	0.06	0.04	0.08	0.06	0.07	0.08		0.05	0.06	0.04	<b>0.07</b>

**Figure 5.3:** Unit 1B grain-size distributions with subpopulation modes in table. Median grain size is marked by dashed line.

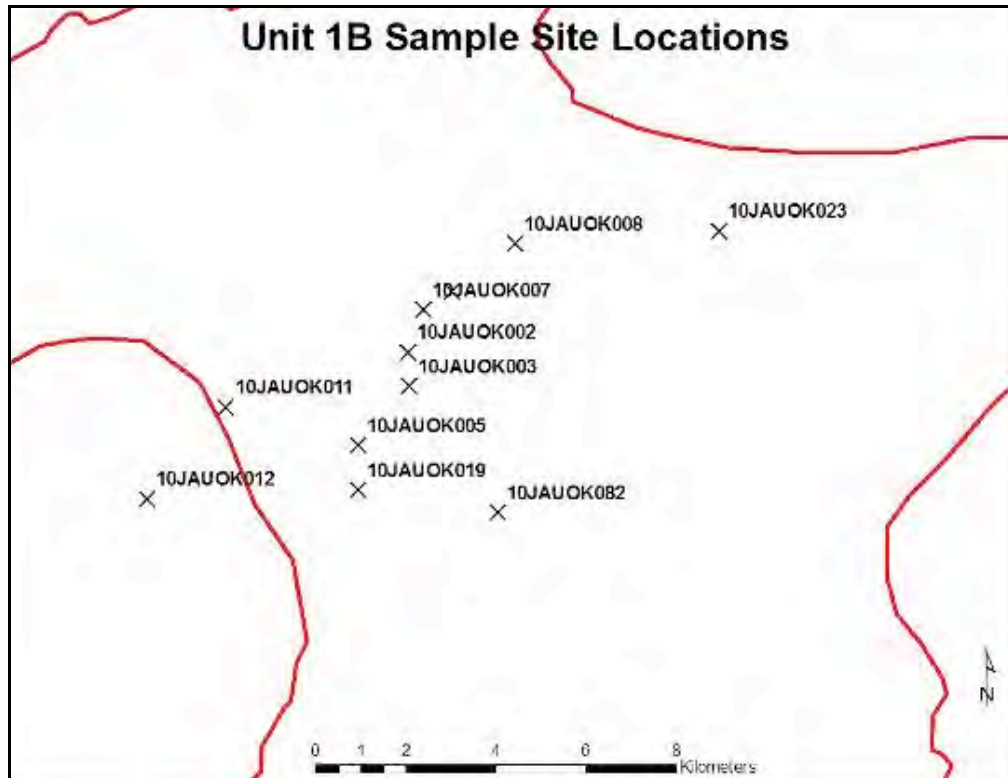


**Figure 5.4:** Unit 1B Sample Sites. Okmok caldera rim and Umnak Island outline shown in red.

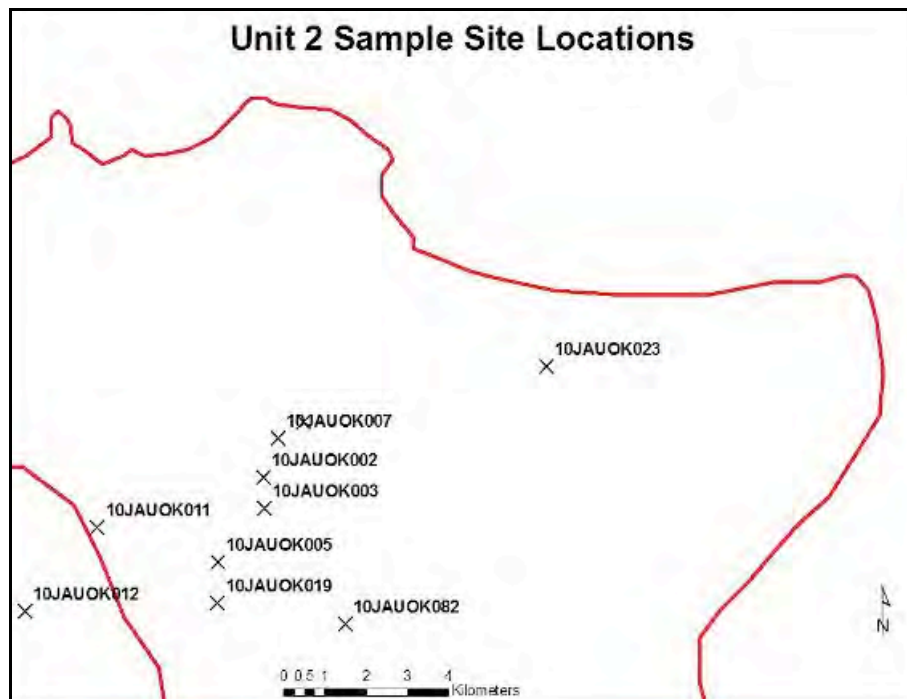
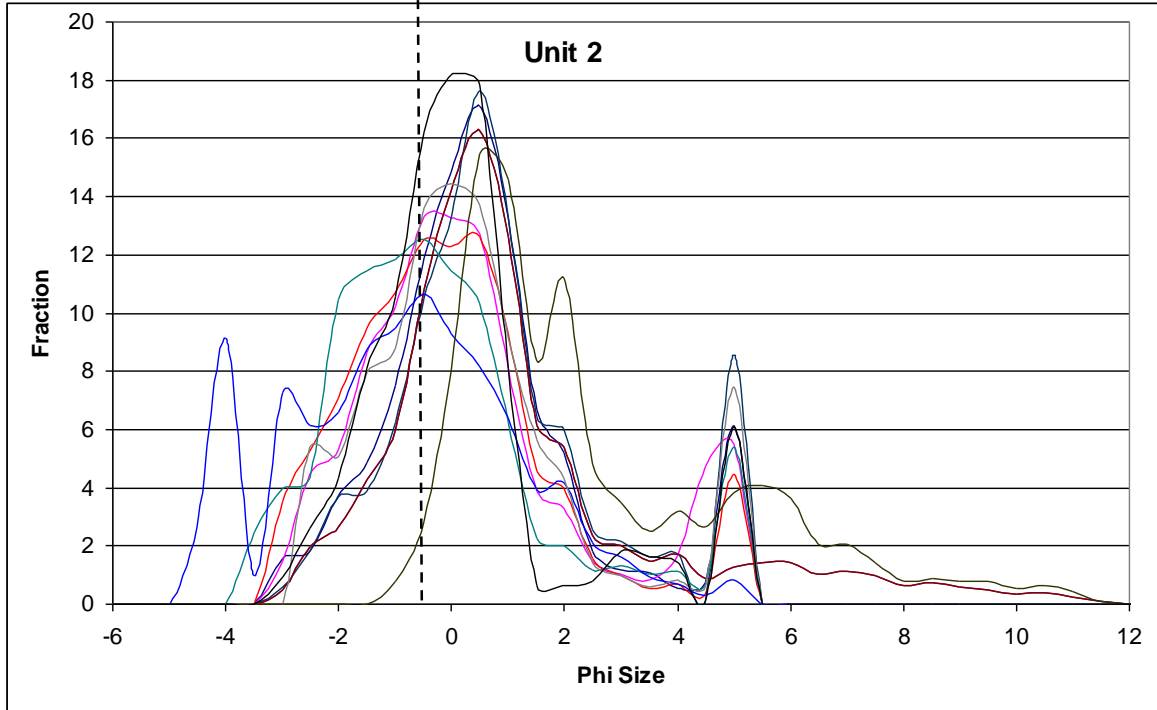


**Figure 5.5:** Unit 2 Sample Sites. Okmok caldera rim and Umnak Island outline shown in red.



Sample	002C	003C	005C	006C	007C	011C	012C	019C	023C	082C	COMP
<b>Mode 1</b>							-4.35				<b>-4.34</b>
<b>Fraction 1</b>							0.13				<b>0.03</b>
<b>Mode 2</b>	-3.26	-2.82	-2.7	-2.31		-3.34	-3.16	-2.73		-2.28	<b>-2.73</b>
<b>Fraction 2</b>	0.02	0.07	0.15	0.07		0.09	0.08	0.07		0.11	<b>0.11</b>
<b>Mode 3</b>	-1.76	-1.62	-1.84	-1.03	-1.65	-2.14	-1.58	-1.61		-1.3	<b>-1.48</b>
<b>Fraction 3</b>	0.16	0.22	0.06	0.18	0.17	0.13	0	0.21		0.22	<b>0.21</b>
<b>Mode 4</b>			-0.59		-0.18	-0.67	-0.91	-0.55		-0.6	<b>-0.63</b>
<b>Fraction 4</b>			0.55		0.42	0.66	0.67	0.05		0.2	<b>0.16</b>
<b>Mode 5</b>	0.12	-0.16	0.52	0.28	0.59	0.27		-0.06	0.45	0.17	<b>0.29</b>
<b>Fraction 5</b>	0.73	0.52	0.13	0.55	0.18	0.02		0.49	0.55	0.34	<b>0.29</b>
<b>Mode 6</b>	1.83	2.12	1.84	1.77	1.72		1.67	1.5	1.79		<b>1.92</b>
<b>Fraction 6</b>	0.02	0.1	0.06	0.05	0.04		0.11	0.1	0.11		<b>0.13</b>
<b>Mode 7</b>				3.1	2.76	2.94			2.69	3.02	
<b>Fraction 7</b>				0.07	0.04	0.05			0.04	0.07	
<b>Mode 8</b>									3.66		
<b>Fraction 8</b>									0.06		
<b>Mode 9</b>					5.63				5.24		
<b>Fraction 9</b>					0.15				0.14		
<b>Mode 10</b>									7.65		
<b>Fraction 10</b>									0.09		

**Figure 5.6:** Unit 2 grain-size distributions with subpopulation modes in table. Median grain size is marked by dashed line.

The change from Unit 2 to Unit 3 marks the start of the transition from coarse basal units to upper fine units. Unit 3 is divided into two subunits; Unit 3A and Unit 3B, based upon a change in ash induration and lamination as well as distribution. Unit 3A was deposited by east-northeast plumes, and Unit 3B was deposited by east-southeast plumes. The locations of sample sites show where each of these subunits were most prominent (Fig 5.7).

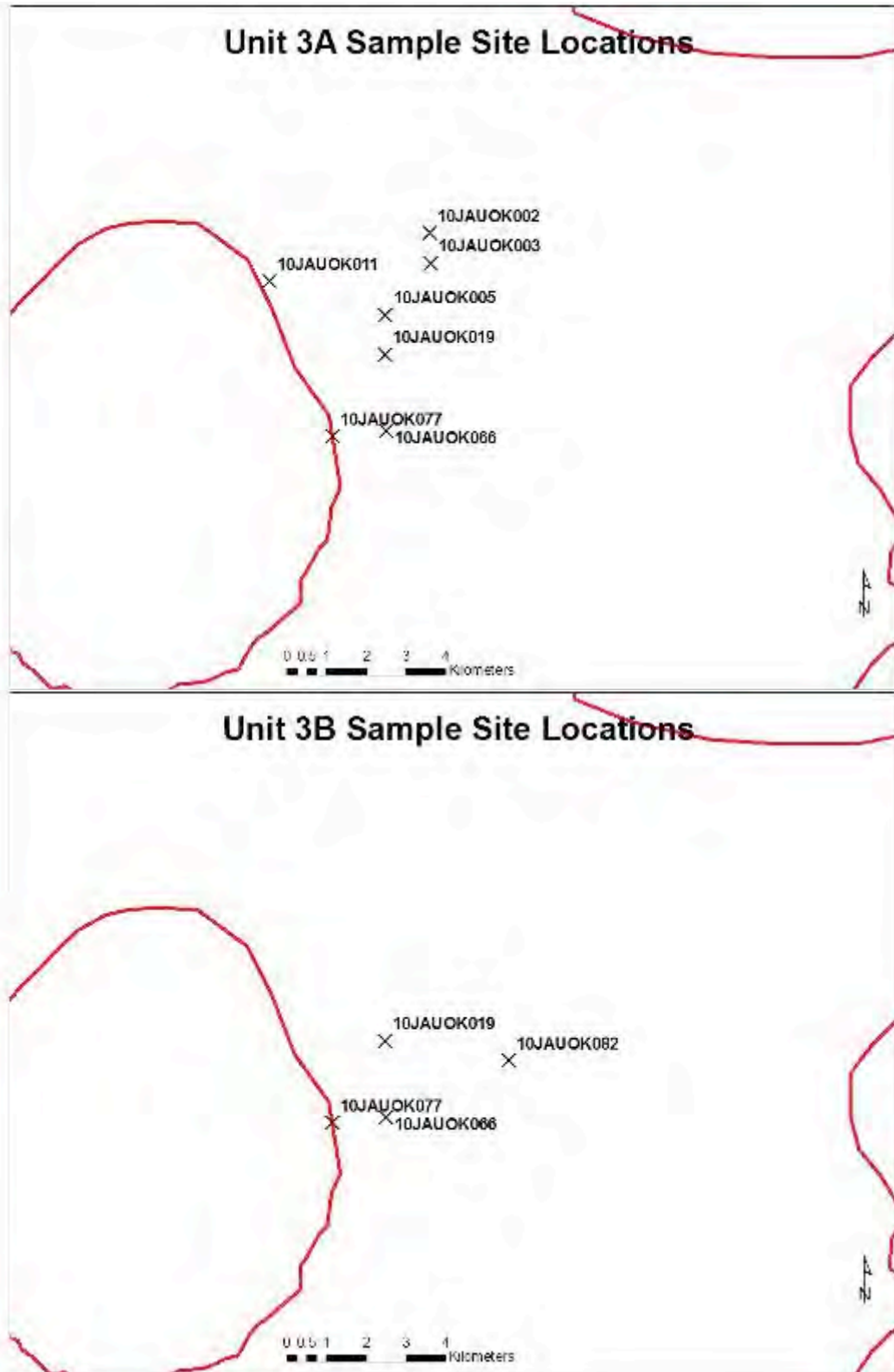
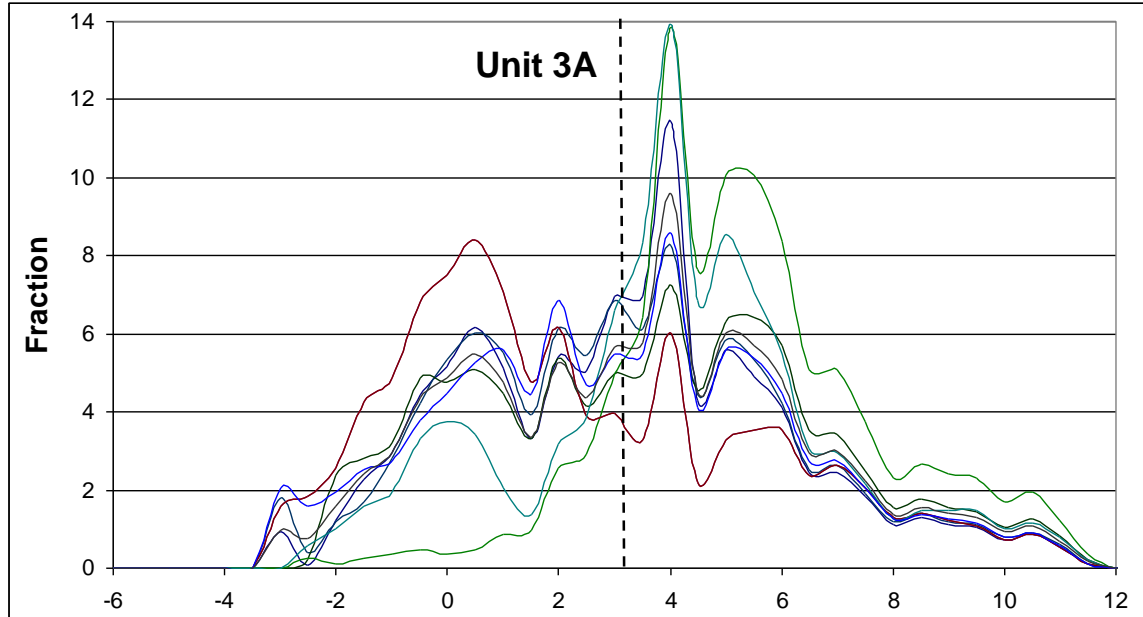


**Figure 5.7:** Units 3A and 3B Sample Sites. Okmok caldera rim and Umnak Island outline shown in red.

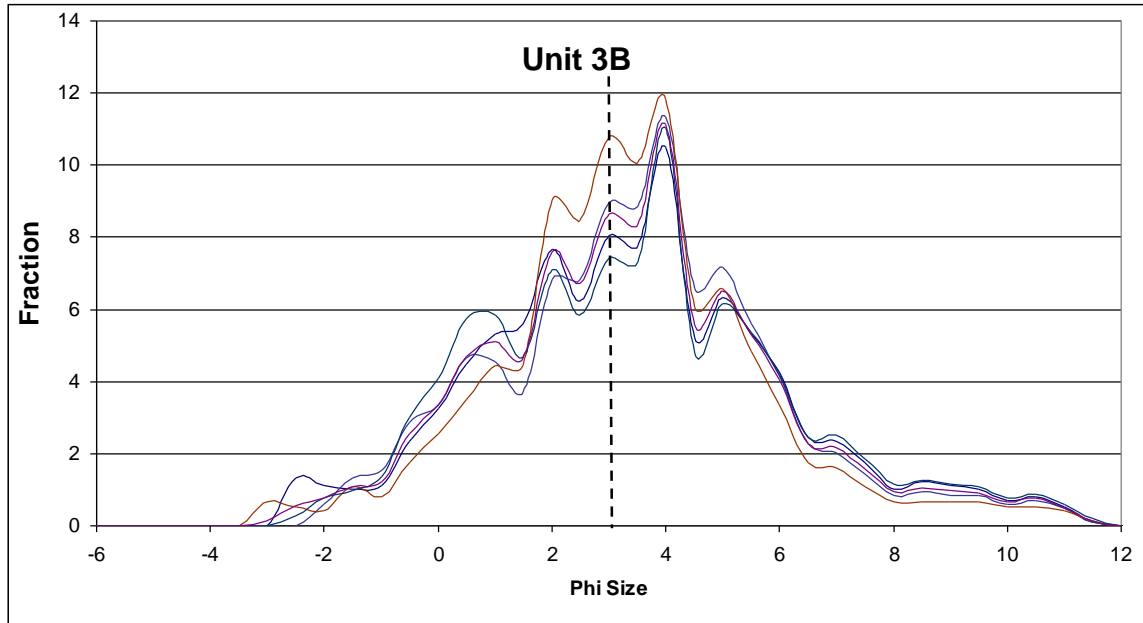
Samples of Unit 3A are very poorly sorted, including all grain sizes from 2-cm-diameter lapilli to very fine ash. The most prominent grain-size peaks are at 0.39, 1.86, 2.87, 3.79, and 5.11 phi, with secondary peaks at -1.22, 6.56, and 8.97 phi (Fig. 5.8). The median grain size of the analyzed Unit 3A samples is 3.25 phi (105  $\mu\text{m}$ ) and the deposits are very poorly sorted, with a graphic standard deviation of 3.15 phi.

Unit 3B was noted in the field to be poorer in lapilli, coarse ash, and fine-very fine ash than Unit 3A and is characterized by indurated laminae of medium ash with scattered lapilli and coarse ash. Grain-size analysis confirms these observations, as samples of Unit 3B are better sorted than Unit 3A and ash is more concentrated in the size range from 1- to 5-phi. Primary grain-size peaks are present around 0.6, 1.9, 2.92, 3.79, and 4.98 phi with secondary peaks at -1.92, -0.66, 6.46, and 9.25 phi (Fig. 5.9). Unit 3B is slightly coarser and significantly better sorted than Unit 3A with a median grain diameter of 3.15 phi (112  $\mu\text{m}$ ) and a graphic standard deviation of 2.43 phi.



Sample	002D	003D	005D	011D	019D	066B	077B	COMP
<b>Mode 1</b>					-2.85		-3.14	<b>-3.08</b>
<b>Fraction 1</b>					0.04		0.04	<b>0.02</b>
<b>Mode 2</b>	-0.88	-1.4	-0.59		-0.68		-1.25	<b>-1.22</b>
<b>Fraction 2</b>	0.17	0.1	0.27		0.33		0.13	<b>0.12</b>
<b>Mode 3</b>	0.45	0.28	0.55		0.56	-0.34	0.58	<b>0.39</b>
<b>Fraction 3</b>	0.16	0.29	0.07		0.16	0.2	0.21	<b>0.2</b>
<b>Mode 4</b>	1.8	1.84	1.91	1.74	1.79	1.84	1.86	<b>1.86</b>
<b>Fraction 4</b>	0.06	0.06	0.09	0.07	0.07	0.04	0.1	<b>0.07</b>
<b>Mode 5</b>	2.85	2.91	2.82	3.05	2.8	3.06	2.75	<b>2.87</b>
<b>Fraction 5</b>	0.16	0.16	0.06	0.15	0.08	0.22	0.06	<b>0.12</b>
<b>Mode 6</b>	3.68	3.75	3.68	3.74	3.76	3.73	3.77	<b>3.79</b>
<b>Fraction 6</b>	0.1	0.09	0.12	0.15	0.09	0.13	0.2	<b>0.16</b>
<b>Mode 7</b>	5.25	5.11	5.28	5.13	5.26	5.03	5.17	<b>5.11</b>
<b>Fraction 7</b>	0.31	0.19	0.27	0.36	0.12	0.25	0.13	<b>0.16</b>
<b>Mode 8</b>		6.82	6.94	6.89	6.83	6.97	6.58	<b>6.56</b>
<b>Fraction 8</b>		0.06	0.05	0.13	0.06	0.1	0.08	<b>0.09</b>
<b>Mode 9</b>		9.05	8.69	9.26	8.97	9.49	8.98	<b>8.97</b>
<b>Fraction 9</b>		0.07	0.07	0.13	0.07	0.06	0.07	<b>0.09</b>
<b>Mode 10</b>			10.38					
<b>Fraction 10</b>			0.02					

Figure 5.8: Unit 3A grain-size distributions with subpopulation modes in table. Median grain size is marked by dashed line.



Sample	019F	066C	077C	082D	COMP
<b>Mode 1</b>	-2.37	-1.49	-1.49	-1.31	-1.92
<b>Fraction 1</b>	0.04	0.04	0.06	0.05	0.04
<b>Mode 2</b>	-0.35	-0.56	-0.11	-0.4	-0.66
<b>Fraction 2</b>	0.09	0.05	0.06	0.07	0.04
<b>Mode 3</b>	0.91	0.59	0.82	0.64	0.6
<b>Fraction 3</b>	0.16	0.14	0.08	0.15	0.17
<b>Mode 4</b>	1.84	2.01	1.9	1.86	1.9
<b>Fraction 4</b>	0.11	0.16	0.21	0.13	0.14
<b>Mode 5</b>	2.86	2.85	2.95	2.89	2.92
<b>Fraction 5</b>	0.16	0.12	0.2	0.14	0.17
<b>Mode 6</b>	3.77	3.78	3.75	3.76	3.79
<b>Fraction 6</b>	0.17	0.25	0.16	0.18	0.18
<b>Mode 7</b>	5.05	5.02	4.9	5.03	4.98
<b>Fraction 7</b>	0.17	0.13	0.13	0.14	0.15
<b>Mode 8</b>	6.74	6.27	6.17	6.43	6.46
<b>Fraction 8</b>	0.08	0.07	0.06	0.08	0.09
<b>Mode 9</b>	9.3	8.81	8.8	8.94	9.25
<b>Fraction 9</b>	0.05	0.06	0.05	0.07	0.05

**Figure 5.9:** Unit 3B grain-size distributions with subpopulation modes in table. Median grain size is marked by dashed line.

### 5.1b: Upper Units

The upper units include several facies that occur without a set stratigraphic order.

Therefore, the grain-size distributions of upper units are examined by facies irrespective

of stratigraphic position. Facies examined include coarse ash, ash pellet, laminated ash, and upper vesicular ash (Chapter 3).

Fifteen samples of coarse ash from upper deposits at eight locations were analyzed for grain-size distribution (Fig. 5.10). Eleven of the fifteen coarse ash samples have their most prominent grain-size peak at 1.81 phi, secondary peaks at 1, 2.62, and 3.6 phi, and minor peaks around 5.5 and 7 phi (Fig. 5.11). The three coarsest samples (10JAUOK075A, 10JAUOK076E, 10JAUOK080D) have their highest grain-size peak between 0.5 and 1 phi and secondary peaks around 2, 3, and 4 phi. Samples 10JAUOK077F and 10JAUOK080B have distinct twin peaks near 1 and 2 phi. The coarse ash samples overall have a median grain size of 2 phi (250  $\mu\text{m}$ ) and are poorly sorted with a graphic standard deviation of 1.73 phi.

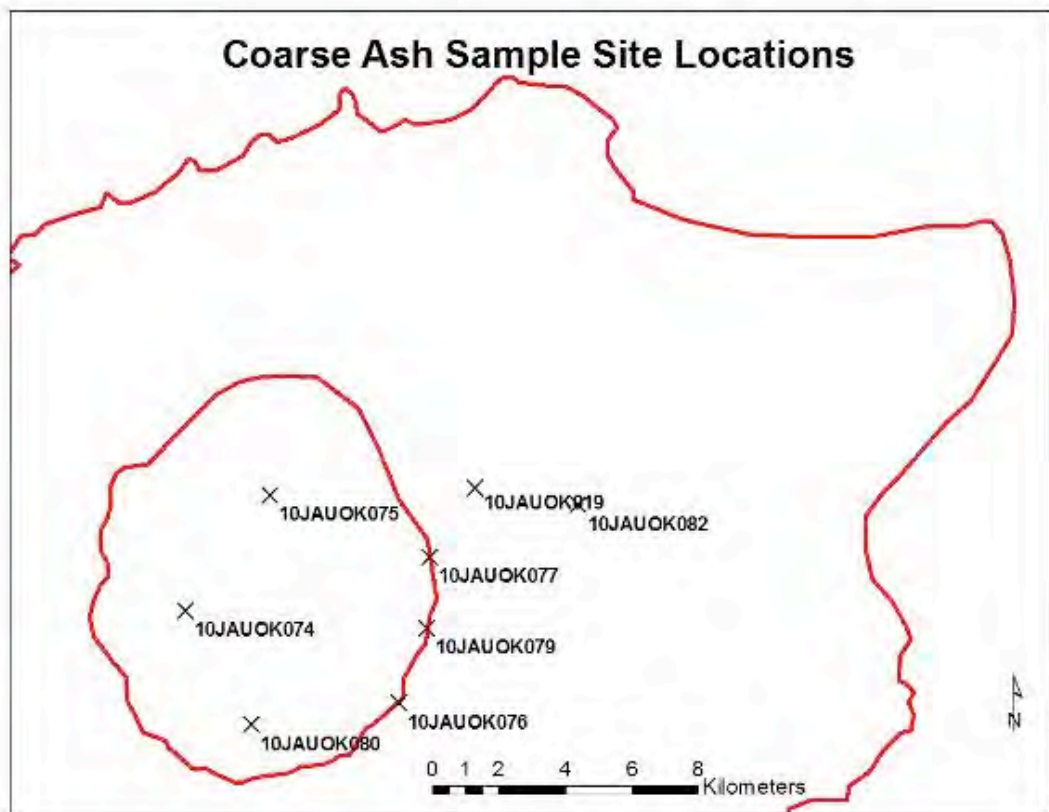
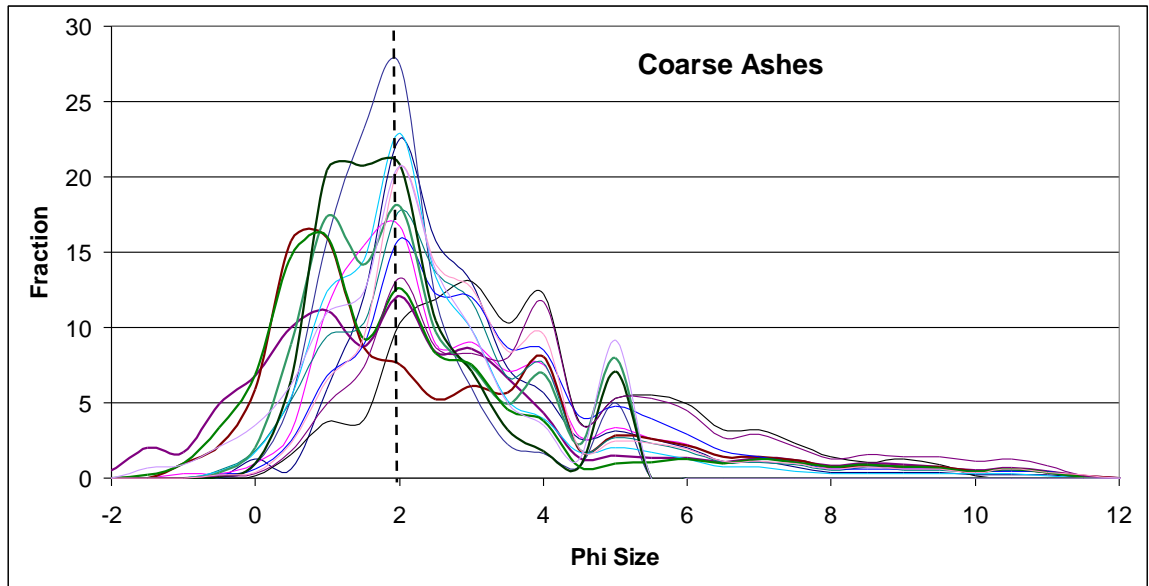


**Figure 5.10:** Coarse Ash Sample Site Locations. Okmok caldera rim and Umnak Island outline shown in red.



Sample	019G	023E	074A	074B	075A	076E	076F	077D	077E	077F	079B	080B	080C	080D	082E	COMP
<b>Mode 1</b>					-1.7											
<b>Fraction 1</b>					0.04											
<b>Mode 2</b>					-0.4											
<b>Fraction 2</b>					0.15											
<b>Mode 3</b>	0.95	0.96	0.88		0.66	0.51	0.85	0.99	1.05	0.81	1.09	1.46	0.57	1.06	1	1
<b>Fraction 3</b>	0.14	0.31	0.1		0.27	0.53	0.3	0.22	0.46	0.48	0.51	0.6	0.56	0.18	0.21	<b>0.45</b>
<b>Mode 4</b>	1.8	1.8	1.83	1.85	1.83	1.75	1.88	1.85	1.8	1.8	1.83	2.3	1.83	1.78	1.8	<b>1.81</b>
<b>Fraction 4</b>	0.44	0.27	0.14	0.8	0.21	0.04	0.3	0.25	0.24	0.22	0.22	0.21	0.12	0.16	0.3	<b>0.16</b>
<b>Mode 5</b>	2.78	2.89	2.81	2.25	3.02	2.87	2.78	2.8	2.75	2.8	2.75	3.2	2.75	2.97	2.8	<b>2.62</b>
<b>Fraction 5</b>	0.19	0.14	0.35	0.1	0.18	0.19	0.17	0.2	0.17	0.13	0.11	0.1	0.14	0.25	0.26	<b>0.11</b>
<b>Mode 6</b>	3.7	3.79	3.72	4.1	6.42	3.69	3.76	3.7	3.65	3.73	3.65	4.1	3.7	3.71	3.72	<b>3.6</b>
<b>Fraction 6</b>	0.07	0.12	0.11	0.02	0.15	0.07	0.1	0.11	0.03	0.09	0.04	0.02	0.04	0.1	0.09	<b>0.15</b>
<b>Mode 7</b>	5.27	5.21	4.98			5.17	5.17	5.04	5.18					5.24	5.68	
<b>Fraction 7</b>	0.11	0.07	0.07			0.06	0.05	0.11	0.07					0.15	0.1	
<b>Mode 8</b>		7.62	6.23			7.42	7.56	6.66					7.05	7.83		
<b>Fraction 8</b>		0.09	0.21			0.09	0.07	0.1					0.11	0.17		

**Figure 5.11:** Coarse Ash grain-size distributions with subpopulation modes in table. Median grain size is marked by dashed line.

Seven samples of units composed of ash pellets from six sites were analyzed (Fig. 5.12). These samples were chosen because they were the samples richest in ash pellets, with around 40-70% of deposit volume made up of ash pellets. All ash-pellet units have very similar grain-size distributions with a dominant grain-size peak at 3.72 phi (Fig.

5.13). Secondary peaks are present at 1.78, 2.98, 5.04, and 6.63 phi in all analyzed samples. The median grain diameter of ash pellet samples is 3.9 phi (67 μm) and units are poorly sorted with a graphic standard deviation of 2.08 phi.

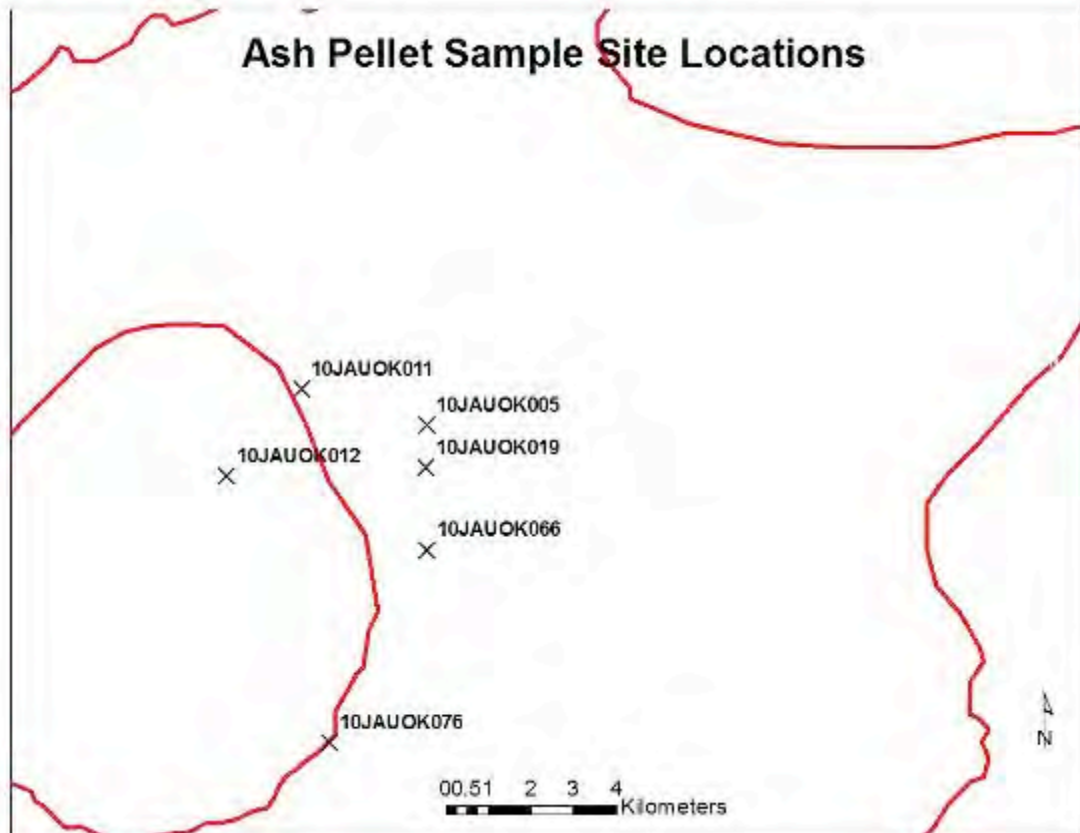
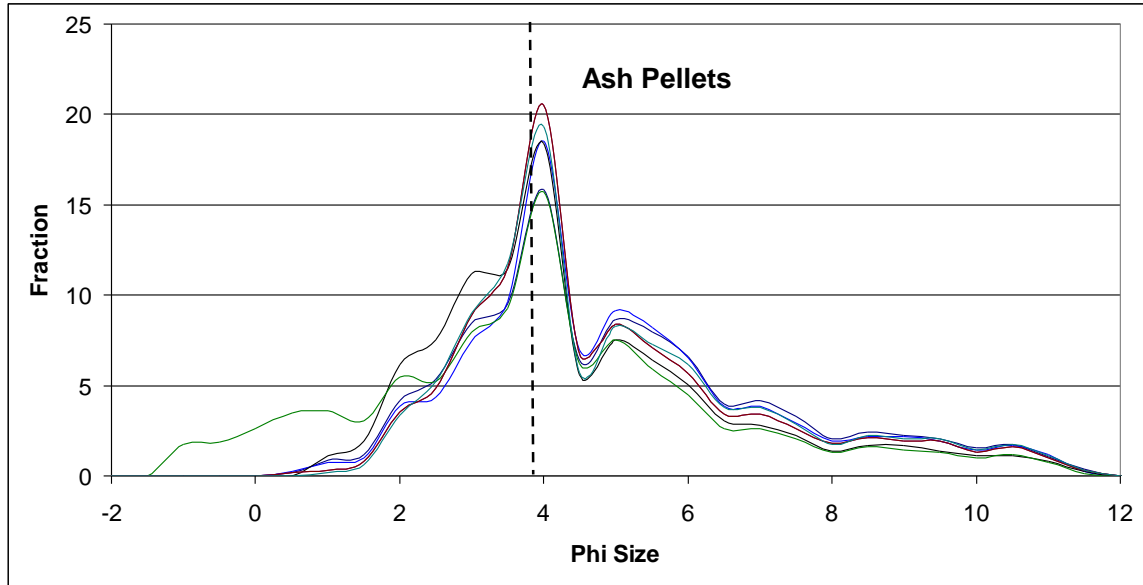


**Figure 5.12:** Ash Pellet Sample Site Locations. Okmok caldera rim and Umnak Island outline shown in red.



Sample	005F	005H	011E	012E	019I	066E	076D	COMP
<b>Mode 1</b>				0.43			0.8	
<b>Fraction 1</b>				0.2			0.05	
<b>Mode 2</b>	1.71	1.79	1.75	1.88	1.76	1.9	1.85	<b>1.78</b>
<b>Fraction 2</b>	0.07	0.07	0.12	0.07	0.06	0.06	0.11	<b>0.1</b>
<b>Mode 3</b>	2.98	3.11	2.98	2.87	3.07	3	2.95	<b>2.98</b>
<b>Fraction 3</b>	0.28	0.26	0.34	0.15	0.32	0.27	0.31	<b>0.26</b>
<b>Mode 4</b>	3.71	3.73	3.72	3.72	3.72	3.74	3.74	<b>3.72</b>
<b>Fraction 4</b>	0.15	0.18	0.18	0.23	0.2	0.23	0.16	<b>0.2</b>
<b>Mode 5</b>	5.17	5.1	5.04	4.93	5.03	5.07	5.16	<b>5.04</b>
<b>Fraction 5</b>	0.28	0.25	0.17	0.1	0.18	0.18	0.18	<b>0.2</b>
<b>Mode 6</b>	6.8	6.73	6.46	6.55	6.57	6.48	7.31	<b>6.63</b>
<b>Fraction 6</b>	0.04	0.11	0.1	0.25	0.14	0.14	0.2	<b>0.13</b>
<b>Mode 7</b>	8.43	9.17	9		9.31	9.16		<b>9.27</b>
<b>Fraction 7</b>	0.19	0.12	0.09		0.1	0.12		<b>0.09</b>

**Figure 5.13:** Ash Pellet grain-size distributions with subpopulation modes in table. Median grain size is marked by dashed line.

Four samples of laminated ash from three sites were analyzed (Fig. 5.14). Three of the samples were very similar in grain-size distribution, and one was significantly coarser grained. The coarser-grained sample was noted in the field to contain more coarse ash than most laminated ash units. Laminated ash units had dominant grain-size peaks at 3.65 phi with secondary peaks at 2.14, 2.75, and 5.07 phi. Laminated ash samples are very similar to ash-pellet samples in grain size, but on average have more 2-

phi ash. Laminated ash samples have a median grain diameter of 3.6 phi (82  $\mu\text{m}$ ) and are poorly sorted with a graphic standard deviation of 2 phi.

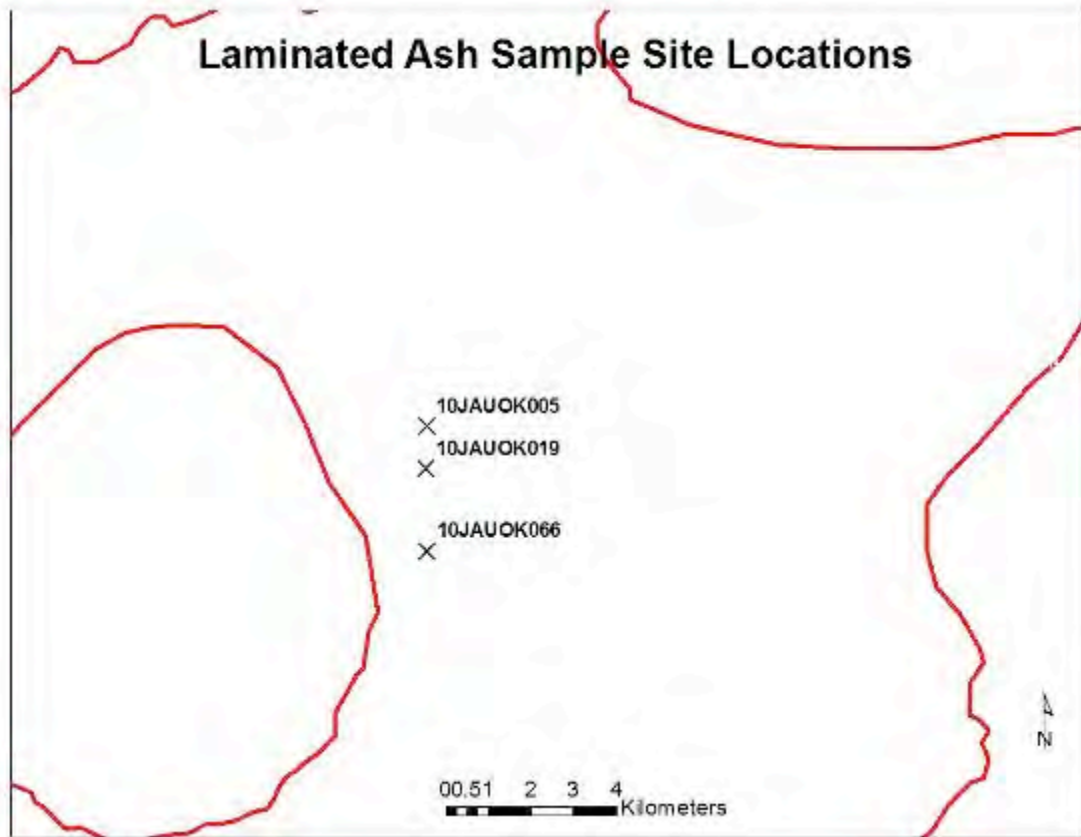
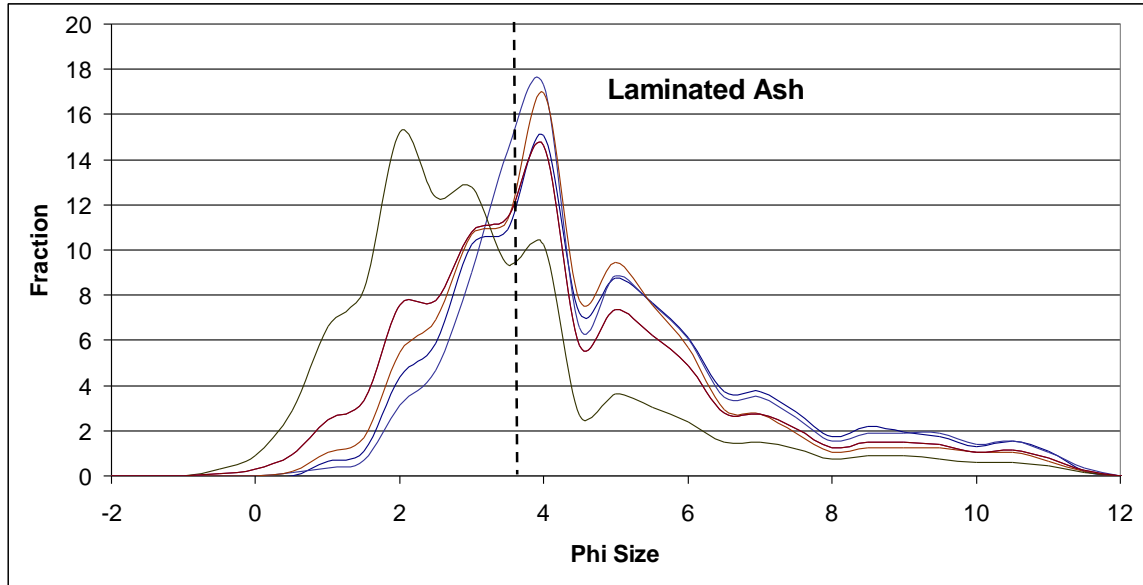


**Figure 5.14:** Laminated Ash Sample Site Locations. Okmok caldera rim and Umnak Island outline shown in red.



Sample	005E	005G	019H	066D	COMP
<b>Mode 1</b>				1.23	
<b>Fraction 1</b>				0.3	
<b>Mode 2</b>	2.52	2.28	2.2	1.84	<b>2.14</b>
<b>Fraction 2</b>	0.26	0.14	0.23	0.16	<b>0.34</b>
<b>Mode 3</b>	2.95	2.72	2.89	2.75	<b>2.75</b>
<b>Fraction 3</b>	0.1	0.05	0.11	0.2	<b>0.05</b>
<b>Mode 4</b>	3.7	3.57	3.72	3.66	<b>3.65</b>
<b>Fraction 4</b>	0.17	0.39	0.28	0.15	<b>0.27</b>
<b>Mode 5</b>	5.09	5.11	5	5.15	<b>5.07</b>
<b>Fraction 5</b>	0.27	0.2	0.21	0.08	<b>0.15</b>
<b>Mode 6</b>	6.87	6.6	6.41		<b>6.47</b>
<b>Fraction 6</b>	0.1	0.11	0.1		<b>0.09</b>
<b>Mode 7</b>	9.21	9.2	9.21	7.61	<b>9.1</b>
<b>Fraction 7</b>	0.1	0.11	0.07	0.1	<b>0.09</b>

**Figure 5.15:** Laminated ash grain-size distributions with subpopulation modes in table. Median grain size is marked by dashed line.

Samples of upper vesicular ash were taken from the surface at six sites (Fig. 5.16). All samples have a dominant grain-size peak at 3.72 phi and secondary peaks at 5.07, 6.85, and 9.42 phi with minor peaks at 1.95 and 3.0 phi (Fig. 5.17). Upper vesicular ash units are the finest-grained samples analyzed from 2008 deposits with a median grain

diameter of 4.25 phi (53  $\mu$ m). These units are poorly sorted with a graphic standard deviation of 2.05 phi.

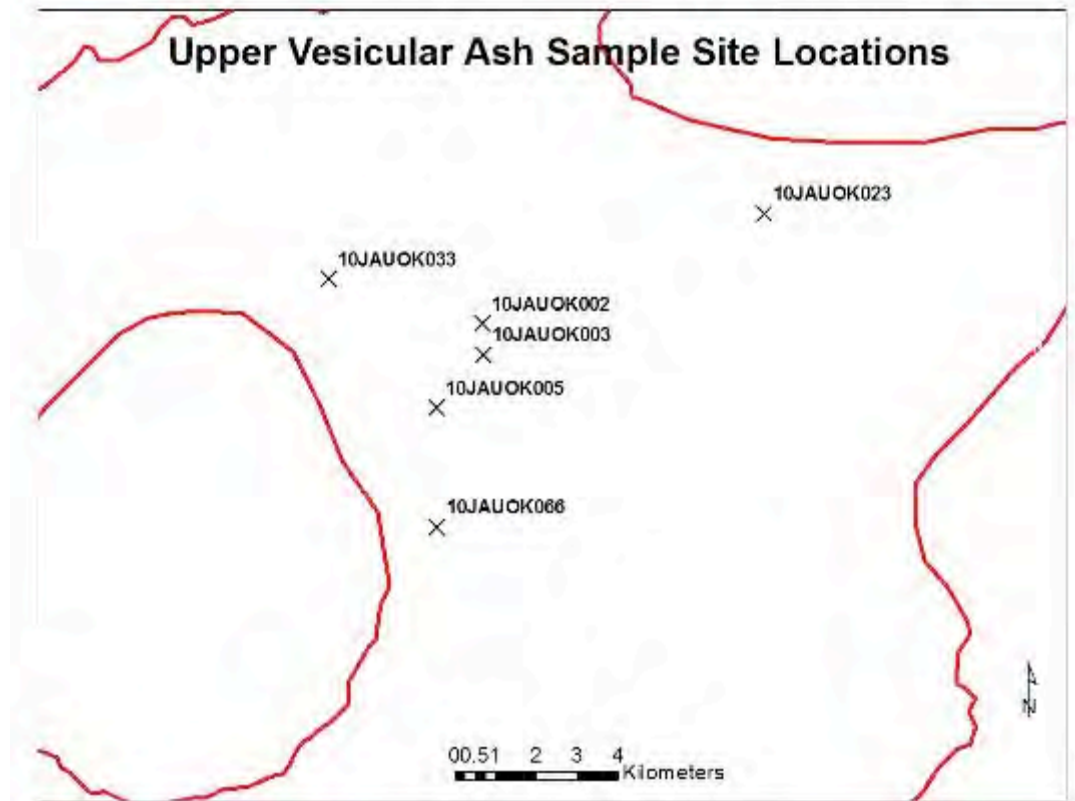
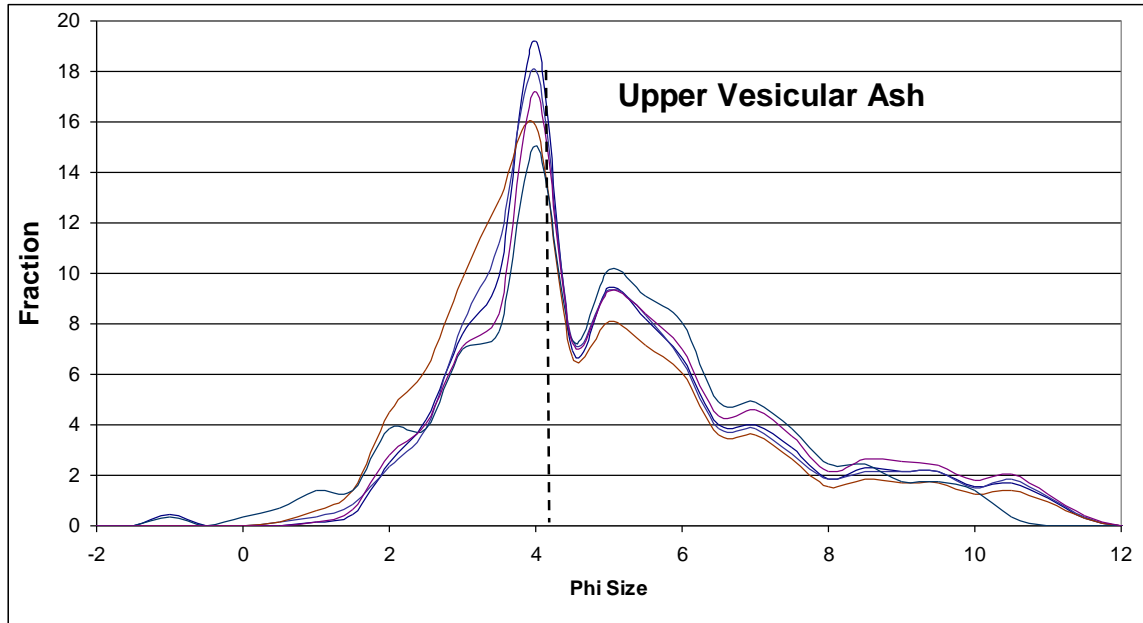


**Figure 5.16:** Upper Vesicular Ash Sample Site Locations. Okmok caldera rim and Umnak Island outline shown in red.



Sample	002G	003G	005I	023F	033A	066E	COMP
<b>Mode 1</b>	1.82	1.76	1.85	2	2.25	1.73	<b>1.95</b>
<b>Fraction 1</b>	0.04	0.05	0.1	0.15	0.12	0.04	<b>0.06</b>
<b>Mode 2</b>	3.04	3.15	3.14	2.93	2.94	3.07	<b>3</b>
<b>Fraction 2</b>	0.26	0.31	0.35	0.11	0.1	0.35	<b>0.24</b>
<b>Mode 3</b>	3.72	3.72	3.71	3.73	3.72	3.7	<b>3.72</b>
<b>Fraction 3</b>	0.2	0.16	0.12	0.2	0.25	0.17	<b>0.2</b>
<b>Mode 4</b>	5.08	5.03	5.1	5.1	5.05	5.05	<b>5.07</b>
<b>Fraction 4</b>	0.25	0.2	0.23	0.31	0.24	0.16	<b>0.25</b>
<b>Mode 5</b>	6.68	6.54	6.76	6.86	6.66	6.38	<b>6.85</b>
<b>Fraction 5</b>	0.12	0.19	0.11	0.16	0.17	0.15	<b>0.15</b>
<b>Mode 6</b>	9.14	9.53	9.31	8.98	9.3	9.12	<b>9.42</b>
<b>Fraction 6</b>	0.12	0.09	0.09	0.07	0.13	0.12	<b>0.1</b>

**Figure 5.17:** Upper Vesicular Ash grain-size distributions with subpopulation modes in table. Median grain size is marked by dashed line.

### 5.1c: Summary of grain-size distribution by unit and facies

Basal Unit 1A is fines poor and the coarsest-grained unit deposited in the 2008 eruption, and Unit 1B is the up-section continuation of 1A with the addition of fine and medium ash. Unit 2 is another fines-poor ash and lapilli layer but is slightly finer grained than Unit 1A (Figure 5.18). The coarse ash and lapilli populations are continuous from Unit 1A through Unit 2 (Table 5.1) but fine slightly from Unit 1A to Unit 2. The coarse ash and lapilli grade continuously from Unit 1A through Unit 1B into Unit 2 (Figure 5.18). The same grain-size peaks are present in the average for each of the three units and, when normalized to eliminate the addition of fine ash in Unit 1B, a decrease in the coarsest size fractions and an increase in the finer populations is apparent from Unit 1A through Unit 2. This suggests that Units 1A, 1B, and 2 were emplaced by a continuous column decreasing in energy. Examination of samples from individual sites (Figs. 5.19, 5.20, 5.21) confirms that coarse material is continuous from Unit 1A through Unit 2.

Sample	Unit Composite Summary					Coarse Ash	Ash Pellets	Laminated Ash	Upper Ash
	1A	1B	2	3A	3B				
Mode 1			-4.34						
Fraction 1			0.03						
Mode 2	-2.72	-2.65	-2.73	-3.08					
Fraction 2	0.33	0.16	0.11	0.02					
Mode 3	-1.74	-1.83	-1.48	-1.22	-1.92				
Fraction 3	0.1	0.05	0.21	0.12	0.04				
Mode 4	-0.71	-0.64	-0.63		-0.66				
Fraction 4	0.29	0.27	0.16		0.04				
Mode 5	0.27	0.64	0.29	0.39	0.6	1			
Fraction 5	0.15	0.08	0.29	0.2	0.17	0.45			
Mode 6	1.74	1.83	1.92	1.86	1.9	1.81	1.78	2.14	1.95
Fraction 6	0.07	0.05	0.13	0.07	0.14	0.16	0.1	0.34	0.06
Mode 7		2.75		2.87	2.92	2.62	2.98	2.75	3
Fraction 7		0.04		0.12	0.17	0.11	0.26	0.05	0.24
Mode 8		3.75		3.79	3.79	3.6	3.72	3.65	3.72
Fraction 8		0.1		0.16	0.18	0.15	0.2	0.27	0.2
Mode 9		5.25		5.11	4.98		5.04	5.07	5.07
Fraction 9		0.14		0.16	0.15		0.2	0.15	0.25
Mode 10		6.82		6.56	6.46		6.63	6.47	6.85
Fraction 10		0.05		0.09	0.09		0.13	0.09	0.15
Mode 11		8.95		8.97	9.25		9.27	9.1	9.42
Fraction 11		0.07		0.09	0.05		0.09	0.09	0.1

**Table 5.1:** Subpopulation modes and fractions for each unit or facies composite.

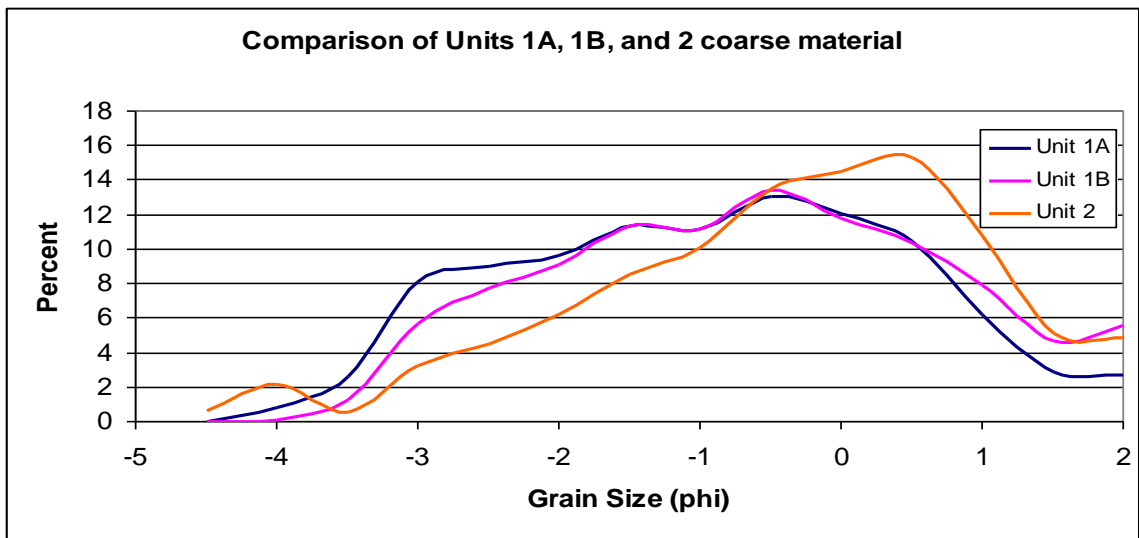


**Figure 5.18:** Coarse material grain-size distribution normalized to 100% (5-phi through 2-phi material) for composite basal units.

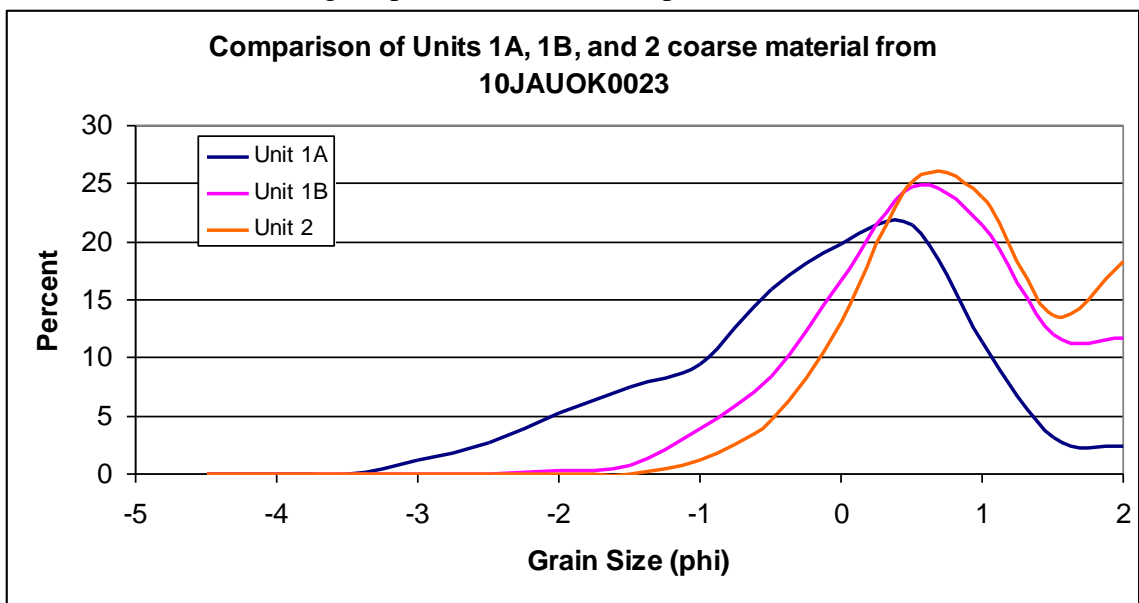


**Figure 5.19:** Coarse material grain-size distribution normalized to 100% (5-phi through 2-phi material) for 10JAUOK0023.

The base of Unit 3 marks the beginning of the transition to fine-grained upper units. The coarse material in Unit 3 is a continuation of the coarse material in Units 1A-2, shown by the similar grain-size peaks and fining trend from Unit 1A through 3B (Figs.

5.20, 5.21). Unit 3A and 3B have much more medium and fine ash than other basal units, but the coarse material present is a continuation of that in lower deposits.

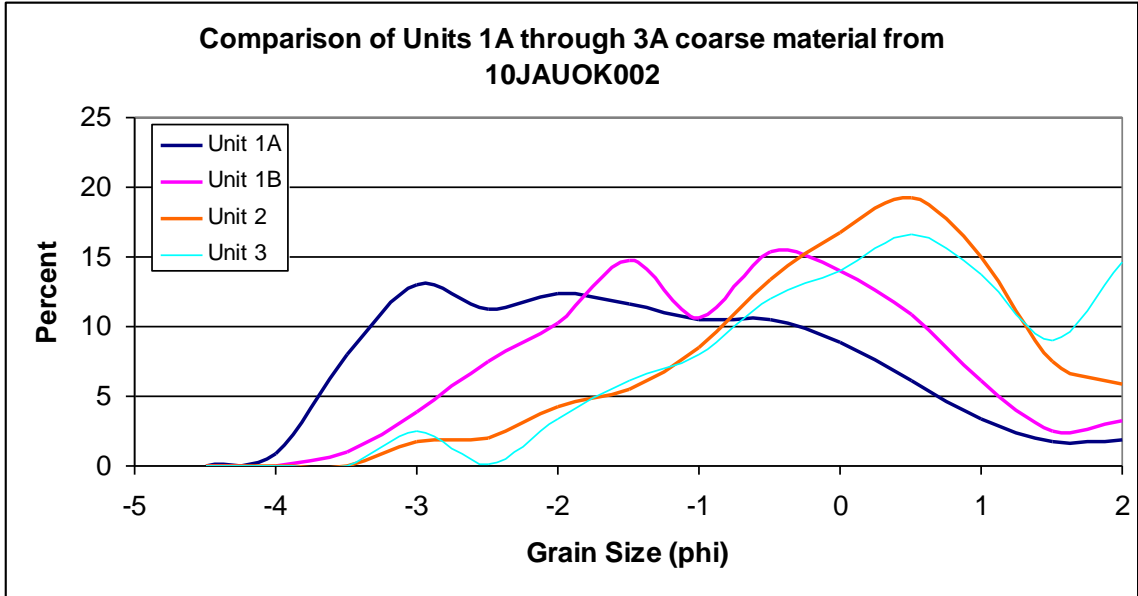


**Figure 5.20:** Coarse material grain-size distribution normalized to 100% (5-phi through 2-phi material) for 10JAUOK002 Units 1A-3.

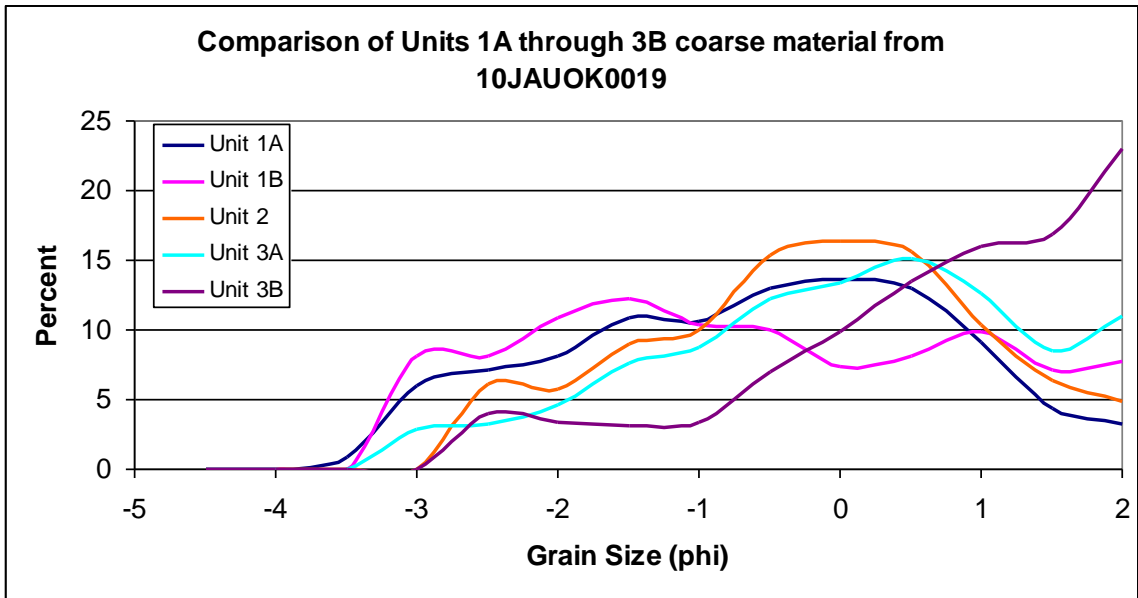


**Figure 5.21:** Coarse material grain-size distribution normalized to 100% (5-phi through 2-phi material) for Units 1-3B from 10JAUOK0019.

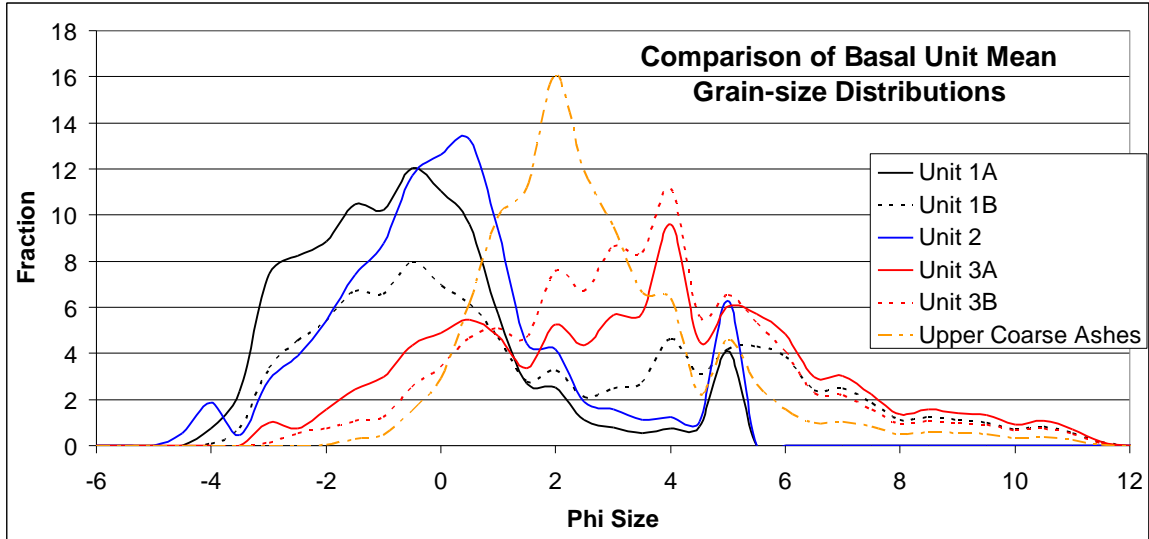


**Figure 5.22:** Grain-size Comparison of Basal Units

Upper units are much finer grained than basal units, with the bulk of upper deposits made up of laminated ash and ash pellets in most locations. Coarse ashes are present as thin layers at many locations, but upper units as a whole are very fine grained (Fig. 5.23). The last-deposited units sampled as upper vesicular ash are the finest grained of all analyzed samples.

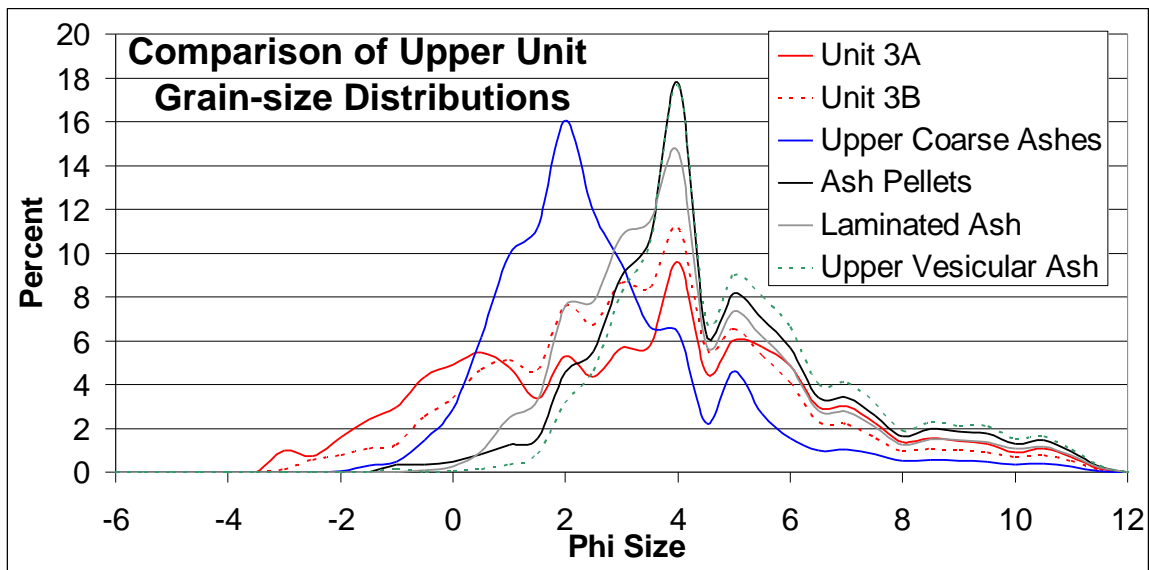


**Figure 5.23:** Grain-size comparison of Upper Units

	<b>Median Diameter (phi):</b>	<b>Graphic Standard Deviation (phi):</b>	<b>Graphic Skewness:</b>
<b>Unit 1A</b>	-1.1	1.58	-0.05
<b>Unit 1B</b>	0.6	3.75	0.33
<b>Unit 2</b>	-0.4	1.5	-0.1
<b>Unit 3A</b>	3.25	3.15	-0.11
<b>Unit 3B</b>	3.15	2.43	-0.05
<b>Coarse Ashes</b>	2	1.73	0.25
<b>Ash Pellets</b>	3.9	2.08	0.33
<b>Laminated Ash</b>	3.6	2	0.23
<b>Upper Vesicular Ash</b>	4.25	2.05	0.32

**Table 5.2:** Grain-size graphical statistics for analyzed averaged units.

## **5.2: Quantitative determination of fragmentation mechanism**

An analysis of fragmentation mechanisms and the determination of the relative contributions of magmatic or phreatomagmatic fragmentation in each unit were carried out following the methods of Wohletz et al. (1995) described in Chapter 2. Grain-size population modal size, fraction, dispersion, and fragmentation factor (mode / dispersion) are used to examine phreatomagmatic and magmatic contributions to grain-size distributions. Phreatomagmatic fragmentation typically produces modes with grain sizes finer than 0 phi and fragmentation factors lower than 0 (Wohletz et al. 1995). Magmatically fragmented modes are typically coarser than 0 phi and have positive fragmentation factors (Wohletz et al. 1995). Wohletz et al. (2005) used samples with bimodal grain-size distributions and assigned the coarse modes to magmatic fragmentation and the fine modes to phreatomagmatic fragmentation. The size for discriminating magmatic from phreatomagmatic contributions on a fraction vs. mode plot (e.g. Fig. 5.24) is around 0.5 phi, but is assigned for each sample to clearly separate modes. A solid black line is drawn on each plot to approximate the average grain-size

distribution for each unit or facies type. The discrimination size used below in fraction vs. mode graphs varies from 0.75 phi in Unit 1A to 2 phi in coarse ashes and is shifted to separate the two groups of grain-size modes in bimodal distributions. Samples without bimodal distributions were assigned discrimination sizes of around 1 phi. The fragmentation factors (Fig. 5.25) of modes with dispersion values around zero range greatly, as slight changes in the denominator of mode/dispersion cause dramatic changes in the resulting fragmentation factor. The phreatomagmatic fraction, R, is calculated by dividing the sum of the fractions of the phreatomagmatic modes by the total of all modes. Thus, it estimates the phreatomagmatic fraction of the particles, but is not a true water-magma ratio.

### Unit 1A

Five subpopulations were found in samples of Unit 1A (Table 5.3). Field observations of the coarse size, sorting, and absence of fine ash in Unit 1A suggest magmatic fragmentation as the primary mechanism for production of Unit 1A and graphing of subpopulation information confirms this.

	<b>Mode</b>	<b>Dispersion</b>	<b>Normalized Fraction</b>	<b>Fraction</b>	<b>Fragmentation Factor</b>
<b>Mode 1</b>	-3.26	-0.19	0.17	0.15	-40.74
<b>Mode 2</b>	-1.80	-0.68	0.34	0.30	2.90
<b>Mode 3</b>	-0.09	-0.70	0.37	0.33	0.18
<b>Mode 4</b>	1.81	-0.14	0.06	0.06	34.39
<b>Mode 5</b>	2.94	-0.69	0.06	0.06	-4.32

**Table 5.3:** Unit 1A subpopulation information. Data presented are averages of individual samples, so the fragmentation factor calculated from the presented mode and dispersion does not equal the average fragmentation factor presented.

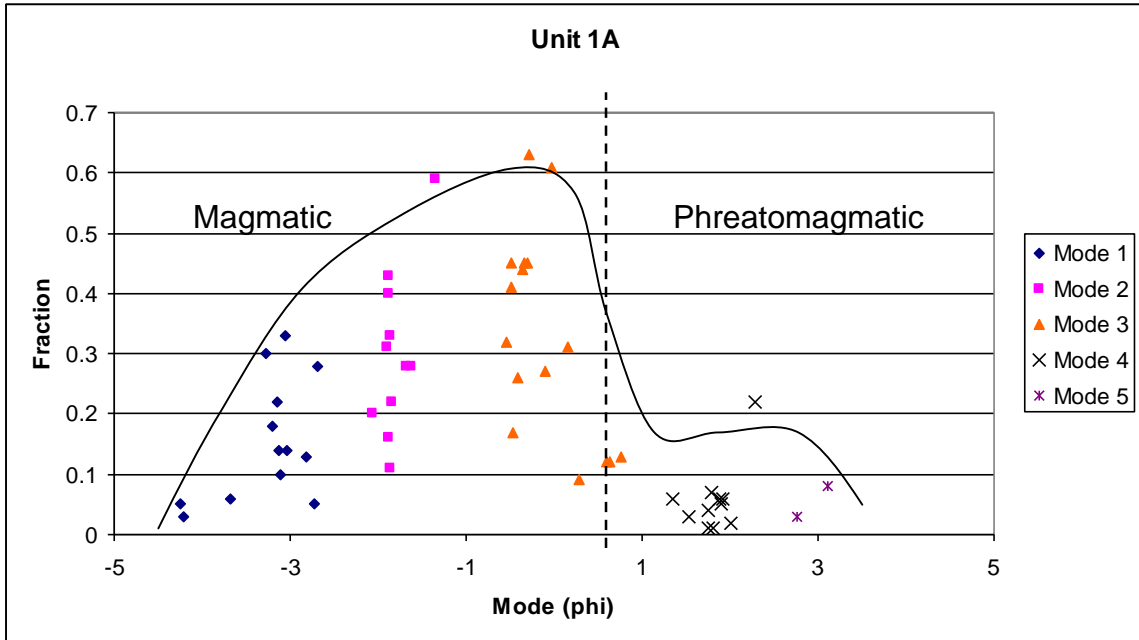


**Figure 5.24:** Subpopulation fraction vs. mode for Unit 1A. Dividing line between magmatic and phreatomagmatic fragmentation modes shown dashed at 0.8 phi.

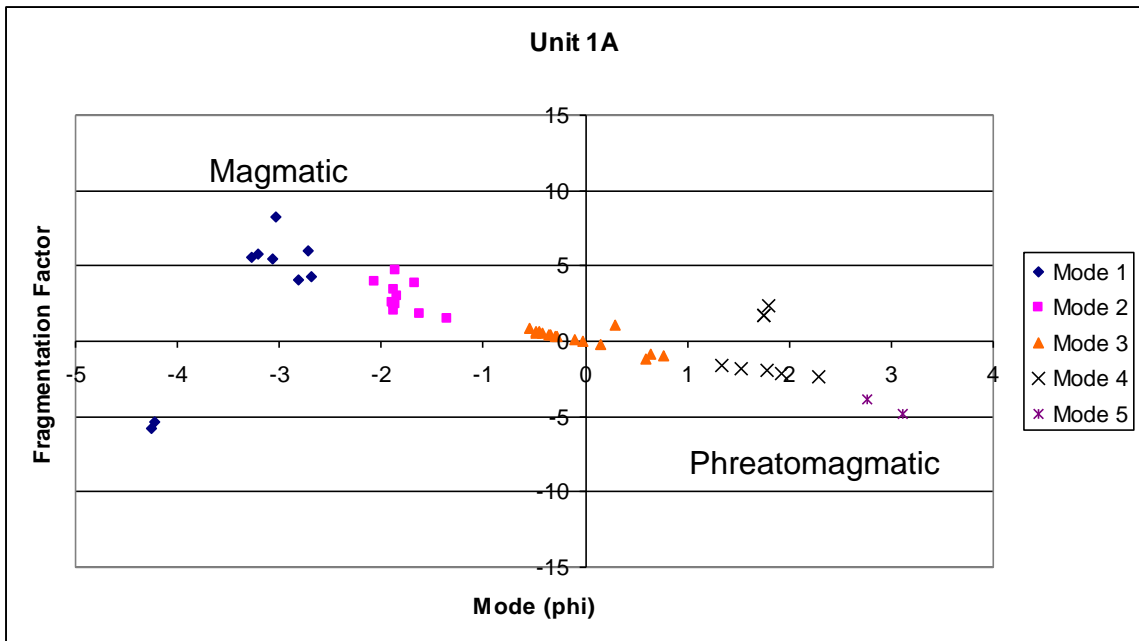


**Figure 5.25:** Subpopulation fragmentation factor vs. mode phi size for Unit 1A. Magmatic regime is  $< 0$ -phi and  $> 0$  fragmentation factor, phreatomagmatic regime is  $> 0$ -phi and  $< 0$  fragmentation factor.

The bulk of the material in Unit 1A samples falls in the magmatic field on plots of subpopulation fraction and fragmentation factor vs. subpopulation mode size (Figs. 5.24 and 5.25). The linear trend on the plot of fragmentation factor vs. subpopulation mode confirms that coarser grain sizes have lower dispersion (magmatic modes) and fine modes have higher dispersion (phreatomagmatic modes). Modes 1-3 are characterized as magmatic (Figs 5.24-5.25) and modes 4 and 5 are characterized as phreatomagmatic. When the subpopulation (mode) fractions are normalized, the fractions of subpopulations 1-3 can be summed to obtain the fraction of magmatic components in Unit 1A. The same can be done with subpopulations 4-5 to obtain the fraction of phreatomagmatic components. The resulting ratio of phreatomagmatic to magmatic components is 12:88 and the non-distance-normalized R (phreatomagmatic factor) is 0.12. R values were not normalized for distance because the subpopulation fractions used in this study are averaged from numerous sites that span medial locations for all units and facies and fall in the medial range. The medial basal samples analyzed are representative of the material produced at the vents and carried in the column. The grain-size distribution and maximum clast size does not change drastically from the caldera rim to the island coast (Fig. 5.1, 5.26). Satellite images during production of Unit 1A show a dark ash-rich column, which was likely water poor and poor in fine ash. The grain-size distributions of basal units sampled at medial locations are representative of the material produced at the vents and carried in the eruption column, allowing the quantitative estimation of water-magma ratio based on these grain-size distributions.

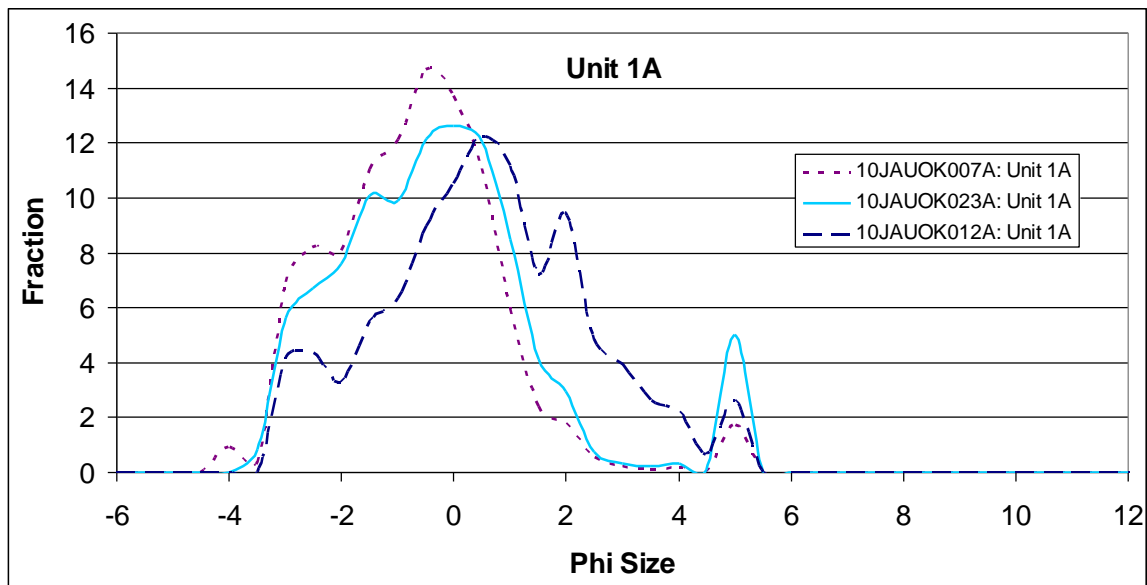


**Figure 5.26:** Grain-size distribution of Unit 1A from caldera-rim (012), mid-flanks (007), and island coast (023) locations.

### Unit 1B

Unit 1B is similar to Unit 1A, but is marked by a significant addition of fine and medium ash, which may indicate an increase in phreatomagmatic fragmentation input.

Ten subpopulations were found in Unit 1B (Table 5.4).

	Mode	Dispersion	Normalized Fraction	Fraction	Fragmentation Factor
<b>Mode 1</b>	-2.87	-0.40	0.12	0.16	-0.32
<b>Mode 2</b>	-1.80	-0.52	0.11	0.14	-31.45
<b>Mode 3</b>	-0.49	-0.64	0.19	0.25	-0.05
<b>Mode 4</b>	0.36	-0.82	0.24	0.31	-0.47
<b>Mode 5</b>	1.86	-0.24	0.04	0.05	24.58
<b>Mode 6</b>	2.88	0.11	0.03	0.04	-8.43
<b>Mode 7</b>	3.79	-0.05	0.07	0.09	112.59
<b>Mode 8</b>	5.26	-0.68	0.11	0.15	-7.82
<b>Mode 9</b>	6.84	-0.68	0.05	0.06	-10.37
<b>Mode 10</b>	9.09	-0.90	0.05	0.06	-10.18

**Table 5.4:** Unit 1B subpopulation information. Data presented are averages of individual samples, so the fragmentation factor calculated from the presented mode and dispersion does not equal the average fragmentation factor presented.

Unit 1B samples have abundant material in both fields on each plot (Figs 5.27-28), suggesting that magmatic and phreatomagmatic fragmentation processes were occurring during the production of Unit 1B. Subpopulations 1-4 can be categorized as magmatic, and subpopulations 5-10 as phreatomagmatic. The ratio of phreatomagmatic to magmatic components calculated from subpopulation fractions is 34:66, giving an R of 0.34, a significant increase from the 0.12 estimated for Unit 1A.

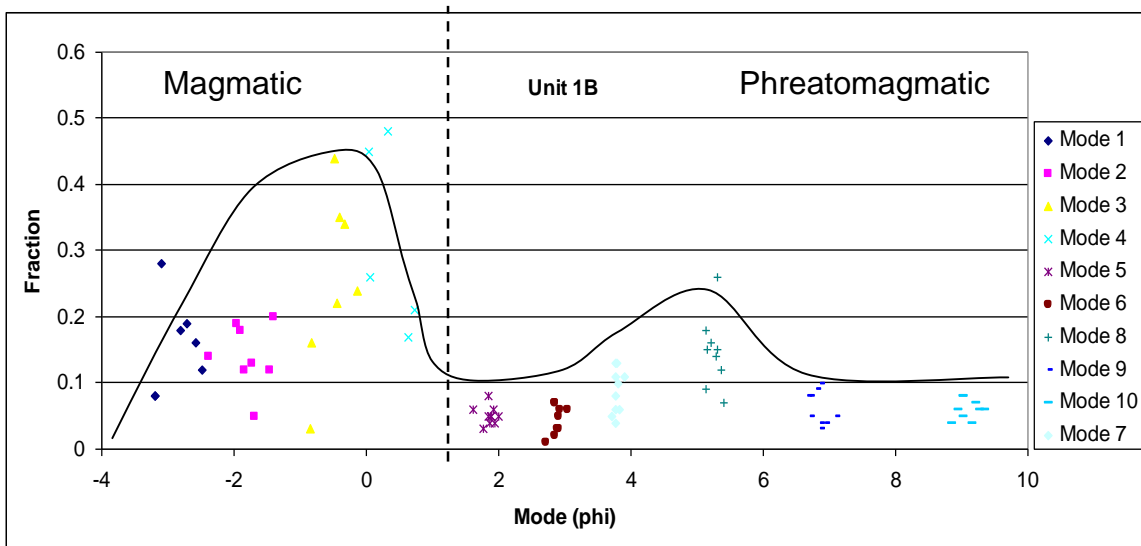


**Figure 5.27:** Subpopulation fraction vs. mode for Unit 1B. Dividing line between magmatic and phreatomagmatic fragmentation modes shown dashed.

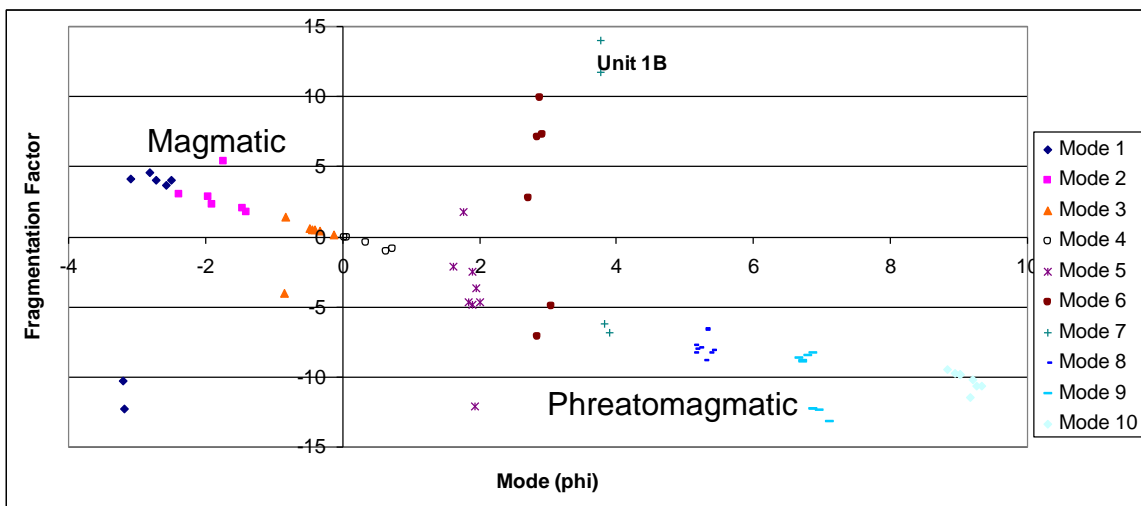


**Figure 5.28:** Subpopulation fragmentation factor vs. mode phi size for Unit 1B. Magmatic regime is < 0-phi and > 0 fragmentation factor, phreatomagmatic regime is > 0-phi and < 0 fragmentation factor.

These estimated phreatomagmatic fractions are significant if the fine material present in Unit 1B was produced with the coarse material present in Unit 1B. If Unit 1B fine material was produced with Unit 1A, remained in the column longer, and was deposited with Unit 1B, then the estimated water-magma ratio for Unit 1A should be higher and that of Unit 1B should be lower. The appearance of a light-colored water-rich plume around two hours after the eruption began indicates an increase in water-magma ratio at the vents, supporting the interpretation that the fine material in Unit 1B was produced with the coarse material present in Unit 1B. Therefore, the estimated water-magma ratios are probably significant for Units 1A and 1B and an increase in water-magma ratio from Unit 1A to Unit 1B is recorded in the grain-size distributions.

## **Unit 2**

Unit 2 is similar in appearance and grain-size to Unit 1A, and magmatic fragmentation is again thought to be the primary mechanism producing this unit. Six subpopulations were found for Unit 2 (Table 5.5). Subpopulations 1, 2, and 3 form a peak in the field of magmatic fragmentation (Fig. 5.29-30). Subpopulations 4-6 appear to be produced by phreatomagmatic fragmentation. The ratio of phreatomagmatic subpopulation fractions to magmatic subpopulation fractions is 22:78. The estimated R for the production of Unit 2 is 0.22.

	Mode	Dispersion	Normalized Fraction	Fraction	Fragmentation Factor
<b>Mode 1</b>	-2.45	-0.11	0.10	0.11	-28.54
<b>Mode 2</b>	-0.61	-0.63	0.36	0.40	-4.97
<b>Mode 3</b>	0.34	-0.44	0.32	0.36	-0.48
<b>Mode 4</b>	1.78	-0.04	0.07	0.07	0.12
<b>Mode 5</b>	2.90	-0.53	0.05	0.05	-1.44
<b>Mode 6</b>	5.55	-0.82	0.10	0.11	-6.77

**Table 5.5:** Unit 2 subpopulation information. Data presented are averages of individual samples, so the fragmentation factor calculated from the presented mode and dispersion does not equal the average fragmentation factor presented.

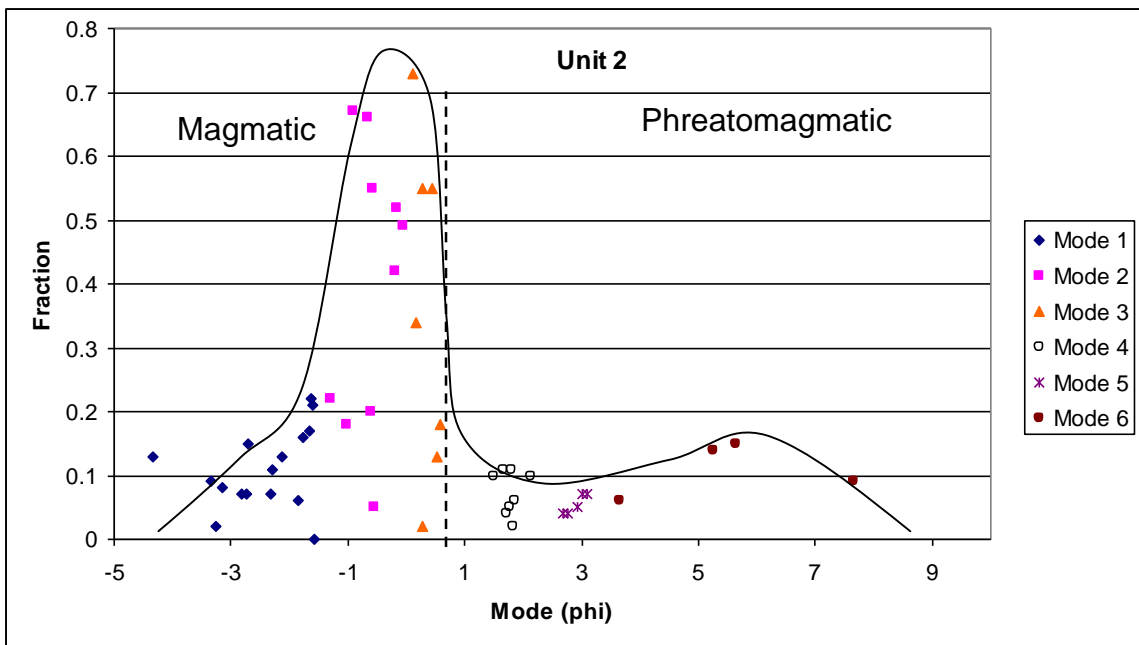


**Figure 5.29:** Subpopulation fraction vs. mode for Unit 2. Dividing line between magmatic and phreatomagmatic fragmentation modes shown dashed.

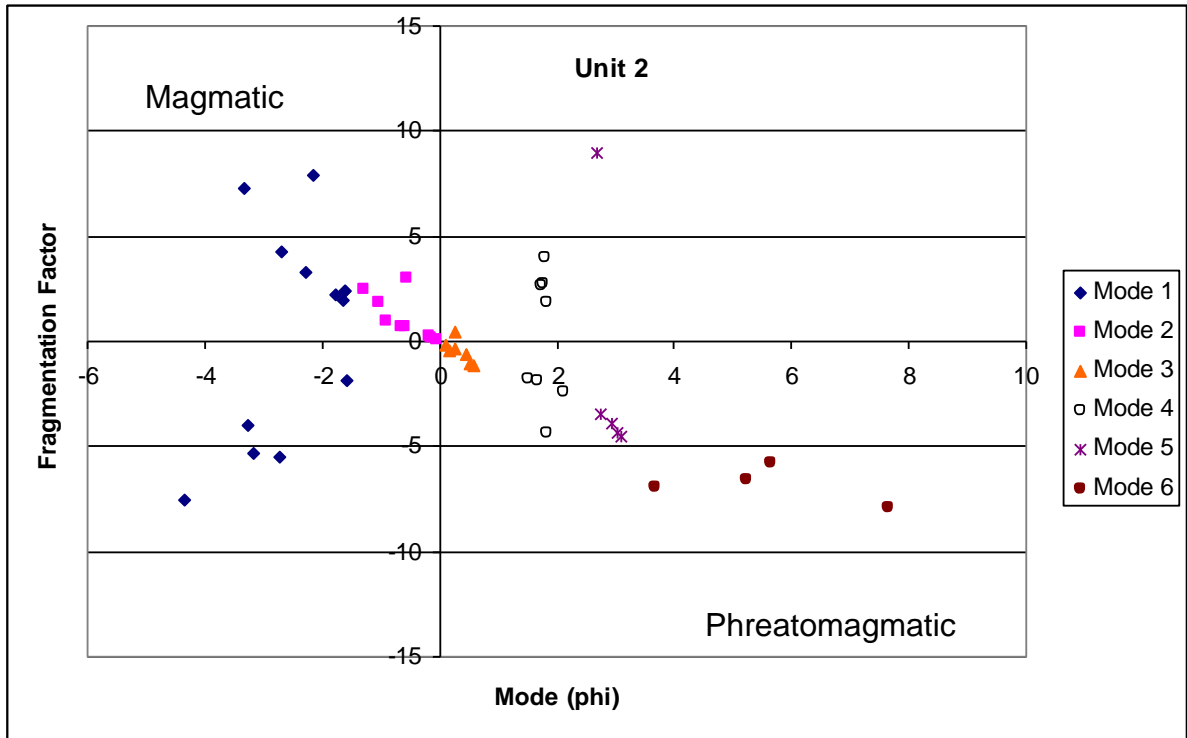


**Figure 5.30:** Subpopulation fragmentation factor vs. mode phi size for Unit 2. Magmatic regime is  $< 0$  phi and  $> 0$  fragmentation factor, phreatomagmatic regime is  $> 0$  phi and  $< 0$  fragmentation factor.

### Unit 3A

The transition from deposition of Unit 2 to Unit 3A shows a significant increase in the amount of fine ash and an increase in the role of phreatomagmatic fragmentation. Unit 3A includes significant material from  $-3$  phi to  $10$  phi, and nine subpopulations describe the analyzed samples (Table 5.6). Unit 3A includes the coarse modes present in the units stratigraphically below it, subpopulations 1-3, which were likely produced by magmatic fragmentation. Subpopulations 4-9 have grain sizes characteristic of phreatomagmatic fragmentation and form a fine-grained grain-size peak (Fig. 5.31-32). Phreatomagmatic subpopulations 4-9 and magmatic populations 1-3 are present in a ratio of 62:38. The R for Unit 3A is estimated at 0.62.

	Mode	Dispersion	Normalized Fraction	Fraction	Fragmentation Factor
<b>Mode 1</b>	-3.00	-0.37	0.04	0.04	24.56
<b>Mode 2</b>	-0.86	-0.91	0.18	0.20	0.94
<b>Mode 3</b>	0.48	-0.81	0.16	0.18	-0.61
<b>Mode 4</b>	1.83	-0.03	0.06	0.07	1.56
<b>Mode 5</b>	2.89	-0.33	0.11	0.13	1.90
<b>Mode 6</b>	3.73	0.23	0.11	0.13	6.30
<b>Mode 7</b>	5.18	-0.73	0.21	0.23	-7.35
<b>Mode 8</b>	6.84	-0.70	0.07	0.08	-10.23
<b>Mode 9</b>	9.26	-0.82	0.06	0.07	-12.74

**Table 5.6:** Unit 3A subpopulation information. Data presented are averages of individual samples, so the fragmentation factor calculated from the presented mode and dispersion does not equal the average fragmentation factor presented.

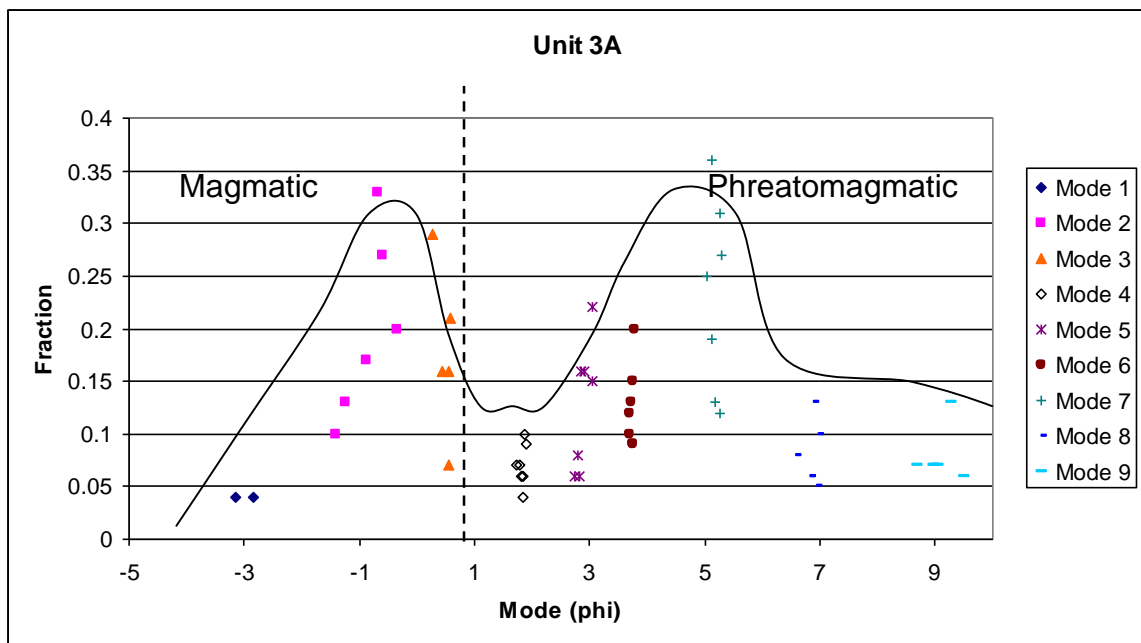


**Figure 5.31:** Subpopulation fraction vs. mode for Unit 3A. Dividing line between magmatic and phreatomagmatic fragmentation modes shown dashed.

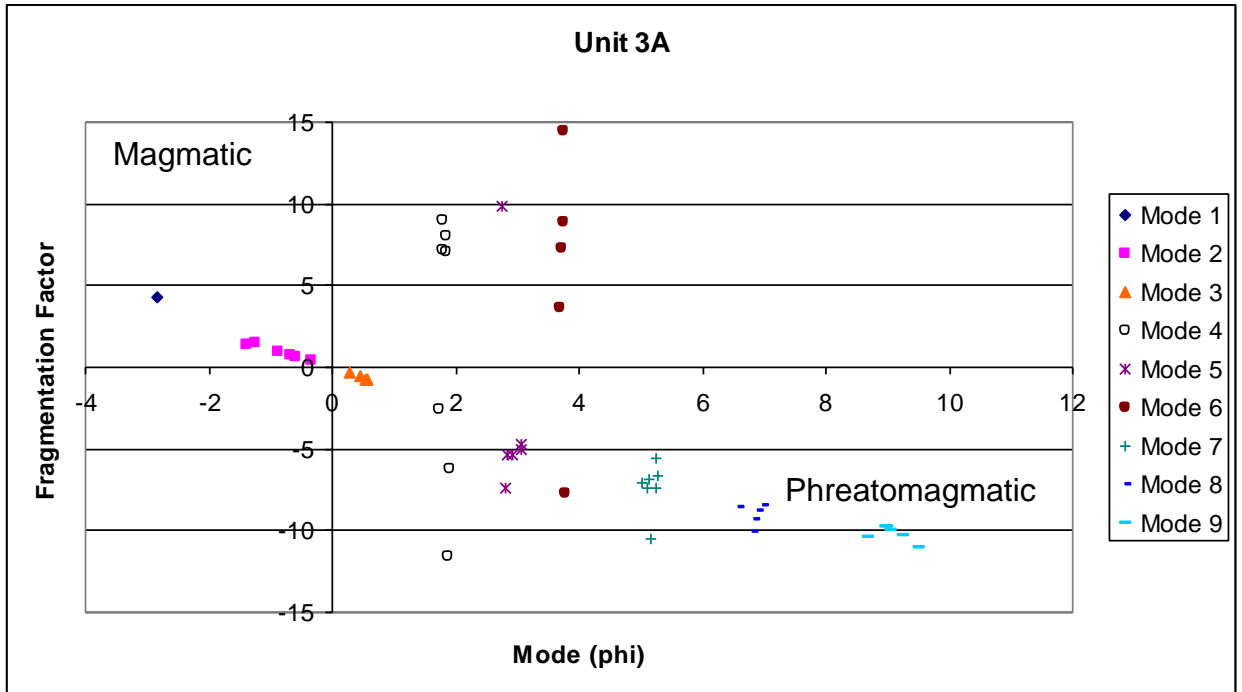


**Figure 5.32:** Subpopulation fragmentation factor vs. mode phi size for Unit 3A. Magmatic regime is  $\phi < 0$  and  $FF > 0$ , phreatomagmatic regime is  $\phi > 0$  and  $FF < 0$ .

### Unit 3B

Unit 3B, the better consolidated upper unit of Unit 3, has similar subpopulations to Unit 3A (Table 5.7). Unit 3B has three magmatic subpopulations as in Unit 3A that are less abundant in Unit 3B, and six phreatomagmatic populations (Figs. 5.33-34). The fraction made up by magmatic populations in Unit 3B is 0.25, and phreatomagmatic populations 4-9 make up 0.75, indicating an increase in contributions by phreatomagmatic fragmentation during the deposition of Unit 3. The estimated R for Unit 3B is 0.75.

	Mode	Dispersion	Normalized Fraction	Fraction	Fragmentation Factor
<b>Mode 1</b>	-1.67	-0.79	0.05	0.05	2.22
<b>Mode 2</b>	-0.36	-0.58	0.07	0.07	0.71
<b>Mode 3</b>	0.74	-0.65	0.13	0.13	-1.15
<b>Mode 4</b>	1.90	-0.37	0.15	0.15	-5.68
<b>Mode 5</b>	2.89	-0.22	0.15	0.16	0.12
<b>Mode 6</b>	3.77	-0.10	0.19	0.19	185.78
<b>Mode 7</b>	5.00	-0.50	0.14	0.14	-10.39
<b>Mode 8</b>	6.40	-0.78	0.07	0.07	-8.19
<b>Mode 9</b>	8.96	-0.93	0.06	0.06	-9.67

**Table 5.7:** Unit 3B subpopulation information. Data presented are averages of individual samples, so the fragmentation factor calculated from the presented mode and dispersion does not equal the average fragmentation factor presented.

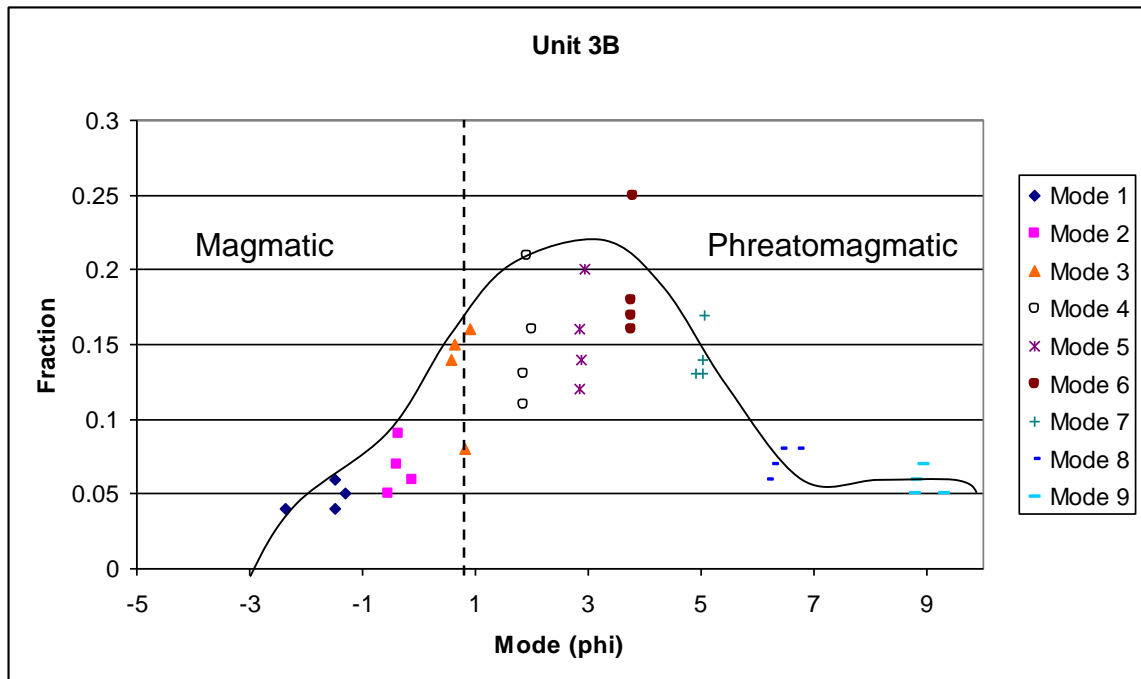


**Figure 5.33:** Subpopulation fraction vs. mode for Unit 3B. Dividing line between magmatic and phreatomagmatic fragmentation modes shown dashed.

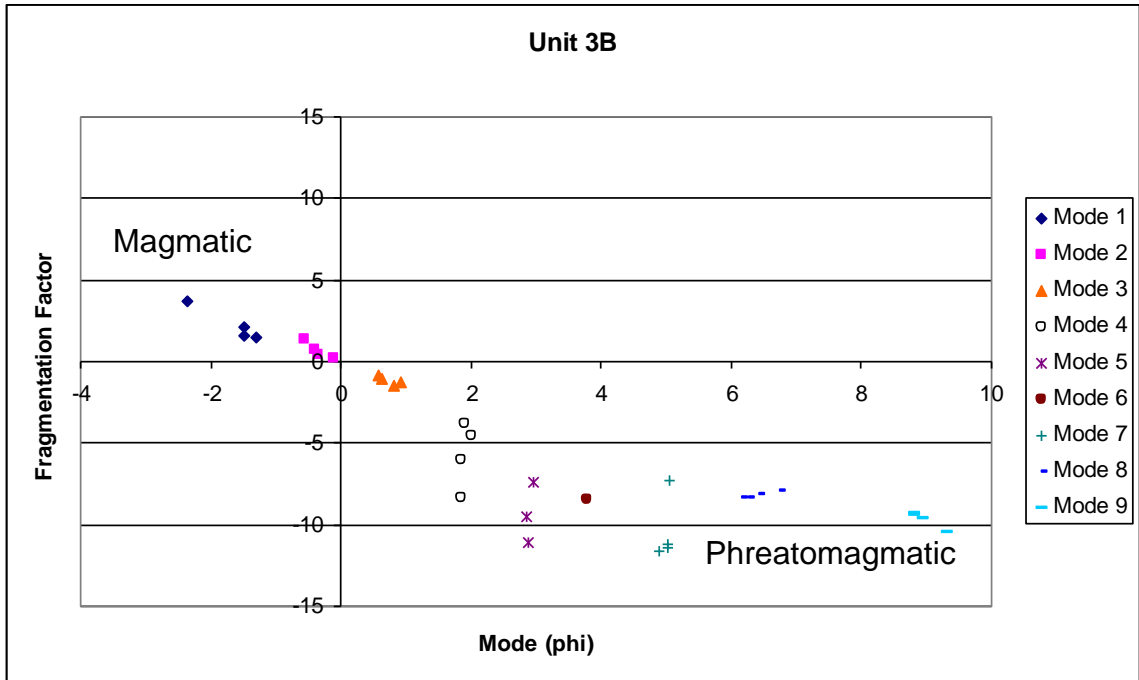


**Figure 5.34:** Subpopulation fragmentation factor vs. mode phi size for Unit 3B. Magmatic regime is  $< 0$  phi and  $> 0$  fragmentation factor, phreatomagmatic regime is  $> 0$  phi and  $< 0$  fragmentation factor.

### Coarse ash units

The upper units are much finer grained than the basal units and are typically devoid of lapilli and very poor in coarse to very coarse ash. Upper units at many sample sites contained thin lenses of coarse ash, which are examined here. Submodes were created for coarse ashes from various sites and stratigraphic positions. Strong modes are present in all coarse ash samples around 1.87, 2.86, and 3.77 phi. These modes are significant, as all samples have modes at nearly identical sizes (Fig. 5.35). This striking consistency in produced grain size indicates that very similar fragmentation mechanisms were taking place during production of all of the analyzed coarse ash units. The componentry of these modes is examined further in Chapter 6.

Seven subpopulations describe the grain-size distribution of coarse ash units (Table 5.8). Subpopulation 1, 2, and 3 form a strong peak in the magmatic fragmentation

field (Fig. 5.35) and were likely produced by magmatic fragmentation. Subpopulations 4-7 fall in the phreatomagmatic field (Fig. 5.35). The ratio of phreatomagmatic to magmatic components is 40:60 and the R is 0.40.

	Mode	Dispersion	Normalized Fraction	Fraction n	Fragmentation Factor
<b>Mode 1</b>	-1.08	-0.35	0.08	0.10	7.06
<b>Mode 2</b>	0.92	-0.63	0.30	0.35	-1.66
<b>Mode 3</b>	1.87	0.03	0.22	0.25	49.72
<b>Mode 4</b>	2.86	-0.37	0.16	0.18	13.90
<b>Mode 5</b>	3.77	0.34	0.06	0.07	35.10
<b>Mode 6</b>	5.22	-0.61	0.08	0.09	20.54
<b>Mode 7</b>	7.10	-0.96	0.11	0.12	-7.39

**Table 5.8:** Coarse ash subpopulation information. Data presented are averages of individual samples, so the fragmentation factor calculated from the presented mode and dispersion does not equal the average fragmentation factor presented.

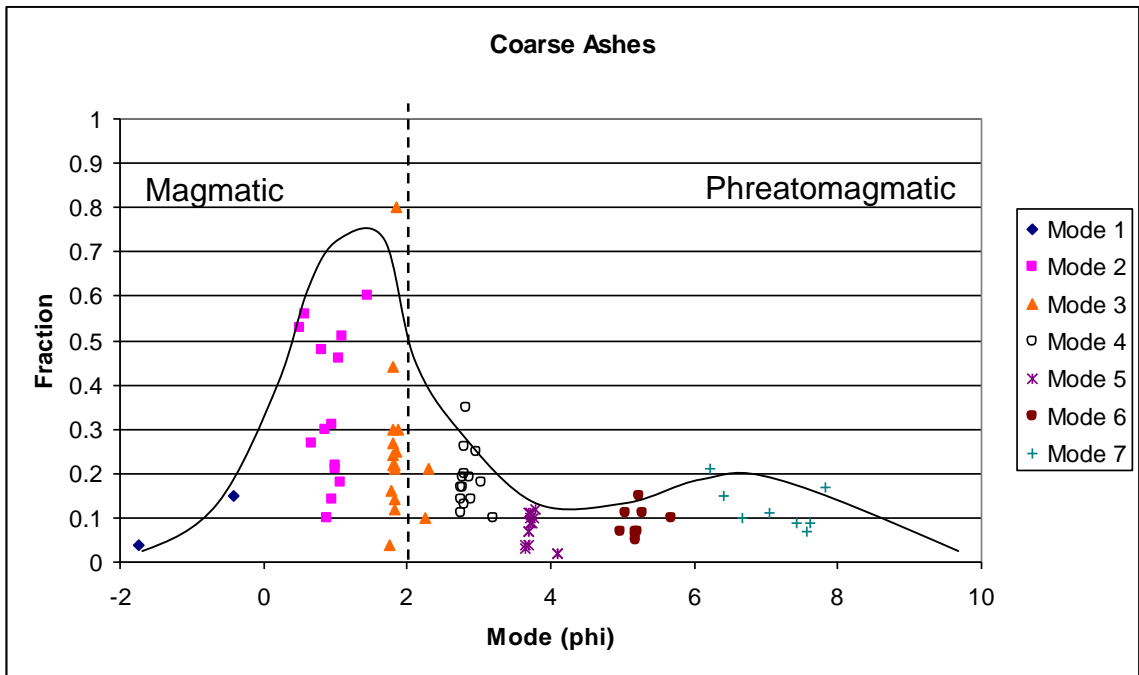


**Figure 5.35:** Subpopulation fraction vs. mode for coarse ashes. Dividing line between magmatic and phreatomagmatic fragmentation modes shown dashed.

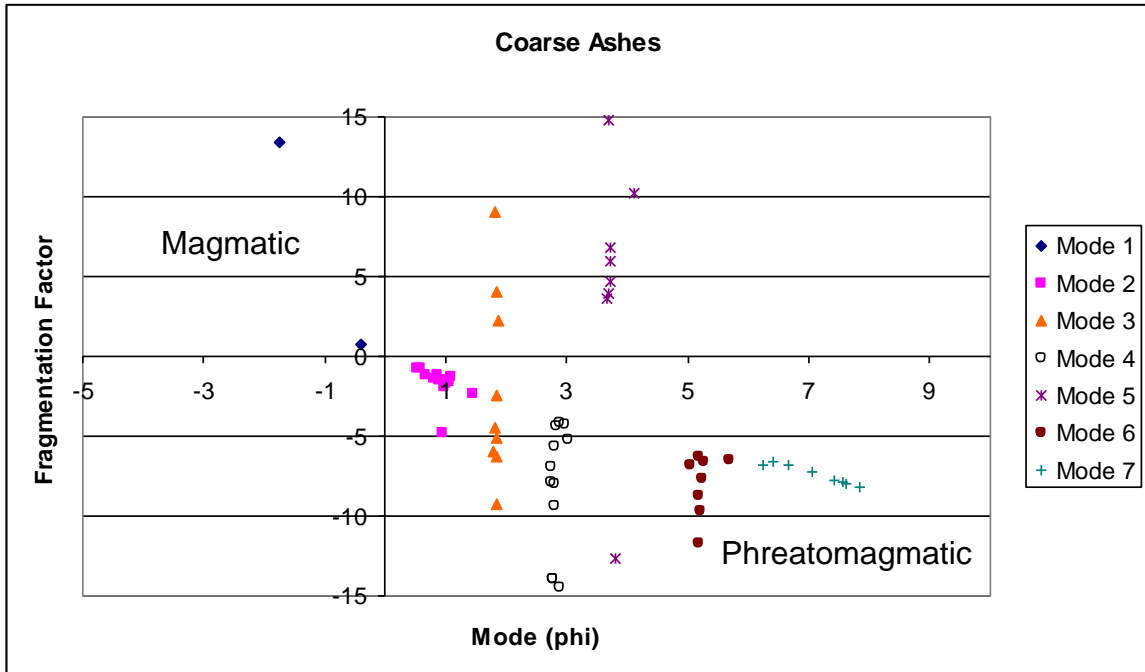


**Figure 5.36:** Subpopulation fragmentation factor vs. mode phi size for coarse ashes. Magmatic regime is  $< 0$  phi and  $> 0$  fragmentation factor, phreatomagmatic regime is  $> 0$  phi and  $< 0$  fragmentation factor.

### Ash pellets

Upper units, with the exception of coarse ash lenses, are characterized by very fine grain sizes. Ash-pellet units make up much of upper units in many locations. Seven subpopulations describe their distribution (Table 5.9). Subpopulation 1 falls in the magmatic field, while the remaining subpopulations 2-7 form a grain-size peak in the phreatomagmatic field (Fig. 5.37-38). The ratio of phreatomagmatic to magmatic subpopulation fractions is 87:13. The R for ash-pellet units is 0.87.

	Mode	Dispersion	Normalized Fraction	Fraction	Fragmentation Factor
<b>Mode 1</b>	0.62	-0.76	0.11	0.13	-0.90
<b>Mode 2</b>	1.81	-0.14	0.07	0.08	43.47
<b>Mode 3</b>	2.99	-0.59	0.24	0.28	-5.78
<b>Mode 4</b>	3.73	0.44	0.17	0.19	15.24
<b>Mode 5</b>	5.07	-0.50	0.17	0.19	62.64
<b>Mode 6</b>	6.70	-0.74	0.12	0.14	90.46
<b>Mode 7</b>	9.01	-0.92	0.11	0.12	-9.79

**Table 5.9:** Ash Pellet subpopulation information. Data presented are averages of individual samples, so the fragmentation factor calculated from the presented mode and dispersion does not equal the average fragmentation factor presented.

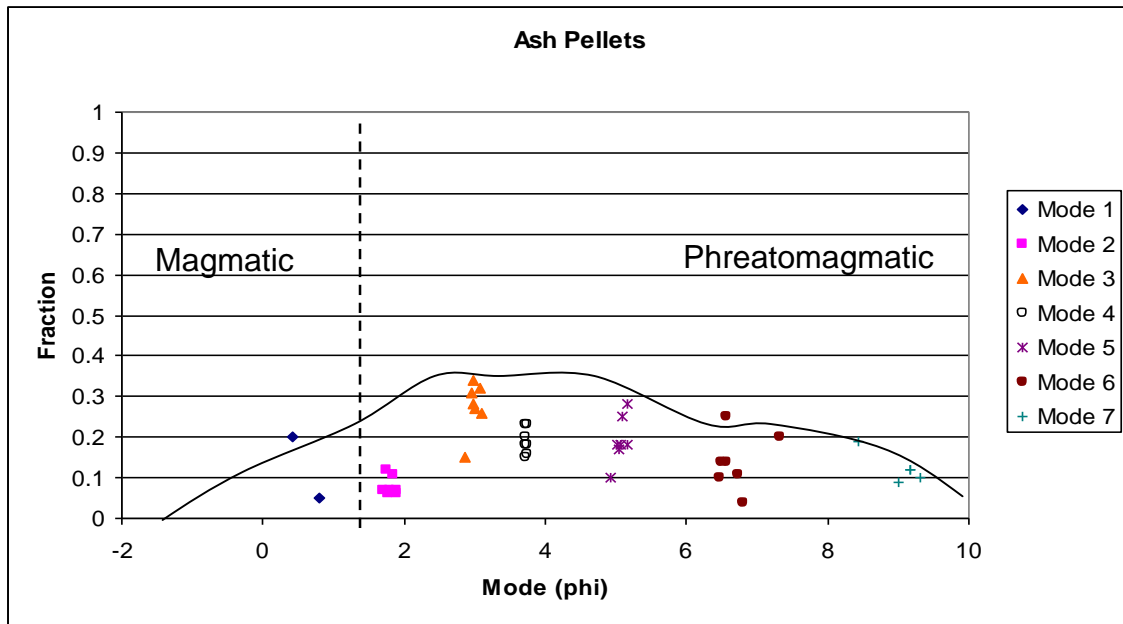


**Figure 5.37:** Subpopulation fraction vs. mode for ash pellets. Dividing line between magmatic and phreatomagmatic fragmentation modes shown dashed.

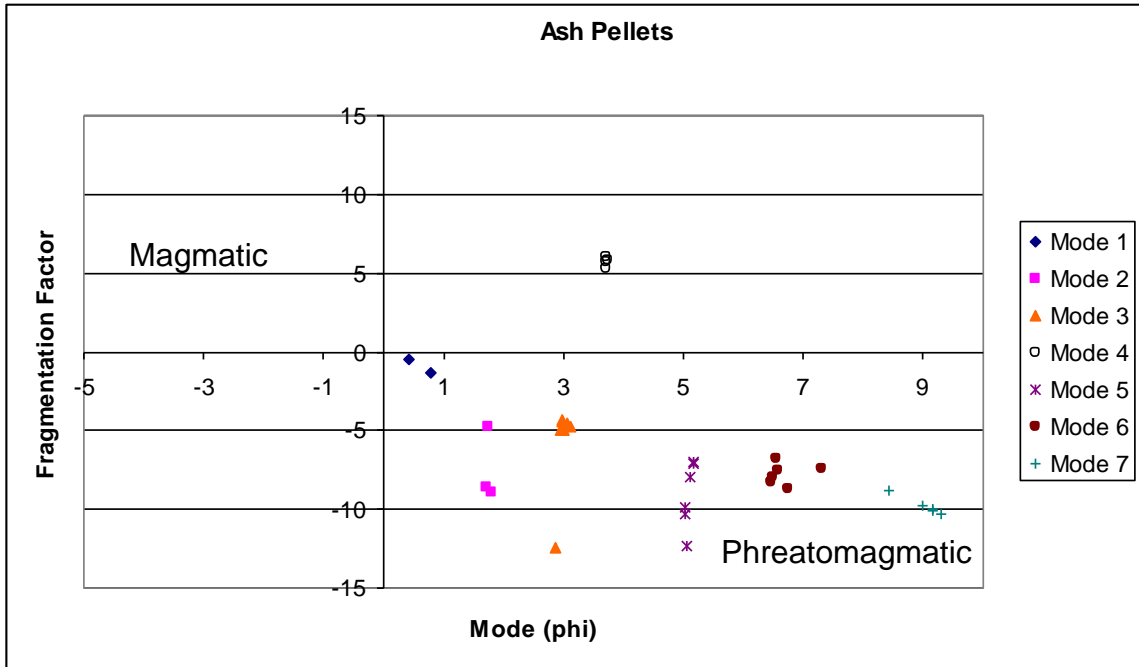


**Figure 5.38:** Subpopulation fragmentation factor vs. mode phi size for ash pellets. Magmatic regime is  $< 0$  phi and  $> 0$  fragmentation factor, phreatomagmatic regime is  $> 0$  phi and  $< 0$  fragmentation factor.

### Laminated ash units

Laminated ash and upper vesicular ash grain-size distributions are very similar to those of ash-pellet units. Seven subpopulations were found for each of these facies types (Tables 5.10, 5.11), and all subpopulations fall in the phreatomagmatic fragmentation field (Figs. 5.39-42). The ratio of phreatomagmatic to magmatic components is 100:0, and the R for both laminated ash units and upper vesicular ash units is 1.0.

	Mode	Dispersion	Normalized Fraction	Fraction	Fragmentation Factor
<b>Mode 1</b>	1.54	-0.37	0.19	0.23	10.74
<b>Mode 2</b>	2.33	-0.76	0.18	0.21	-3.09
<b>Mode 3</b>	2.83	0.17	0.10	0.12	42.63
<b>Mode 4</b>	3.66	-0.07	0.21	0.25	-54.72
<b>Mode 5</b>	5.09	-0.58	0.16	0.19	-8.97
<b>Mode 6</b>	6.87	-0.83	0.09	0.10	-8.30
<b>Mode 7</b>	9.21	-0.91	0.08	0.09	-10.12

**Table 5.10:** Laminated ash subpopulation information. Data presented are averages of individual samples, so the fragmentation factor calculated from the presented mode and dispersion does not equal the average fragmentation factor presented.

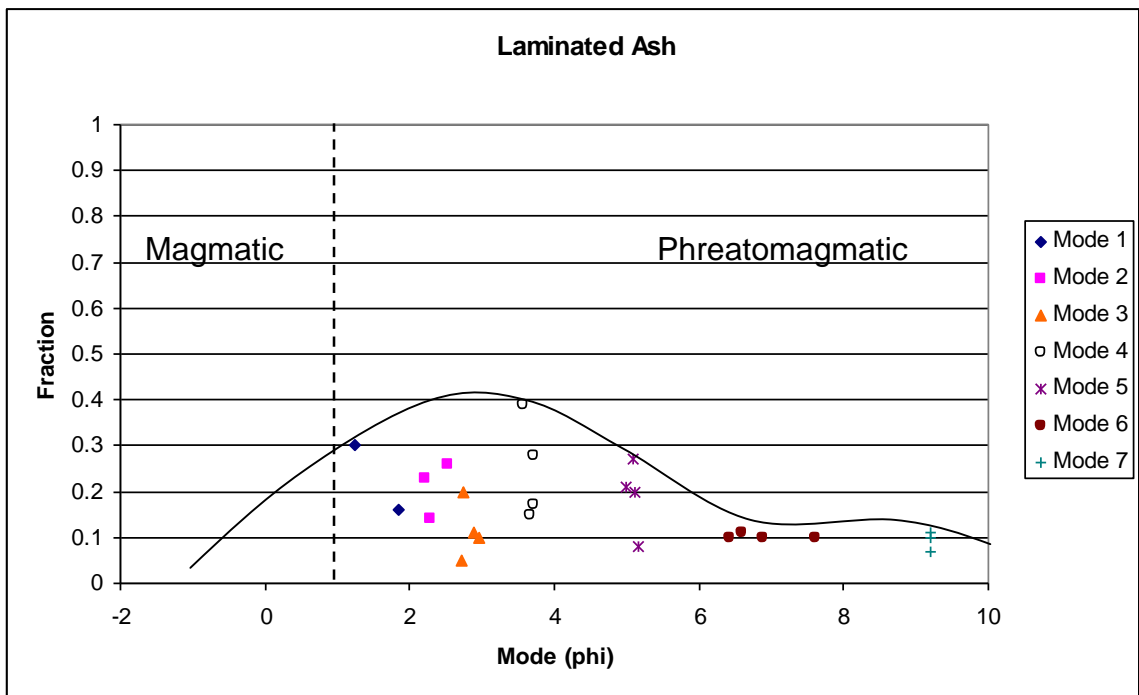


**Figure 5.39:** Subpopulation fraction vs. mode for laminated ash. Dividing line between magmatic and phreatomagmatic fragmentation modes shown dashed.

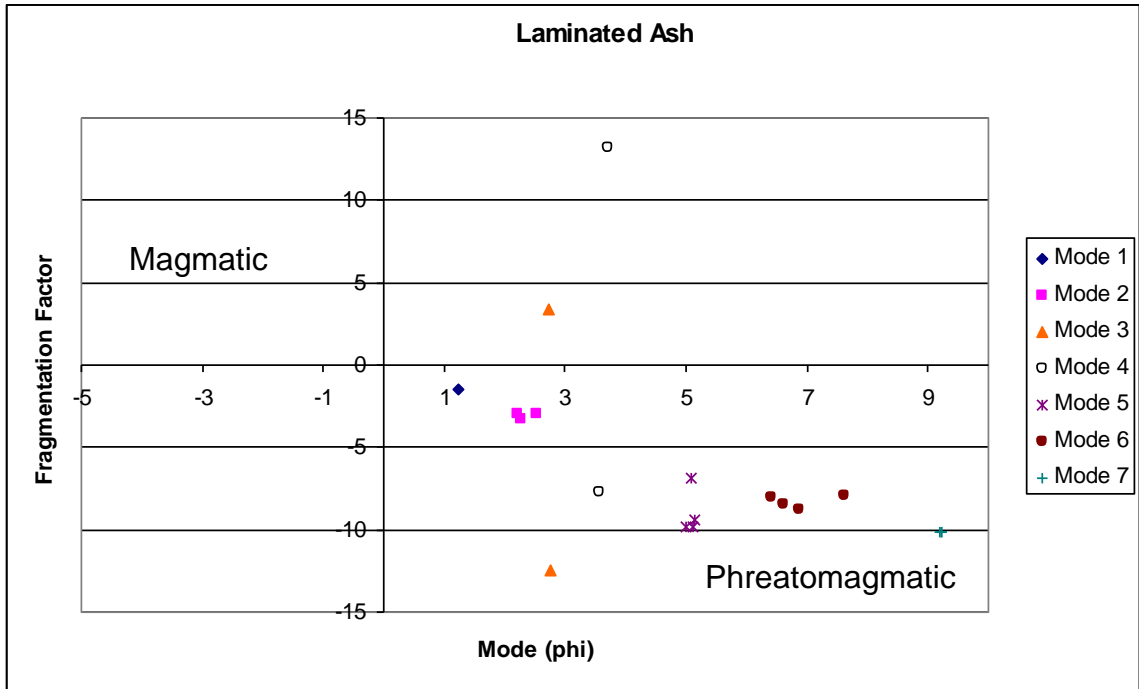


**Figure 5.40:** Subpopulation fragmentation factor vs. mode phi size for laminated ash. Magmatic regime is  $< 0$  phi and  $> 0$  fragmentation factor, phreatomagmatic regime is  $> 0$  phi and  $< 0$  fragmentation factor.

## Upper vesicular ash units

	Mode	Dispersion	Normalized Fraction	Fraction	Fragmentation Factor
<b>Mode 1</b>	1.90	-0.35	0.08	0.08	29.47
<b>Mode 2</b>	3.05	-0.48	0.25	0.25	43.08
<b>Mode 3</b>	3.72	0.51	0.18	0.18	9.01
<b>Mode 4</b>	5.07	-0.61	0.23	0.23	-8.48
<b>Mode 5</b>	6.65	-0.83	0.15	0.15	-8.00
<b>Mode 6</b>	9.23	-0.89	0.10	0.10	-10.45

**Table 5.11:** Upper vesicular ash subpopulation information. Data presented are averages of individual samples, so the fragmentation factor calculated from the presented mode and dispersion does not equal the average fragmentation factor presented.

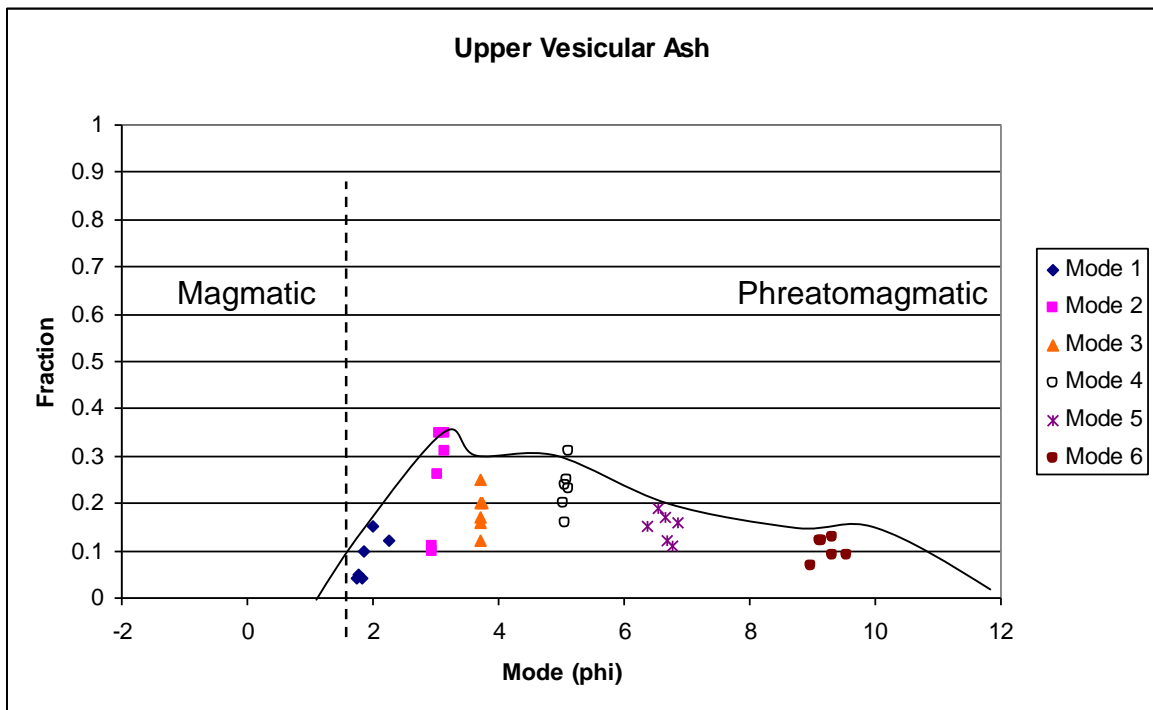


**Figure 5.41:** Subpopulation fraction vs. mode for upper vesicular ash. Dividing line between magmatic and phreatomagmatic fragmentation modes shown dashed.

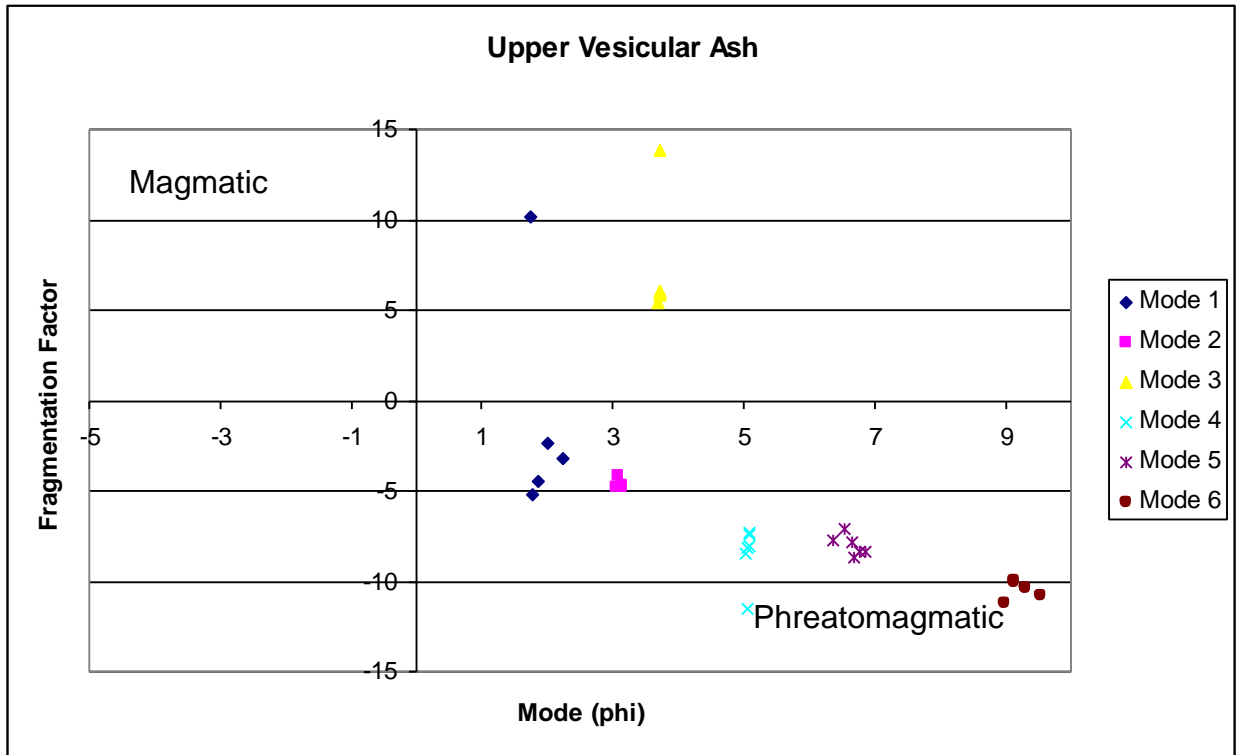


**Figure 5.42:** Subpopulation fragmentation factor vs. mode phi size for upper vesicular ash. Magmatic regime is  $< 0$  phi and  $> 0$  fragmentation factor, phreatomagmatic regime is  $> 0$  phi and  $< 0$  fragmentation factor.

### Interpretations of quantitative grain-size data

The water-magma ratio estimated from grain-size distribution varies in the deposits from throughout the eruption (Table 5.12). The opening sequence had two pulses of primarily magmatic activity in Units 1A and 2 separated by a period of increased phreatomagmatic contribution depositing Unit 1B. After deposition of Unit 2, the water-magma ratio increased to produce Unit 3A and continued to increase during deposition of Unit 3B. Upper fine-grained units with ash pellets, laminated fine ash, and vesicular ash show the highest water-magma ratio, with grain-size distributions almost entirely produced by phreatomagmatic fragmentation. Upper units contain lenses of coarse ash, evidence of periods with decreased water-magma ratios.

The R values calculated here are most useful for examining the contributions of phreatomagmatic and magmatic fragmentation in a relative, rather than absolute, manner. Modes assigned to magmatic or phreatomagmatic fragmentation may not be entirely produced by one type of fragmentation, but may have contributions from both magmatic and phreatomagmatic fragmentation. Increases or decreases in R between units are reliable, whereas the water-magma mass ratio estimated from R is quite uncertain. The R values calculated here are plotted and compared with results from qualitative grain-size analysis in section 5.3.

	<b>PHM fraction</b>	<b>MAG fraction</b>	<b>R</b>
<b>Unit 1A</b>	12	88	0.12
<b>Unit 1B</b>	34	66	0.34
<b>Unit 2</b>	22	78	0.22
<b>Unit 3A</b>	62	38	0.62
<b>Unit 3B</b>	88	12	0.88
<b>Coarse Ashes</b>	40	60	0.40
<b>Ash Pellets</b>	89	11	0.89
<b>Laminated Ash</b>	100	0	1.00
<b>Upper Vesicular Ash</b>	100	0	1.00

**Table 5.12:** R (phreatomagmatic fraction) estimated for units and upper facies.

### **5.3 Qualitative examination of grain-size distributions**

Subpopulation dispersion or sorting is sensitive to fragmentation mechanism (Wohletz et al. 1995). Populations produced by magmatic fragmentation have coarser grain sizes and poorer sorting than those produced by phreatomagmatic fragmentation (Wohletz 1983; Wohletz and Sheridan 1983). Sudden fragmentation processes that occur in one or few stages often produce coarse grain sizes and poor sorting (Wohletz and Brown 1995). In phreatomagmatic fragmentation processes, the growth and detachment

of instabilities at fragment surfaces produce finer median grain sizes and better sorting (Wohletz and Brown 1995).

The subpopulation modes and dispersions sorted by subpopulation modes for composite samples from each unit or facies were used to examine contributions from phreatomagmatic and magmatic fragmentation (Fig. 5.13). The modes with the highest dispersion ( $\gamma$ ) may be the populations most likely produced by phreatomagmatic fragmentation. The population around 4 phi has the highest  $\gamma$  value and is present in all units and facies types except Unit 1A and Unit 2. The 4-phi size is known to be an important population for discriminating fragmentation mechanism (Dellino and Liotino 2002), and it may be the most phreatomagmatically fragmented size population in the Okmok 2008 deposits. The populations around 2 and 3 phi are the next best sorted populations after the 4-phi population. Coarser populations around -2, -1, 0, and 1 phi have low dispersion values and poorer sorting, suggesting a greater influence of magmatic fragmentation. The coarsest population, around -3 phi, has a high dispersion value and is better sorted, but is almost certainly produced by magmatic fragmentation. The clasts in the -3-phi size are predominantly pumiceous, showing evidence of gas expansion and magmatic fragmentation. Sorting in the eruption column may have produced the well-sorted -3-phi population, as column sorting is efficient with coarse fragments.

The finest populations, with modes around 5, 7, and 9 phi, are poorly sorted with low dispersion values. These populations were expected to have higher dispersion values because of their fine grain size, but they formed poorly sorted, broad peaks. There may be several subpopulations within each of these very fine populations that were too small

to detect and model in SFT or a fragmentation mechanism other than phreatomagmatism may have produced these fine-grained broad peaks. The units and facies with the highest fraction 2, 3, and 4 phi modes were likely produced by events with the highest water-magma ratios (Table 5.14).

Unit 1A		Unit 1B		Unit 2		Unit 3A		Unit 3B		Upper Coarse Ash		Ash Pellets		Laminated Ash		Upper Vesic Ash		AVG	AVG
Mode	$\gamma$	Mode	$\gamma$	Mode	$\gamma$	Mode	$\gamma$	Mode	$\gamma$	Mode	$\gamma$	Mode	$\gamma$	Mode	$\gamma$	Mode	$\gamma$	Mode	$\gamma$
-3.26	-0.19	-2.87	-0.40	-2.45	-0.11	-3.00	-0.37											-2.89	-0.27
-1.80	-0.68	-1.80	-0.52					-1.67	-0.79									-1.75	-0.66
		-0.49	-0.64	-0.61	-0.63	-0.86	-0.91	-0.36	-0.58	-1.08	-0.35							-0.68	-0.62
-0.09	-0.70	0.36	-0.82	0.34	-0.44	0.48	-0.81											0.27	-0.69
								0.74	-0.65	0.92	-0.63	0.62	-0.76	1.54	-0.37			0.95	-0.53
1.81	-0.14	1.86	-0.24	1.78	-0.04	1.83	-0.03	1.90	-0.37	1.87	0.03	1.81	-0.14	2.33	-0.76	1.90	-0.35	1.90	-0.19
2.94	-0.69	2.88	0.11	2.90	-0.53	2.89	-0.33	2.89	-0.22	2.86	-0.37	2.99	-0.59	2.83	0.17	3.05	-0.48	2.91	-0.34
		3.79	-0.05			3.73	0.23	3.77	-0.10	3.77	0.34	3.73	0.44	3.66	-0.07	3.72	0.51	3.74	0.10
		5.26	-0.68	5.55	-0.82	5.18	-0.73	5.00	-0.50	5.22	-0.61	5.07	-0.50	5.09	-0.58	5.07	-0.61	5.18	-0.63
		6.84	-0.68			6.84	-0.70	6.40	-0.78	7.10	-0.96	6.70	-0.74	6.87	-0.83	6.65	-0.83	6.77	-0.82
		9.09	-0.90			9.26	-0.82	8.96	-0.93			9.01	-0.92	9.21	-0.91	9.23	-0.89	9.13	-0.89
<b>AVG <math>\gamma</math></b>	<b>-0.48</b>		<b>-0.48</b>		<b>-0.43</b>		<b>-0.50</b>		<b>-0.55</b>		<b>-0.36</b>		<b>-0.46</b>		<b>-0.48</b>		<b>-0.44</b>		<b>-0.46</b>

**Table 5.13:** Subpopulation modes and dispersion sorted by mode. Yellow cells indicate lowest dispersion (poor sorting) for a population, and blue cells mark highest dispersion (best sorting) for a population.

Unit 1A			Unit 1B		
Mode	Dispersion	Normalized Fraction	Mode	Dispersion	Normalized Fraction
-3.26	-0.19	0.17	-2.87	-0.40	0.12
-1.80	-0.68	0.34	-1.80	-0.52	0.11
-0.09	-0.70	0.37	-0.49	-0.64	0.19
1.81	-0.14	0.06	0.36	-0.82	0.24
2.94	-0.69	0.06	1.86	-0.24	0.04
			2.88	0.11	0.03
			3.79	-0.05	0.07
			5.26	-0.68	0.11
			6.84	-0.68	0.05
			9.09	-0.90	0.05
<b>% PHM populations</b>		<b>0.13</b>	<b>% PHM populations</b>		<b>0.14</b>
Unit 2			Unit 3		
Mode	Dispersion	Normalized Fraction	Mode	Dispersion	Normalized Fraction
-2.45	-0.11	0.10	-3.00	-0.37	0.04
-0.61	-0.63	0.36	-0.86	-0.91	0.18
0.34	-0.44	0.32	0.48	-0.81	0.16
1.78	-0.04	0.07	1.83	-0.03	0.06
2.90	-0.53	0.05	2.89	-0.33	0.11
5.55	-0.82	0.10	3.73	0.23	0.11
			5.18	-0.73	0.21
			6.84	-0.70	0.07
			9.26	-0.82	0.06
<b>% PHM populations</b>		<b>0.12</b>	<b>% PHM populations</b>		<b>0.29</b>
Unit 3B			Upper Coarse ashes		
Mode	Dispersion	Normalized Fraction	Mode	Dispersion	Normalized Fraction
-1.67	-0.79	0.05	-1.08	-0.35	0.08
-0.36	-0.58	0.07	0.92	-0.63	0.30
0.74	-0.65	0.13	1.87	0.03	0.22
1.90	-0.37	0.15	2.86	-0.37	0.16
2.89	-0.22	0.15	3.77	0.34	0.06
3.77	-0.10	0.19	5.22	-0.61	0.08
5.00	-0.50	0.14	7.10	-0.96	0.11
6.40	-0.78	0.07			
8.96	-0.93	0.06			
<b>% PHM populations</b>		<b>0.49</b>	<b>% PHM populations</b>		<b>0.44</b>
Ash pellets			Laminated Ash		
Mode	Dispersion	Normalized Fraction	Mode	Dispersion	Normalized Fraction
0.62	-0.76	0.11	1.54	-0.37	0.19
1.81	-0.14	0.07	2.33	-0.76	0.18
2.99	-0.59	0.24	2.83	0.17	0.10
3.73	0.44	0.17	3.66	-0.07	0.21
5.07	-0.50	0.17	5.09	-0.58	0.16
6.70	-0.74	0.12	6.87	-0.83	0.09
9.01	-0.92	0.11	9.21	-0.91	0.08
<b>% PHM populations</b>		<b>0.48</b>	<b>% PHM populations</b>		<b>0.48</b>
Upper vesicular ash					
Mode	Dispersion	Normalized Fraction			
1.90	-0.35	0.08			
3.05	-0.48	0.25			
3.72	0.51	0.18			
5.07	-0.61	0.23			
6.65	-0.83	0.15			
9.23	-0.89	0.10			
<b>% PHM populations</b>		<b>0.51</b>			

**Table 5.14 (cont):** Percentages of phreatomagmatic modes (2, 3, 4 phi) in units and facies

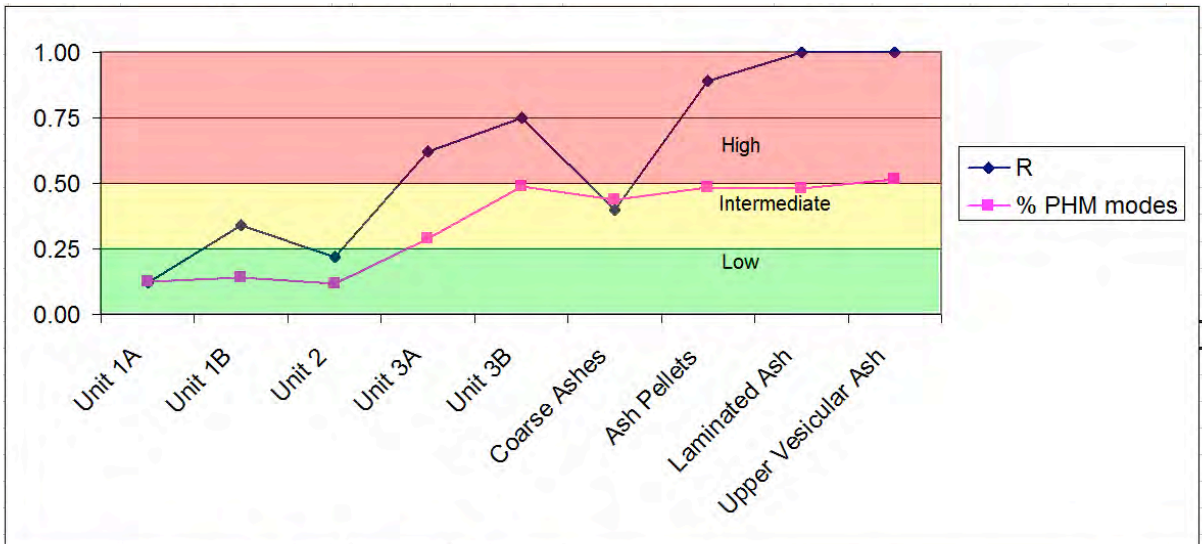


**Figure 5.43:** R values and % of 2, 3, and 4-phi subpopulations plotted for each unit and facies type. Low, Intermediate, and High represent level of water-magma interaction.

The relative changes in the R values of units and facies calculated in section 5.2 are confirmed by the fraction of phreatomagmatic subpopulations (Figure 5.39). By both methods, Units 1A and 2 have the lowest level of water-magma interaction, Units 1B, 3A, 3B, and upper coarse ashes are intermediate, and ash-pellet units, laminated ash units, and upper vesicular ash units have high levels of water-magma interaction.

## **Chapter 6: Componentry Results**

### **6.1 Componentry categories**

Ash grains were examined and separated into three broad categories; lithic grains, juvenile grains, and free crystals. Images of each category from the microscope using reflected light are presented below, and SEM images and fractal analyses of each grain type in the 2-phi size are presented in Chapter 7.

#### **6.1a Lithic grains**

Lithic grains in the 2008 Okmok deposits include lava fragments, black opaque scoria and dense pyroclasts, and other material not produced by the 2008 eruption. The distinction between the various lithic categories and juvenile fragments was based on a number of factors. Grain types showing oxidation, rounded edges, and other signs of significant weathering or alteration were inferred not to be juvenile 2008 material. Grains of dense lava with sharp edges and no surfaces of weathering or oxidation were inferred to be newly broken fragments of older material. The grains are visually categorized into two general groups: black grains and brown grains. Brown grains are pumiceous, vesicular and glassy, or dense and glassy. All brown grains have sharp edges and lack signs of oxidation or weathering. Black grains are dense lava fragments, poorly vesicular scoria, or dense cauliflower-shaped pyroclasts. Many black grains show rounded edges and exhibit signs of weathering and oxidation. These factors were used to determine that black grains are non-juvenile lithic fragments and brown grains are 2008 juvenile material.

### **Plagioclase-rich lava fragments**

The most abundant lithic grain type is dense plagioclase-rich lava (Fig. 6.1A). Plagioclase-rich lava grains are typically around 20% plagioclase crystals 120-250  $\mu\text{m}$  in diameter in a dark grey opaque groundmass. Pyroxene is present as a rare phenocryst with diameters similar to plagioclase crystals. The lava fragments are typically equant, show no vesicularity, and have sharp irregular edges indicating brittle breakage. I infer that these fragments are sourced from lava flows making up the Cone D bench that were broken up and entrained in eruption columns during vent openings in the 2008 eruption. The area west of Cone D, where 2008 vents opened, is underlain by plagioclase-rich lava flows (J. Larsen, personal communication, 2010, Byers 1959).

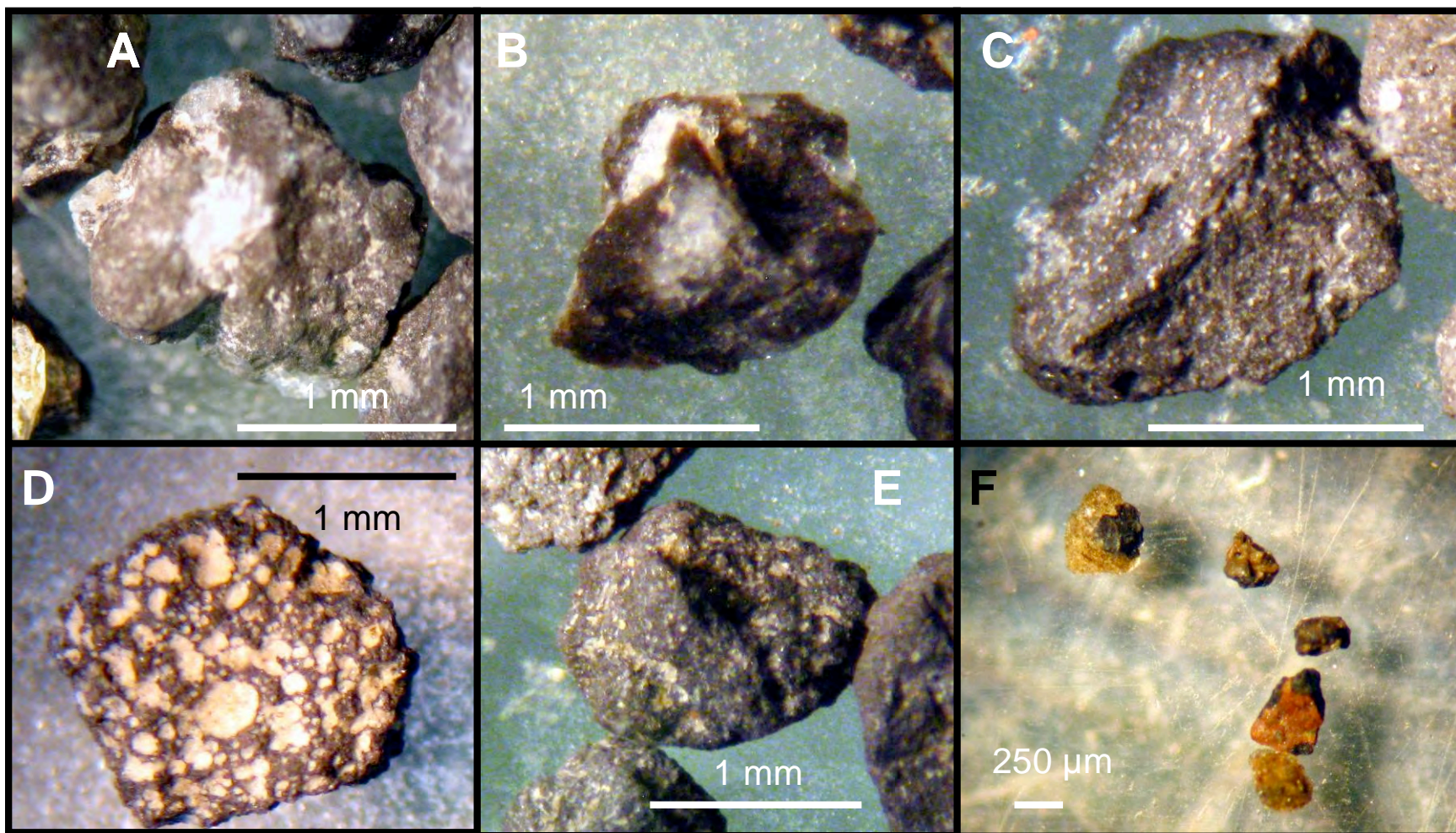


**Figure 6.1:** Lithic grain componentry category examples. **A:** Plagioclase-rich lava **B:** Dark plagioclase-rich lava **C:** Other lava  
**D:** Black scoria **E:** Cauliflower-shaped dense black pyroclasts **F:** Assorted other lithic grains

### **Dark plagioclase-rich lava fragments**

A population of dark plagioclase-rich lava fragments is less abundant, but present in many samples (Fig. 6.1B). Dark plagioclase-rich lava fragments are similar in shape and appearance to the more abundant plagioclase-rich lava fragments, but the groundmass is black, glossy, and rarely translucent. These dark plagioclase-rich lava fragments also appear to have been broken in a brittle fashion and are probably sourced from lava flows on the Cone D bench.

### **Other lava fragments**

Several other types of lava fragments are present in 2008 ash deposits but are rare and have been counted in a combined category. Lava fragment types include light gray lava fragments with pyroxene crystals and aphyric black lava (Fig. 6.1C). Some lava fragments are vesicular, and the distinction between vesicular lava fragments and black scoria clasts was based on the appearance of grain surfaces and edges. Grains that appeared to have been broken in a brittle manner were counted as lava fragments, while grains with rounded edges and scoria-clast shapes were counted as black scoria or cauliflower-shaped black pyroclasts. Pre-2008 phreatomagmatic fragments could be dense and have blocky shapes and may have been misidentified as lava fragments based on shape and vesicularity.

### **Black scoria clasts**

Scoria clasts from previous eruptions are also abundant in 2008 deposits (Fig 6.1D). These were distinguished from 2008 juvenile material by their rounded edges,

weathered surfaces, and opacity. Grains with ‘complete’ non-broken shapes and visible vesicularity were counted as black scoria and were commonly equant and subround.

Byers (1959) describes marshy alluvial sediments north of Cone D that may be the source of these older scoria clasts.

### **Cauliflower-shaped dense black pyroclasts**

Black opaque pyroclasts without visible vesicularity and with ‘complete’ non-broken shapes typically have cauliflower-textured exteriors (Fig. 6.1E) and were counted as dense black pyroclasts. These clasts are typically slightly rounded and weathered.

### **Other lithic grains**

Several other types of lithic grains are rare in samples and were counted in a combined category (Fig 6.1F, Fig 6.2F). These grain types included orange oxidized scoria clasts and other altered and weathered rock fragments.

### **6.1b Juvenile grains**

Juvenile material produced in the 2008 eruption is primarily brown vesicular glass. Vesicularity ranges from frothy pumice to nearly dense poorly vesicular clasts.

#### **Blocky poorly vesicular brown glass**

One of the three primary juvenile clast types present in 2008 deposits is blocky, dense, poorly vesicular brown glass (Fig. 6.2A). Grains of brown glass that are poorly vesicular and show edges controlled by brittle fracture were included in this category,

whereas grains with expanded vesicle exteriors were counted as vesicular brown glass. Blocky brown glass grains typically have sharp edges, curvilinear faces, and vesicles cut by the fractured surfaces. These grains are commonly translucent in the 2-phi size and nearly opaque in the -0.5 phi size. Dark-colored dense juvenile clasts are found in the coarse lapilli sizes, especially in proximal locations, and may be larger examples of this ash component.

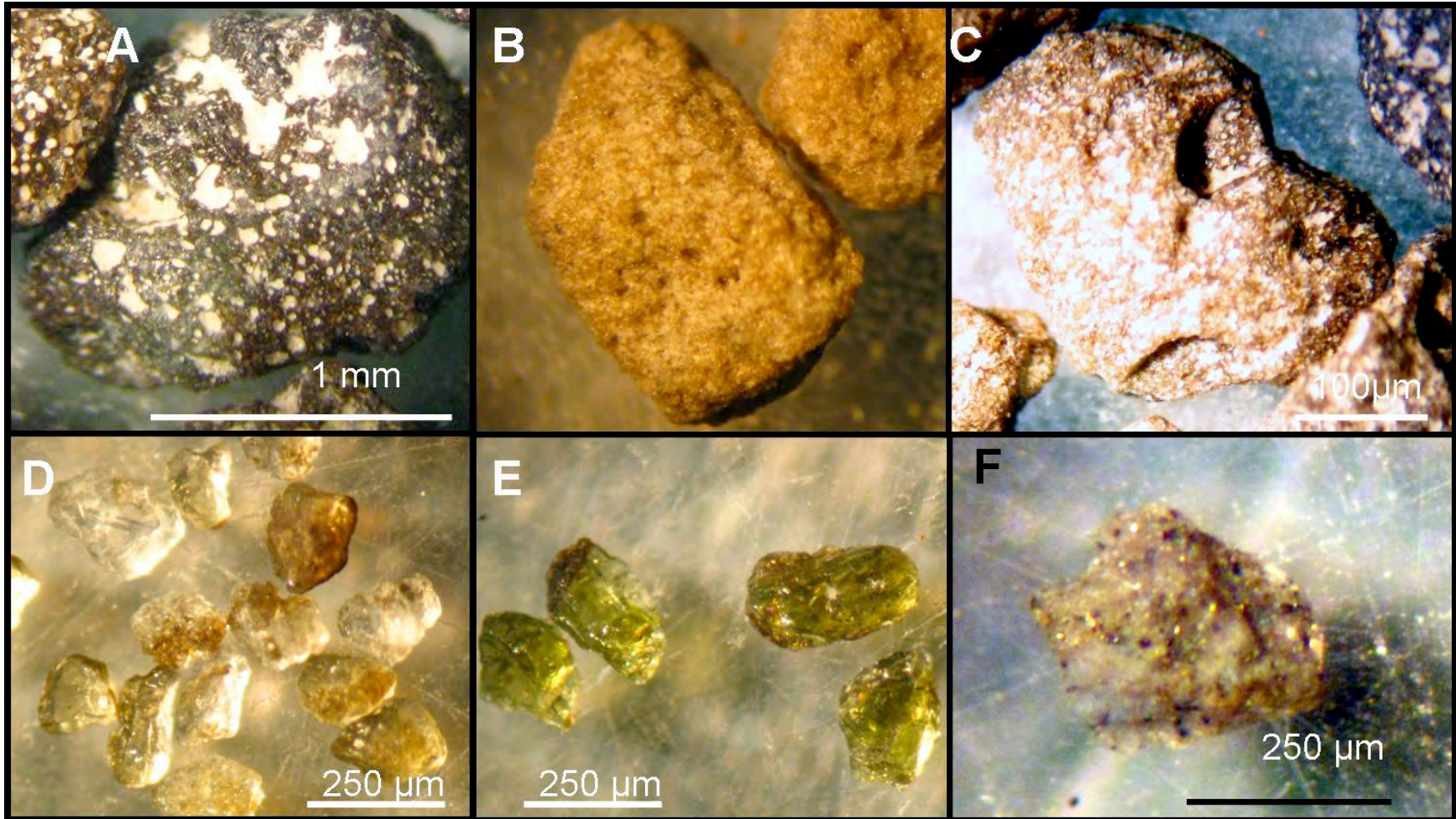


**Figure 6.2:** Juvenile grain and free crystal componentry category examples. **A:** Blocky dense glass **B:** Brown pumice **C:** Brown vesicular glass **D:** Free plagioclase **E:** Free olivine **F:** Clear lithic with dark grains

### **Brown pumice**

The third juvenile clast type present in 2008 deposits is brown pumice (Fig 6.2B). These clasts are distinguished from brown vesicular glass by their smaller vesicle size and much higher fraction of vesicles. Many of these pumice clasts are buoyant in water and are thus easily separated by immersing samples during component separation.

### **Brown vesicular glass**

Another common juvenile grain type is brown vesicular glass (Fig 6.2C). These clasts are predominantly brown glass with abundant vesicles, with small textural vesicles and larger vesicles defining grain shapes. Vesicle shapes range from spherical to elongate and ribbon like, but most are slightly elongated ellipsoids.

### **6.1c Free crystals**

Free crystals are present in all samples, but among the size fractions examined, only the 2-phi samples contain free crystals. Larger size fractions are devoid of free crystals. Crystals are commonly present as phenocrysts or microlites in other glass clasts, but were counted as free crystals only if a single crystal made up more than two thirds of the volume of the entire grain. Thus, the size range of the crystals controls the sample size fraction in which the free crystals can be found.

### **Plagioclase crystals**

Plagioclase is the most abundant free crystal type in 2008 deposits. The shape of plagioclase crystals varies from rounded and equant to sharp cleavage-defined forms

(Fig. 6.2D). Free plagioclase crystals in 2008 deposits may be juvenile 2008 crystals, free crystals entrained from alluvial sediments, or crystals broken out of plagioclase-rich lava.

### **Olivine crystals**

Free olivine crystals are typically less abundant than plagioclase crystals in 2008 deposits, but are present in nearly every 2-phi sample. Olivine crystals are bright green and translucent (Fig. 6.2E). Crystal shapes range from broken fragments with sharp edges and conchoidal fractures to rounded grains. Olivine crystals are found within larger (cm-sized) 2008 juvenile scoria clasts, so many of these free olivine crystals may be phenocrysts from juvenile 2008 material.

### **6.2 Error bound calculation**

Four samples of 2-phi ash were counted for 10JAUOK011A. Each time a unique set of 200-300 grains was scooped from the sieved sample and analyzed to calculate total error in the componentry analysis. The first analysis of 10JAUOK011A was one of the first samples analyzed and identification of categories improved rapidly within the first 3 samples analyzed, so the first analysis of 10JAUOK011A is thrown out, and error bounds were calculated with the last three samples run.

	Count 1	Count 2	Count 3	Count 4	Average	SD
<b>Lithic</b>	33.5%	33.8%	36.8%	34.1%	34.9%	1.7%
<b>Juvenile</b>	57.4%	55.2%	51.9%	54.8%	54.0%	1.8%
<b>Crystal</b>	9.1%	11.0%	11.3%	11.1%	11.1%	0.2%
<b>Plag-rich</b>	21.7%	26.7%	22.2%	21.1%	23.3%	2.9%
<b>Dark plag-rich lava</b>	0.0%	0.0%	0.0%	0.0%	0.0%	0.0%
<b>Other lava</b>	7.0%	2.4%	6.6%	3.0%	4.0%	2.3%
<b>Black Scoria</b>	3.9%	1.0%	1.4%	3.3%	1.9%	1.3%
<b>Dense Pyroclast</b>	0.0%	1.9%	5.2%	6.3%	4.5%	2.3%
<b>Other lithic types</b>	0.9%	1.9%	1.4%	0.4%	1.2%	0.8%
<b>Brown Vesicular</b>	22.6%	30.5%	31.1%	28.9%	30.2%	1.2%
<b>Brown dense</b>	6.1%	14.8%	17.0%	19.3%	17.0%	2.2%
<b>Brown pumice</b>	28.7%	10.0%	3.8%	6.7%	6.8%	3.1%
<b>Plagioclase</b>	5.7%	9.5%	9.9%	8.5%	9.3%	0.7%
<b>Olivine</b>	3.5%	1.4%	1.4%	2.6%	1.8%	0.7%
<b>Total</b>	100.0%	100.0%	100.0%	100.0%		

**Table 6.1:** Error bound calculation from repeat analysis of sample 10JAUOK011A.

Statistics calculated from repeat grain counts of sample 10JAUOK011A give standard deviations at or below 3% for each category and below 2% for the major categories (greater than 10% of the sample) of lithic grains, juvenile grains, and free crystals.

### **6.3 Componentry results by location: on-axis sites**

Samples taken from five or six individual units each at four on-axis locations for basal fall units were examined; 10JAUOK011, 10JAUOK002, 10JAUOK006, and 10JAUOK023 (Fig. 6.3).

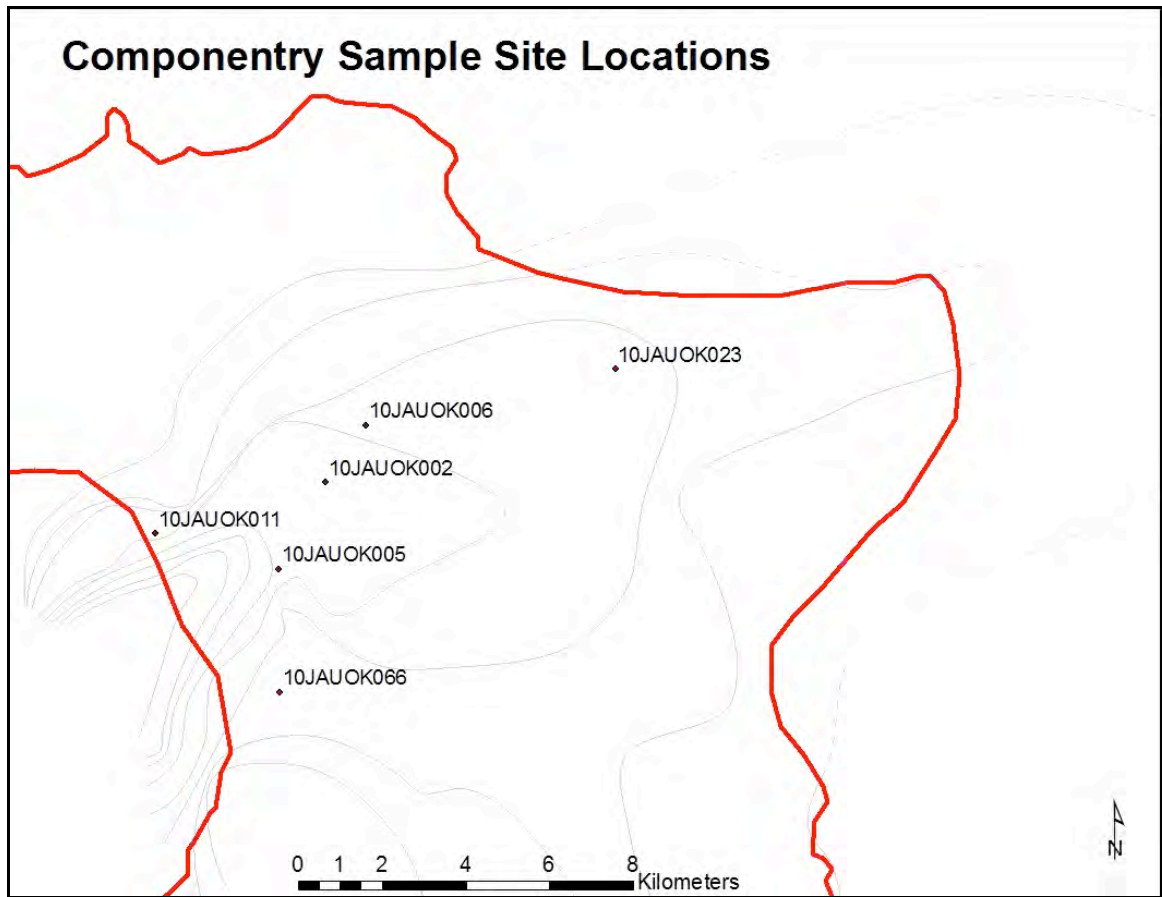


**Figure 6.3:** Componentry sample site locations with basal isopachs.

### **Sample 10JAUOK011**

Sample 10JAUOK011 was collected high on the east caldera flanks near the axis of deposition for basal units (Fig. 6.3). Componentry counts were performed for six samples from this site, as marked on Figure 6.4.

# 10JAUOK011

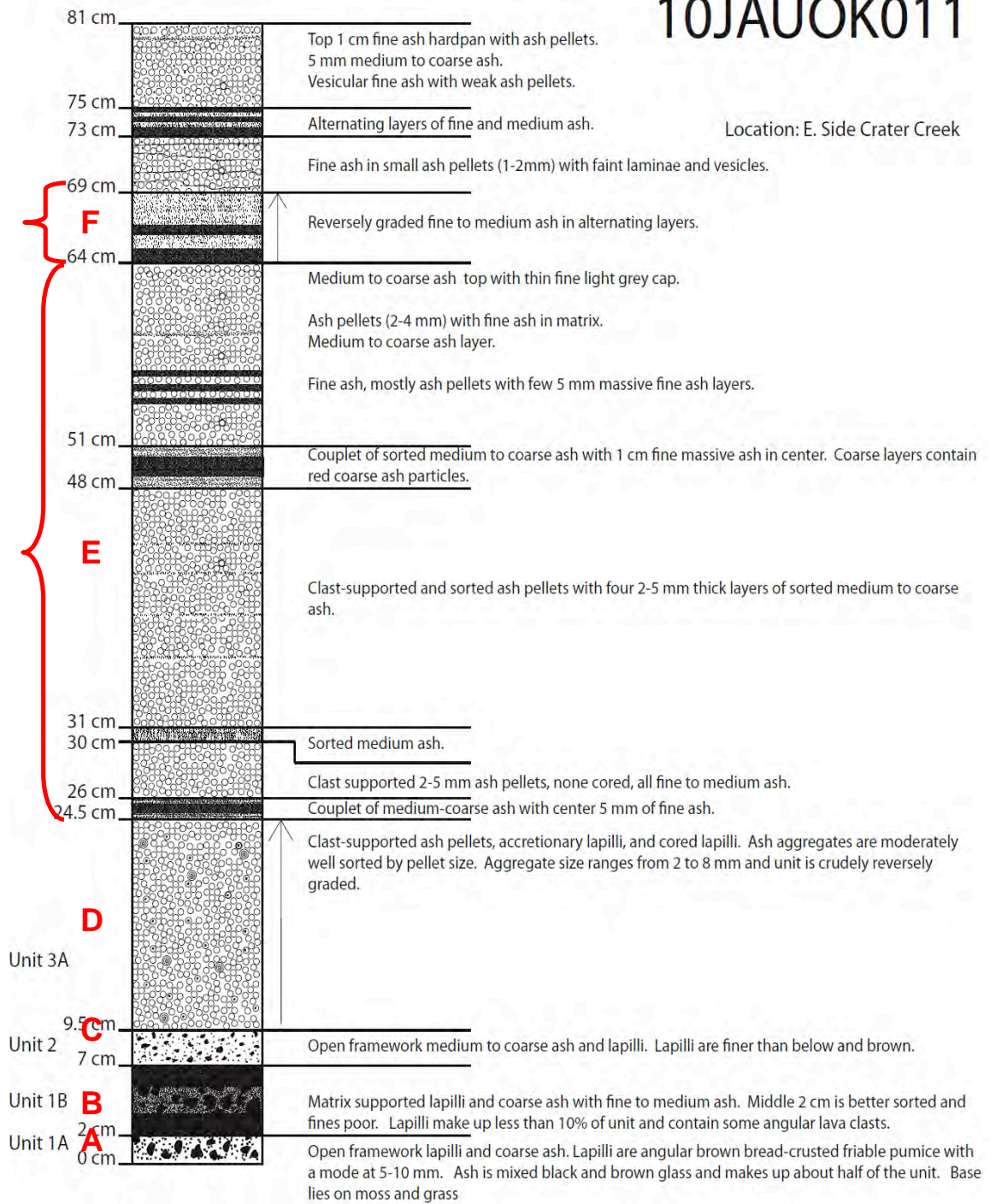


**Figure 6.4:** Stratigraphic section for 10JAUOK011 with samples analyzed for componentry shown in red.

## Sample 10JAUOK002

Sample 10JAUOK002 was collected on the middle caldera flanks 4 km from the caldera rim. Six samples were analyzed from this site as shown on Figure 6.5.

# 10JAUOK002

Location: E. Side Crater Creek

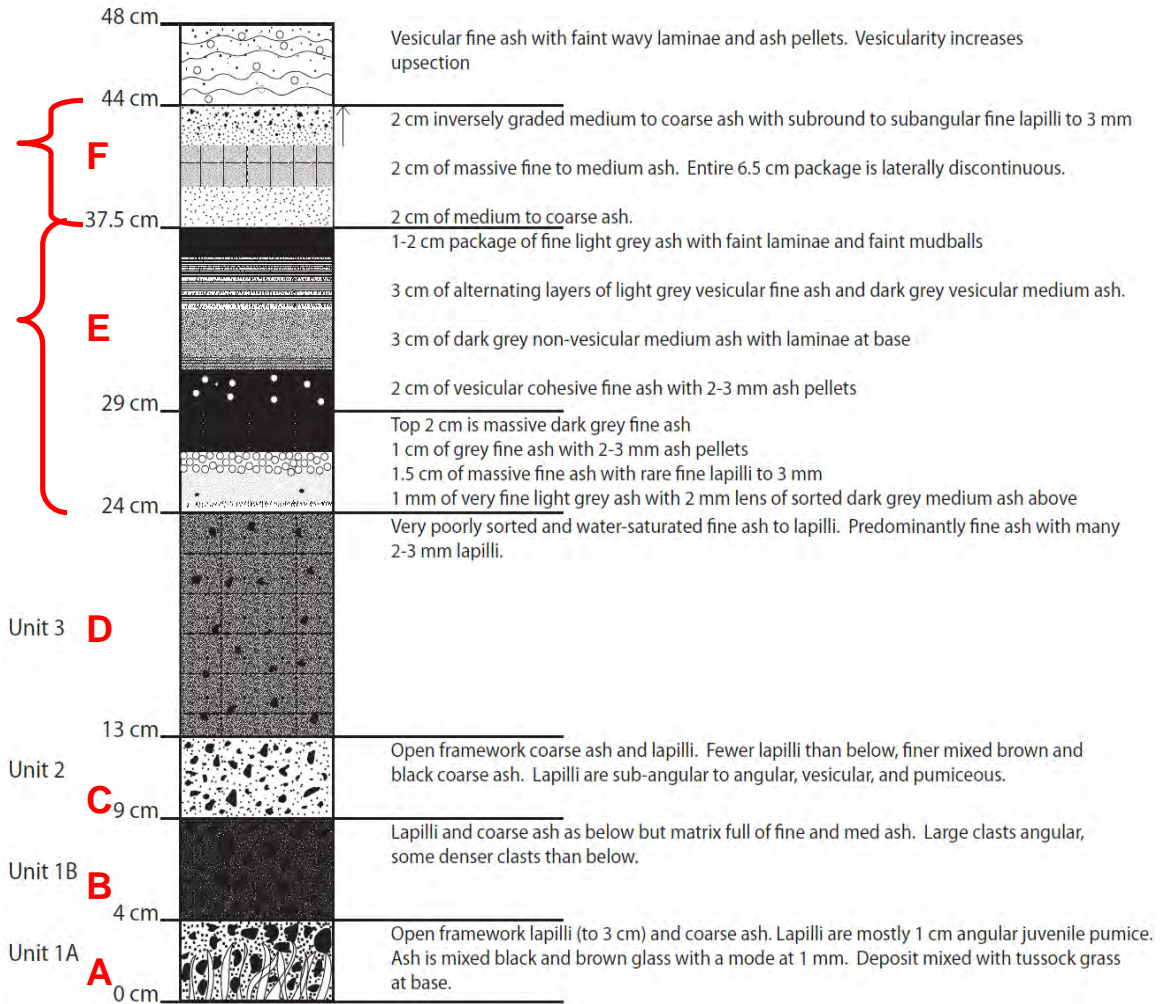


**Figure 6.5:** Stratigraphic section for 10JAUOK002 with analyzed samples in red.

## Sample 10JAUOK006

Sample 10JAUOK006 was collected on-axis 6 km from the caldera rim and five units were analyzed for componentry as shown in Figure 6.6.

# 10JAUOK006

Location: E. Side Crater Creek

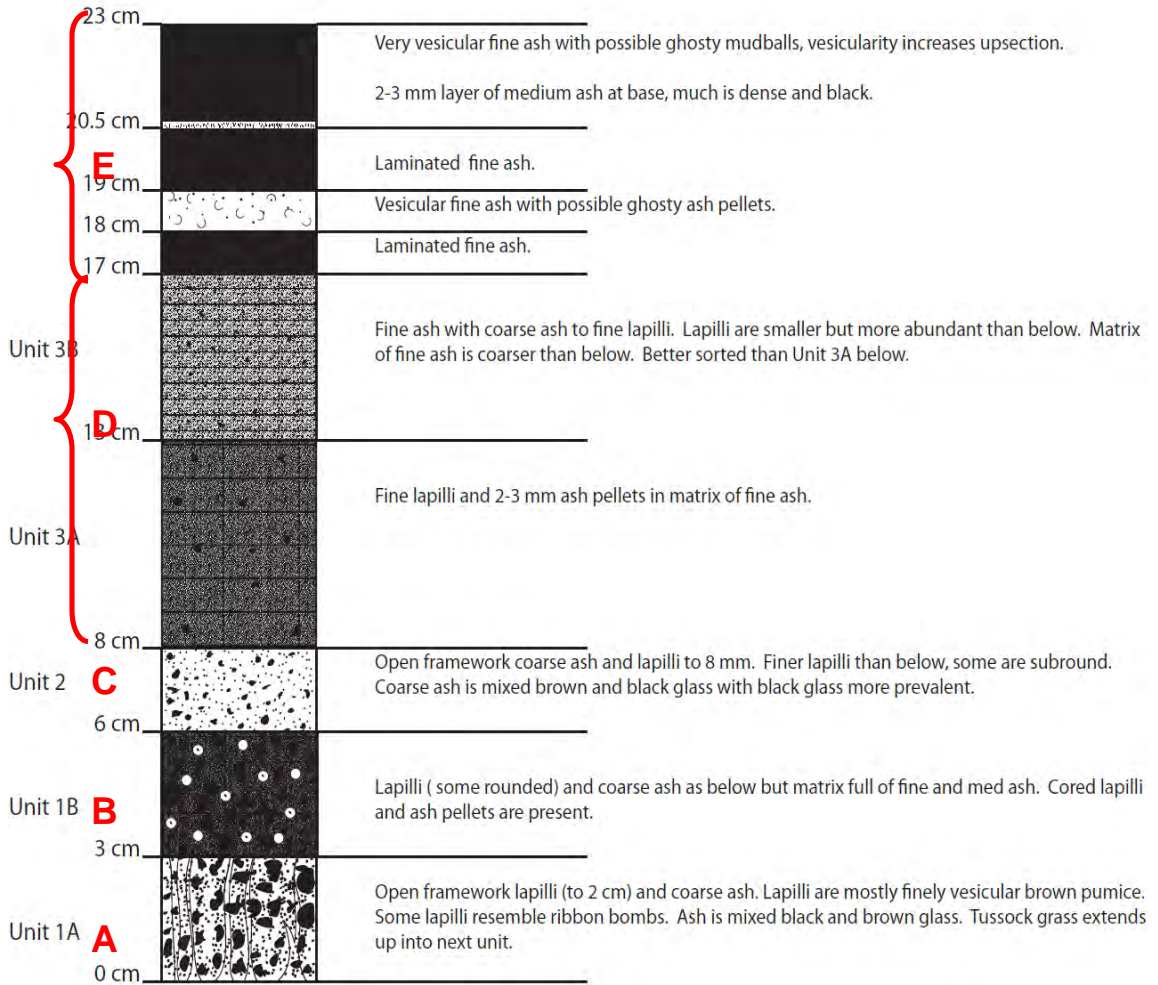


**Figure 6.6:** Stratigraphic section for 10JAUOK006 with analyzed units shown in red.

## Sample 10JAUOK023

The most distal on-axis site analyzed for componentry was 10JAUOK023, an on-axis site 11 km from the caldera rim. Six units were analyzed at this site as shown in Figure 6.7.

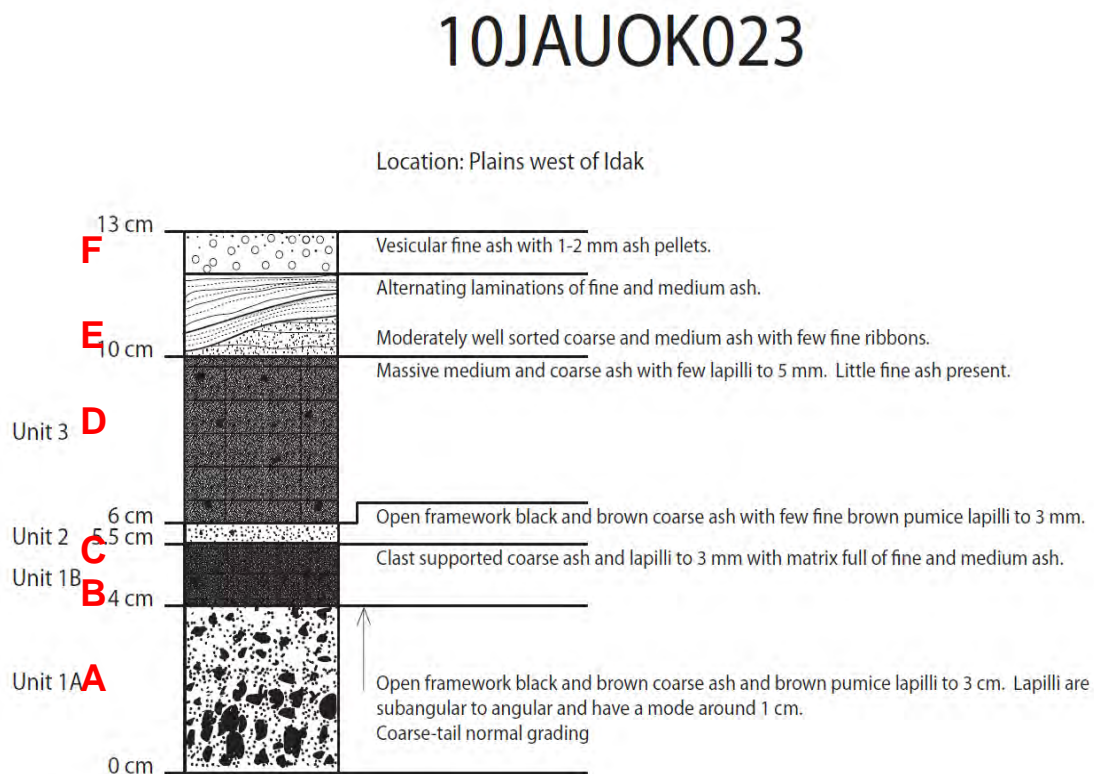


**Figure 6.7:** Stratigraphic section for 10JAUOK023 with analyzed units shown in red.

### On-axis componentry results by unit:

Units 1A, 1B, 2, 3, and some upper units were examined from these four sites and results are displayed below grouped by unit (Tables 6.2-6.6). Grain-size distributions of all analyzed samples are also presented by unit (Figs. 6.8-6.12)

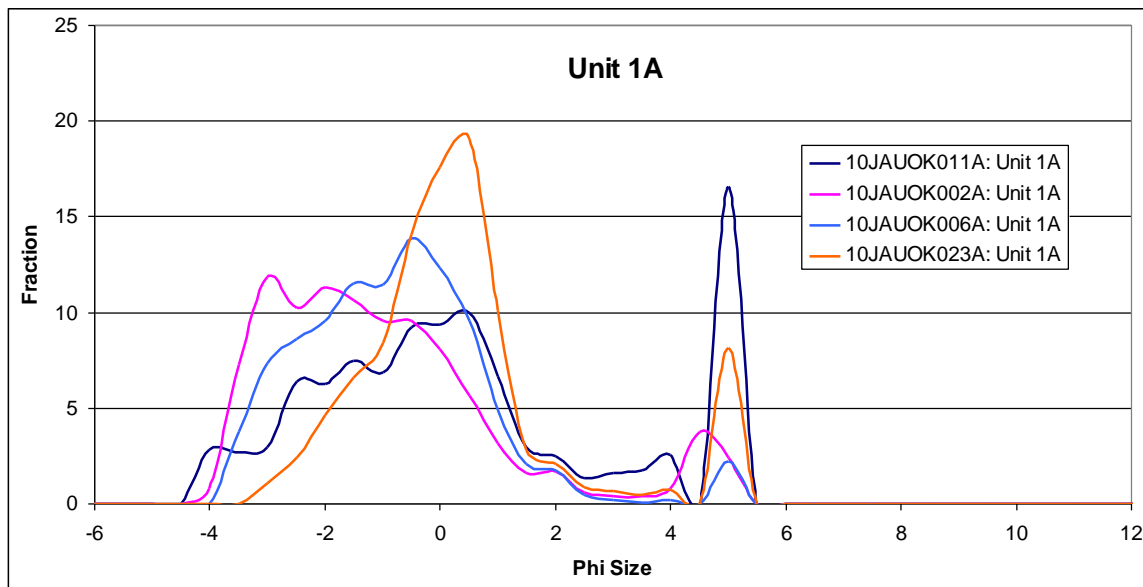


**Figure 6.8:** Grain-size distribution of Unit 1A samples

	2 phi					-0.5 phi				
	011A	002A	006A	023A	Average	011A	002A	006A	023A	Average
<b>Lithic</b>	33.8%	32.5%	32.7%	37.3%	<b>34.1%</b>	27.1%	48.0%	47.0%	24.7%	<b>36.7%</b>
<b>Juvenile</b>	55.2%	54.0%	53.8%	48.7%	<b>52.9%</b>	72.5%	52.0%	53.0%	75.3%	<b>63.2%</b>
<b>Crystal</b>	11.0%	13.5%	13.6%	14.0%	<b>13.0%</b>	0.5%	0.0%	0.0%	0.0%	<b>0.1%</b>
<b>Plag-rich</b>	26.7%	23.0%	22.1%	23.2%	<b>23.8%</b>	13.0%	32.9%	34.6%	12.9%	<b>23.4%</b>
<b>Dark plag-rich</b>	0.0%	0.0%	0.0%	0.0%	<b>0.0%</b>	2.4%	3.6%	2.8%	0.4%	<b>2.3%</b>
<b>Other lava</b>	2.4%	3.5%	1.0%	4.4%	<b>2.8%</b>	2.4%	0.9%	0.0%	2.3%	<b>1.4%</b>
<b>Black Scoria</b>	1.0%	2.0%	4.0%	3.0%	<b>2.5%</b>	1.9%	3.6%	2.3%	2.3%	<b>2.5%</b>
<b>Cauliflower</b>										
<b>Dense</b>	1.9%	1.0%	2.5%	4.8%	<b>2.6%</b>	5.3%	6.2%	3.7%	5.7%	<b>5.2%</b>
<b>Other lithic grains</b>	1.9%	3.0%	3.0%	1.8%	<b>2.4%</b>	1.9%	0.4%	2.3%	1.1%	<b>1.5%</b>
<b>Brown vesicular</b>	30.5%	27.5%	28.1%	26.6%	<b>28.2%</b>	40.1%	29.8%	27.2%	41.4%	<b>34.6%</b>
<b>Brown dense</b>	14.8%	19.5%	18.6%	19.2%	<b>18.0%</b>	15.9%	11.6%	8.8%	8.0%	<b>11.1%</b>
<b>Brown pumice</b>	10.0%	7.0%	7.0%	3.0%	<b>6.7%</b>	16.4%	10.7%	17.1%	25.9%	<b>17.5%</b>
<b>Plagioclase</b>	9.5%	10.5%	12.6%	10.3%	<b>10.7%</b>	0.0%	0.0%	0.0%	0.0%	<b>0.0%</b>
<b>Olivine</b>	1.4%	3.0%	1.0%	3.7%	<b>2.3%</b>	0.5%	0.0%	0.0%	0.0%	<b>0.1%</b>

**Table 6.2:** 2-phi and -0.5-phi componentry results for Unit 1A at on-axis sites

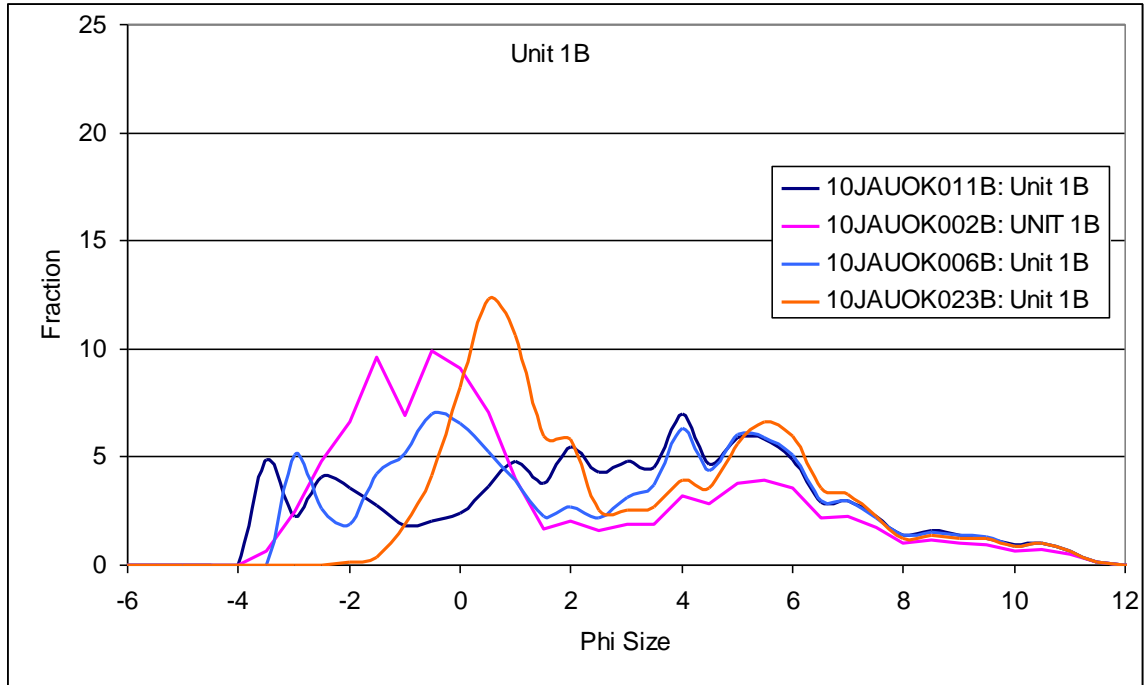


**Figure 6.9:** Grain-size distribution of Unit 1B samples

	2 phi					-0.5 phi				
	011B	002B	006B	023B	Average	011B	002B	006B	023B	Average
<b>Lithic</b>	27.5%	33.1%	27.3%	39.3%	<b>31.8%</b>	45.0%	51.3%	47.0%	20.4%	<b>40.9%</b>
<b>Juvenile</b>	64.5%	55.2%	62.9%	48.0%	<b>57.6%</b>	55.0%	48.7%	53.0%	79.6%	<b>59.1%</b>
<b>Crystal</b>	8.1%	11.7%	9.8%	12.7%	<b>10.6%</b>	0.0%	0.0%	0.0%	0.0%	<b>0.0%</b>
<b>Plag-rich</b>	6.2%	13.8%	17.1%	18.0%	<b>13.8%</b>	9.7%	23.0%	34.6%	9.5%	<b>19.2%</b>
<b>Dark plag-rich</b>	0.0%	0.0%	0.0%	0.0%	<b>0.0%</b>	1.9%	1.9%	2.8%	0.0%	<b>1.6%</b>
<b>Other lava</b>	5.7%	10.9%	2.9%	11.5%	<b>7.7%</b>	13.4%	7.3%	0.0%	3.5%	<b>6.0%</b>
<b>Black Scoria</b>	6.2%	2.1%	2.9%	5.3%	<b>4.1%</b>	4.5%	4.2%	2.3%	2.5%	<b>3.4%</b>
<b>Cauliflower Dense</b>	8.5%	2.5%	4.0%	2.5%	<b>4.4%</b>	13.4%	11.9%	3.7%	5.0%	<b>8.5%</b>
<b>Other lithic grains</b>	0.9%	2.9%	0.4%	2.0%	<b>1.6%</b>	1.5%	2.3%	2.3%	0.0%	<b>1.5%</b>
<b>Brown vesicular</b>	29.4%	32.6%	44.0%	27.0%	<b>33.3%</b>	28.6%	31.0%	27.2%	43.3%	<b>32.5%</b>
<b>Brown dense</b>	15.2%	17.2%	13.8%	16.8%	<b>15.7%</b>	7.4%	6.1%	8.8%	8.0%	<b>7.6%</b>
<b>Brown pumice</b>	19.9%	5.4%	5.1%	4.1%	<b>8.6%</b>	19.0%	11.5%	17.1%	28.4%	<b>19.0%</b>
<b>Plagioclase</b>	4.7%	8.4%	8.4%	9.8%	<b>7.8%</b>	0.0%	0.0%	0.0%	0.0%	<b>0.0%</b>
<b>Olivine</b>	3.3%	3.3%	1.5%	2.9%	<b>2.7%</b>	0.0%	0.0%	0.0%	0.0%	<b>0.0%</b>

**Table 6.3:** 2-phi and -0.5-phi componentry results for Unit 1B at on-axis sites.

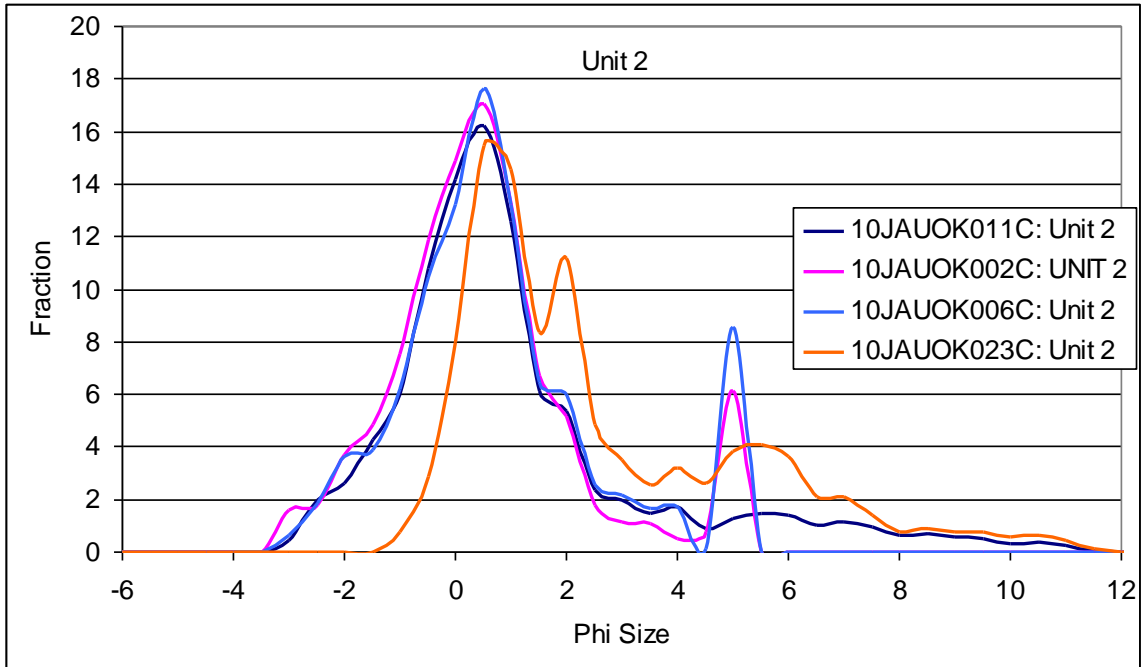


**Figure 6.10:** Grain-size distribution of Unit 2 samples

	2 phi					-0.5 phi				
	011C	002C	006C	023C	Average	011C	002C	006C	023C	Average
<b>Lithic</b>	27.0%	26.3%	40.0%	30.1%	<b>30.8%</b>	40.5%	25.9%	41.3%	21.8%	<b>32.4%</b>
<b>Juvenile</b>	63.5%	52.6%	42.7%	55.0%	<b>53.4%</b>	59.5%	74.1%	58.7%	78.2%	<b>67.6%</b>
<b>Crystal</b>	9.5%	21.1%	17.3%	14.9%	<b>15.7%</b>	0.0%	0.0%	0.0%	0.0%	<b>0.0%</b>
<b>Plag-rich</b>	9.5%	11.3%	23.8%	16.3%	<b>15.2%</b>	18.0%	18.9%	18.3%	1.4%	<b>14.1%</b>
<b>Dark plag-rich</b>	0.0%	0.0%	0.0%	0.0%	<b>0.0%</b>	2.0%	1.8%	1.3%	0.0%	<b>1.3%</b>
<b>Other lava</b>	7.0%	4.1%	7.7%	5.2%	<b>6.0%</b>	3.5%	2.2%	3.5%	5.1%	<b>3.6%</b>
<b>Black Scoria</b>	7.0%	2.1%	3.5%	1.7%	<b>3.6%</b>	5.5%	1.3%	7.0%	2.8%	<b>4.1%</b>
<b>Cauliflower Dense</b>	1.5%	4.6%	2.3%	5.5%	<b>3.5%</b>	8.5%	0.9%	10.9%	9.3%	<b>7.4%</b>
<b>Other lithic grains</b>	1.5%	4.1%	2.7%	1.4%	<b>2.4%</b>	3.0%	0.9%	0.4%	0.9%	<b>1.3%</b>
<b>Brown vesicular</b>	34.0%	28.9%	21.9%	34.6%	<b>29.8%</b>	28.0%	49.1%	33.9%	44.9%	<b>39.0%</b>
<b>Brown dense</b>	21.0%	20.6%	20.8%	20.1%	<b>20.6%</b>	27.0%	18.4%	10.9%	11.6%	<b>17.0%</b>
<b>Brown pumice</b>	8.5%	3.1%	0.0%	0.3%	<b>3.0%</b>	4.5%	6.6%	13.9%	21.8%	<b>11.7%</b>
<b>Plagioclase</b>	6.5%	18.0%	14.6%	12.1%	<b>12.8%</b>	0.0%	0.0%	0.0%	0.0%	<b>0.0%</b>
<b>Olivine</b>	3.0%	3.1%	2.7%	2.8%	<b>2.9%</b>	0.0%	0.0%	0.0%	0.0%	<b>0.0%</b>

**Table 6.4:** 2-phi and -0.5-phi componentry results for Unit 2 at on-axis sites.

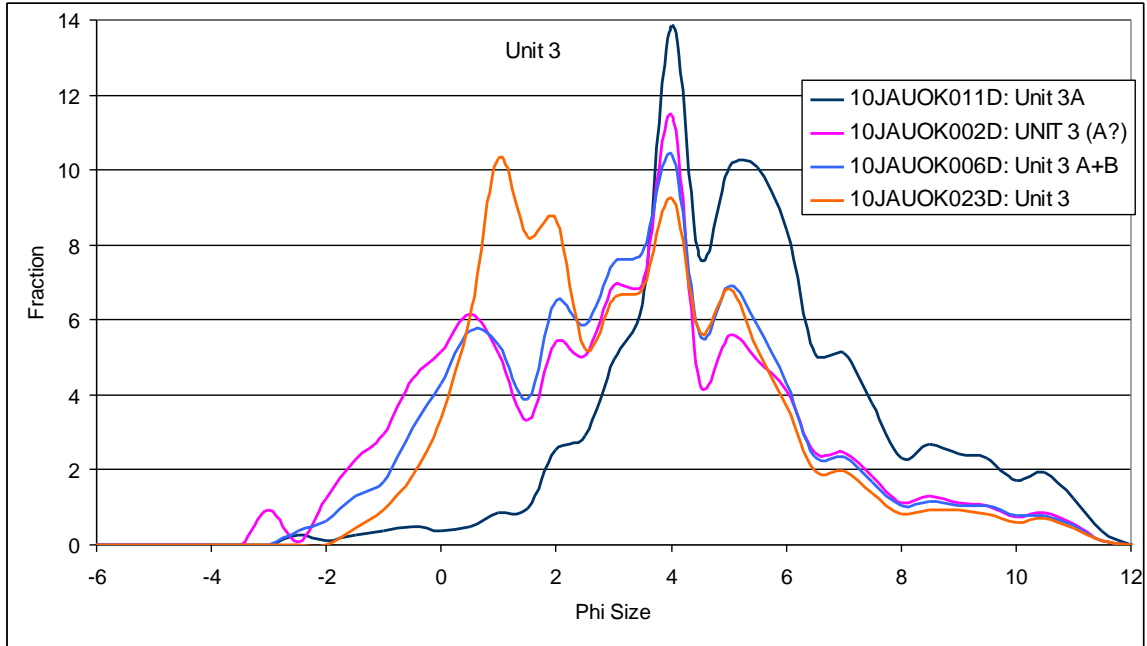
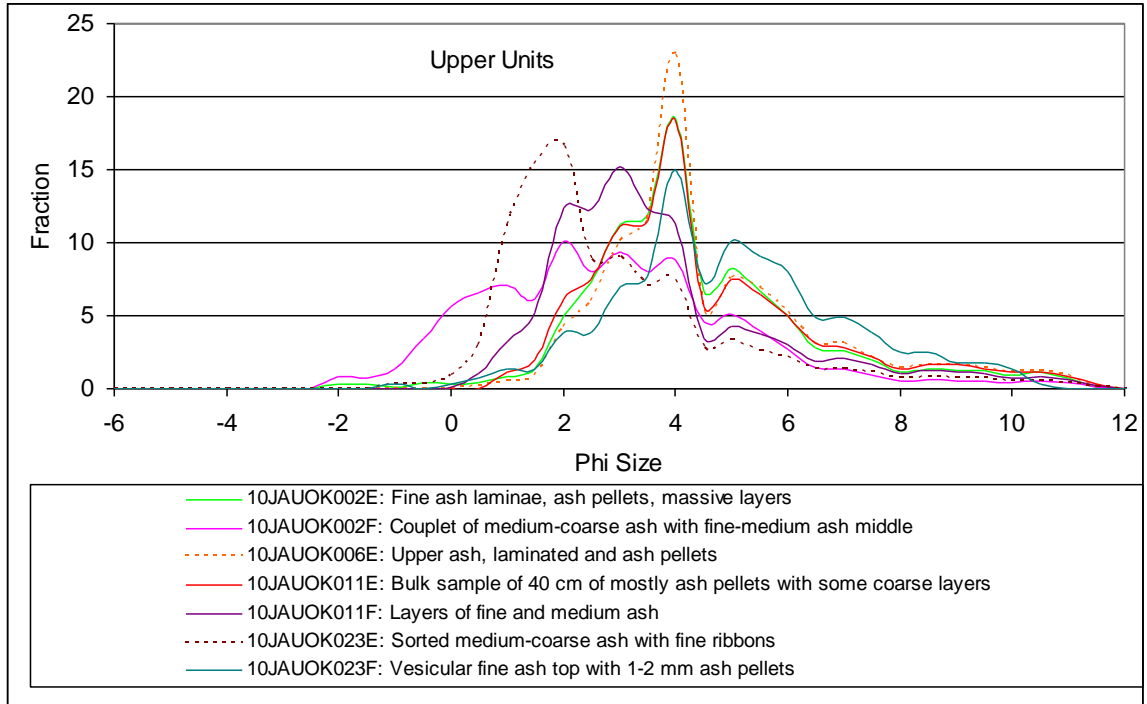


Figure 6.11: Grain-size distribution of Unit 3 samples

	2 phi					-0.5 phi				
	011D	002D	006D	023D	Average	011D	002D	006D	023D	Average
<b>Lithic</b>	28.2%	35.5%	33.8%	30.2%	<b>31.9%</b>	34.4%	38.3%	36.4%	24.9%	<b>33.5%</b>
<b>Juvenile</b>	59.2%	56.1%	57.3%	57.1%	<b>57.4%</b>	65.6%	61.7%	63.6%	75.1%	<b>66.5%</b>
<b>Crystal</b>	12.6%	8.4%	8.9%	12.7%	<b>10.6%</b>	0.0%	0.0%	0.0%	0.0%	<b>0.0%</b>
<b>Plag-rich</b>	12.1%	15.7%	13.1%	15.1%	<b>14.0%</b>	16.4%	16.5%	13.0%	7.7%	<b>13.4%</b>
<b>Dark plag-rich</b>	0.0%	0.0%	0.0%	0.0%	<b>0.0%</b>	0.0%	2.5%	1.3%	1.0%	<b>1.2%</b>
<b>Other lava</b>	7.3%	8.4%	9.4%	4.4%	<b>7.4%</b>	3.3%	6.2%	4.3%	3.8%	<b>4.4%</b>
<b>Black Scoria</b>	1.9%	6.3%	3.8%	2.9%	<b>3.7%</b>	9.8%	6.2%	5.6%	4.3%	<b>6.5%</b>
<b>Cauliflower Dense</b>	4.4%	2.4%	4.2%	5.4%	<b>4.1%</b>	4.9%	6.2%	10.0%	4.8%	<b>6.5%</b>
<b>Other lithic grains</b>	2.4%	2.8%	3.3%	2.4%	<b>2.7%</b>	0.0%	0.8%	0.0%	1.0%	<b>0.4%</b>
<b>Brown vesicular</b>	34.0%	38.7%	34.3%	28.3%	<b>33.8%</b>	37.7%	38.7%	41.1%	39.2%	<b>39.2%</b>
<b>Brown dense</b>	23.8%	15.7%	19.7%	22.4%	<b>20.4%</b>	21.3%	13.2%	16.0%	14.8%	<b>16.3%</b>
<b>Brown pumice</b>	1.5%	1.7%	3.3%	6.3%	<b>3.2%</b>	6.6%	9.9%	6.5%	21.1%	<b>11.0%</b>
<b>Plagioclase</b>	9.2%	7.0%	6.6%	10.7%	<b>8.4%</b>	0.0%	0.0%	0.0%	0.0%	<b>0.0%</b>
<b>Olivine</b>	3.4%	1.4%	2.3%	2.0%	<b>2.3%</b>	0.0%	0.0%	0.0%	0.0%	<b>0.0%</b>

Table 6.5: 2-phi and -0.5-phi componentry results for Unit 3 at on-axis sites.



**Figure 6.12:** Grain-size distribution of upper unit samples

	2 phi							-0.5 phi			
	011E	011F	002E	002F	006E	023E	023F	Average	002F	023E	Average
<b>Lithic</b>	21.5%	28.0%	31.0%	28.3%	32.8%	29.7%	32.0%	<b>29.0%</b>	81.5%	14.1%	<b>47.8%</b>
<b>Juvenile</b>	74.6%	61.0%	60.9%	59.1%	58.9%	62.9%	60.3%	<b>62.5%</b>	18.5%	85.9%	<b>52.2%</b>
<b>Crystal</b>	3.9%	11.0%	8.1%	12.6%	8.3%	7.4%	7.8%	<b>8.4%</b>	0.0%	0.0%	<b>0.0%</b>
<b>Plag-rich</b>	12.7%	12.6%	13.7%	16.2%	17.4%	12.4%	11.4%	<b>13.8%</b>	57.5%	3.1%	<b>30.3%</b>
<b>Dark plag-rich</b>	0.0%	0.0%	0.0%	0.0%	0.0%	0.0%	0.0%	<b>0.0%</b>	7.5%	0.0%	<b>3.8%</b>
<b>Other lava</b>	0.0%	4.1%	9.6%	4.5%	5.5%	5.9%	12.8%	<b>6.1%</b>	5.0%	3.1%	<b>4.1%</b>
<b>Black Scoria</b>	5.9%	3.3%	3.7%	2.5%	4.7%	6.9%	3.7%	<b>4.4%</b>	5.5%	4.7%	<b>5.1%</b>
<b>Cauliflower Dense</b>	1.5%	4.9%	1.8%	2.5%	1.6%	3.5%	2.3%	<b>2.6%</b>	4.0%	3.1%	<b>3.6%</b>
<b>Other lithic grains</b>	6.3%	3.3%	2.2%	2.5%	3.6%	1.0%	1.8%	<b>3.0%</b>	2.0%	0.0%	<b>1.0%</b>
<b>Brown vesicular</b>	32.2%	32.5%	23.6%	28.8%	26.9%	28.7%	32.9%	<b>29.4%</b>	8.5%	31.3%	<b>19.9%</b>
<b>Brown dense</b>	41.0%	28.5%	36.5%	30.3%	31.6%	31.7%	24.7%	<b>32.0%</b>	7.5%	12.5%	<b>10.0%</b>
<b>Brown pumice</b>	1.5%	0.0%	0.7%	0.0%	0.4%	2.5%	2.7%	<b>1.1%</b>	2.5%	42.2%	<b>22.3%</b>
<b>Plagioclase</b>	2.9%	10.2%	7.0%	10.1%	7.5%	7.4%	6.8%	<b>7.4%</b>	0.0%	0.0%	<b>0.0%</b>
<b>Olivine</b>	1.0%	0.8%	1.1%	2.5%	0.8%	0.0%	0.9%	<b>1.0%</b>	0.0%	0.0%	<b>0.0%</b>

**Table 6.6:** 2-phi and -0.5-phi componentry results for upper fine units at on-axis sites.

### On-axis componentry trends

Several trends are visible in the 2-phi and -0.5-phi data from these four sites. Samples of each individual unit were averaged and those averages compared to examine changes by unit. Three notable trends are visible in the 2-phi results by unit (Fig. 6.13). Plagioclase-rich lava makes up about 24% of grains in Unit 1A whereas it makes up 13-16% in other units. The abundance of plagioclase-rich lava may indicate a vent-opening eruption phase. Vents on the west side of Cone D overlie a bench of plagioclase-rich lava, and new vents opening likely fragmented part of this lava bench and carried clasts into the plume. The units deposited later have lower concentrations of plagioclase-rich lava because vents were largely established and juvenile material could pass through without as much addition of plagioclase-rich bench lava. The abundance of plagioclase-rich lava fragments in Units 1B, 2, 3, and upper units varies by less than one standard deviation (3%), so everything above Unit 1A is within errors.

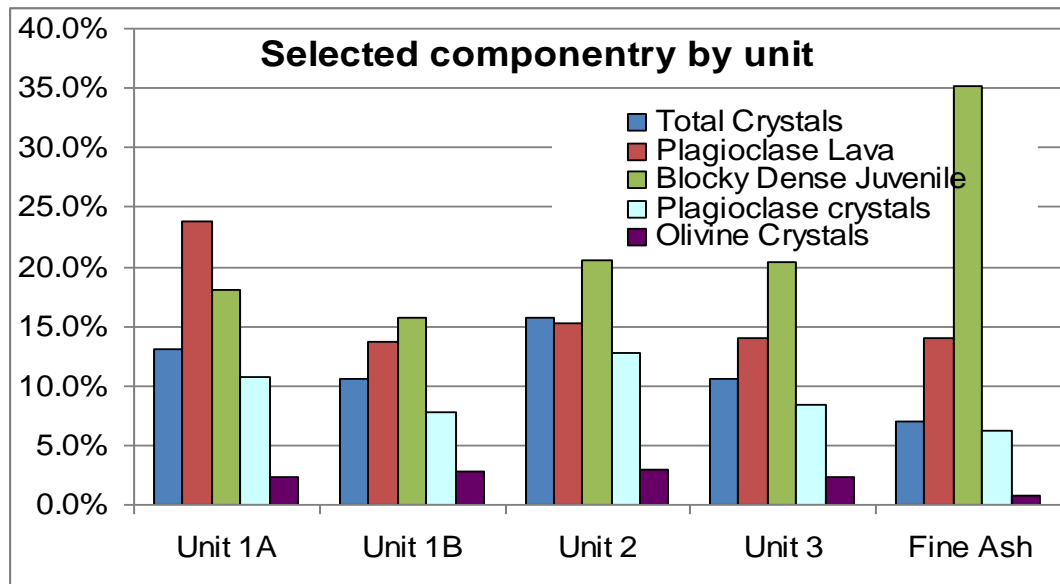


**Figure 6.13:** Selected 2-phi componentry results.

Another significant result is the high concentration of free crystals in Unit 2 compared to other units. Unit 2 in the 2-phi size contains 15.7% crystals, while other units range from 8.4-13% crystals. This result confirms field observations of the crystal-rich nature of Unit 2 and its 'salt and pepper' appearance, produced by free plagioclase crystals and dark glass fragments. The olivine content of Unit 2 is similar to other units and free plagioclase crystals make up the increased free crystal population in Unit 2 (Fig. 6.13). These plagioclase crystals may be sourced in the plagioclase-rich bench lava or sediments underlying the bench lava. If the source of plagioclase crystals is the plagioclase-rich lava, then this indicates that the level of vent widening and reaming was high during the production of Unit 2. If the crystals are sourced in the alluvial sediments beneath the bench lavas, the increase in plagioclase crystals in Unit 2 may indicate that the vent had excavated deeper through bench lavas and was entraining more of the sediments beneath.

The upper fine ash units have the highest content of blocky dense brown glass, which makes up 35% of the grains in fine ash units and 15-20% of grains in Units 1-3. Upper units have the finest median grain size, suggesting that they were produced by the most efficient phreatomagmatic eruptions, and the abundance of blocky dense grains supports this idea.

Results from -0.5-phi componentry display one significant trend; an increase of brown pumice with distance from the vents. Site 10JAUOK023, the most distal site, contains around 27% brown pumice grains while the next closer site, 10JAUOK006, contains around 13% brown pumice grains (Fig. 6.14). The two most proximal sites 10JAUOK011 and 10JAUOK002 are poorer in brown pumice (12% and 8%,

respectively). The brown pumice grains are likely the least dense of any component in the 2008 Okmok ash, which may allow them to be preferentially carried in greater amounts to distal sites compared to more dense lava fragments or poorly vesicular juvenile fragments. This trend is consistent through basal units, with the exception of the most proximal location 10JAUOK011 Units 1A and 1B, which have more brown pumice than the same units at sites 10JAUOK002 and 10JAUOK006. Site 10JAUOK023 has the most pumice clasts in the -0.5-phi size for all units. The upper fine unit 10JAUOK023E has the highest pumice content at 42%.

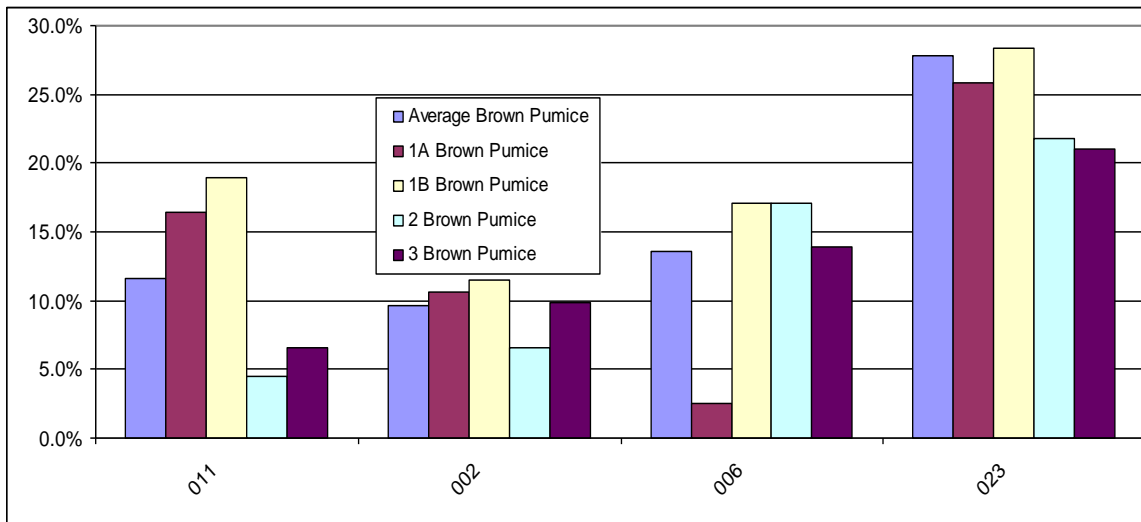


**Figure 6.14:** -0.5-phi brown pumice abundance by location and unit. Distance from vents increases to the right.

#### 6.4 Componentry results for upper fine units

Selected units from site 10JAUOK011 were analyzed along with additional units from 10JAUOK005 (Fig. 6.15) and 10JAUOK066 (Fig. 6.16) to examine componentry differences between laminated ash units and ash-pellet units (Fig. 6.3). Samples from sites 10JAUOK005 and 10JAUOK066 were chosen because they are characteristic

examples of either ash-pellet deposits or laminated ash and are approximately the same distance from vents as site 10JAUOK011.

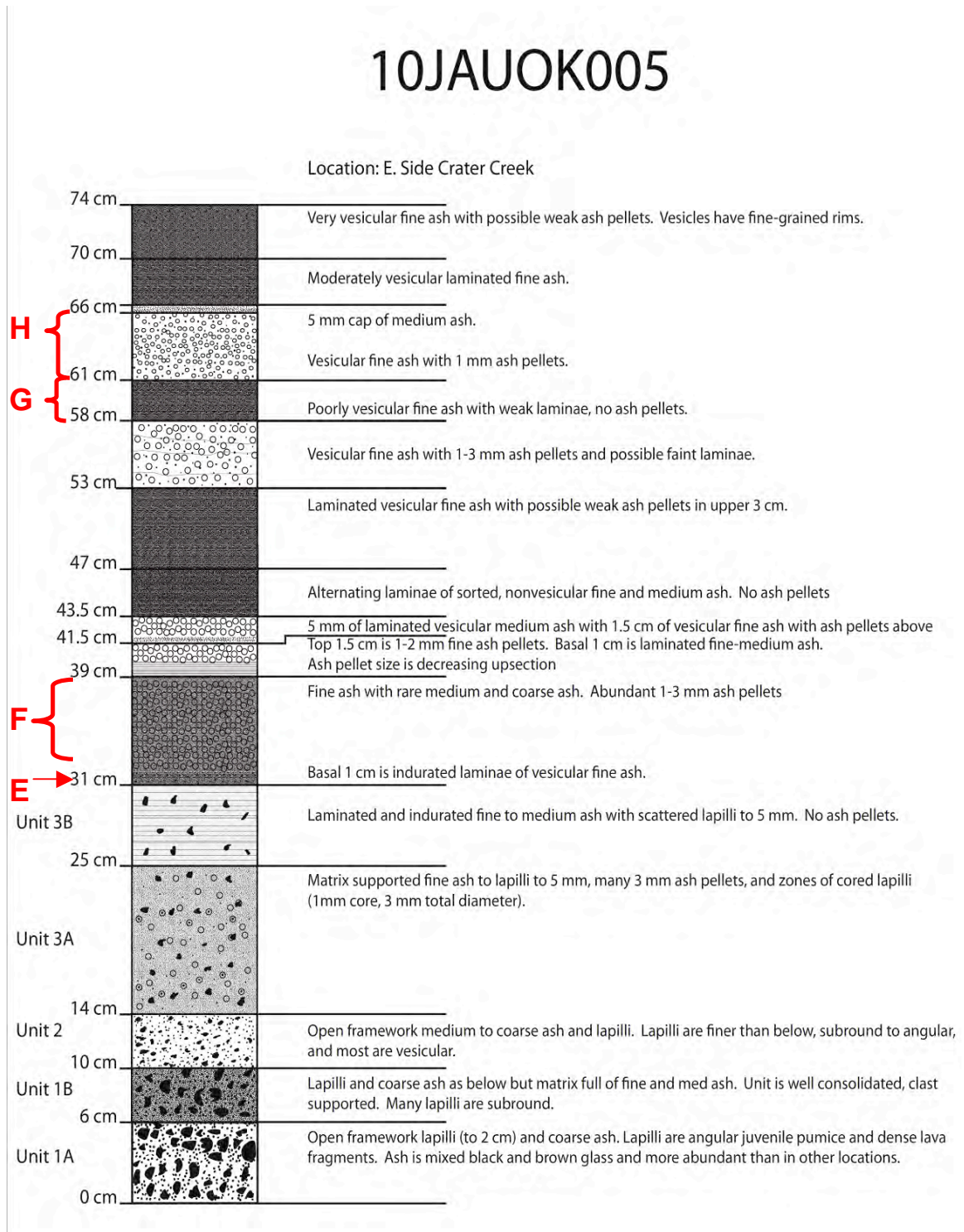


**Figure 6.15:** Stratigraphic section for 10JAUOK005 with analyzed units shown in red.

# 10JAUOK066

Location: Upper East Flanks

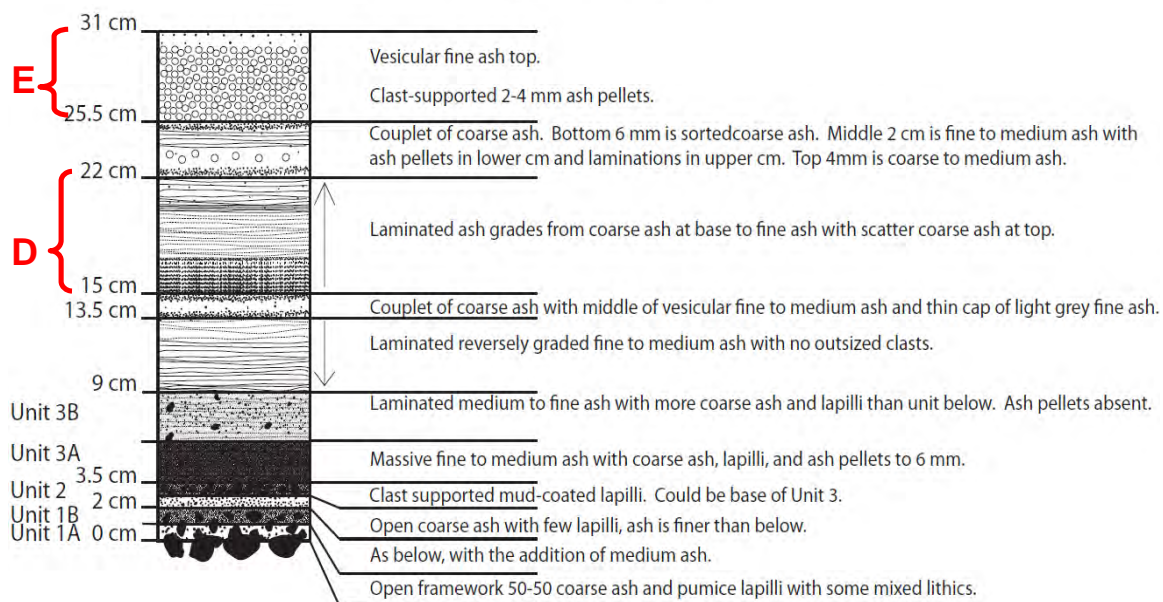


**Figure 6.16:** Stratigraphic section for 10JAUOK066 with analyzed units shown in red.

Ash-pellet deposits and laminated ash deposits are very similar in componentry, with the only significant difference being free crystal content (Fig. 6.18). Ash-pellet units have free crystal percentages of 3.4-6.8% with a mean at 4.8%. Laminated ash units contain 7.6-10.1% crystals with a mean of 8.2%. This difference falls just within error bounds for major (2%) or minor (3%) categories. Laminated ash units are slightly coarser grained than ash-pellet layers, with much of the coarser material in the 2-phi range, the size analyzed here for componentry. Crystals may not be preferentially incorporated into ash aggregates, as their surfaces are smooth and free of imperfections that may aid aggregate binding. The smooth surfaces, regular shapes, and density of crystals may allow them to fall faster than pumice fragments or vesicular glass of a

similar size when deposition is occurring grain-by-grain, resulting in an increase in crystals in laminated ash relative to ash-pellet units in the upper ash deposits.

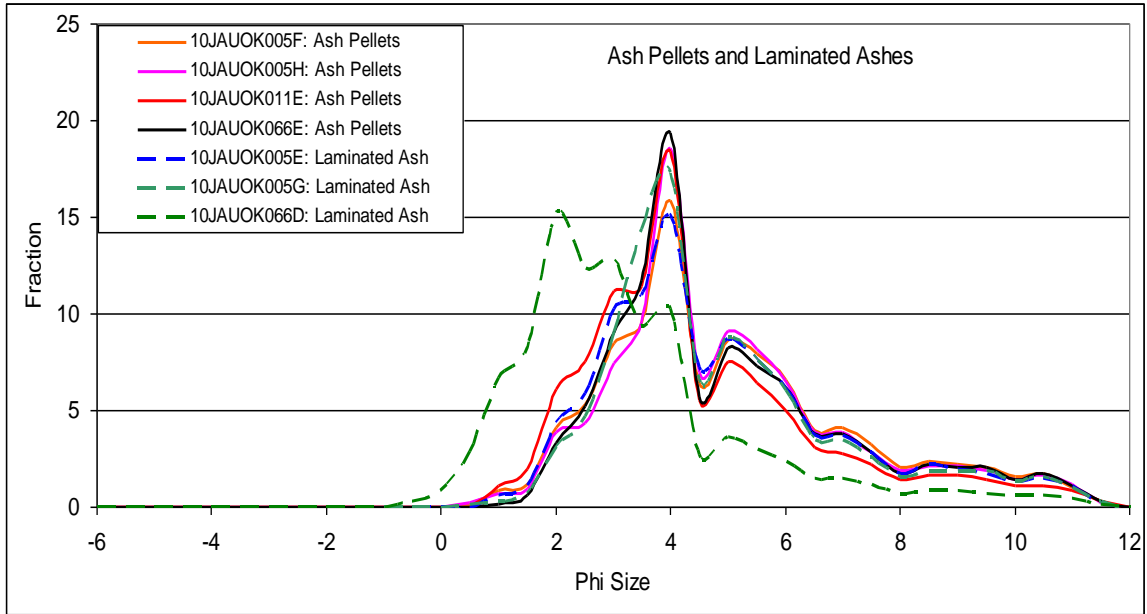


**Figure 6.17:** Grain-size distribution of ash-pellet and laminated ash units

	011E	005F	005H	066E	Ash Pellet mean	005E	005G	066D	Laminated Ash mean
<b>Lithic</b>	21.5%	39.2%	30.6%	22.3%	28.4%	29.1%	29.1%	28.4%	28.9%
<b>Juvenile</b>	74.6%	55.9%	62.6%	74.3%	66.9%	60.8%	63.8%	64.0%	62.9%
<b>Crystal</b>	3.9%	4.9%	6.8%	3.4%	4.8%	10.1%	7.0%	7.6%	8.2%
<b>Plag-rich</b>	12.7%	16.2%	12.8%	4.9%	11.6%	11.1%	13.6%	12.0%	12.2%
<b>Dark plag-rich</b>	0.0%	0.0%	0.0%	0.0%	0.0%	0.0%	0.0%	0.0%	0.0%
<b>Other lava</b>	0.0%	9.8%	7.3%	3.4%	5.1%	6.0%	3.5%	6.0%	5.2%
<b>Black Scoria</b>	5.9%	4.4%	2.7%	6.8%	4.9%	4.5%	7.0%	2.8%	4.8%
<b>Cauliflower Dense</b>	1.5%	4.9%	3.7%	4.5%	3.6%	5.0%	3.0%	4.4%	4.1%
<b>Other lithic grains</b>	6.3%	3.9%	4.1%	2.6%	4.3%	2.5%	2.0%	3.2%	2.6%
<b>Brown vesicular</b>	32.2%	21.6%	27.9%	33.6%	28.8%	32.2%	27.6%	21.6%	27.1%
<b>Brown dense</b>	41.0%	33.8%	34.7%	40.8%	37.6%	27.1%	34.7%	41.6%	34.5%
<b>Brown pumice</b>	1.5%	0.5%	0.0%	0.0%	0.5%	1.5%	1.5%	0.8%	1.3%
<b>Plagioclase</b>	2.9%	3.9%	6.8%	3.0%	4.2%	8.0%	5.5%	7.2%	6.9%
<b>Olivine</b>	1.0%	1.0%	0.0%	0.4%	0.6%	2.0%	1.5%	0.4%	1.3%

**Table 6.7:** 2-phi componentry results for upper ash-pellet and laminated ash units.

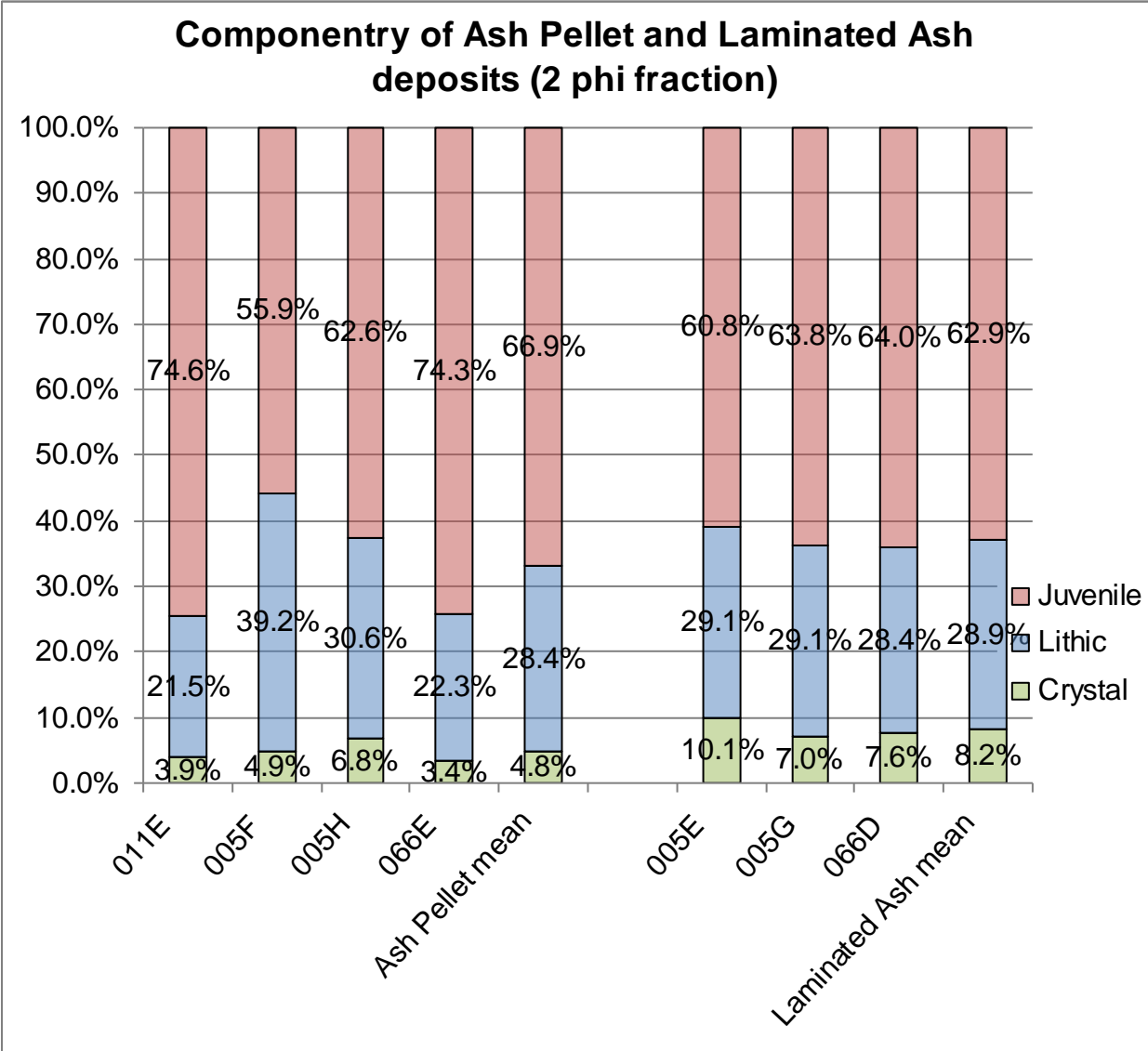


**Figure 6.18:** 2-phi componentry for upper ash-pellet and laminated ash units.

## **Chapter 7: Grain-shape, surface feature, and glass geochemistry results from SEM analysis**

Grain shapes and surface features of glass particles from 2008 deposits were examined using the scanning electron microscope (SEM). Energy-dispersive spectroscopy (EDS) on the SEM was used to obtain glass geochemical data and ensure that the particles analyzed for shape and surface features were indeed glass rather than free crystals.

### **7.1 Examination of componentry categories by SEM**

Grains from each separated component type from the 2-phi fraction of Unit 1B from site 10JAUOK011 were examined on the SEM to examine chemical differences between component types and correlate component identification between binocular microscope and SEM (Fig. 7.1-2). This was done because I could be confident of the identification of these grains in the 2-phi size, but wanted to be able to identify much smaller grains on the SEM using chemical composition.

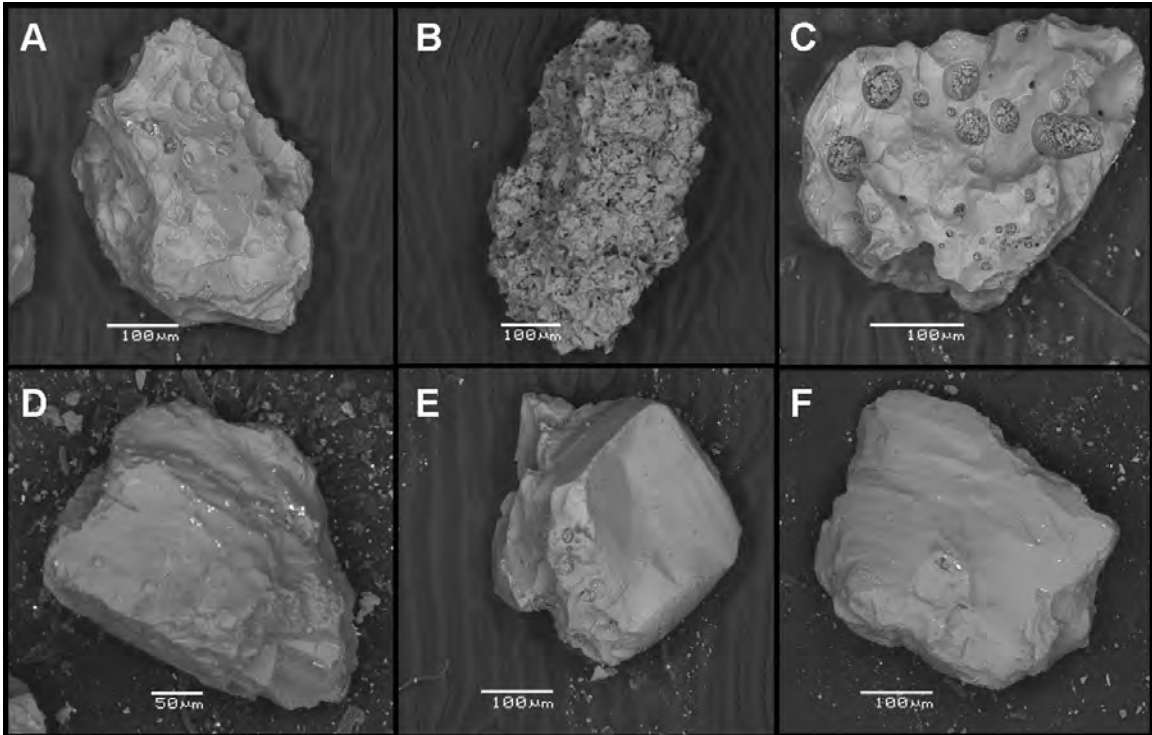


**Figure 7.1:** SEM images of juvenile grains and free crystals from componentry categories described in Chapter 6. **A.** Dense brown glass **B.** Brown pumice **C.** Brown vesicular glass **D.** Feldspar **E.** Olivine **F.** Pyroxene

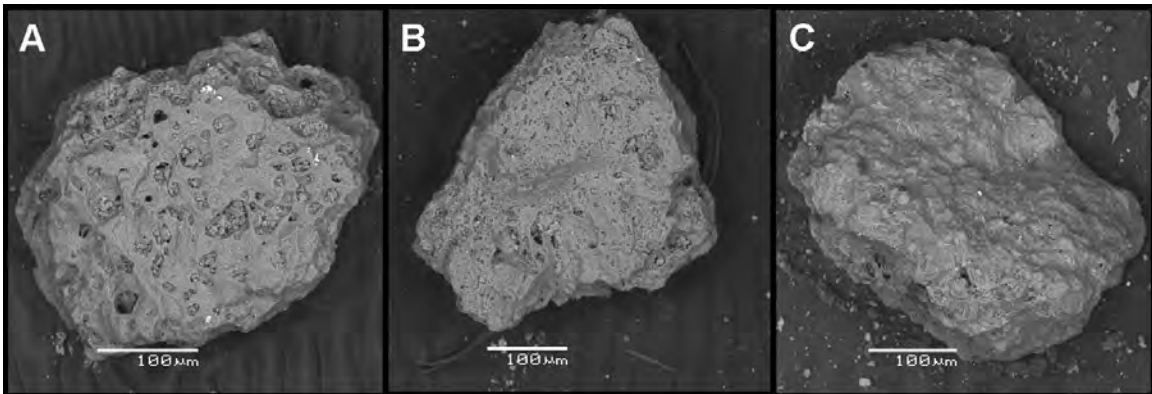


**Figure 7.2:** SEM images of lithic grains from componentry categories described in Chapter 6. **A.** Black scoria **B.** Dense black pyroclast **C.** Plagioclase-rich lava

Examination of these grains that had been previously identified on the binocular microscope aided in identification of juvenile grains when smaller (4-phi) grains were studied. Plagioclase-rich lava fragments commonly had uneven surface textures. Black

scoria, dense pyroclasts, and plagioclase-rich lava fragments commonly had visible microlites, while juvenile grains typically had no visible microlites.

### Glass geochemistry of identified components

Analysis of the glass geochemistry of the 2-phi components by energy-dispersive spectroscopy reveals that all component types have a range of silica contents ( Fig. 7.3). The ranges of compositions measured for each component type overlap each other almost completely for all analyzed elements, showing that there are no measurable chemical differences between component types.

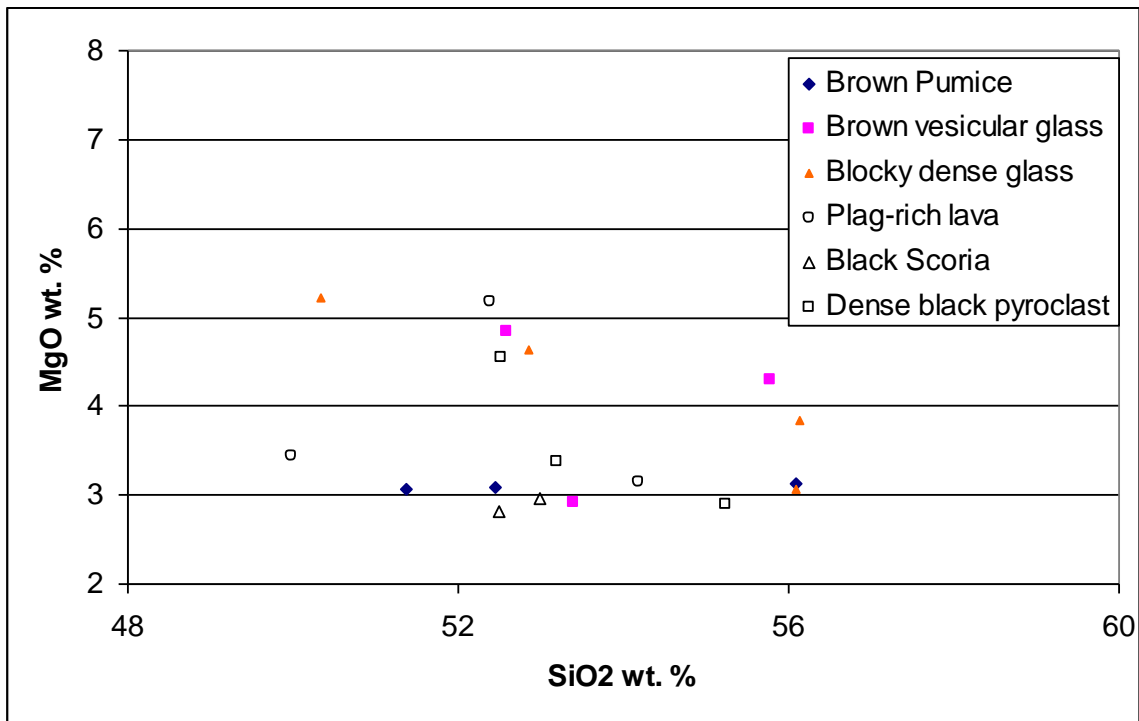


**Figure 7.3:** Glass geochemistry of 2-phi component types. Juvenile components are represented by solid symbols and lithic components are shown by open symbols.

Juvenile grains including brown pumice, vesicular brown glass, and dense brown glass have silica contents ranging from 50-56.2 wt. % SiO<sub>2</sub>. Lithic grains including

plagioclase-rich lava, black scoria, and dense black pyroclasts have silica contents ranging from 49.9-55.5 wt. % SiO<sub>2</sub>.

## **7.2 Qualitative description of surface features**

Glass particles from the 4-phi size fraction were imaged from eleven samples from three sites; 10JAUOK005, 10JAUOK011, and 10JAUOK074 (see Chapter 6, figs. 6.3, 6.4, 6.10, 6.13). These samples were chosen because they had been analyzed for componentry and provided a set to examine changes from basal deposits through upper units and differences between upper ash pellets, laminated ash, and coarse ashes. The glass particles examined showed a variety of textures and surface features. Each imaged particle was counted for the following characteristics: vesicular, dense, blocky, quenching cracks, stepped surfaces, vesicles cut by curvilinear fractures, fluidal shapes, and microlitic textures (Fig. 7.4). Particles that had uneven textures or other characteristics suggesting a non-2008 juvenile origin were not counted. Phreatomagmatic fragmentation typically produces pyroclasts that are poorly vesicular with blocky shapes or fluidal particles. Quenching cracks and stepped surfaces are surface features produced in phreatomagmatic fragmentation (Büttner et al. 1999). Of all glass particles examined, 48% were vesicular and 52% dense (Table 7.1).

	Unit	Vesicular	Dense	Blocky	Quench cracks	Stepped surfaces	Cut vesicles	fluidal	Microlitic
011A	1A	64%	36%	50%	0%	29%	36%	0%	7%
011B	1B	64%	36%	64%	0%	10%	50%	27%	0%
011C	2	50%	50%	50%	0%	29%	86%	14%	0%
011D	3A	33%	67%	42%	8%	58%	67%	8%	0%
011E	Ash pellet	43%	57%	64%	7%	38%	36%	21%	0%
011F	Laminated	67%	33%	67%	0%	54%	80%	7%	7%
074A	Coarse ash	29%	71%	93%	7%	57%	64%	7%	14%
074B	Coarse ash	36%	64%	57%	0%	43%	86%	21%	7%
005E	Laminated	47%	53%	60%	0%	60%	80%	20%	7%
005F	Ash pellet	60%	40%	73%	0%	58%	80%	7%	0%
005G	Laminated	38%	67%	92%	0%	92%	69%	0%	15%
Overall		48%	52%	65%	2%	48%	67%	12%	5%

**Table 7.1:** Qualitative description of pyroclast shapes, textures and surface features.

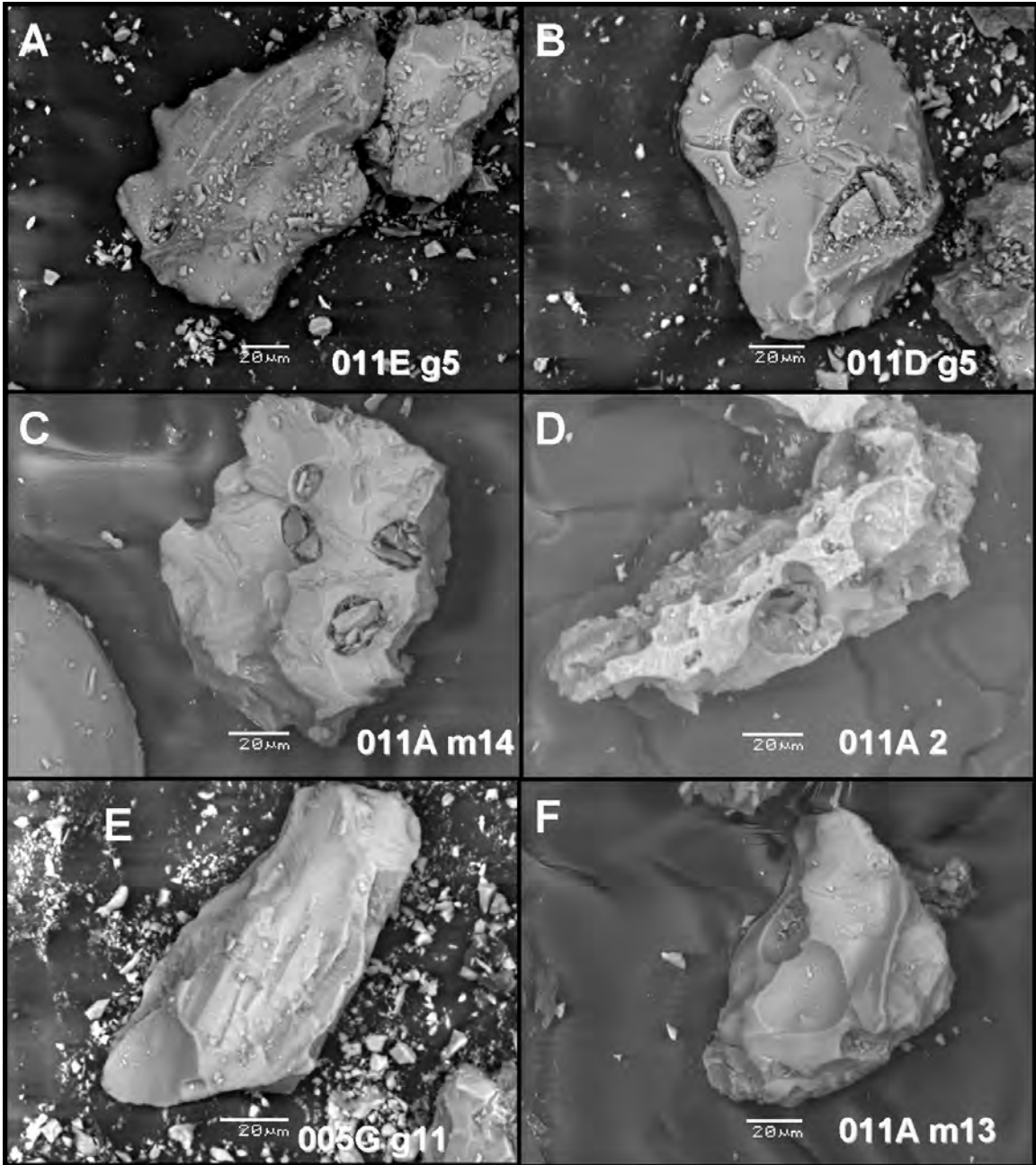


**Figure 7.4:** SEM images showing characteristic textures, surfaces features and grain shapes. **A.** Fluidal particle **B.** Dense particle with a blocky shape, quenching cracks, and cut vesicle **C.** Vesicular microlitic particle with cut vesicles and a blocky shape **D.** Vesicular glass with a shape formed by vesicle walls **E.** Blocky dense particle with prominent stepped surfaces **F.** Dense particle with cross-cut vesicles and stepped surfaces

Around 65% of grains had blocky shapes, 12% had fluidal shapes, and the remaining 23% had shapes controlled primarily by vesicle walls and gas expansion. Stepped surfaces and vesicles cut by curvilinear fractures were both abundant, while quenching cracks were present in only a few grains. The abundance of stepped surfaces generally increases from basal units to upper units (Fig. 7.5). Sample 011A, taken from Unit 1A, is distinct from other samples, as many of the grains in 011A are highly vesicular and have shapes formed by vesicle walls rather than blocky shapes resulting from brittle fracture.

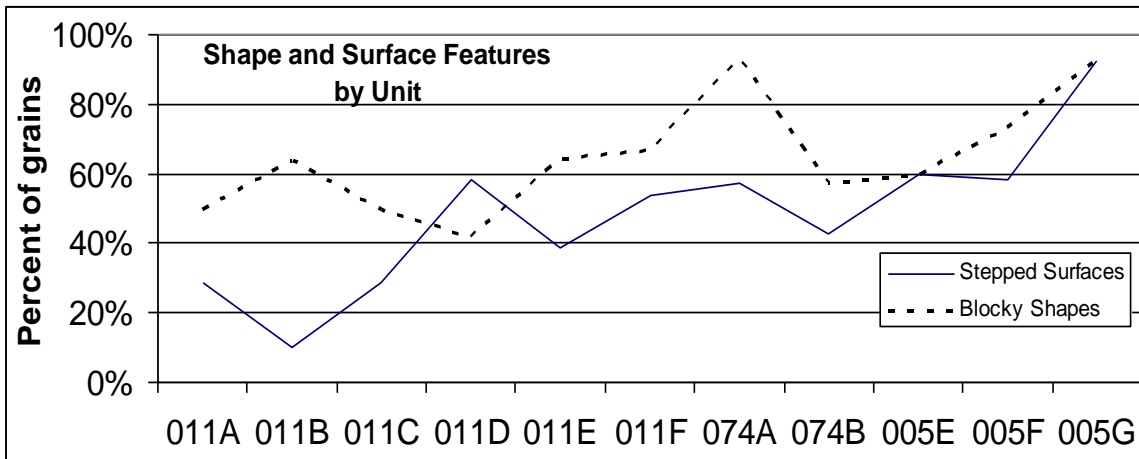


**Figure 7.5:** Percentage of grains with stepped surfaces and blocky shapes in analyzed samples.

**Interpretation of qualitative examination of surface features, textures, and shapes**

The increase in stepped surfaces and grains with blocky shapes from Unit 1A to upper units suggests that phreatomagmatic fragmentation increased during the eruption. This observation is corroborated by the grain-size results (Chapter 5) and field observations of deposit characteristics indicating an increasing water-magma ratio throughout the eruption. Unit 1A has the most grains with high vesicularity and shapes

controlled by gas expansion, supporting the interpretation of a magmatic first stage of the eruption. The overall dominance of blocky and fluidal grains with cut vesicles and stepped surfaces indicates that phreatomagmatic fragmentation was dominant in the 4-phi size during most of the eruption.

### 7.3 Glass geochemistry from Energy Dispersive Spectroscopy (EDS)

Five or more glass geochemistry analyses were performed for ten samples using the Energy Dispersive Spectroscopy function on the SEM. Most grains had silica contents ranging from 52-58 wt.% SiO<sub>2</sub> and magnesium contents ranging from 2.5-4.5 wt.% MgO (Fig. 7.6). The error in geochemical analyses is based on the number of counts obtained for each element by energy-dispersive spectroscopy and is around 1.5% for SiO<sub>2</sub> and 0.5% for MgO (absolute percentage errors) (Appendix D). The range in glass compositions is much greater than the error of analysis, indicating that there is true variation in the glass chemistry.

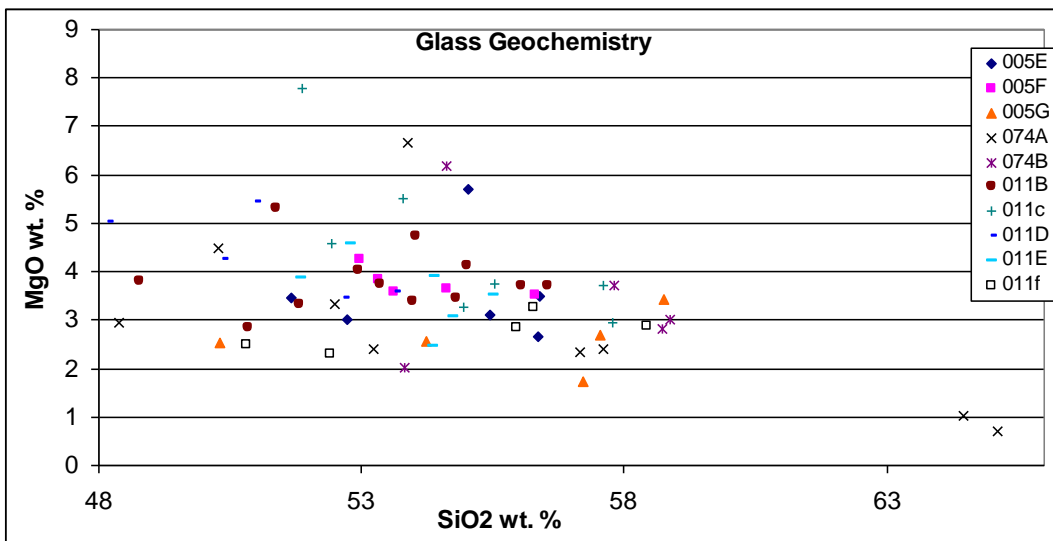


**Figure 7.6:** Glass geochemistry for analyzed samples, from EDS analysis on the NAU SEM.

There are no apparent correlations between silica content and grain shape, texture, or surface features or between silica content and stratigraphic position. Each sample has grains with a range of silica contents and no patterns are visible in these data. Two outlying grains are present in sample 074A, a coarse ash sample. These two grains have silica contents around 65 wt.%  $\text{SiO}_2$  and low magnesium contents around 1 wt.%  $\text{MgO}$ . These grains, shown in Figure 7.7, have no visible differences from other 2008 juvenile grains when examined on the SEM, but may be high-silica grains included from previous eruptions.

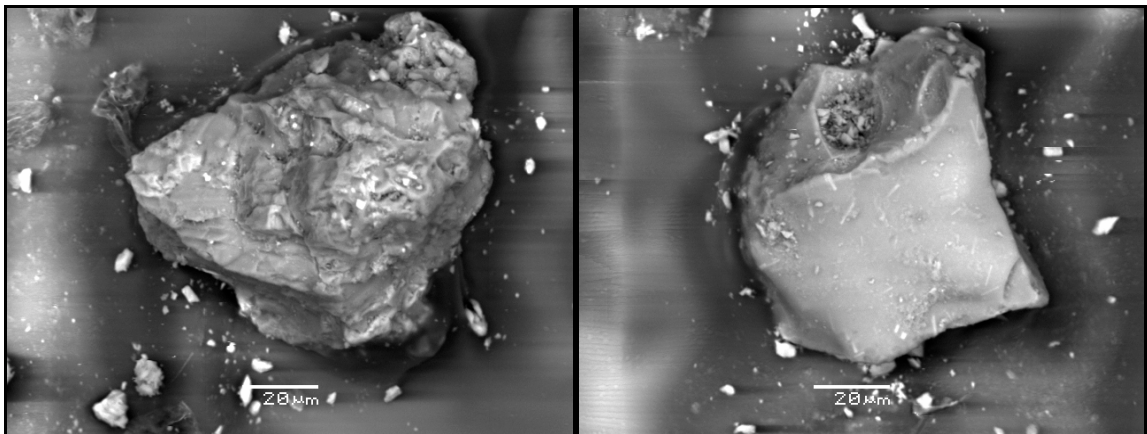


**Figure 7.7:** Glass grains 074A g5 (left) and 074A g6 (right), two grains with 65 wt%  $\text{SiO}_2$ .

#### **Interpretations from glass geochemistry:**

The range of glass compositions in all grains analyzed and the range in grains from each unit indicates that the magma source for the 2008 eruption may have been heterogeneous. This heterogeneity may have been produced by magma mingling and incomplete mixing at depth. No systematic change in silica content occurs between any units. Compositional magma chamber zoning or flux from chemically distinct reservoirs is not supported by these data.

#### 7.4 Fractal analysis of glass particles

Fractal analysis using the FRACCALC macro in the NIH program, Image, was performed following the procedures of Dellino and Liotino (2002) for five to fifteen grains (64-125  $\mu\text{m}$ ) per sample. Most grains analyzed were found to be true (mono) fractal, and only a few were multi-fractal. Fractal analysis was performed on 133 individual glass particles; 14 were found to be multifractal, 48 were low fractal dimension monofractal, 47 were intermediate fractal dimension monofractal, and 24 were high fractal dimension monofractal. Fractal dimension (D) is calculated by subtracting the slope of the best-fit line on the M-R plot from 1 ( $D=1.08$  in Fig. 7.12). Low fractal dimension monofractal grains have D values below 1.06, intermediate fractal dimension monofractal grains have D values between 1.06 and 1.09, and high fractal dimension monofractal grains have D values above 1.09. Multifractal grains have two fractal dimensions, the smaller scale (textural) D value is smaller (1.01-1.1) and the larger-scale (structural) D value is larger (1.2-1.6).

Particles with low fractal dimensions have simple shapes and simple textures on a fine scale and grains with high fractal dimensions have more complex shapes and textures. Particles with a single D value (fractal dimension) plot as a straight line in an M-R plot and are formed when a single fragmentation regime is dominant at a fine textural scale and a larger structural scale. This method of fractal analysis examines textural scale irregularity by approximating particle shapes with a small step size and structural scale irregularity by approximating particle shapes with a larger step size. Phreatomagmatic fragmentation causes brittle breakage of particles on all scales, producing simple blocky shapes and non-complex textures (Dellino and Liotino 2002).

Multi-fractal particles have even more complex shapes at a large scale but comparatively simple textures on a fine scale. These particles have two D values from the slopes of two different line segments on an M-R plot. Dellino and Liotino (2002) found that magmatic particles have higher D values at larger step sizes (structural scale irregularity) and lower D values at smaller step sizes (textural scale irregularity). The fragmentation regime producing grain shapes of magmatic particles is gas expansion and vesicle formation, while the breakage of magmatic particles on a textural scale is brittle (Dellino and Liotino 2002).

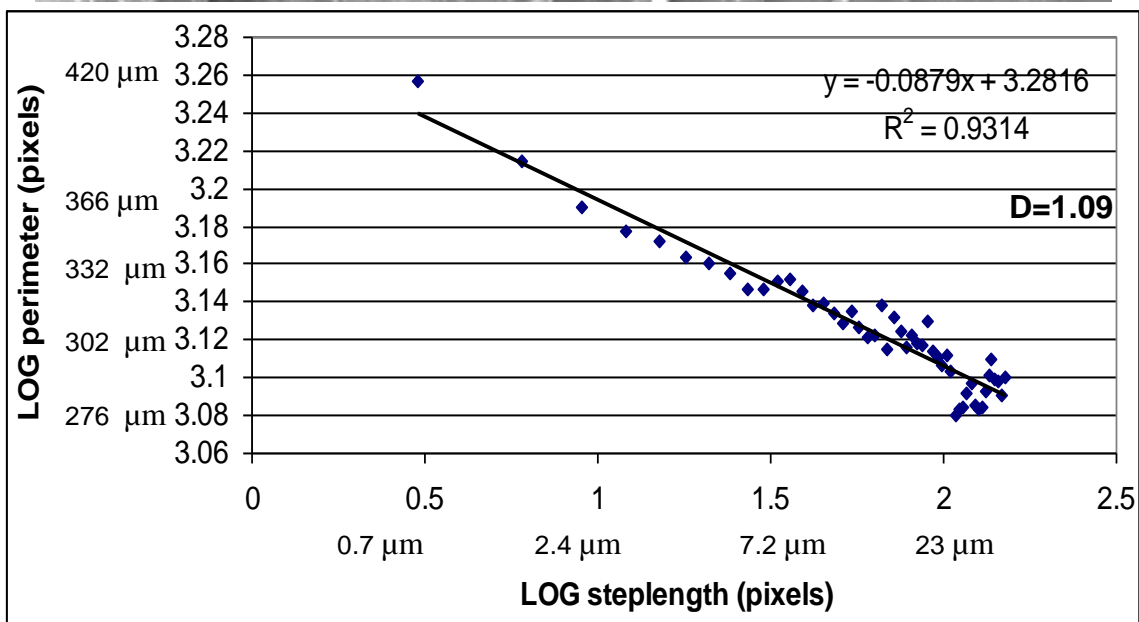
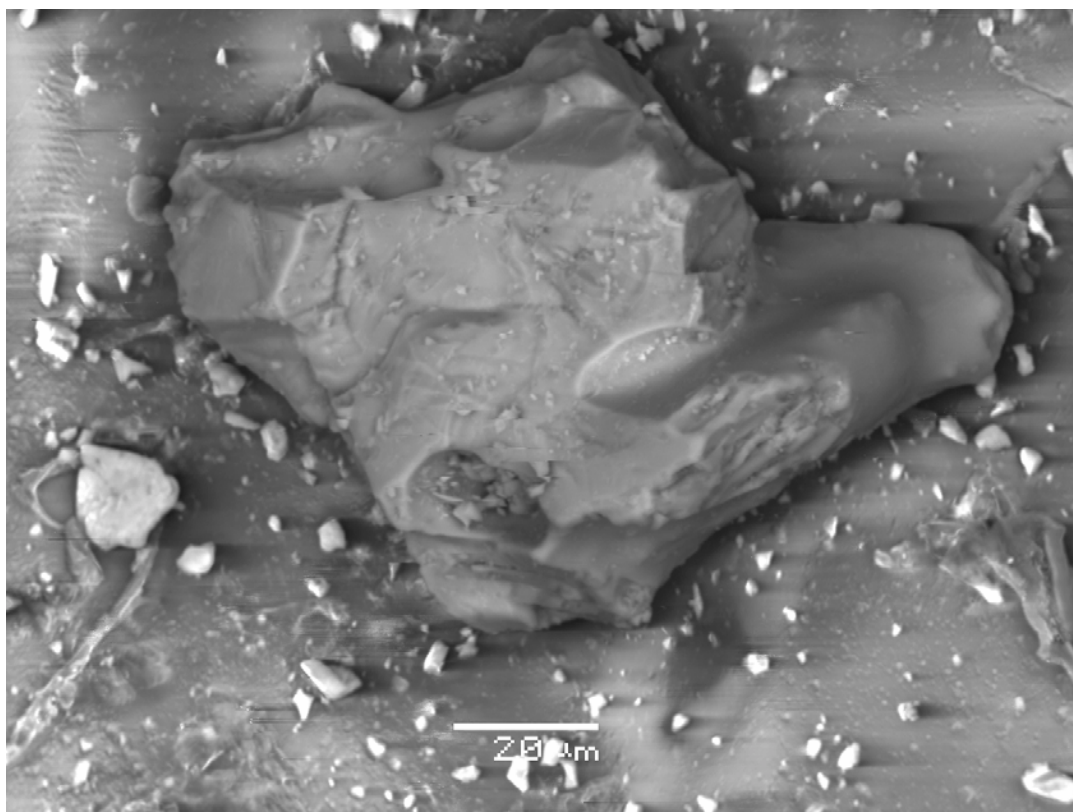


**Figure 7.8:** SEM image and fractal analysis of high fractal dimension particle 011C g6.

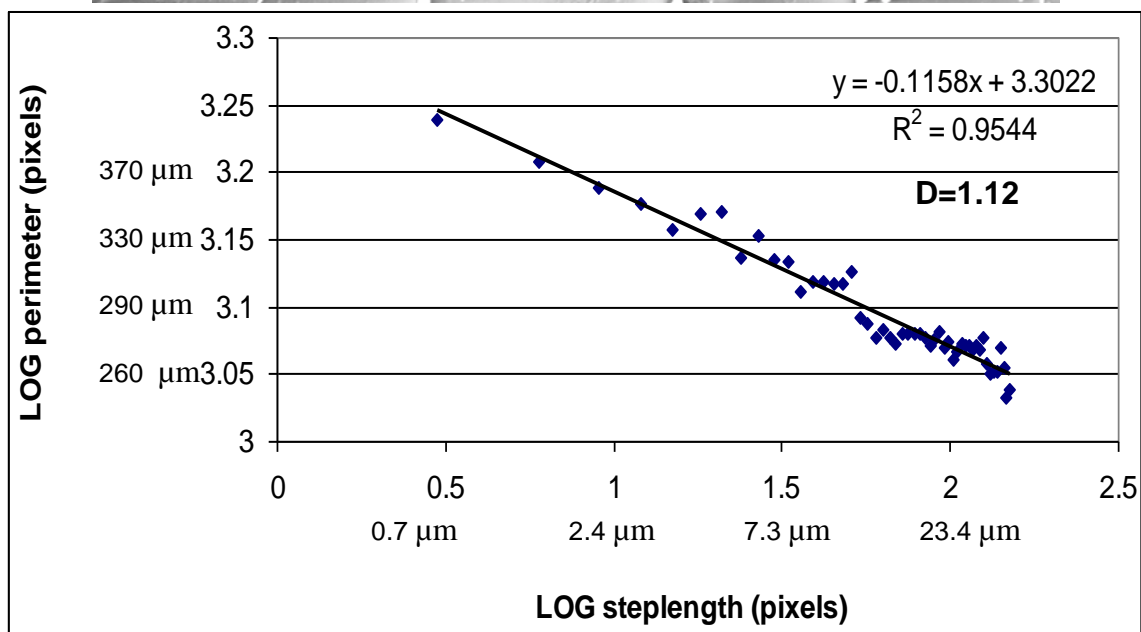
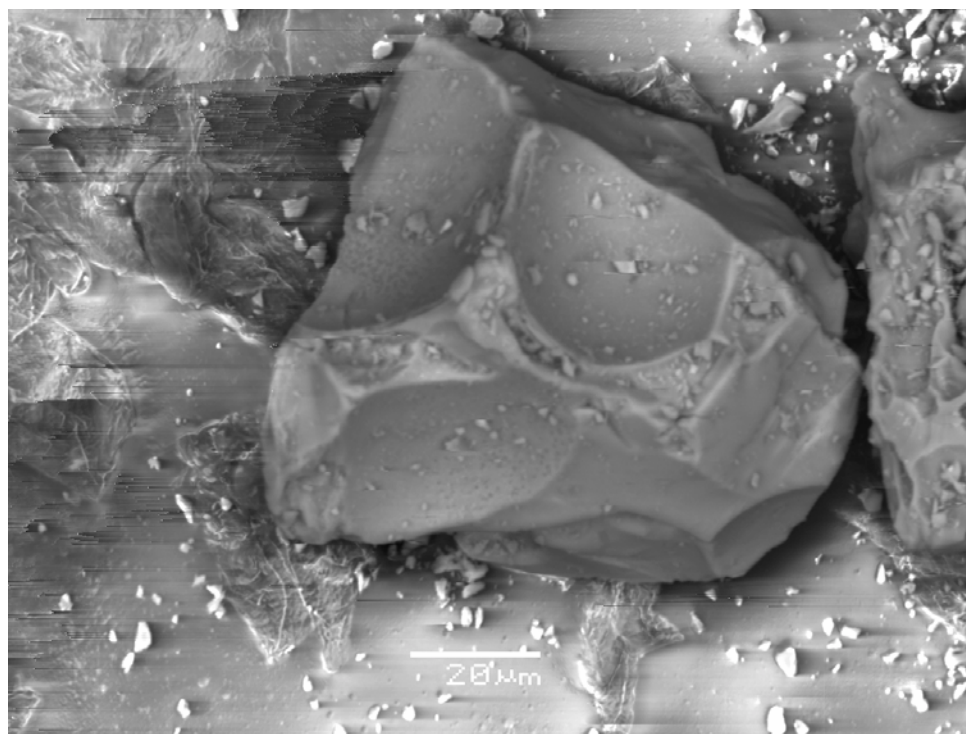


**Figure 7.9:** SEM image and fractal analysis of high fractal dimension particle 011B g10.

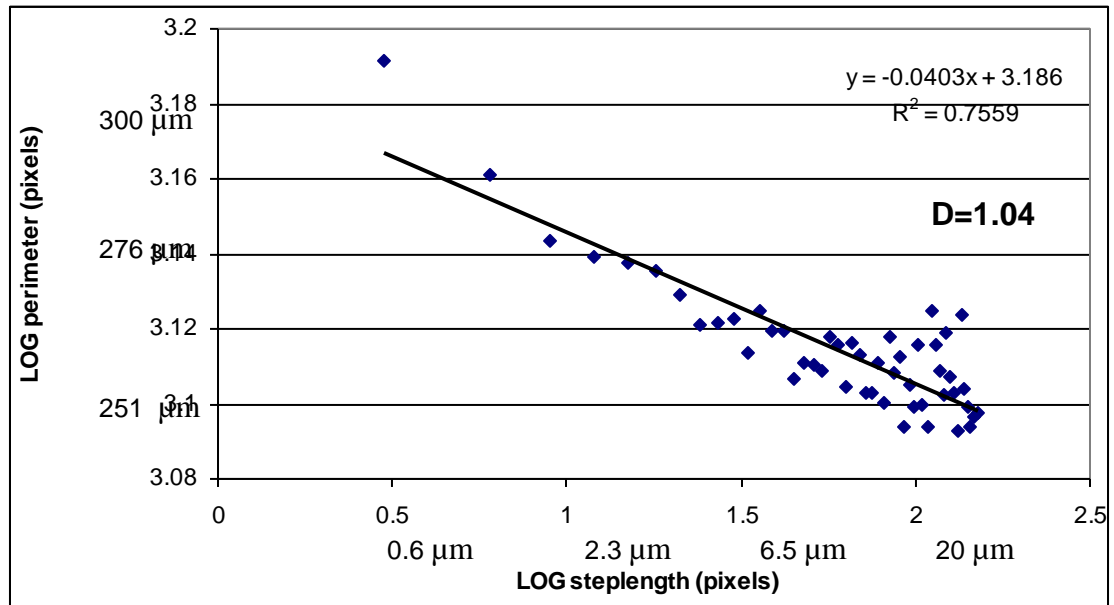
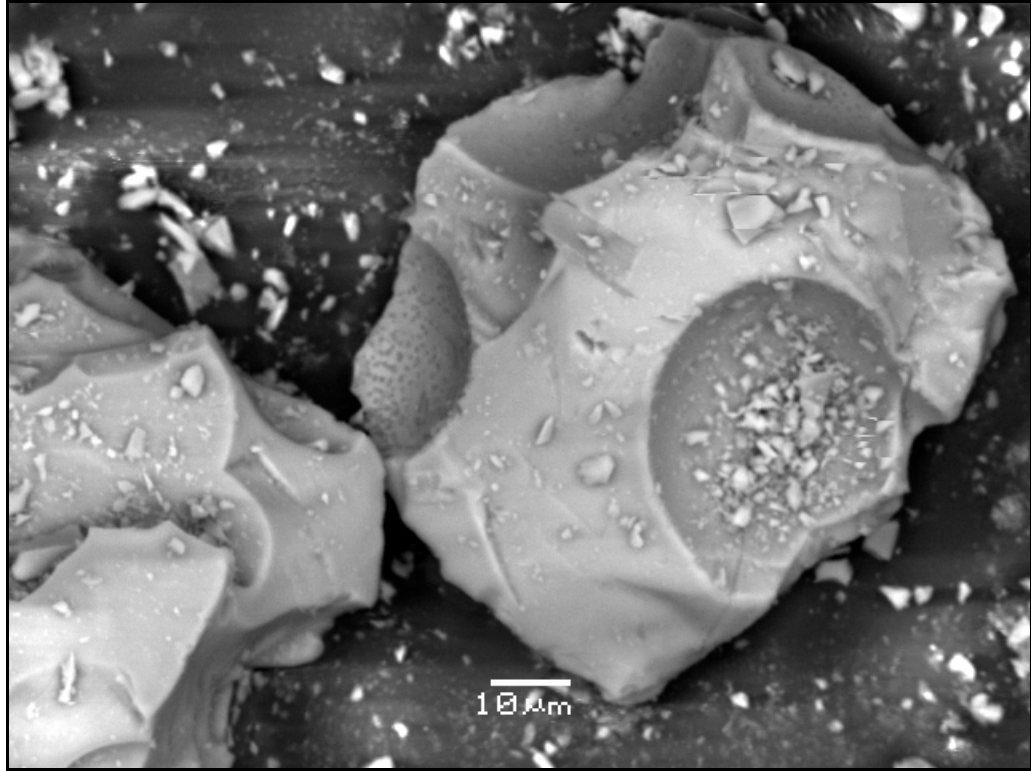


**Figure 7.10:** SEM image and fractal analysis of low fractal dimension particle 011D g12.

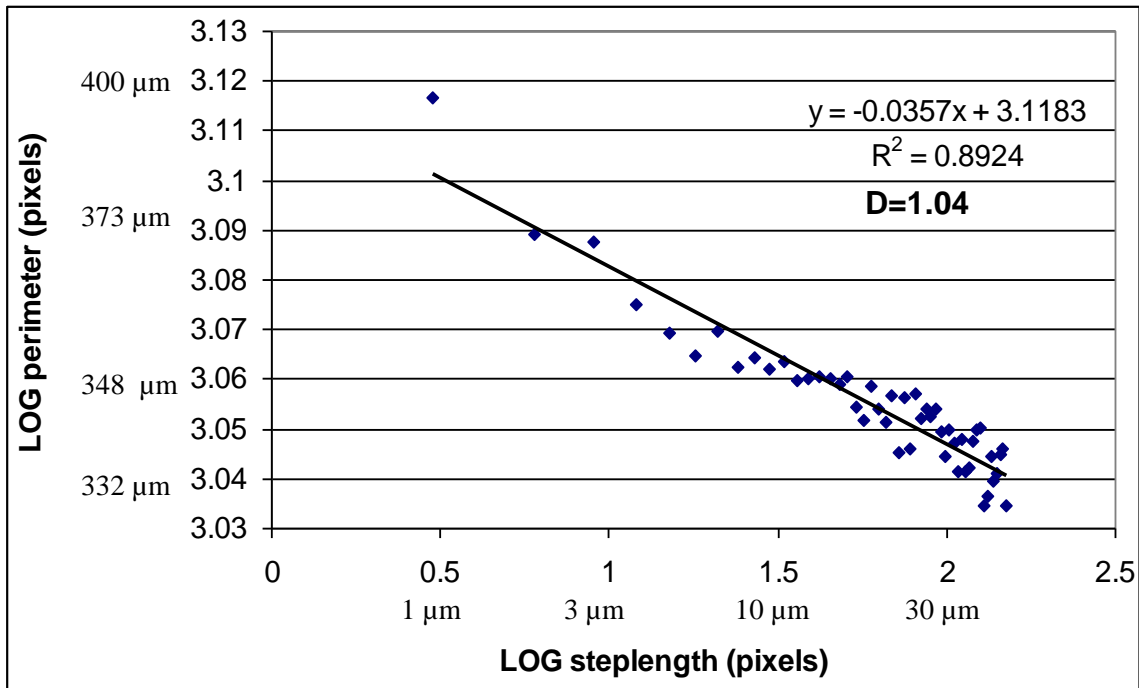
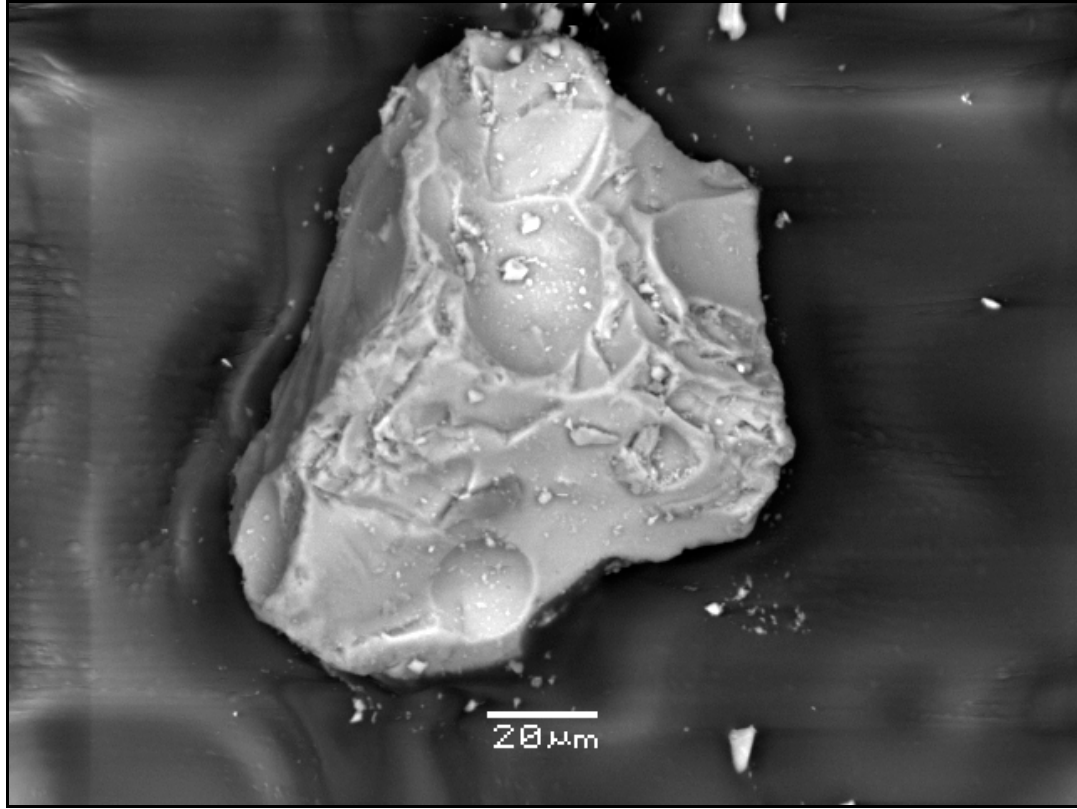


**Figure 7.11:** SEM image and fractal analysis of low fractal dimension particle 074A g13.

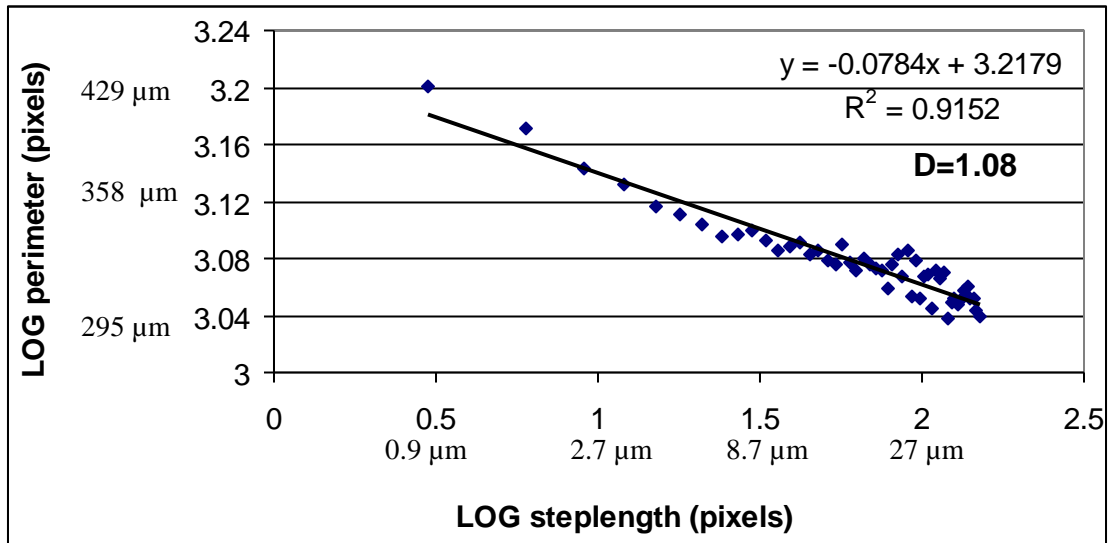
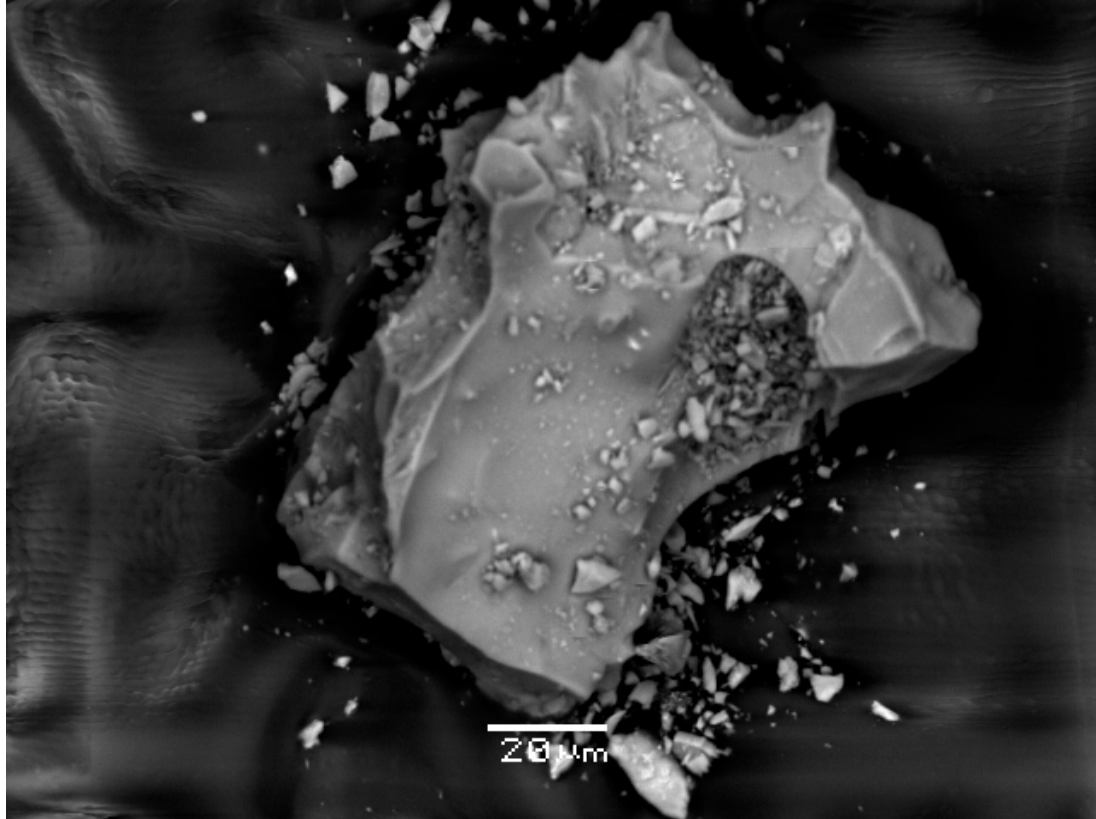


**Figure 7.12:** SEM image and fractal analysis of intermediate fractal dimension particle 011F g10.

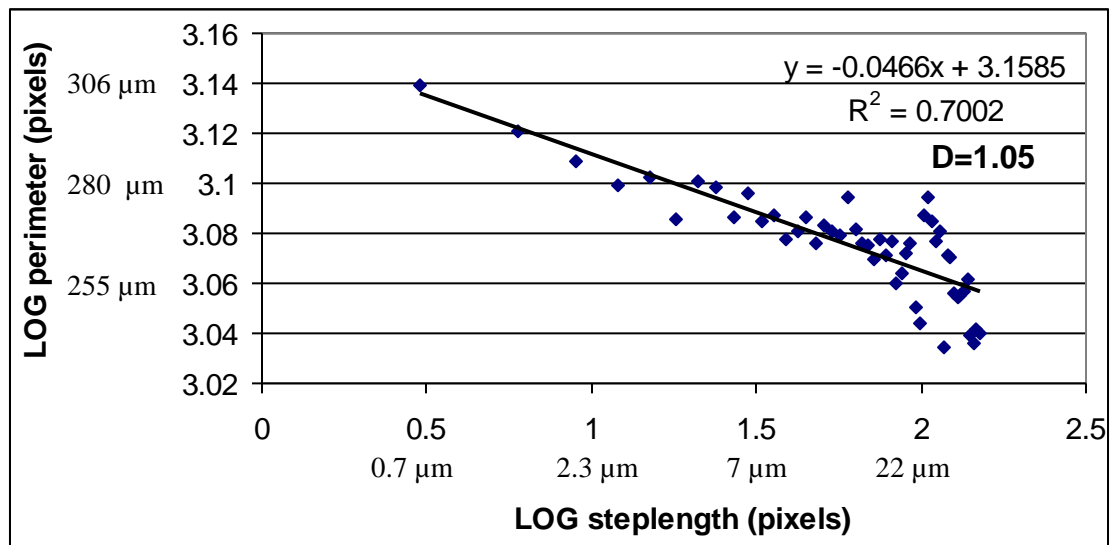
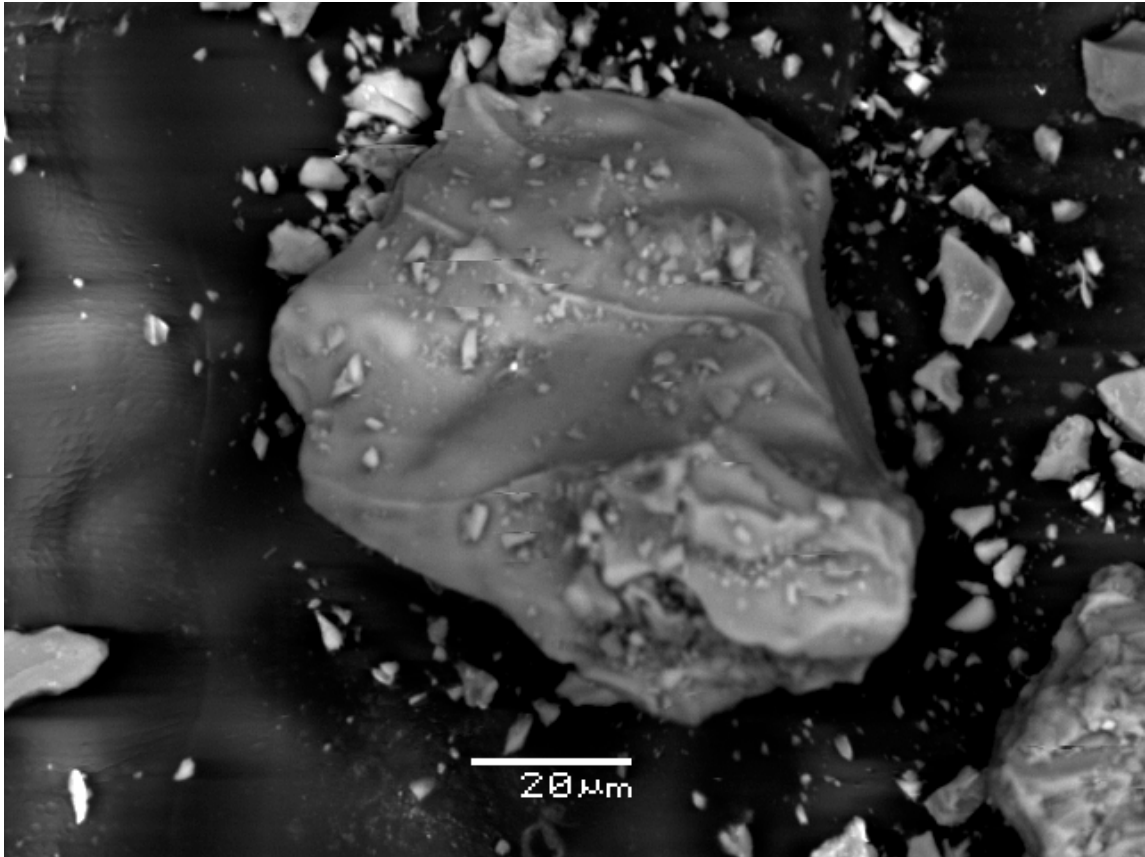


**Figure 7.13:** SEM image and fractal analysis of intermediate fractal dimension particle 011E g6.

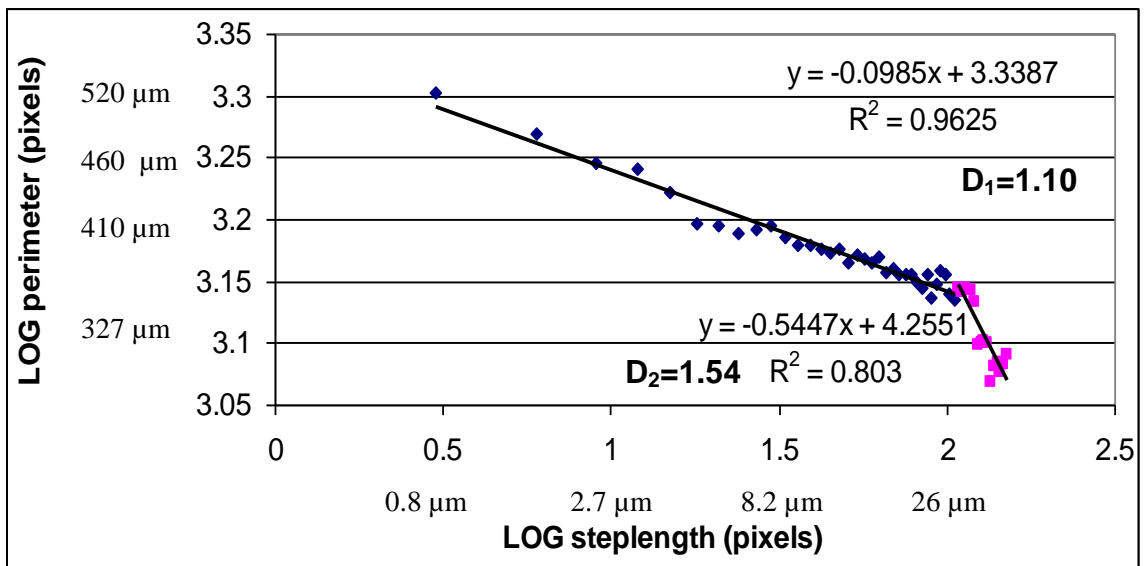
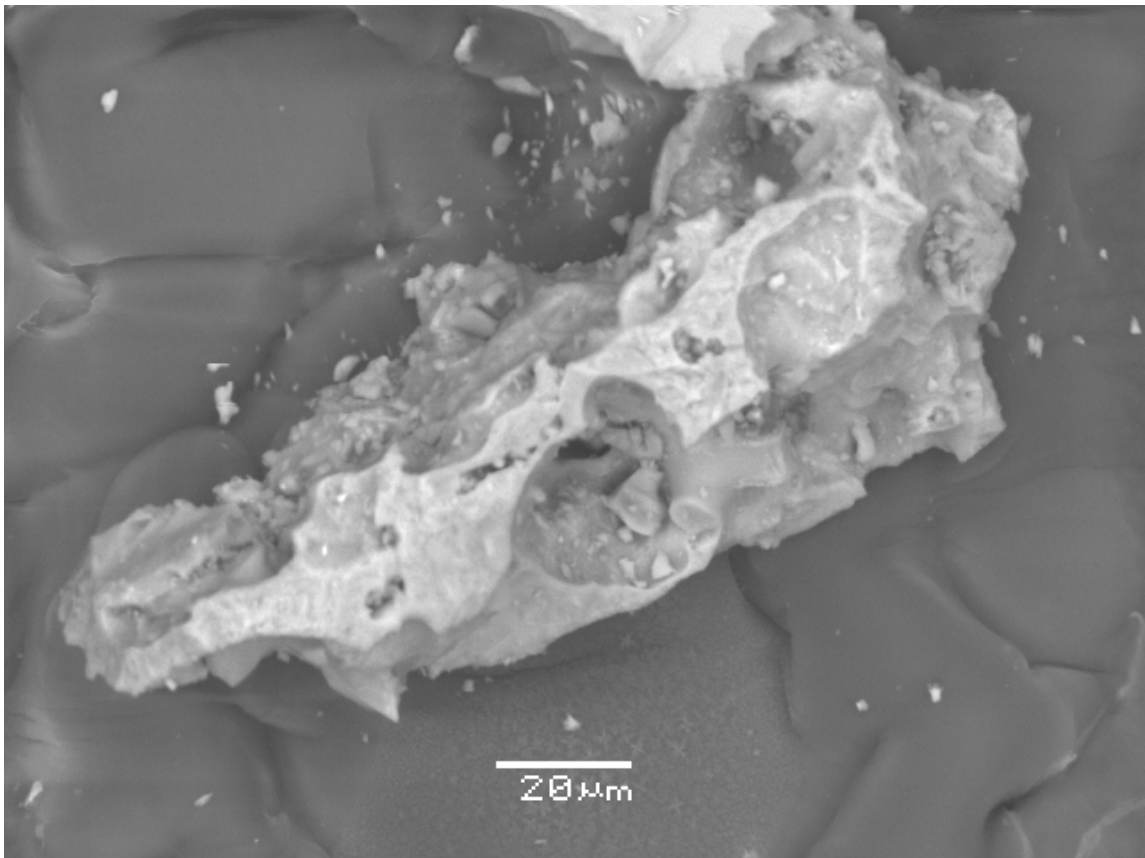


**Figure 7.14:** SEM image and fractal analysis of multifractal particle 011A 2.

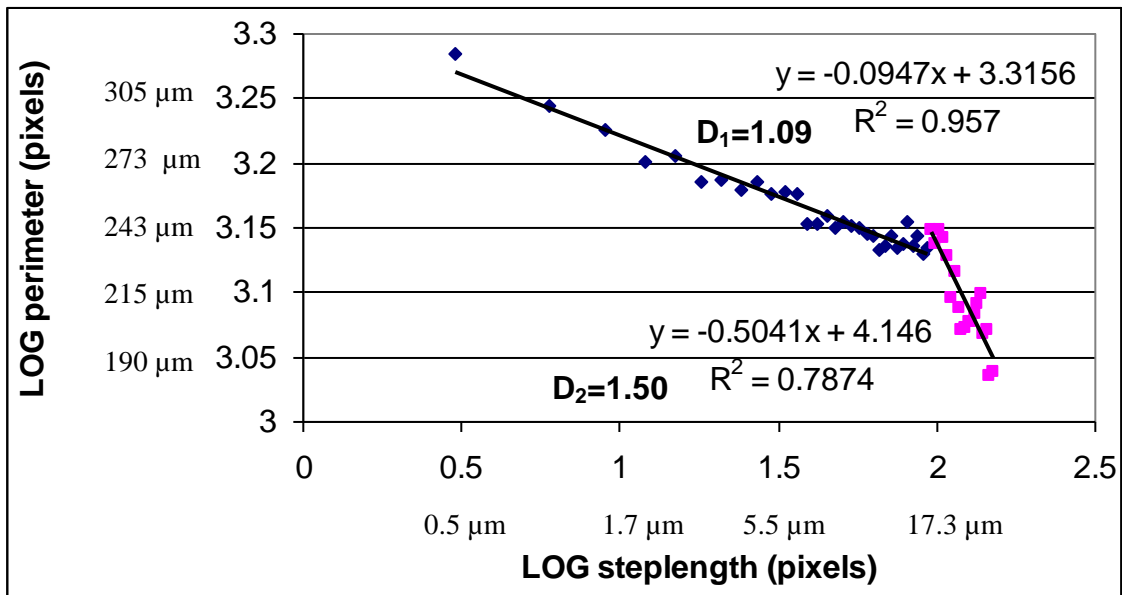
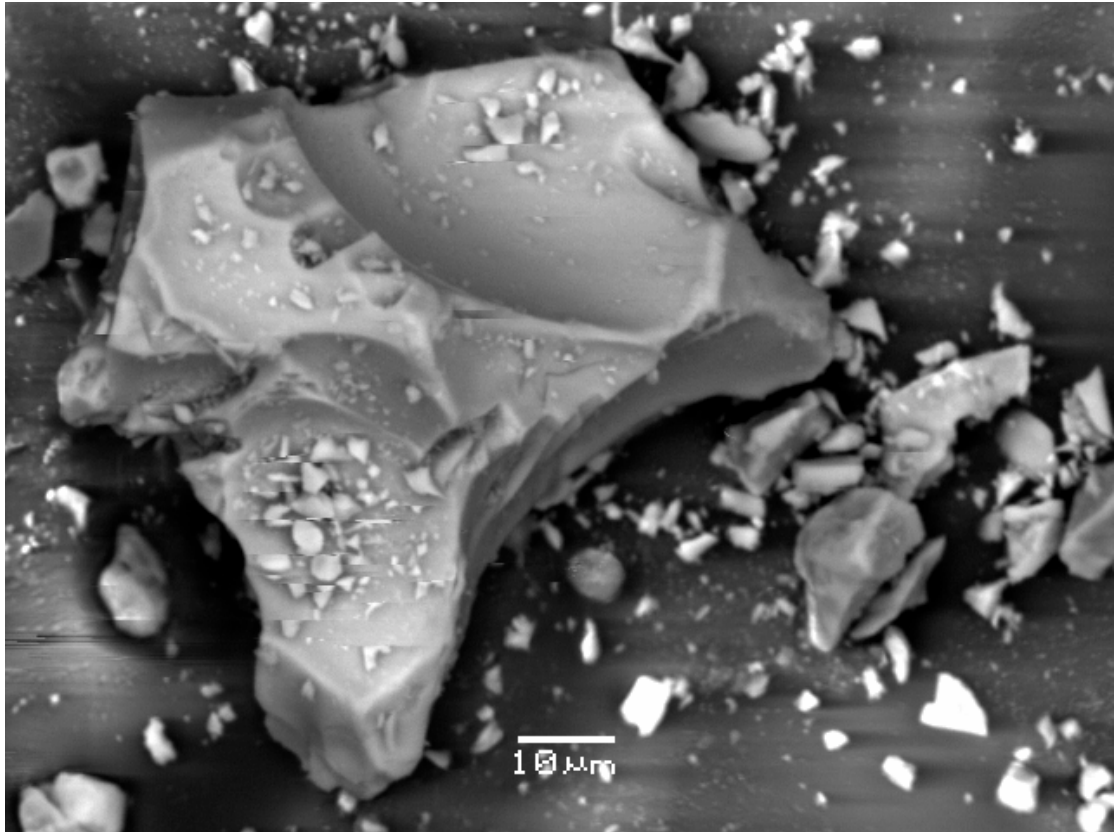
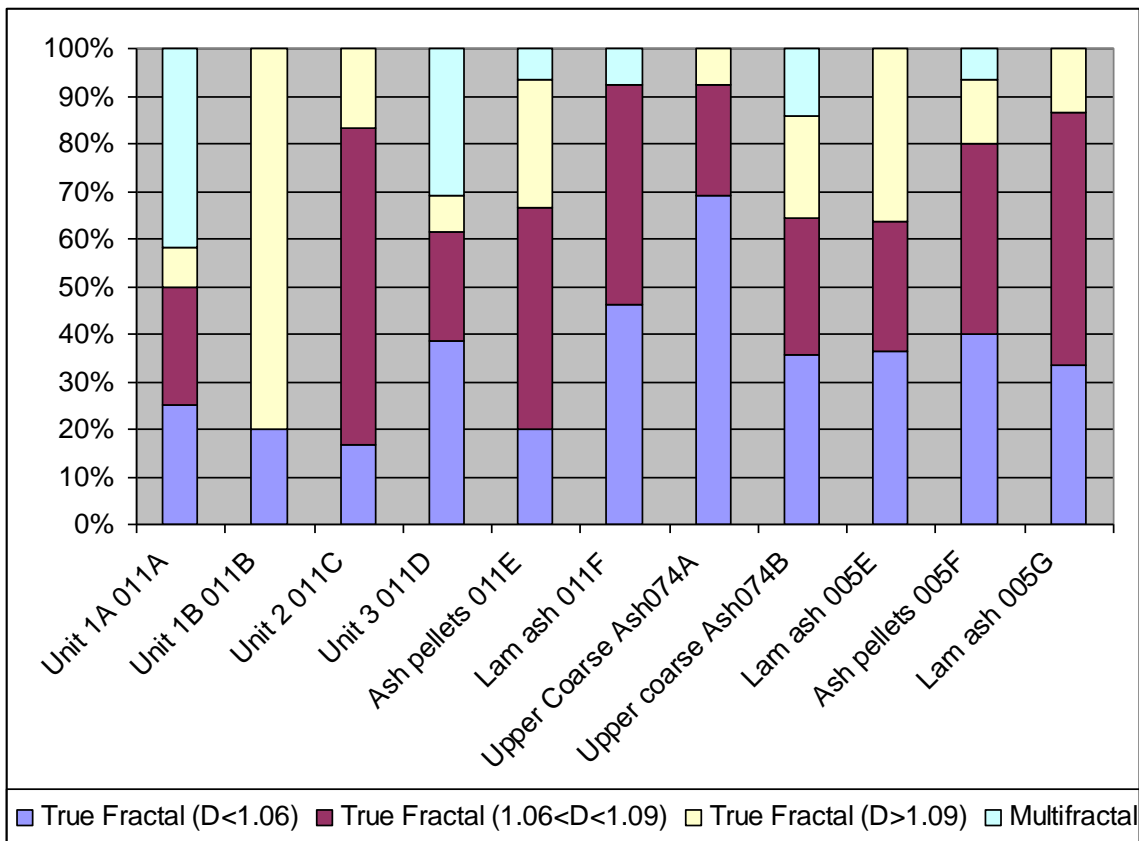


Figure 7.15: SEM image and fractal analysis of multifractal particle 011D g16.

The fraction of each of these grain types in each sample was plotted to show trends in grain types by unit and stratigraphic position (Fig. 7.16). Samples 10JAUOK011A (Unit 1A), 10JAUOK011D (Unit 3), and 10JAUOK074B (Upper Coarse Ash) have the most multifractal particles of all analyzed units. Sample 10JAUOK011A (Unit 1A) has the most multifractal particles at around 40%, and qualitative examination of these particles confirms that their shapes are different from the majority of 2008 grains. The multifractal particles from Unit 1A are highly vesicular and have shapes likely controlled by gas expansion and formed by vesicle walls (Fig. 7.14).



**Figure 7.16:** Percentage of fractal grain types by unit.

There appears to be little difference between the shapes, surface features, or vesicularity of true fractal particles of low, intermediate, or high fractal dimension, as

grains from each of these categories appear similar, and no trends are visible in the abundance of these categories by stratigraphic position (Fig. 7.16). The monofractal particles analyzed generally have simple blocky shapes, low to no vesicularity, and stepped surfaces, supporting a phreatomagmatic origin. The main significant difference is between monofractal and multifractal particles, as qualitative examination of each group confirms that multifractal particles appear to be magmatically fragmented and monofractal particles show evidence of phreatomagmatic fragmentation. Vesicular grains with blocky shapes are present in the 4-phi size and most of these vesicular blocky grains are monofractal particles (Fig. 7.4b, c). SEM images and fractal analyses of all grains are included in Appendix C.

#### **Interpretations from fractal analysis:**

From the dominance of true fractal particles over multifractal particles, I infer that phreatomagmatic fragmentation was dominant in the production of 4-phi pyroclasts for most of the eruption. The few multifractal particles analyzed are found mostly in Unit 1A, Unit 3, and an upper coarse ash. Unit 1A has a grain-size distribution indicating magmatic fragmentation, and the relative abundance of multifractal particles compared to other units supports this. Unit 2, the other open-framework coarse unit, was expected to contain more magmatic particles, but this is not shown by fractal analysis. Unit 3 contains coarse material and fine ash, and a magmatic component of fragmentation may have contributed multifractal particles. The upper coarse ash units may have been produced with a lower water-magma ratio than other upper deposits, and the presence of multifractal particles in 10JAUOK074B appears to support this inference.

## **Chapter 8: Discussion**

I begin this chapter in section 8.1 with estimations of erupted volumes, magma mass fluxes, and column heights in the 2008 Okmok eruption. Section 8.2 includes discussions of eruption mechanisms active at vents and within the eruption column. In section 8.3, I present a model for the eruption based on field observations and lab measurements.

### **8.1 Eruption Parameters:**

The volume of total erupted material, the mass flux during basal unit production, and the heights of eruption columns are important eruption parameters that quantify the magnitude of the 2008 Okmok eruption and facilitate comparisons with other eruptions. Calculations of these parameters are presented in the following sections (Tables 8.1-2)

Eruption volume calculations											
	Volume (km <sup>3</sup> )	Tephra Density (kg/m <sup>3</sup> )	Magma Density (kg/m <sup>3</sup> )	Total Mass (kg)	Magma + Lithic Dense Rock Equivalent (DRE) (km <sup>3</sup> )	Juvenile Percentage	Magma DRE (km <sup>3</sup> )	Magmatic Equivalent Mass (kg)	Time for eruption (s)	Mass Flux (kg/s)	Magma mass flux (kg/s)
<b>Total Eruption Products</b>	0.808	1600	2962	1.2928E+12	0.436	50%	0.218	6.46E+11	3283200	3.94E+05	1.97E+05
<b>Total Eruption Products</b>	0.808	1600	2962	1.2928E+12	<b>0.436</b>	60%	0.262	7.76E+11	3283200	3.94E+05	<b>2.36E+05</b>
<b>Total Eruption Products</b>	0.808	1600	2962	1.2928E+12	0.436	70%	0.306	9.05E+11	3283200	3.94E+05	2.76E+05
<b>Basal Units minimum</b>	0.078	1600	2962	1.24576E+11	0.042	60%	0.025	7.47E+10	15420	8.08E+06	4.85E+06
<b>Basal Units maximum</b>	0.090	1600	2962	1.4471E+11	0.049	60%	0.029	8.68E+10	13620	1.06E+07	6.37E+06
<b>Basal Unit best est.</b>	0.090	1600	2962	1.4471E+11	0.049	60%	0.029	8.68E+10	<b>14400</b>	<b>1.00E+07</b>	<b>6.03E+06</b>
<b>Upper Units</b>	0.718	1600	2962	1.14809E+12	0.388	60%	0.233	6.89E+11	3268800	3.51E+05	2.11E+05

**Table 8.1:** Eruption Parameter Calculations using ArcGIS method

Eruption volume calculations											
	Volume (km <sup>3</sup> )	Tephra Density (kg/m <sup>3</sup> )	Magma Density (kg/m <sup>3</sup> )	Total Mass (kg)	Magma + Lithic Dense Rock Equivalent (DRE) (km <sup>3</sup> )	Juvenile Percentage	Magma DRE (km <sup>3</sup> )	Magmatic Equivalent Mass (kg)	Time for eruption (s)	Mass Flux (kg/s)	Magma mass flux (kg/s)
<b>Total Eruption Products</b>	0.730	1600	2962	1.16721E+12	0.394	50%	0.197	5.84E+11	3283200	3.56E+05	1.78E+05
<b>Total Eruption Products</b>	0.730	1600	2962	1.16721E+12	<b>0.394</b>	60%	<b>0.236</b>	7.00E+11	3283200	3.56E+05	<b>2.13E+05</b>
<b>Total Eruption Products</b>	0.730	1600	2962	1.16721E+12	0.394	70%	0.276	8.17E+11	3283200	3.56E+05	2.49E+05
<b>Basal Units minimum</b>	0.127	1600	2962	2.02646E+11	0.068	60%	0.041	1.22E+11	15420	1.31E+07	7.89E+06
<b>Basal Units maximum</b>	0.127	1600	2962	2.02646E+11	0.068	60%	0.041	1.22E+11	13620	1.49E+07	8.93E+06
<b>Basal Unit best est.</b>	0.127	1600	2962	2.02646E+11	0.068	60%	0.041	1.22E+11	<b>14400</b>	<b>1.41E+07</b>	<b>8.44E+06</b>
<b>Upper Units</b>	0.603	1600	2962	9.64568E+11	0.326	60%	0.195	5.79E+11	3268800	2.95E+05	1.77E+05

**Table 8.2:** Eruption Parameter Calculations using method of Fierstein and Nathanson (1992)

### 8.1a Estimation of total eruption volume

The total erupted volume of proximal through distal deposits has been estimated by surface analysis in ArcGIS and by a two-straight-line exponential fit following the methods of Fierstein and Nathanson (1992) (Figure 8.1). The two-straight-line exponential fit model accounts for distal deposits falling in the ocean that are neglected in the ArcGIS surface analysis. The ArcGIS estimate directly uses each thickness measurement and assumes nothing other than straight line changes between each point. The bulk volume estimated by the ArcGIS method is  $0.808 \text{ km}^3$  and that estimated by the two-line exponential fit is  $0.730 \text{ km}^3$ , values that are within the errors of each method. Since the distribution of deposits was altered by plume scrubbing, the direct surface analysis method may provide a better estimate of total deposit volume because it does not rely on assumptions of thinning trends.

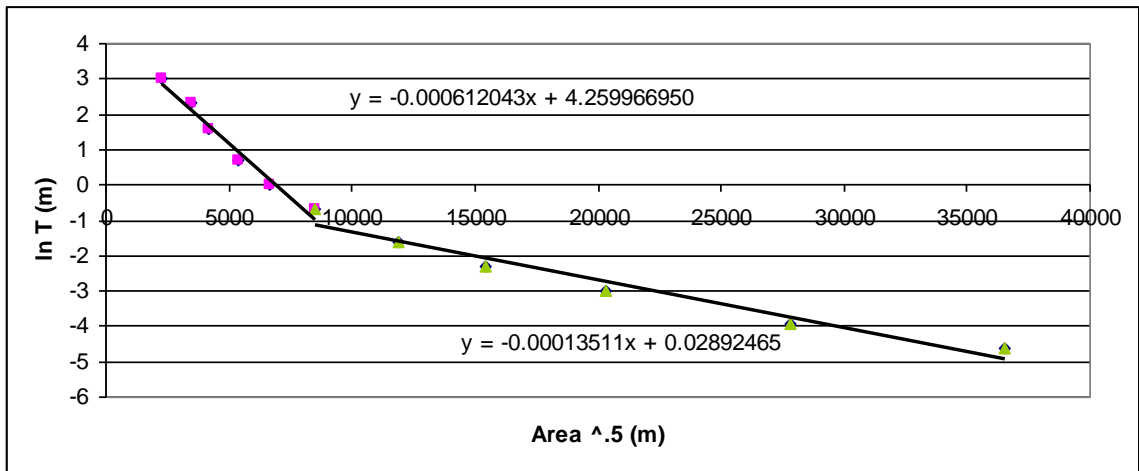


**Figure 8.1:** Log of thickness versus the square root of area for Okmok 2008 total deposits along with calculated best-fit straight lines for calculating volume. Purple and green data points define the proximal-medial and medial-distal thinning trends.

The dense-rock equivalent (DRE) magmatic volume of the 2008 eruption were calculated assuming a tephra density of  $1600 \text{ kg/m}^3$  and a glass density of  $2962 \text{ kg/m}^3$ .

Componentry analysis reveals that 50-80% of grains in 2008 Okmok material in the 2-phi and -0.5-phi sizes is juvenile. The average juvenile grain percentage is 57% in the 2-phi size and 63% in the -0.5-phi size, producing a best estimate of 60% juvenile material for the 2008 deposits. The dense rock equivalent (DRE) magmatic volume based on a bulk volume of 0.808 km<sup>3</sup> and juvenile content of 60% is 0.262 km<sup>3</sup> DRE.

### 8.1b Estimation of basal unit volume

The total volume of Units 1A, 1B, 2, and 3A is estimated by calculating their volume in GIS and by the methods of Fierstein and Nathanson (1992) (Fig 8.2). For basal units, a larger proportion of material was lost into the sea than for the total deposits and plume scrubbing processes were not as dominant as for total deposits, so the estimate following Fierstein and Nathanson (1992) is likely more accurate than the direct surface estimate using ArcGIS. The total bulk volume calculated by the two-straight-line exponential fit is 0.127 km<sup>3</sup>. The bulk density of basal units was similar to the total bulk density for 2008 deposits so 1600 kg/m<sup>3</sup> is used as well as a juvenile content of 60% to estimate the magmatic DRE at 0.041 km<sup>3</sup>.

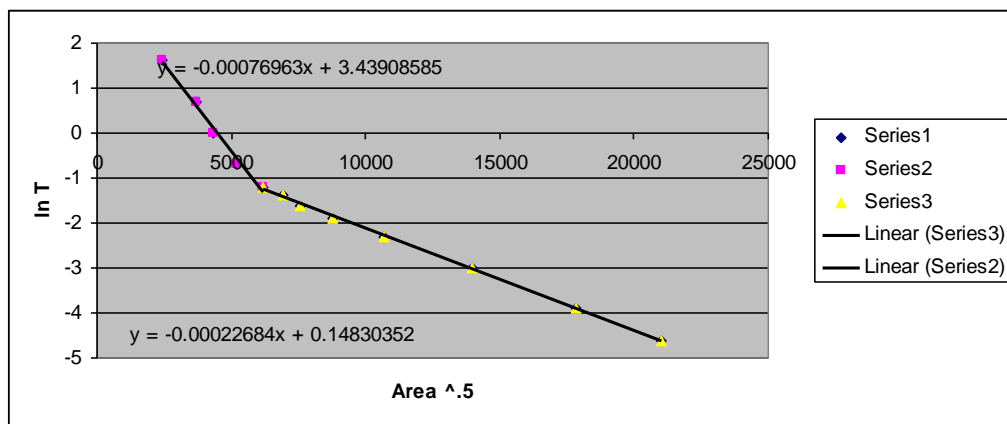


**Figure 8.2:** Log of thickness versus the square root of area for Okmok 2008 Units 1-3A along with calculated best-fit straight lines for calculating volume.

Subtracting the DRE volume of basal units ( $0.041 \text{ km}^3$ ) from that of total deposits ( $0.262 \text{ km}^3$ ) provides  $0.221 \text{ km}^3$  as the DRE volume of material erupted after the first four-hour opening sequence. The volume of tephra produced in the first four hours of eruption is around 16% of the total erupted volume, and was erupted in 0.4% of the total duration of the eruption. The remaining five weeks of eruption produced about 84% of the total volume over 99.6% of the eruption duration.

The volume of Unit 1A was estimated using the ArcGIS method as above, but the number of sites with well-defined thicknesses of Unit 1A was less than those with measured total basal deposits. The resulting volume estimate is  $1.83 \times 10^7 \text{ m}^3$ . Isopach resolution was too poor for accurate estimation using the methods of Fierstein and Nathanson (1992).

### **8.1c Estimation of mass flux during opening sequence**

The mass of tephra erupted per second is an eruption parameter important for understanding conduit processes, classifying eruptive intensity, and comparing eruptions from different volcanoes. The data available for the opening sequence of the 2008 Okmok eruption from field thickness measurements and satellite imagery allow a precise estimation of the mass flux for the opening sequence.

To estimate mass flux, the total mass of the opening sequence deposits and the length of time for deposition are needed. The time period in which Units 1, 2, and 3A were deposited is well constrained by satellite data to the first ~4.5 hours of the eruption. The eruption began around 19:43 UTC July 12, and the shift in wind direction occurred

between images taken at 23:30 UTC July 12 and 00:00 UTC July 13. Therefore, the minimum time for basal unit deposition is around 227 minutes, and the maximum is around 257 minutes. The best estimate case was made using a volume of  $1.267 \times 10^8 \text{ m}^3$ , bulk density of  $1600 \text{ kg/m}^3$ , a time of 240 minutes, and a juvenile content of 60%, resulting in a magma mass flux of  $8.44 \times 10^6 \text{ kg/s}$ .

Magma mass flux was also calculated for Unit 1A. The appearance of white steam plumes at 21:30 UTC July 12 may constrain the deposition of Unit 1A to the first 107 minutes of the eruption. The resulting estimate for magma mass flux (assuming 60% juvenile material and bulk density of  $1600 \text{ kg/m}^3$ ) is  $2.74 \times 10^6 \text{ kg/s}$ . Unit 1A is the coarsest deposit of the 2008 eruption and some of the highest columns were measured during Unit 1A deposition, suggesting that the Unit 1A magma flux should be as great as or greater than the average for all basal units. The estimate for Unit 1A magma flux is probably low due to a low estimate of the volume of Unit 1A, as the number of sites with accurately measurable thicknesses was limited and thicknesses of Unit 1A were very difficult to measure in proximal sites around the vents. The magma flux for Unit 1A may have been higher than the average of basal units, but it cannot be confirmed through this calculation.

The magma mass flux for the remainder of the eruption after basal unit deposition (after Unit 3A) is much lower than for basal units (Table 8.1). The estimated magma mass flux is around  $2 \times 10^5 \text{ kg/s}$  (Table 8.2), about 2.4% of the basal unit flux. The average magma flux for the entire eruption is only slightly higher, at  $2.36 \times 10^5 \text{ kg/s}$  (Table 8.1). Field characteristics of upper units, such as thin laminations and fine grain

size, support interpretations of low magma flux and slow tephra deposition during the last five weeks of the eruption.

### **8.1d Comparison of measured column height with calculated column height**

#### **Isopleth Areas**

Isopleth data were sufficient to make estimates of column height for Unit 1 as a whole. I calculated the area of the isopleths (Figure 8.3) and then plotted these data onto Carey and Sparks (1986) graphs for  $1500 \text{ kg/m}^3$  pumice and  $2500 \text{ kg/m}^3$  lithic clasts (Figs. 8.4-5). Using  $1500 \text{ kg/m}^3$  for pumice density, the height of buoyancy is 13-17 km and the column-top height is 17-23 km. Using the plot assuming  $2500 \text{ kg/m}^3$  lithic clasts gives a column height of buoyancy of 14-18 km and a column-top height of 19-25 km. The density of basal deposits is around  $1600 \text{ kg/m}^3$ , and the large clasts are slightly denser than the overall deposits, so the best estimates will be intermediate between values estimated with  $1500 \text{ kg/m}^3$  and  $2500 \text{ kg/m}^3$  clasts. My best estimate for the column depositing Unit 1 is a height of neutral buoyancy of 16 km and a column top height of 20 km.

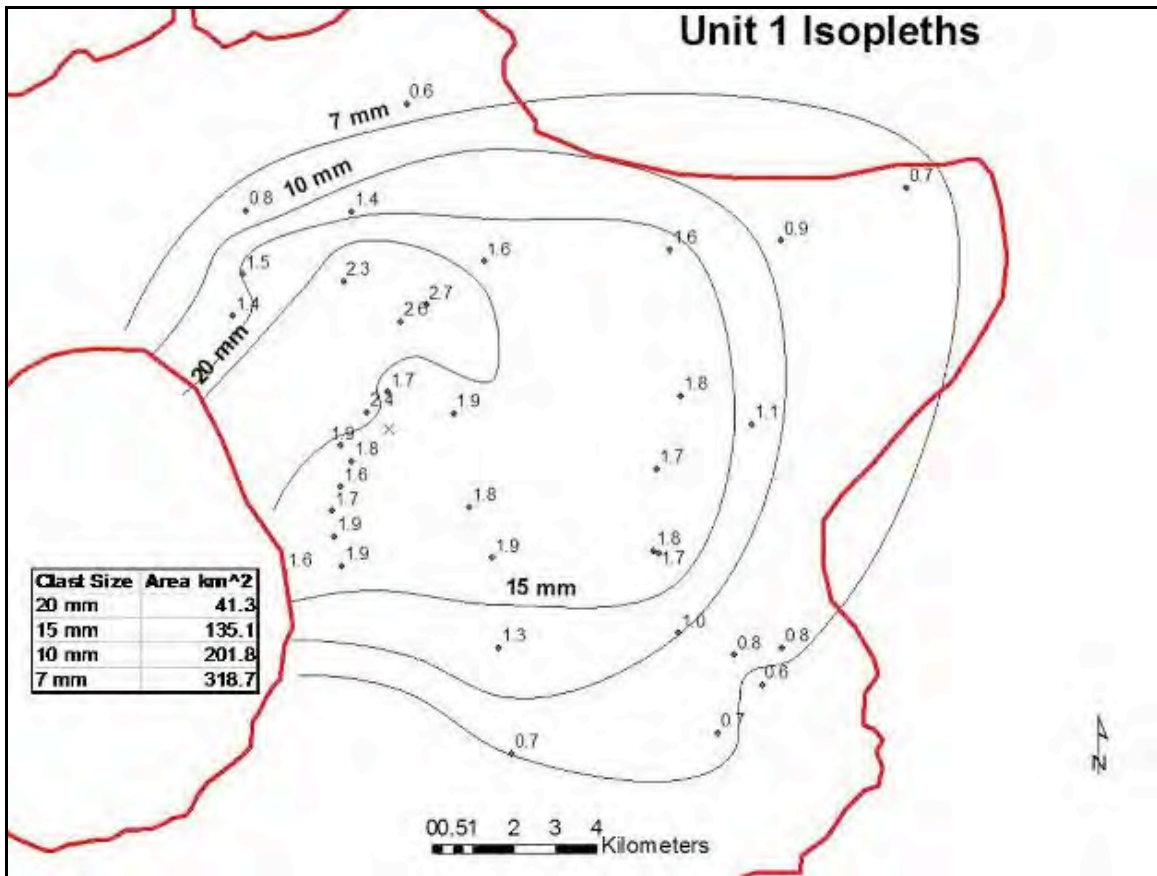


**Figure 8.3:** Isopleths for Unit 1 with calculated areas.

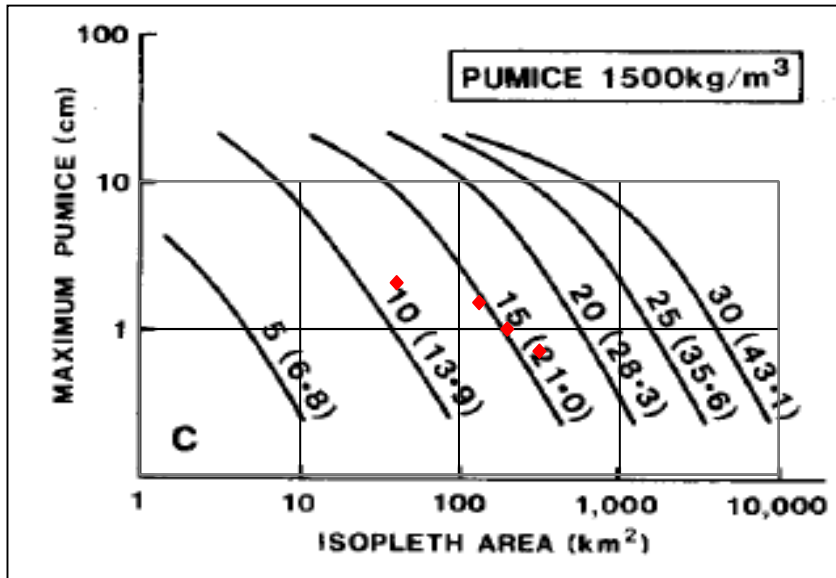


**Figure 8.4:** Isopleth area vs. maximum pumice size for lithic clasts with density of 1500 kg/m<sup>3</sup>. Black curved lines are lines of equal plume height, and the height of neutral buoyancy is shown first, followed by the plume-top height in parentheses. 2008 Okmok data is plotted as red diamonds (Carey and Sparks 1986).

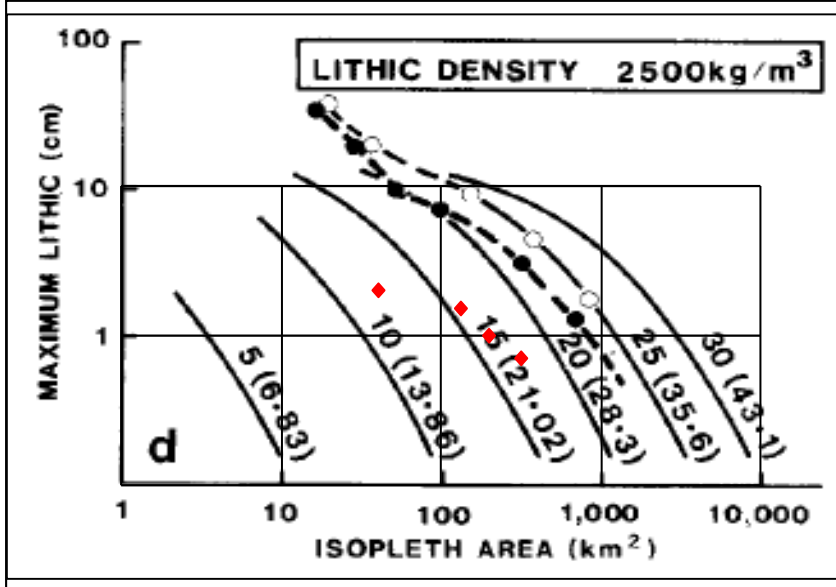


**Figure 8.5:** Isopleth area vs. maximum pumice size for lithic clasts with density of 2500 kg/m<sup>3</sup>. Black curved lines are lines of equal plume height, and the height of neutral buoyancy is shown first, followed by the plume-top height in parentheses. 2008 Okmok data is plotted as red diamonds (Carey and Sparks 1986).

## **Column heights measured by remote sensing**

Column heights during the opening sequence of the eruption were estimated by geometric image analysis of Geostationary Operational Environmental Satellite (GOES) images (Fig. 3.8) (Larsen et al., 2009). The maximum column height measured was 16 km above mean sea level (AMSL). Column heights estimated using the methods of Carey and Sparks (1986) agree within a few km with these measured column heights for the opening sequence, as the calculated column-top height was around 20 km and the maximum measured column-top height was 16 km. The column heights measured by remote sensing are probably more accurate, as remote sensing estimates are a more direct measurement than estimations based on isopleth areas.

## **8.2 Eruption Mechanisms**

### **8.2a Vent Mechanisms**

#### **Classifying Eruptive Style**

Violent eruptions of mafic magmas are an active topic of study and are becoming better understood and classified through work on modern and ancient eruptions. The violent strombolian mechanism was first defined by MacDonald (1972), included in Walker's (1973) classification of eruption styles, and has become better defined through the work of Arrighi et al. (2001) and Pioli et al. (2008). Subplinian basaltic eruptions have been described in the historic record of Vesuvius by Arrighi et al. (2001). Costantini et al. (2008) described the Fontana Lapilli, a deposit from a basaltic Plinian eruption.

Explosive basaltic eruptions were classified by Walker (1973) based on fragmentation and dispersion values, but more recent studies have placed more value on magma mass flux and column height. Violent strombolian eruptions have been defined as having column heights of 2-6 km, magma mass flux values of  $10^4$ - $10^5$  kg/s (Pioli et al. 2008), and dispersal (D value from Walker 1973) in the 10's of square km. Subplinian eruptions have column heights greater than 10 km, magma fluxes of greater than  $10^6$  kg/s, and dispersals of greater than around 150 km<sup>2</sup> (Arrighi et al. 2001). The 2008 eruption of Okmok is characterized by two distinct phases, the opening sequence and the remainder of the eruption, and these phases should be dealt with separately.

The opening sequence produced 16 km columns and had a magma flux around  $9 \times 10^6$  kg/s. These parameters fit well with the subplinian values proposed by Arrighi et al. (2001). The dispersal, defined as the area within the  $0.01 \times T_{\max}$  isopach is around 40-50 km<sup>2</sup> for basal units, fitting better with a violent strombolian dispersal than subplinian.

Wong and Larsen (2009) described the Middle Scoria sequence, deposits of a similar mid-Holocene eruption of Okmok. The Middle Scoria eruption produced columns with estimated heights over 10 km and mass discharge exceeding  $10^6$  kg/s early in the eruption and total dispersal of 142-249 km<sup>2</sup>, suggesting subplinian intensities in the early phases of eruption. The duration of the Middle Scoria eruption was probably of violent strombolian intensity, with plume heights and discharge rates slightly lower than those in the early eruption phase.

The 2008 eruption is very similar in intensity to the Middle Scoria eruption, but parameter constraints are much better for the 2008 eruption, as column heights were directly measured and mass discharge estimates are more precise. Measured plume

heights in the 2008 eruption were mostly 2-8 km, with 16 km heights in the opening sequence and heights of 10-12 km around 5 times in the last five weeks of eruption. The average magma mass flux for the duration of the eruption was around  $2.36 \times 10^5$  kg/s, and the dispersal value for the total eruption products is around 50-100 km<sup>2</sup>. Based on these values, the majority of the 2008 eruption was violent strombolian in intensity and strongly phreatomagmatic with the opening sequence reaching strong subplinian intensity for a short duration.

Houghton (2000) characterized explosive basaltic eruptions based on thickness and isopach area. Wong and Larsen (2009) used this method and found the Middle Scoria units intermediate between Houghton's strombolian and subplinian fields. The isopach data for the 2008 total and basal deposits is plotted on a thickness vs. isopach area graph with examples from the basaltic-plinian Fontana lapilli eruption (Fig 8.7). The total 2008 deposits plot centrally in the subplinian field, while basal deposits are intermediate between strombolian and subplinian.

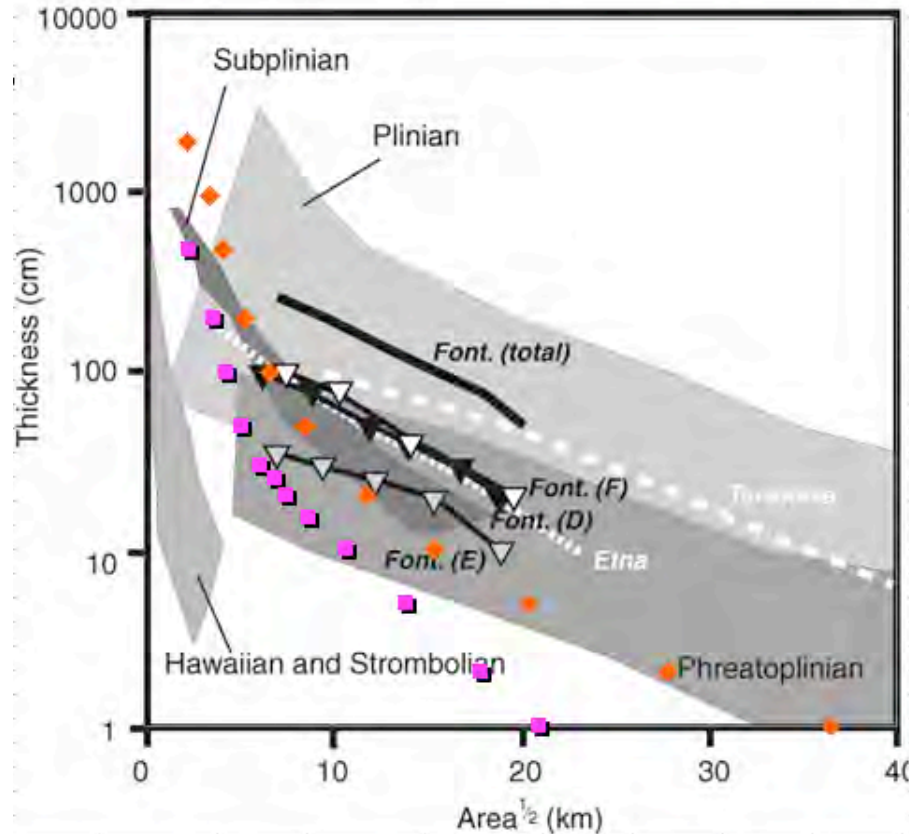


**Figure 8.6:** Plot of tephra thickness vs. isopach area with fields in grey for typical explosive basaltic eruption types and data from other explosive basaltic eruptions shown. Okmok total deposits are plotted as orange diamonds, basal units 1-3A are plotted as rose squares (modified from Wehrmann et al. 2006).

Eruptions with subplinian sequences include the 1822 and 1906 eruptions of Vesuvius, the 1970 eruption of Hekla volcano, Iceland, eruptions of Mono Craters, and the 1980 eruption of Mt. St. Helens (Arrighi et al. 2001). These events produced tephra volumes from  $1 \times 10^6 \text{ m}^3$  to  $189 \times 10^6 \text{ m}^3$ . The Okmok 2008 opening sequence produced a bulk tephra volume of  $127 \times 10^6 \text{ m}^3$ , similar to the  $70 \times 10^6 \text{ m}^3$  observed for Hekla and  $189 \times 10^6 \text{ m}^3$  observed in the May 18 event of the 1980 St. Helens eruption. Ash dispersals in subplinian eruptions are significantly less than those observed for Plinian eruptions. This may result from the short duration of subplinian events preventing complete eruption cloud development (Self 1976). The short (4 hour) time of the Okmok

opening sequence may fit well with the subplinian characteristic of short times, and may have prevented complete column development and limited tephra dispersal.

Arrighi et al. (2001) stated that the most important characteristic for defining eruption intensity may be the mass discharge rate (MDR), or the total mass flux of magma and lithic material, which ranges from  $10^6$  -  $10^7$  kg/s for subplinian eruptions. The MDR of the Okmok opening phase is  $1.41 \times 10^7$  kg/s (greater than calculated magma mass flux, as it includes lithic material). On the basis of MDR, the Okmok opening sequence falls at the high-intensity end of the range of values for subplinian eruptions.

The violent strombolian mechanism has been well defined through the eruption of Parícutin as described by Pioli et al. (2008). The 2008 eruption of Okmok is similar to the Parícutin eruption in many ways. For the majority of both eruptions, column heights were 2-8 km and compositions were basaltic andesite to andesitic. Two populations of juvenile material were produced in each eruption, a tan scoria and a darker scoria. Pajarito clasts are abundant in Parícutin lapilli and were observed in basal deposits from Okmok volcano. The grain-size distributions of the products of Parícutin are also very similar to those of 2008 Okmok deposits (Fig. 8.8). Deposits in the coarse-grained better-sorted field from Parícutin were produced during more energetic violent strombolian phases of the eruption, while those in the finer-grained poorly sorted field were produced during less energetic phases (Pioli et al. 2008).

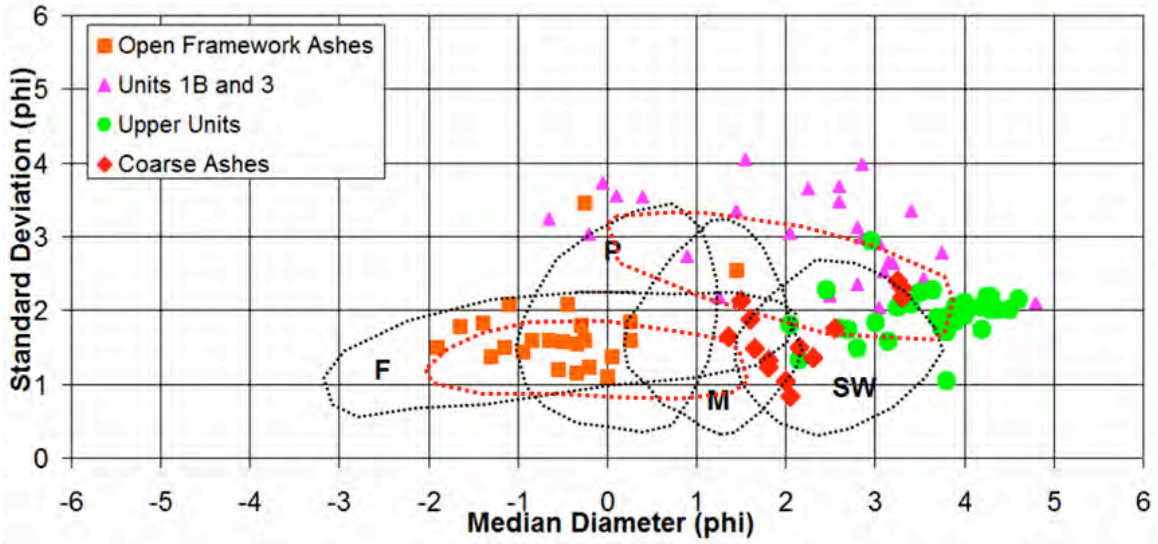


**Figure 8.7:** Plot of standard deviation versus median diameter (phi size) for samples from 2008 Okmok Deposits. Fields from Wohletz (1983) are shown in black dotted lines for fall (F), planar (P), massive (M), and sandwave (SW) surge deposits. Fields of Parícutin deposits (Pioli et al. 2008) are shown in red dotted lines.

The 2008 Okmok eruption was different from the Parícutin eruption in a number of important ways. The duration of the 2008 eruption was five weeks rather than many years, and while total tephra volume was similar, the mass flux was much higher in the 2008 eruption. No lava effusion was associated with the 2008 Okmok eruption, and lava effusion was cited as a defining characteristic of the Parícutin eruption. Pioli et al. (2008) hypothesize that fluxes beyond the observed  $10^5$  kg/s would have produced an eruption with subplinian characteristics and no lava effusion, a fitting description of the 2008 Okmok event. The Parícutin eruption shows little evidence of water-magma interaction and was inferred to be primarily magmatic with limited water-magma interaction in some of the late phases (Pioli et al. 2008). Observations of the 2008 eruption and deposit characteristics indicate that phreatomagmatism was a primary form of fragmentation in the last five weeks of the 2008 eruption.

The Volcanic Explosivity Index (VEI) discussed by Newhall and Self (1982) is a useful scale for defining eruption explosivity and magnitude. VEI 4 events have plumes rising to 10-25 km above sea level and total bulk tephra eruption volumes from 0.1-1.0 km<sup>3</sup>. The 2008 eruption had a volume of 0.808 km<sup>3</sup> bulk and a maximum column height of 16-19 km above sea level, placing it in the middle of the VEI 4 category. VEI 4 events typically have continuous blast phases lasting from 1-6 hours, and the 4-hour opening sequence in the 2008 eruption fits that window well. The 1997 Okmok eruption was a VEI 2-3 event at its highest intensity, producing around 0.05 km<sup>3</sup> total material, primarily in lava flows (Smithsonian Global Volcanism Program 2011). After the initial four-hour opening sequence, the 2008 Okmok eruption settled down to a lower magnitude eruption (VEI 2-3). Other eruptions of Okmok reaching a VEI 4 magnitude include the Middle Scoria eruption and likely the 1817 eruption.

Recent eruptions of magnitude similar to the 2008 Okmok eruption include the 1976 eruption of Augustine Volcano, Alaska, the 1992 eruption of Mt. Spurr, Alaska, and the 2010 eruption of Eyjafjallajökull Volcano, Iceland (Newhall and Self 1982, Gudmundsson et al. 2010, McGimsey et al. 2001). The 1992 Mt. Spurr eruption produced plumes up to 14 km above sea level (McGimsey et al. 2001). The total volume of the 1992 Mt. Spurr eruption was only around 0.04 km<sup>3</sup> DRE, but all tephra was produced in three short-lived (3.5 to 4 hour) Vulcanian to sub-Plinian events (McGimsey et al. 2001). Mass fluxes calculated for these three events are around  $3.0 \times 10^6$  kg/s, on an order similar to the initial four hours of the 2008 Okmok eruption.

The 2008 Okmok eruption occurred around two years before the 2010 eruption of Eyjafjallajökull volcano, Iceland, and these eruptions have some significant similarities.

The 2010 Eyjafjallajökull eruption occurred over a similar length of time as the Okmok eruption and produced around half the volume of tephra ( $\sim 0.17 \text{ km}^3$  DRE), but maximum column heights in the 2010 Eyjafjallajökull eruption were around 10 km above sea level (Gudmundsson et al. 2010). The average magma mass flux of the 2008 Okmok eruption for the entire duration is around  $2.36 \times 10^5 \text{ kg/s}$  and the maximum magma mass flux, during the first four hours, is  $8.4 \times 10^6 \text{ kg/s}$ . The 2010 eruption of Eyjafjallajökull had magma mass fluxes of  $\sim 4 \times 10^5 \text{ kg/s}$  during the phase of highest discharge (Gudmundsson et al. 2010b) and the average rate for the duration of the eruption was around  $40 \text{ m}^3/\text{s}$  DRE ( $\sim 1.1 \times 10^5 \text{ kg/s}$  assuming  $2900 \text{ kg/m}^3$  magma) (Höskuldsson et al. 2010). The average magma mass fluxes for the Okmok eruption were around double that of the Eyjafjallajökull eruption, but the magma flux during the first few hours of the 2008 Okmok eruption was much higher than that of any events during the 2010 Eyjafjallajökull eruption.

### **Water-magma Interaction**

Basaltic phreatomagmatic eruptions range widely in eruptive style from low-explosivity pillow-basalt effusion and thermal granulation (Sonder et al. 2011) to high energy vapor explosions (Wohletz and Zimanowski 2000). The style of water-magma varies depending on the rates of surface cooling and deformation or new-surface formation (Mastin 2007). Rapid cooling coupled with high deformation rates produces vapor explosions, the explosive end member of phreatomagmatic interaction (Mastin 2007). Water-magma ratios are an important factor in controlling the rate of magma cooling, the efficiency of fragmentation, and the grain sizes produced (Wohletz 1983).

Water-magma interaction was an important process in the 2008 Okmok eruption, causing the efficient fragmentation that produced large amounts of fine ash. Evidence for water-magma interaction includes the availability of water in the caldera, observed steam plumes, fine grain size of deposits, and the shapes and surface features of fine-ash particles. Lakes and aquifers within the caldera provided the water at the vents for phreatomagmatic interaction. The area around the 2008 vents within the caldera is underlain by alluvium and water-saturated bedded volcanic sediments deposited before the 1958 eruption (Byers 1959). Lava flows from the 1958 eruption from Cone A blocked drainage within the caldera, prevented surface drainage to Crater Creek, the only outlet, and formed the Cone D lake (Fig. 8.9). The lakes and saturated alluvium and volcanic sediments held water that moved over the surface and through the subsurface to interact with magma rising to vents north and west of Cone D (Fig. 8.9).

The Cone D lake drained during the 2008 eruption, but its basin was enlarged by eruptive activity and refilled after the cessation of eruption in August 2008 (J. Larsen, personal communication, August 2010). The lake west of Cone D was formed during the 2008 eruption (Fig. 8.9). Meteoric water within the caldera was available and active during the 2008 Okmok eruption, providing the necessary water for phreatomagmatic interaction. White steam plumes observed during the eruption and visible in satellite imagery show that excess (non-interactive) water was carried into eruption columns. The plumes during the deposition of Unit 1A and from July 30 through August 4 were ash rich but most plumes for the duration of the eruption were steam dominated.

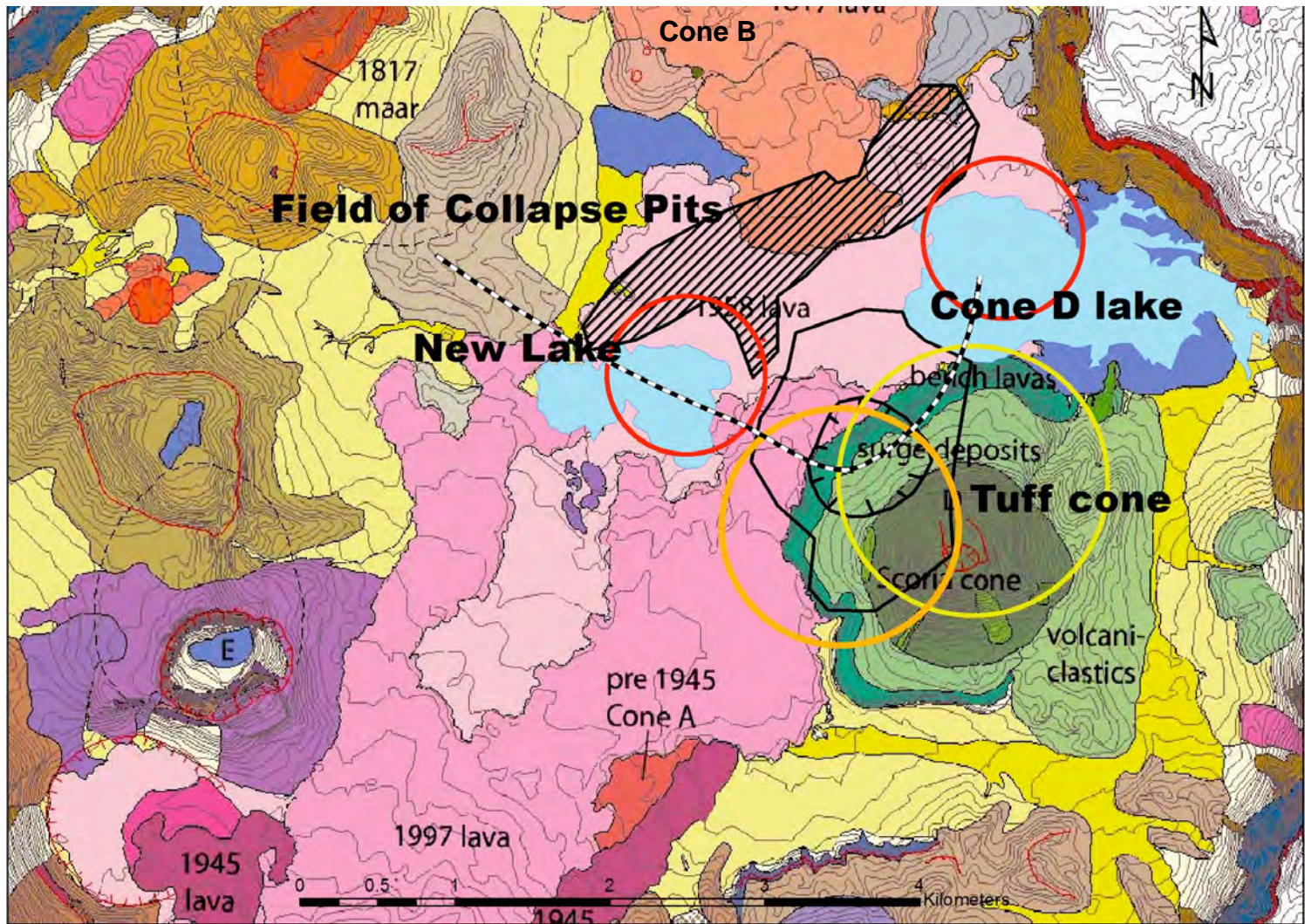


**Figure 8.8:** Post-eruption geology and features of Okmok Caldera (modified from Neal et al. 2011). July 13 vents in red, July 20 vent in orange, July 22 vent in yellow, and estimated dike location shown in dashed line.

The 1817 Okmok eruption was the most recent phreatomagmatic eruption at Okmok preceding the 2008 event (Begét et al 2004). The 1817 eruption was the largest from Okmok in historic times and was sourced from vents near Cone B (Fig. 8.9). It produced pyroclastic density currents that exited the caldera and destroyed an Aleut village on the coast of Umnak Island (Begét et al. 2004). The hydrologic setting of the northeast sector of the caldera, where the 1817 and 2008 eruptions occurred, is different from that of the southwest part of the caldera, where the majority of historic activity has taken place. Drainage from the entire caldera moves toward the lower-lying northeast sector of the caldera and exits through Crater Creek. Because of this drainage pattern, water is more available in lakes and shallow aquifers in the northeast sector of the caldera than the southwest sector. The availability of water in the northeast sector may explain the phreatomagmatic nature of the 1817 and 2008 events and the magmatic style of the events centered in the southwest, such as the 1997 eruption.

The availability of water varies in phreatomagmatic eruptions based on local hydrology and the form of water available. Eyjafjallajökull is much more heavily glaciated than Okmok, and subglacial eruptions occurred as well as phreatomagmatic eruptions fed by melted glacier ice (Gudmundsson et al. 2010). The rate of glacier ice melting controlled the supply of water available in the 2010 Eyjafjallajökull eruption and the eruption types seen are significantly different than those observed at Okmok. The 2010 eruption had three distinct phases: a) four days of subglacial and subaerial explosive activity with semi-continuous phreatomagmatic explosions; b) two weeks of weak magmatic eruptions and lava effusion; and c) twenty-one days of moderate Vulcanian activity (Larsen et al. 2010).

The fine average grain sizes of 2008 deposits are typical for the products of phreatomagmatic eruptions. Samples from 2008 deposits span the range of all fields for basaltic phreatomagmatic tephra on the sorting vs. median diameter plot of Wohletz (1983) (Fig. 8.8). The average 2008 Okmok deposit plots very near the average for all basaltic phreatomagmatic tephra. The grain-size distributions of basal units 1A and 2 fall within the field for fall deposits, as expected, but all other 2008 Okmok deposits do not fit well in the fields designated by Wohletz (1983). The other phreatomagmatic deposit types described by Wohletz (1983) are sandwave (SW), planar (P), and massive (M) surges. Some of the coarse ash units and other upper units plot within the sandwave surge or massive deposit fields, which are clearly not their depositional facies. Many upper units are much finer grained than any of the samples examined by Wohletz (1983). The poorly sorted basal and transitional units 1B and 3 do not fall within the described fields, as they are intermediate in median grain size but more poorly sorted than samples described by Wohletz (1983).

High water-magma ratios may have produced the very fine median grain sizes seen in many upper units. The grain-size distribution of the 2008 Okmok eruption deposits is consistent with other basaltic phreatomagmatic deposits, but some Okmok deposits exhibit poorer sorting and finer grain sizes than most basaltic phreatomagmatic eruptions. Observations during the eruption and abundant field evidence suggest that nearly all extracaldera deposits were emplaced by fallout from columns, whether 'normal' non-water-flushed fallout or water-flushed fallout in the form of ash pellets or 'ash rain'.

Self et al. (1980) presented an analysis of the 1977 eruption of Ukinrek Maars, which was the most recent phreatomagmatic eruption in North America prior to the Okmok eruption, and it occurred over ten days and formed two maar craters. The eruption was transitional between phreatomagmatic and strombolian, with plumes rising up to 6 km above sea level. The median grain size and sorting of medial deposits from Ukinrek have the same range of values as Okmok deposits, but most Ukinrek deposits are coarser grained, similar to Okmok Units 1A and 2. Samples with fine median grain sizes like most upper units from the 2008 Okmok deposits are rare in Ukinrek deposits. Water-magma ratios were likely much lower at Ukinrek than at Okmok and the supply of water to magma at Ukinrek may have been sporadic, allowing for alternating phreatomagmatic and magmatic eruption styles. The supply of water to magma at Okmok was continuous and plentiful, with changes in magma flux producing the variations in water-magma ratio.

Tephra produced in the Eyjafjallajökull 2010 eruption have similar grain-size characteristics to those produced in the Okmok eruption (Larsen et al. 2010). Around 50% of tephra deposited in medial sites at Eyjafjallajökull was finer than 63  $\mu\text{m}$  (4 phi) during the initial phase of the eruption. Interaction with glacial ice and meltwater with trachyandesitic magma at Eyjafjallajökull produced the fine-grained tephra that caused such significant aviation hazards (Larsen et al. 2010). The upper units of the 2008 Okmok eruption at medial sites contain 40-50% ash finer than 4 phi, similar to amounts seen in the Eyjafjallajökull tephra.

Fractal analysis of fine ash grain shapes from 2008 Okmok samples suggests that most fine ash particles were fragmented phreatomagmatically rather than magmatically. Particles with magmatic fractal characteristics are most concentrated in Unit 1A, the unit

with the lowest estimated water-magma ratio and largest magmatic component of fragmentation. Fractal analysis of fine ash shapes complements the qualitative examination of fine ash grain shapes and surface features and supports an interpretation that the eruption was characterized by mostly phreatomagmatic fragmentation with the exception of Units 1A and 2. The dominance of poorly vesicular blocky clasts with stepped surfaces and monofractal shapes in the important 4-phi size indicates that phreatomagmatic fragmentation was dominant in the production of both the 4-phi size and in the production of the entire grain-size population of fine-grained units and facies. Coarse-grained deposits, like Units 1A and 2, as well as the coarse fractions of Units 1B, 3, and upper coarse ash units, were probably fragmented magmatically, as indicated by the grain size, vesicularity, and shapes of coarse clasts in these units.

The deposits of explosive phreatomagmatic eruptions can have lithic contents greater than 90% (Wohletz and Zimanowski 2000). Explosions at depth fracture country rock, entrain fragments, and emplace these lithic fragments in deposits. Deposits from the 1977 eruption of Ukinrek Maars have lithic contents of 65-100%, with the highest lithic contents in units with the most phreatomagmatic character (Self et al. 1980). A typical maar volcano in the West Eifel volcanic field (PV) has an average lithic content of 80% (Raue 2004). The 2008 Okmok deposits contain 30-50% lithic material, with a mean around 30%.

The depth of water-magma interaction may control the amount of lithic fragments included in deposits, as deeper interactions, such as those at Ukinrek and other maar volcanoes, fragment more country rock than shallow interactions. The depth of interaction in the 2008 Okmok eruption was likely quite shallow, as the available water is

at the surface in lakes or near the surface in aquifers within a few hundred meters of the surface. The only identifiable lithic grains in the 2008 deposits are plagioclase-rich lava fragments from the bench lavas underlying Cone D that extend up to around 100 m below the caldera floor, a depth estimated from a cross section from Byers (1959). The depth of water-magma interaction is constrained above by the caldera floor and 100 m depth of plagioclase-rich lava flows and below by the 3-4 km depth estimates for the top of the magma chamber (Masterlark et al. 2005). The depth of water-magma interaction in the 2008 eruption was likely within a few hundred meters of the caldera floor, based on the relatively low lithic content and estimated aquifer depths, but may have been deeper, as identification of lithic fragments from greater depths would be difficult in this setting.

### **Style of Phreatomagmatism**

Water-magma interaction is well evidenced in the 2008 Okmok eruption and was an important factor in controlling the eruptive style and deposits emplaced. The deposit characteristics were influenced by the number of concurrently active vents and the processes occurring at each of these vents. The vent sites visible in satellite imagery and determined by field observations are limited to perhaps the tuff cone, the west side of Cone D lake, and the new lake (Figure 8.9). AVO geologists observed multiple vents concurrently active north of the tuff cone on August 2-3 (Larsen, personal communication, 2011).

The concurrent activity of multiple vents, especially during the later stages of the eruption, fits well with observations of the eruption column during that time. Videos taken during the 2008 eruption show some pulsing in the eruption column, but pulsing is

not consistently represented in deposits. The post July 13 eruption was characterized by periodic events that produced discrete low level plumes combined into a single continuous eruption column at height and with distance downwind. The overall column was one continuous expanding mass above the height of the discrete pulses. The upper deposits of the 2008 eruption lack the repetitive bedding typical of maar sequences, but this also may be explained by the concurrent activity of multiple vents. MFCI-type interactions at multiple simultaneously active vents could produce the observed pulses merging into a continuous column and emplace the non-repetitive massive fine ash deposits observed.

The cm-scale lapilli to medium ash pyroclasts produced in the 2008 eruption are dominantly vesicular rather than dense. The fine ash grains examined on the SEM had predominantly low vesicularity and other features consistent with MFCI fragmentation. The vesicularity of larger clasts suggests that mechanisms other than MFCI may have been important at points during the eruption, but the features of fine ash are consistent with MFCI fragmentation. The phreatomagmatism model of Mastin (2007) may provide a mechanism for fine ash production in a vesicular magma. Bubbly magma fragments can develop glassy rinds and shed them, producing fine ash and vesicular pyroclasts (Mastin 2007) in a continuous process, fitting well with observations of a continuous column. The growth and generation of glassy rinds requires external momentum inputs to cause the turbulent deformation or shredding of magma particles in order to shed glassy rinds. In settings like the vents within Okmok caldera, momentum may be supplied by a primary magmatic eruption driven by gas expansion, and water-magma interaction may serve to reduce grain size rather than provide explosive energy. Thermal

granulation, another regime of water-magma interaction, could occur in a continuous column but fails to produce the fine ash observed in the upper units (Sonder et al. 2011).

Plate-like or curved rind glass particles in the very fine ash sizes or fine ash particles with adhering rinds would provide evidence that the growth and disintegration of glassy rinds contributed to fine and very fine ash production. Plate-like very fine ash particles and fine ash grains with adhering plate-like ash are both present in the 2008 deposits but are not the dominant shapes present. Thermal granulation experiments produced fragments with primarily blocky shapes and secondarily limu or sheet-like shapes (Sonder et al. 2011). Thermal granulation does not produce significant material smaller than 3 phi and is not a likely mechanism in the production of fine ash in the 2008 eruption. The growth and disintegration of glassy rinds likely played a role in fragmentation and the production of fine ash in the 2008 Okmok eruption, but was not the primary mechanism.

Vapor explosions occurring at multiple vents in rapid succession may provide the best explanation for the observed column dynamics and deposit character. ‘Wet’ surges at La Fossa di Vulcano (Büttner et al. 1999) produced by MFCI interactions with excess water were less efficient in the conversion of thermal to mechanical energy than ‘dry’ interactions in which all water was consumed. Wet surges produced deposits with median grain sizes finer than those produced by dry interactions, around 4 phi, similar to the upper units of the 2008 Okmok deposits. The low efficiency and fine median grain size produced by MFCI explosions with excess water may fit well with the low-energy pulses merging to form continuous columns and massive fine-grained deposits from the 2008 eruption.

## **Eruption conduit and multiple vents**

Multiple vents were active both simultaneously and at different times during the 2008 eruption. Satellite imagery shows at least three main plume sources during the eruption and Synthetic Aperture Radar (SAR) images show several more extending west-northwest from the tuff cone (J. Larsen, C. Neal, personal communication 2011). Observations of the eruption on August 2 and 3 confirm the simultaneous activity of multiple vents to the northwest of the tuff cone. The number of vents and spatial organization suggests that this eruption was fed by a dike trending west-northwest from the tuff cone through the location of the new lake (Figure 8.9).

Multiple points of eruption along a dike each had unique interaction with ground and surface water, producing a range of potential eruptive styles occurring simultaneously. The coarse-grained basal sequence was probably produced by a high-mass-flux eruption sourced from one main vent, but the opening of another vent along the dike with a lower mass flux and higher water-magma ratio may have produced the fine-grained material present in Unit 1B. MFCI-style vapor explosions occurring at a number of vents along a dike could have produced discrete pulses that merged together into a continuous column and emplaced the fine-grained upper units that lack repetitive bedding. Periodic episodes of high mass flux at a main vent, possibly the tuff cone, may have produced the coarse ash units in upper deposits. The activity of multiple vents along a dike suggested by satellite and ground observations provides compelling explanations for many of the complexities in the described deposits.

The primary control on the water-magma mass ratio at each vent was the magma mass flux, as excess water was available during the entire eruption. Periods of high

magma flux, such as the opening sequence and periods of coarse ash production during the late parts of the eruption, produced deposits with magmatic characteristics. The high magma flux overwhelmed available water and erupted without time for significant interaction. Lower magma-mass-flux periods produced the fine grain sizes characteristic of upper deposits, as low flux allowed sufficient time for effective water-magma interaction and fine fragmentation.

### **8.2b Eruption column mechanisms**

Ash aggregation and plume scrubbing were important column processes in the 2008 Okmok eruption, controlling the character and distribution of upper deposits. Plume scrubbing is well evidenced in the deposits by the presence of ash pellets and the enhanced deposition of fine ash in proximal and medial sites relative to distal locations. Ash aggregation likely occurred by liquid film binding rather than electrostatic attraction, as excess water was present in plumes throughout the eruption. Ash aggregates formed when plume water contents were 10-25 wt.% and ash rain fell when water content exceeded the aggregation window above 25 wt.%. Ash aggregation and plume scrubbing occurred to limited extents during the deposition of Units 1B and 3, evidenced by ash pellets and cored lapilli, but these processes began to control tephra facies and distribution after the deposition of Unit 3B. Ash-pellet units and layers of alternating laminae of fines-rich and fines-depleted ash evidence plume scrubbing and are abundant in upper units, showing the importance of ash aggregation and ash rain in the emplacement of upper units.

The local variations in upper unit stratigraphy suggest that ash pellet fall and ash rain occurred in localized storms. Conditions for producing these storms were controlled in part by the eruption column conditions, and also influenced by meteorologic conditions over the island. The upper fine units emplaced during these storms dominate proximal and medial sites to the east and southeast of vents, but thin rapidly farther east of vents (Fig. 8.10). In a 10-km transect east from the vents, the percentage of tephra thickness composed of fine-grained upper units decreases from over 75% to less than 15%. The enhanced deposition of fine ash in proximal and medial sites limited fine-ash emplacement in distal sites and reduced the distance travelled by fine ash. This process reduced the size of areas of fine ash content hazardous to air traffic.

The Okmok eruption showed that: a) phreatomagmatic eruptions occur without warning at Aleutian volcanoes; b) phreatomagmatic eruptions of mafic composition can produce significant amounts of fine ash and columns of sufficient height to inject ash into the stratosphere; and c) the column processes of plume scrubbing and ash aggregation can serve to reduce the distribution of fine ash and decrease the size of aviation hazards from ash plumes. The effects of plume scrubbing on aviation hazards should be taken into consideration when hazards assessment is performed on volcanoes with the potential to produce phreatomagmatic eruptions.

Ash aggregation and water flushing of plumes are an increasingly important topic in the study of volcanic plumes, as these processes significantly impact tephra distributions. Recent eruptions like the 2010 Eyjafjallajökull eruption, which interrupted air traffic for weeks and deposited trace amounts of ash in Europe, have brought ash dispersal monitoring to the forefront of modeling research (Gudmundsson et al. 2010).

Most ash distribution models have not addressed aggregation or have had difficulty in constraining its effects on plume distribution, but current model development is addressing aggregation (Folch et al. 2010). The data sets of 2008 Okmok tephra distribution and grain-size distribution may help constrain new models addressing ash aggregation in proximal and medial locations.



### **8.3 Eruption Model**

#### **Subplinian opening sequence**

The 2008 eruption began after five hours of low-level precursory seismicity and opened through the northeast sector of the caldera near Cone D. The first vents visible in satellite imagery, on July 13, are west of the 2008 tuff cone and in the west part of the lake north of Cone D (Fig. 8.9). The opening subplinian sequence was characterized by 16-km-high columns and emplaced Units 1A, 1B, and 2, deposits that show continuous normal grading of coarse ash and lapilli. The grain-size, sorting, and fine-ash characteristics of Units 1 and 2 suggest that the opening sequence of the eruption was predominantly magmatic, as high magma flux ( $9 \times 10^6$  kg/s) may have overwhelmed the available water. The abundance of plagioclase-rich lava fragments in Unit 1A shows that the initial vents opened through the plagioclase-rich lava bench beneath the Cone D bench. The activity of multiple vents suggests that the 2008 eruption was fed by a dike that brought magma to the surface in several locations. Water and magma were brought into contact in the 2008 eruption, probably at depths within 1 km of the surface. Dike propagation into the northeast sector of the caldera could have brought magma into contact with groundwater there, or a pathway for water may have opened to bring water to greater depths to interact with magma.

The first evidence of phreatomagmatism in observations of the 2008 eruption was at 21:30 UTC, around 107 minutes into the eruption, when the plume became lighter in color, likely due to an increase in water. This change may have been caused by an increase in water flux into the active vent, a decrease in magma flux at the active vent, or the opening of a new vent, possibly in the enlarged area of Cone D lake. The first

satellite image showing vent locations was taken on July 13, after basal unit deposition, and radar images are not available for the first few hours of the eruption, so no vent-opening timeline can be confirmed for the opening sequence. The opening of a second vent and the addition of a high water-magma ratio eruptive source could have produced the observed plume water contents and the fine ash present in Unit 1B.

Unit 1B contains the first significant fine ash in deposits, evidence of water-magma interaction and the first ash pellets, showing the onset of plume scrubbing. The initiation of phreatomagmatic eruption at a second vent likely produced the fine ash seen in Unit 1B, but meteorological effects like a rainstorm unrelated to eruption processes may have initiated that fine-ash deposition. Whatever processes began the deposition of fine ash in Unit 1B ceased for the emplacement of Unit 2. Decreasing magma flux and column height produced a decrease in median grain size (Pioli et al. 2008), seen in the normal grading of coarse ash and lapilli from Unit 1A through 2. Eruption column heights remained around 14 km above sea level through 00:00 UTC July 13, after deposition of Unit 2, and the plume remained light in color and apparently water-rich. The deposition of fine ash and ash aggregates that began in Unit 1B ceased during emplacement of Unit 2, perhaps due to a decrease in plume water or fine ash content, or the cessation of a rainstorm that may have initiated fine ash deposition in Unit 1B.

### **Transition to higher water-magma ratio: Unit 3**

After the subplinian opening sequence emplaced Units 1 and 2, the eruption transitioned from magmatic to phreatomagmatic. Deposition rates remained high for Unit 3A, as it was emplaced in the few hours between Unit 2 deposition and 00:00 UTC

July 13, when the wind direction shifted for the first time. Unit 3A is typically rich in fine ash, ash pellets, and cored lapilli, indicating that fine ash and water content in the plume had increased back to a level conducive to ash aggregation.

The change in distribution from Unit 3A to 3B is accompanied by changes in deposit character. The ash pellets and cored lapilli present in Unit 3A are absent in Unit 3B, which is better indurated and characterized by laminated ash. The increase in water-magma ratio at the vent may have increased plume water content beyond the conditions of ash aggregate formation and caused plume washing and ash rain deposition, producing the laminations seen in Unit 3B. Both Units 3A and 3B contain scattered lapilli, which are absent in all deposits above Unit 3B. Lapilli were still being produced at the vent and eruption columns still had sufficient energy to transport lapilli to sites 10 km from the vent through the deposition of Unit 3B.

### **High water-magma ratio late-stage eruption: Upper Units**

After Unit 3B was deposited, the rate of deposition was slow for the remaining five weeks of eruption. The median grain size of tephra produced during the remainder of the eruption is around 3.5 to 4 phi, much finer than that of basal deposits (-1 to 1 phi for Units 1-2). Magma flux was much lower during the last five weeks of eruption than in the first four hours of basal unit deposition, allowing for higher water-magma ratio interactions to occur, producing very fine grained tephra units and high plume water contents. The grain-size distributions of all upper deposits except coarse ash units suggest the highest water-magma ratios of the eruption, around a 1:1 mass ratio based upon quantitative grain-size analysis. Pulses of increased magma flux during which

water-magma ratios decreased occurred during the last five weeks of eruption and are recorded in deposits as coarse ash units. Plume heights exceeded 10 km around five times during the last five weeks of eruption, and coarse ash units were likely deposited during these times of increased magma flux. The increased magma flux overwhelmed the addition of external water and caused magmatic fragmentation, producing energetic eruptions and coarse ash deposits.

The active vents producing the upper units changed at several points during the last five weeks of eruption. At the beginning of upper unit deposition, vents in the new lake and Cone D lake were active. Satellite images from July 20 and July 22 show that activity had settled in to the location of the 2008 tuff cone. Multiple vents, perhaps along a dike, remained active throughout the eruption, and water-magma interaction, perhaps in the form of vapor explosions likely occurred simultaneously at these vents.

A variety of facies were deposited in the upper units and stratigraphy varies between locations. Ash-pellet, laminated ash, coarse ash, and massive vesicular ash units comprise the upper units and were deposited in localized units, producing the local variations in stratigraphy. While vent processes controlled the timing of coarse ash deposition, the changes between ash-pellet, laminated ash, and massive vesicular ash units were likely driven by changes in column water and fine-ash content and external meteorological conditions such as rainstorms.

The plume water content was controlled in part by the water-magma ratio of eruptive activity at vents, as higher water-magma ratios contribute more water as steam and non-interactive liquid water to plumes. External weather systems may have contributed water vapor to plumes or released precipitation that washed ash from eruption

columns. Aleutian weather in July and August is commonly wet and windy, with persistent fog and occasional rain. Non-volcanic clouds and rainstorms may have interacted with plumes to alter plume water content and affect the facies deposited. Weather and air conditions are often variable from ground level to a few hundred meters of altitude. During fieldwork, we noted that fog often moved in and out of areas and commonly extended around 100 meters up from the ground. The presence of fog could affect the deposit type, as moisture in fog could facilitate aggregation and the deposition of very fine ash particles, whereas dry conditions might prevent very fine ash from settling out. Weather conditions on Okmok are very dynamic and localized, often changing several times during each day, bringing times of fog and mist as well as brief periods of clear skies.

## **Conclusions**

The hypotheses tested in this study address water-magma interaction and plume processes in the 2008 Okmok eruption. Water-magma interaction increased the explosivity of the 2008 Okmok eruption and the level of water-magma interaction varied throughout the eruption, producing variations in grain size, shape, and componentry. The highest intensity phases of the eruption, the opening sequence, had the highest mass flux and most magmatic characteristics. The water-magma ratio and role of phreatomagmatism was largely controlled by magma mass flux.

Ash pellets and mud rain were deposited under different eruption column conditions but no significant differences were found in the grain-size distribution or componentry of these facies. Plume water contents and meteorologic conditions controlled the structures

and deposit types of upper fine-grained units. Plume scrubbing deposits, ash pellets and mud rain, enhanced the deposition of fine ash within the caldera and on the upper caldera flanks, limiting fine-ash deposition in distal sites.

## References:

- Alfano, F., C. Bonadonna, A. Volentik, C. Connor, S. Watt, D. Pyle, and L. Connor (2010), Tephra stratigraphy, and eruptive volume of the May, 2008, Chaitén eruption, Chile, *Bulletin of Volcanology* 2010-12-06 .
- Arrighi, S., C. Principe, and M. Rosi (2001) Violent strombolian and subplinian eruptions at Vesuvius during post-1631 activity. *Bulletin of Volcanology* 63:126–150
- AVO Okmok eruption reports (2008), Smithsonian Institute Global Volcanism Program, <http://www.volcano.si.edu/world/volcano.cfm?vnum=1101-29-&volpage=weekly>.
- Alaska Volcano Observatory (2011), About Alaska's Volcanoes, 2011(7/12). <http://www.avo.alaska.edu/volcanoes/about.php>.
- Begét, J. E., J. F. Larsen, C. A. Neal, C. J. Nye, and J. R. Schaefer (2004), Preliminary volcano-hazard assessment for Okmok Volcano, Umnak Island, Alaska, 32 pp., Alaska Division of Geological and Geophysical Surveys, College, AK, United States (USA), United States (USA).
- Behncke, B., S. Falsaperla, and E. Pecora (2008), Correlation between seismic and volcanic activity: A tale of three eruptive episodes at Mount Etna (Italy) in November 2006, *Geophysical Research Abstracts EGU General Assembly*, 10.
- Brady, J., and D. Perkins (2010), Mineral Formulae Recalculation, 2010(November 15).
- Burgisser, A. (2005), Physical volcanology of the 2,050 BP caldera-forming eruption of Okmok volcano, Alaska, *Bulletin of Volcanology*, 67(6), 497-525.
- Büttner, R., P. Dellino, L. La Volpe, V. Lorenz, and B. Zimanowski (2002), Thermohydraulic explosions in phreatomagmatic eruptions as evidenced by the comparison between pyroclasts and products from Molten Fuel Coolant Interaction experiments, *Journal of Geophysical Research-Solid Earth*, 107(B11), 2277.
- Büttner, R., P. Dellino, and B. Zimanowski (1999), Identifying magma–water interaction from the surface features of ash particles, *Nature*, 401(6754), 688-690.
- Byers, F. M. (1959), Geology of Umnak and Bogoslof Islands, Aleutian Islands, Alaska. *US Geological Survey Bulletin*, 1028-L, 167--369.
- Carey, S., and R. Sparks (1986), Quantitative models of the fallout and dispersal of tephra from volcanic eruption columns, *Bulletin of Volcanology*, 48(2), 109-125.

- Carrasco-Núñez, G., M. H. Ort, and C. Romero (2007), Evolution and hydrological conditions of a maar volcano (Atexcac crater, Eastern Mexico), *Journal of Volcanology and Geothermal Research*, 159(1-3), 179-197, doi: DOI: 10.1016/j.jvolgeores.2006.07.001.
- Casadevall, T. J. (1994), *Volcanic ash and aviation safety: proceedings of the first international symposium on volcanic ash and aviation safety*, DIANE Publishing.
- Cashman, K. V. (1992), Groundmass crystallization of Mount St. Helens dacite, 1980–1986: a tool for interpreting shallow magmatic processes, *Contributions to Mineralogy and Petrology*, 109(4), 431-449.
- Dellino, P., and L. L. Volpe (1995), Fragmentation versus transportation mechanisms in the pyroclastic sequence of Monte Pilato-Rocche Rosse (Lipari, Italy), *Journal of Volcanology and Geothermal Research*, 64(3-4), 211-231, doi: DOI: 10.1016/0377-0273(94)00084-T.
- Dellino, P., and G. Liotino (2002), The fractal and multifractal dimension of volcanic ash particles contour: a test study on the utility and volcanological relevance, *Journal of Volcanology and Geothermal Research*, 113(1-2), 1-18, doi: DOI: 10.1016/S0377-0273(01)00247-5.
- Fierstein, J., and M. Nathanson (1992), Another look at the calculation of fallout tephra volumes, *Bulletin of Volcanology*, 54, 156, 1992.
- Finney, B., S. Turner, C. Hawkesworth, J. Larsen, C. Nye, R. George, I. Bindeman, and J. Eichelberger (2008), Magmatic Differentiation at an Island-arc Caldera: Okmok Volcano, Aleutian Islands, Alaska, *Journal of Petrology*, 49(5), 857.
- Ford, C. E., D.G. Russell, J.A. Craven, and M. R. Fisk (1983), Olivine-Liquid Equilibria: Temperature, Pressure and Composition Dependence of the Crystal/Liquid Cation Partition Coefficients for Mg, Fe<sup>2+</sup>, Ca and Mn, *Journal of Petrology*, 24(3), 256-266, doi: 10.1093/petrology/24.3.256.
- Folch, A., A. Costa, A. Durant, and G. Macedonio (2010), A model for wet aggregation of ash particles in volcanic plumes and clouds: 2. Model application, *Journal of Geophysical Research*, 115, B09202, doi:10.1029/2009JB007176.
- Gudmundsson, M. T., R. Pedersen, K. Vogfjörð, B. Thorbjarnardóttir, S. Jakobsdóttir, M. J. Roberts (2010), Eruptions of Eyjafjallajökull Volcano, Iceland, *Eos Transactions AGU*, 91(21), 190, doi:10.1029/2010EO210002.

- Gudmundsson, M.T., Hoskuldsson, A., Larsen, G., Sigmarsson, O., Hognadottir, T., Oddsson, B., Magnusson, E., Oskarsson, N., Sigmundsson, F., Einarsson P., Hreinsdottir, S., Pedersen, R. Jonsdottir, I, Thordarson, T., Hayward C., Hartley, M., Meara, R., Vogfjord, K., Kjartansson, E., Jakobsdottir, S., Bjornsson, H. Karlsdottir, S., Zophoniasson, S., (2010). The April 2010 eruption of the ice-capped Eyjafjallajökull, South Iceland. EGU General Assembly 2010. <http://adsabs.harvard.edu/abs/2010EGUGA..1215733G>
- Gudmundsson, M., E. Magnusson, B. Oddsson, T. Hognadottir, A. Hoskuldsson, et al. (2011) The complex interplay between magma, water and ice in the 2010 Eyjafjallajökull eruption. IUGG General Assembly 2011.
- Höskuldsson, A. et al. (2010), The Eyjafjallajökull eruption April to May 2010: Magma fragmentation, plume and tephra transport, and course of events. Volcanological Workshop Abstracts AGU Fall Meeting, 2010.
- Larsen, J., C. Nye, and L. Ray (2000), The 2050 BP Okmok caldera forming event: evidence for magma mixing as an eruption trigger, EOS Transactions AGU, 81.
- Larsen, J. F., C. Neal, J. Schaefer, J. Begét, and C. Nye (2007), Late Pleistocene and Holocene caldera-forming eruptions of Okmok Caldera, Aleutian Islands, Alaska; Volcanism and subduction; the Kamchatka region, Geophysical Monograph, 172, 343-364, doi: 10.1029/172GM24.
- Larsen, J., C. Neal, P. Webley, J. Freymueller, M. Haney, S. R. McNutt, D. Schneider, S. Prejean, J. Schaefer, and R. Wessels (2009), Eruption of Alaska volcano breaks historic pattern, EOS Transactions AGU, 90(20), 173-174.
- Larsen, G., et al (2010), On-land distribution and modes of deposition of the Eyjafjallajökull 2010 tephra, American Geophysical Union, Fall Meeting 2010.
- Lassalle, J., and D. Pyle (1995), Assessment of the minimum volume of tephra fall deposits, Journal of Volcanology and Geothermal Research, 69(3), 379-382.
- Macdonald GA (1972). *Volcanoes*. Prentice-Hall Inc., Englewood Cliffs. 510 pp.
- Mann, D., J. Freymueller, and Z. Lu (2002), Deformation associated with the 1997 eruption of Okmok volcano, Alaska, Journal of Geophysical Research, 107(B4).
- Masterlark, T., M. Haney, H. Dickinson, T. Fournier, and C. Searcy (2010) Rheologic and structural controls on the deformation of Okmok volcano, Alaska: FEMs, InSAR, and ambient noise tomography, Journal of Geophysical Research, Solid Earth, 115, B02409. doi:10.1029/2009JB006324
- Mastin, L. G. (2007), Generation of fine hydromagmatic ash by growth and disintegration of glassy rinds, Journal of Geophysical Research-Solid Earth, 112(B2), B02203.

- McGimsey, R. G., C. A. Neal, and C. M. Riley, (2001), Areal distribution, thickness, mass, volume, and grain size of tephra-fall deposits from the 1992 eruptions of Crater Peak vent, Mt. Spurr volcano, Alaska, U.S. Geological Survey Open File Report, 01– 370, 2001.
- McNutt, S.R., (1989), Some seismic precursors to eruptions at Pavlof Volcano, Alaska, October 1973 - April 1986. in: Latter, J.H. (ed.), IAVCEI Proceedings in Volcanology, v. 1, pp. 463-485, 1989.
- Miller, T.P., R.G. McGimsey, D.H. Richter, J.R. Riehle, C.J. Nye, M.E. Yount, and J. A. Dumoulin (1998), Catalog of the historically active volcanoes of Alaska, U.S. Geological Survey Open-File Report 98-582, , 104 p.
- Miyagi, Y., J. T. Freymueller, F. Kimata, T. Sato, and D. Mann (2004), Surface deformation caused by shallow magmatic activity at Okmok Volcano, Alaska, detected by GPS campaigns 2000-2002, *Earth, Planets and Space*, 56(12), e29-e32.
- Neal, C.A., R.G. McGimsey, J.P. Dixon, C.E. Cameron, A.A. Nuzhdaev, and M. Chibisova (2011), 2008 Volcanic activity in Alaska, Kamchatka, and the Kurile Islands: Summary of events and response of the Alaska Volcano Observatory: U.S. Geological Survey Scientific Investigations Report 2010-5243, 94 p.
- Newhall, C. G., and S. Self (1982), The Volcanic Explosivity Index (VEI) An Estimate of Explosive Magnitude for Historical Volcanism, *Journal of Geophysical Research*, 87(C2), 1231–1238, doi:10.1029/JC087iC02p01231.
- Patrick, M. R., A. J. L. Harris, M. Ripepe, J. Dehn, D. A. Rothery, and S. Calvari (2007), Strombolian explosive styles and source conditions: insights from thermal (FLIR) video, *Bulletin of Volcanology*, 69(7), 769-784.
- Pioli, L., E. Erlund, E. Johnson, K. Cashman, P. Wallace, M. Rosi, and H. Delgado Granados (2008), Explosive dynamics of violent Strombolian eruptions: The eruption of Parícutin Volcano 1943–1952 (Mexico), *Earth and Planetary Science Letters*, 271(1-4), 359-368, DOI: 10.1016/j.epsl.2008.04.026.
- Raue, H. (2004), A new model for the fracture energy budget of phreatomagmatic explosions, *Journal of Volcanology and Geothermal Research*, 129(1-3), 99-108.
- Resmini, R. G. (2010), On a Model for Generating Theoretical Crystal Size Distributions (CSDs) in Igneous Systems: A Moment Transformation Approach, *Mathematical Geosciences*, 1-8.
- Rose, W. I., and A. J. Durant (2009), Fine ash content of explosive eruptions, *Journal of Volcanology and Geothermal Research*, 186(1-2), 32-39, DOI: 10.1016/j.jvolgeores.2009.01.010.

- Schumacher, R., and H. Schmincke (1995), Models for the origin of accretionary lapilli, *Bulletin of Volcanology*, 56, 626--639.
- Self, S., J. Kienle, and J. Huot (1980), Ukinrek Maars, Alaska, II. Deposits and formation of the 1977 craters, *Journal of Volcanology and Geothermal Research*, 7(1-2), 39-65, DOI: 10.1016/0377-0273(80)90019-0.
- Self, S. (1976) The recent volcanology of Terceira, Azores. *Journal of the Geologic Society of London* 132:645-666
- Shea, T., J. F. Larsen, L. Gurioli, J. E. Hammer, B. F. Houghton, and R. Cioni (2009), Leucite crystals: Surviving witnesses of magmatic processes preceding the 79AD eruption at Vesuvius, Italy, *Earth and Planetary Science Letters*, 281(1-2), 88-98, DOI: 10.1016/j.epsl.2009.02.014.
- Sheridan, M. F., and K. H. Wohletz (1983), Hydrovolcanism: Basic considerations and review, *Journal of Volcanology and Geothermal Research* 17(1-4), 1-29, DOI: 10.1016/0377-0273(83)90060-4.
- Smithsonian Global Volcanism Program (2011), Eyjafjallajökull Monthly Reports, 2011(3/13).
- Smithsonian Global Volcanism Program (2011), Okmok Eruptive History, 2011(3/13).
- Sorem, R. K. (1982), Volcanic ash clusters: Tephra rafts and scavengers, *Journal of Volcanology and Geothermal Research*, 13(1-2), 63-71, DOI: 10.1016/0377-0273(82)90019-1.
- Sparks, R., S. Self, and G. Walker (1973), Products of ignimbrite eruptions, *Geology*, 1(3), 115.
- Textor, C., H. F. Graf, M. Herzog, J. M. Oberhuber, W. I. Rose, and G. G. J. Ernst (2006), Volcanic particle aggregation in explosive eruption columns. Part I: Parameterization of the microphysics of hydrometeors and ash, *Journal of Volcanology and Geothermal Research*, 150(4), 359-377, DOI: 10.1016/j.jvolgeores.2005.09.007.
- Textor, C., H. F. Graf, M. Herzog, J. M. Oberhuber, W. I. Rose, and G. G. J. Ernst (2006), Volcanic particle aggregation in explosive eruption columns. Part II: Numerical experiments, *Journal of Volcanology and Geothermal Research*, 150(4), 378-394, DOI: 10.1016/j.jvolgeores.2005.09.008.
- Vergnolle, S., and M. Mangan (2000), Hawaiian and Strombolian eruptions, in *Encyclopedia of Volcanoes* edited by H. Sigurdsson, pp. 447–461, Academic Press.

- Walker, G. P. L. (1981), Characteristics of two phreatoplinian ashes, and their water-flushed origin, *Journal of Volcanology and Geothermal Research*, 9(4), 395-407, DOI: 10.1016/0377-0273(81)90046-9.
- Wallace, K. L. (2003), Characterization and Discrimination of Holocene Tephra-Fall Deposits, Mount Spurr Volcano, Alaska. M.S. Thesis
- Webley, P., and L. Mastin (2009), Improved prediction and tracking of volcanic ash clouds, *Journal of Volcanology and Geothermal Research*, 186(1-2), 1-9, DOI: 10.1016/j.jvolgeores.2008.10.022.
- Wehrmann, H., C. Bonadonna, A. Freundt, B.F. Houghton, and S. Kutterolf (2006) Fontana tephra: a basaltic Plinian eruption in Nicaragua. In: Rose, W.I., et al. (Ed.), *Volcanic Hazards in Central America: Geological Society of America*, pp. 209–224.
- Wohletz, K., M. Sheridan, and W. Brown (1989), Particle size distributions and the sequential fragmentation/transport theory applied to volcanic ash, *Journal of Geophysical Research*, 94(B11), 15,703–15,721.
- Wohletz K.H. and W. Brown 1995, Particulate size distributions and sequential fragmentation/transport theory, *Proceedings of NSF/JSPS AMIGO-IMI Seminar*, Santa Barbara, CA, June 8-13, 1995.
- Wohletz, K., G. Orsi, and S. de Vita (1995), Eruptive mechanisms of the Neapolitan Yellow Tuff interpreted from stratigraphic, chemical, and granulometric data, *Journal of Volcanology and Geothermal Research*, 67(4), 263-290, DOI: 10.1016/0377-0273(95)00002-C.
- Wohletz, K. H. (1983), Mechanisms of hydrovolcanic pyroclast formation: Grain-size, scanning electron microscopy, and experimental studies, *Journal of Volcanology and Geothermal Research*, 17(1-4), 31-63, DOI: 10.1016/0377-0273(83)90061-6.
- Wohletz, K.H. and B. Zimanowski (2000), Physics of phreatomagmatism, part I: explosion physics, *Terra Nostra* 2000/6, 515-523.
- Wong, L. J., and J. F. Larsen (2009), The Middle Scoria sequence: A Holocene violent strombolian, subplinian and phreatomagmatic eruption of Okmok volcano, Alaska, *Bulletin of Volcanology*, doi: 10.1007/s00445-009-0301-y.
- Zimanowski, B. (1998). Phreatomagmatic explosions. In: Freundt, A., Rosi, M. (Eds.), *From Magma to Tephra, Modelling Physical Processes of Volcanic Eruptions*. Elsevier, Amsterdam.
- Zimanowski, B., G. Fröhlich, and V. Lorenz (1995), Experiments on steam explosion by interaction of water with silicate melts, *Nuclear Engineering and Design*, 155(1-2), 335-343, DOI: 10.1016/0029-5493(94)00880-8.

Zimanowski, B., K. Wohletz, P. Dellino, and R. Büttner (2003), The volcanic ash problem, *Journal of Volcanology and Geothermal Research*, 122(1-2), 1-5.

Zimanowski, B., G. Froehlich, and V. Lorenz (1991), Quantitative experiments on phreatomagmatic explosions, *Journal of Volcanology and Geothermal Research*, 48(3-4), 341-358.